



UNIVERSITÀ DEGLI STUDI DI TRIESTE

XXVII Ciclo del Dottorato di Ricerca in
Environmental and Industrial Fluid Mechanics

LARGE-EDDY SIMULATIONS OF
CONJUGATE HEAT TRANSFER WITH
EVAPORATION-CONDENSATION AND
THERMAL RADIATION

Settore scientifico-disciplinare: ICAR/01

Ph.D. Student: Carlo Cintolesi

Supervisor and Director: Prof. Vincenzo Armenio

Co-Supervisor: Dr Andrea Petronio

Academic Year 2014–2015

Author: Carlo Cintolesi

e-mail: carlo.cintolesi@gmail.com

Affiliation: Doctoral School in
“Environmental and Industrial Fluid Mechanics”.
Dipartimento di Ingegneria e Architettura,
University of Trieste, Piazzale Europa 1,
I-34127 Trieste, Italy

Supervisor: Prof. Vincenzo Armenio

e-mail: armenio@dica.units.it

Affiliation: Dipartimento di Ingegneria e Architettura,
University of Trieste, Piazzale Europa 1,
I-34127 Trieste, Italy

Co-Supervisor: Dr Andrea Petronio

e-mail: a.petronio@iefluids.com

Affiliation: IEFLUIDS S.r.l., Piazzale Europa 1,
I-34127 Trieste, Italy

Day of the defence: 29.04.2016

To cite this work: Carlo Cintolesi, *Large-eddy simulations of conjugate heat transfer with evaporation-condensation and thermal radiation*, Ph.D. Thesis, School of Environmental and Industrial Fluid Mechanics, University of Trieste (2016).

To the tightrope walkers

Abstract

Heat transfer in fluids and between a fluid and a surrounding solid body is often encountered in practical applications. Numerical investigations of such phenomena are of great interest for a number of practical applications, both on industrial and environmental side. Among the others, we mention: home appliances optimisation (ovens, dishwashers, refrigerators), building design (ventilation and heating systems), electronic equipment design (solar collectors, device cooling systems), environmental flow analysis (atmospheric thermal stratification, evaporation from lakes and channels, solar thermal radiation).

Despite the wide range of applications, the correct numerical simulation of such systems poses big challenges. First, the physics governing wet-surface evaporation/condensation processes and thermal radiation is extremely complex; thus, a mathematical model is derived only under simplification hypotheses. Second, the transient nature of surface heat transfer, along with the complex geometry and the anisotropic turbulence flow, requires a careful numerical resolution technique of fluid flow equations. Third, particular attention has to be paid when the different heat transfer modes are coupled, because of their mutual strong interaction.

The present work focuses on numerical investigation of the heat transfer mechanisms in fluid dynamics systems. Specifically, this topic is declined in three different studies: (i) turbulent buoyant flow in a confined cavity with conjugate heat transfer; (ii) thin film evaporation and condensation from a vertical plate inside an enclosure; (iii) radiative heat transfer in systems involving participating media. All these points are tackled. A complete numerical solver is presented and employed.

In all cases, the large-eddy simulation method is adopted in conjunction with a dynamic Lagrangian sub-grid scale turbulent model. Also, the thermal interaction between fluid and solid media is considered by means of conjugate heat transfer; the evaporation and condensation over solid surfaces are studied taking advantage of the thin film assumption; the P_1 -model for radiative heat transfer is integrated in the numerical solver. The heat exchange, through fluid and solid interface, is due to conduction, water change of phase and surface thermal radiation. The temperature alteration into conductive solids, can substantially change the system thermodynamic

equilibrium and can eventually lead to significant variations on the overall fluid dynamics.

An in-house solver, developed within the open-source software package OpenFOAM, is used for the numerical studies and, later, extended to include the effects of thermal radiation and surface radiative heat exchange.

The influence of various solid boundary materials on natural convection in a closed cavity is investigated, pointing out the different effects induced on the fluid motion by thermal conductors and insulators (this part of the research has been published in *Physics of Fluids* [13]). The study has shown that thermal conductive boundaries strongly influence the fluid flow; the use of simplified boundary condition (such as the adiabatic condition) instead of conjugate heat transfer, leads to unrealistic results. Successively, the cooling effects of water evaporation from a plate are studied. The plate materials are changed, and the different behaviour of each substance is analysed (this work has been submitted for publication as journal paper in the *International Journal of Heat and Mass Transfer*). This study has shown that water change of phase completely rules the interface heat exchange and that material heat capacity governs the cooling process of wet bodies. Finally, the thermal radiation in participating media is considered: the physics of thermal radiation is reviewed, the mathematical derivation of the spherical harmonic approximation model is reported and its accuracy studied, the numerical implementation carefully documented and validated. The last part of the work will be extended and submitted in a journal for future publishing. This study has demonstrated that the P_1 -approximation gives satisfactory prediction of thermal radiation effects in participating media, despite its simplicity and fast computation.

Acknowledgements

Finally, my Ph.D. experience has arrived to its end. These have been years of great challenges and intense learning, not only on the scientific side but also within my personal life. Nothing would have been possible without people who have shared with me this range of time and have contributed in different ways to lead me to this conclusion.

First of all, I would like to express my gratitude to Prof. Vincenzo Armenio. Throughout my academical path he has been a valuable mentor, always providing comprehension and support to face many difficulties, along with a constant confidence in my capability. This has been precious for my growth as a researcher. I am extremely indebted with Dr Andrea Petronio, for his daily encouragement and enthusiasm. Through these years he has always been there in several disheartened moments; ready for discuss, giving valuable suggestions and guidance. I am really grateful to Prof. Håkan Nilsson who has given me the possibility to work with him at Chalmers University, as well as for having an outstanding research period in Sweden. Thank for his warm welcome in his cold country, his patience and all the time dedicated to me. I also wish to thank Prof. Pierpaolo Omari for his useful advices and our interesting discussions.

I take this opportunity to sincerely acknowledge my labmates. Thank to Chiara, without whom nothing would have been started; Anthony, for his limitless and contagious enthusiasm; Giulia and Marco, fellows in everyday adventures. And of course to Santiago, Foteini, Marta, Sabrina, and all Iranian colleagues. Thank to Pelmo who rescued me from the long and cold Swedish nights. My research would not have been possible without all of them.

I will be so much grateful to my family, for the many years of patience and unfailing support, for being the strength source of whatever I do.

My last, too few, words for Alessandra, who is still the centre of my thoughts. For everything we did, for everything we will do, come what may.

Trieste, 29 April 2016

Carlo Cintolesi

Contents

Abstract	v
Acknowledgements	vii
Contents	xi
1 Introduction	1
2 Simulation methodology	7
2.1 Governing equations	8
2.1.1 Evaporation and condensation of thin water film	9
2.1.2 Solid-fluid thermal coupling	11
2.2 Review of simulation approaches	12
2.2.1 Direct Numerical Simulation	14
2.2.2 Reynolds-Average Simulation	14
2.2.3 Large-Eddy Simulation	15
2.2.4 Hybrid approaches	16
2.3 LES turbulent model	16
2.3.1 Smagorinsky model	17
2.3.2 Dynamic Lagrangian turbulent model	18
2.3.3 Extension of dynamic Lagrangian model to active scalars	20
2.3.4 LES governing equations	21
2.4 Numerical implementation	21
3 Turbulent buoyant flow in a confined cavity with CHT	23
3.1 Introduction	24
3.2 Simulation methodology	28
3.2.1 Mathematical model	28
3.2.2 Numerical methods	28
3.2.3 Algorithm and implementation	29
3.3 Non-dimensional parameters	29
3.4 Problem description and settings	30
3.4.1 Case geometry	31
3.4.2 Computational domain	32

3.4.3	Characteristic parameters and physical coefficients . . .	32
3.4.4	Validation: initial and boundary conditions	33
3.5	The flow field without CHT	34
3.5.1	The mean field	34
3.5.2	Second order statistics	38
3.6	Simulation with conjugate heat transfer	38
3.6.1	Temperature profile within mild steel walls	41
3.7	Analysis of thermo-fluid dynamics interaction using different materials	44
3.7.1	Simulations settings and procedure	45
3.7.2	First order flow statistics	47
3.7.3	Fluid flow turbulent statistics	54
3.7.4	Temperature distribution within the solid media	57
3.8	Conclusions	62
3.9	Appendix: additional validation analysis	64
4	Thin film evap./cond. from a hot plate in enclosure	69
4.1	Introduction	70
4.2	Problem description	74
4.3	Mathematical and numerical approach	75
4.4	Simulation settings	75
4.4.1	Computational grid	75
4.4.2	Boundary and initial conditions	76
4.4.3	Non-dimensional parameters	78
4.5	Results and discussion	79
4.5.1	Preliminary simulation	79
4.5.2	Drying-process simulations	82
4.6	Conclusions	95
4.7	Appendix: turbulence analysis	97
5	Radiative Heat Transfer	103
5.1	Principles of thermal radiation	104
5.1.1	Definition and generation mechanisms	104
5.1.2	Qualitative aspects	106
5.1.3	Surface interactions with radiation	109
5.1.4	Spectral and directional dependency	111
5.1.5	Radiative quantities	111
5.1.6	Radiative behaviour of materials	114
5.2	Blackbody thermal radiation	118
5.3	RHT for participating media	121
5.3.1	Enclosure framework	122
5.3.2	Radiative transfer equation	122
5.3.3	Radiation scaling parameters	126
5.3.4	Energy and heat flux	127

5.3.5	Contribution to temperature equation	128
5.3.6	Radiative heat transfer on solid boundary	129
6	Spherical harmonics approximation	131
6.1	Review of approximation methods	132
6.1.1	Discrete ordinates method	133
6.1.2	Spherical approximation method	134
6.1.3	Monte Carlo method	136
6.2	Spherical harmonics approximation	137
6.2.1	First order approximation: P_1 -model	140
6.2.2	Boundary conditions	142
6.2.3	Surface radiative heat flux	143
6.3	Modified differential approximation	144
7	Numerical implementation and validation	147
7.1	Radiative model summary	148
7.2	Implementation	153
7.2.1	Radiative heat transfer equations	153
7.2.2	Radiative heat source into the medium	154
7.2.3	Surface radiative heat transfer	158
7.3	Validation	160
7.3.1	Numerical model validation	162
7.3.2	Pure radiative heat transfer	164
7.3.3	Combined conduction and radiation	169
7.3.4	Combined conduction, convection and radiation	170
7.3.5	Surface radiative heat transfer	172
7.4	Conclusions	174
7.5	Appendix: Marshak's boundary condition	175
	Bibliography	179

Chapter 1

Introduction

The thesis is devoted to the numerical study of heat transfer in fluid dynamics systems composed by multiple material domains. The minimal system where heat transfer takes place is composed by two domains, namely a fluid one and a solid one, in contact. If a difference of temperature arises, energy is transferred within the domains and through the interface. Thence, thermal interaction alters the temperature distribution in both media, influencing the overall thermal-fluid dynamics of the system.

Generally speaking, heat transfer is the exchange of energy between physical systems. In a wide range of practical applications, it plays an important role and cannot be neglected in accurate analyses. The fundamental modes of heat transfer are: conduction, convection and thermal radiation. Additionally, water evaporation and condensation can considerably alter the system thermodynamics.

In practical applications, heat transfer effects rule, or strongly influence, many different environmental and industrial systems. A short review on the main applications follows.

In natural convection problems, a correct reproduction of thermal interaction among solid bodies and fluid flow is crucial, since it governs: the boundary layer arising over the buildings surfaces; the night-time thermal stratification above the city in summertime, as well as the general air circulation in sunny days; the sea breeze generation due to the different heat capacities of water and land; the cooling process of electrical equipments, such as home appliances and electronic devices; the air ventilation in buildings; solar collectors efficiency.

In processes where humid air is involved, water evaporation and condensation strongly affect heat transfer. It plays a decisive role in working principles of domestic devices, such as the drying process in a dishwasher; the cooking procedure and food evaporation in oven; the water condensation in fridges, and so on. Optimisation of appliance performances together with improvement of their design requires an accurate investigation of heat

exchange along with evaporation, condensation and vapour transport.

High-temperature systems are characterised by the presence of thermal radiation. It is the case of combustion events (engines, rocket nozzles, furnaces), sun emission for greenhouses or solar collectors, nuclear reaction in power plants. Nevertheless, radiation can also influence low-temperature systems leading to non-negligible effects if combined with convection and conduction (electric ovens, lamp bulb enclosures, room heating systems).

An experimental investigation of the above-mentioned problems can be expensive and laborious. Hence, numerical simulation is an useful tool for studying such thermal-fluid dynamics systems.

The OpenFOAM software package has been used to develop a numerical solver able to numerically reproduce the aforementioned heat transfer modes, along with the surfaces heat transfer and fluid motion. The main solver has been developed in previous projects, within the Doctoral School *Environmental and Industrial Fluid Mechanics* of University of Trieste. It contains the modelling of conduction-convection modes, the surface heat transfer by conduction and the vapour transport, evaporation and condensation phenomena. Within the present project the turbulent dynamic Lagrangian model has been improved and extended for computing the temperature and vapour sub-grid scale contribution. Also, the P_1 thermal radiation model and the surface radiative heat transfer on solid media has been implemented.

Accurate reproduction by numerical simulation of the fluid dynamics of complex systems, involving heat transfer in the fluid and across solid surfaces in presence of liquid films, is a formidable challenge from both theoretical and modelling point of view.

If, from one side, the physics and the equations governing the fluid dynamics are well established, the physical processes behind water evaporation and condensation is extremely complex, and a mathematical model can be derived only under simplified assumptions. Also, thermal radiation poses some theoretical problems: the radiative properties of materials can depend on a number of different variables, and even an experimental measure is hard to be carried out. Moreover, the directional and spectral dependency of radiation considerably increase the complexity of the mathematical formulation. Hence, the radiative heat transfer equation is derived under very strict hypotheses. A complete mathematical model, that includes all the thermal radiation features, is so complex that results useless.

From numerical perspective, the correct resolution of the governing equations is not less problematic. The fluid flow arising in practical applications is often turbulent (*exempli gratia*, the buoyancy driven flows) and an accurate numerical model has to be adopted in order to obtain trustworthy results. The large-eddy simulation approach is used here, leading to a three-dimensional transient simulation. The fluid equations are numerically

resolved over a discrete computational grid; the scales of motion bigger than the grid width are directly solved, while the contribution of the small scales has to be modelled by a suitable sub-grid scale model. Among the large number of models available, the dynamic Lagrangian one is adopted: the small scales contribution mimics an increase of fluid viscosity (eddy viscosity hypothesis), the viscosity is considered proportional to the spatial variation of the resolved fluid velocity (resolved strain rate tensor), the proportionality constant is determined using information from the large scales of motion along some flow homogeneous directions (dynamic models) or the streamlines (Lagrangian dynamic model). The dynamic models prove to be highly accurate, and the Lagrangian model has a wide range of practical applications, since it does not need any direction of homogeneity. We extend the computation of the sub-grid scale contribution to temperature and vapour equations, *idem est* we consider also the sub-grid scale thermal and vapour diffusivity.

The surface heat transfer is performed by means of the conjugate heat transfer technique. A number of different techniques are reported in literature, trying to overcome the two main problems intrinsic in such methods: numerical instability arising in case of high difference of temperature or thermal conductivity between the materials; the long time eventually required to reach the surface thermal equilibrium. The following approach is adopted here: onto the fluid-solid boundary a balance of the heat flux is performed and iterated over a loop, since the local thermal equilibrium is reached. In practical applications, this method is found to be numerically stable.

The water evaporation and condensation phenomena are modelled under the thin film approximation: solid surfaces are wet by a thin water film, that can evaporate or condensate. Water phase is not directly solved, but the variation of its film thickness is accounted for by mass conservation law. Evaporation absorbs energy, whereas condensation releases it. The resulting heat source or sink term is added to the temperature equation of the cells near the interface.

Thermal radiation heat transfer is a new feature implemented in the solver. The governing equation for radiation results in an integro-differential equation for each possible direction of propagation of radiation. Different methods for solving such complex equation have been developed. Among the others, the P_1 -approximation has been chosen by virtue of its simplicity, completeness (can simulate radiative participating media) and the small computational efforts required. Indeed, when radiation is coupled with conjugate heat transfer, a transient solver has to perform coupling loops in order to reach the local thermal equilibrium between radiation, temperature and surface heat transfer. Therefore, a computational demanding model for radiation can considerably increase the computational time, eventually leading to unfeasible simulations. For this reason, the P_1 -approximation is adopted for modelling the radiative heat transfer in the fluid medium. A suitable

condition to compute the surface radiative heat transfer through fluid and solid interface is also derived and implemented.

To the best of our knowledge, a complete solver able to deal with all the heat transfer modes, and provided by an accurate turbulent flow solver, is not reported in literature. Moreover, the above-mentioned surface radiative heat transfer method is not documented.

The thesis is essentially divided into two main parts:

first: the numerical solver is described and applied to the archetypal cases of turbulent natural convection into a closed square cavity, and water evaporation from a plate in enclosure. The results are validated against experimental data (for the first case); then an analysis of the physical process underlying the systems is reported (cf. chapters 2,3,4);

second: the physics behind thermal radiation is reviewed, along with the complete mathematical model. The mathematical derivation of the approximated model is presented, the numerical implementation is described, the validation and investigation on the model accuracy is carried out (cf. chapters 5,6,7).

Therefore, our work is focused to both investigation of heat transfer phenomena in engineering systems and numerical implementation of thermal radiation. Particularly, the main contributions ascribed to the author are: (i) improvement and extension of the dynamic Lagrangian model implementation for active scalars (temperature and vapour concentration); (ii) investigation of natural convective flow in cavity with conjugate heat transfer; (iii) investigation of water evaporation and condensation from a plate, in an enclosure with surface heat transfer; (iv) implementation of the P_1 -model for radiative heat transfer in participating media; (v) derivation and implementation of a surface radiative heat transfer between fluid and solid media, associated to the P_1 -model. The numerical implementation has been done within the framework of OpenFOAM simulation tools box.

The structure of the present thesis is now depicted. Every chapter has been written to be as self-consistent as possible. Thus, the main equations are sometimes repeated as well as some acronyms redefined. Each chapter is provided by a short introduction and, wherever it makes sense, short conclusions. Due to the different topics approached, an overall conclusion is not given in the end of the thesis.

Chapter 2 presents the simulation methodology adopted in our investigations. First, the mathematical model for fluid flow simulation with conjugate heat transfer and vapour transport, evaporation and condensation is described. Then, the principal simulation methodologies for turbulent flows are briefly reviewed and the large-eddy simulation methodology is presented,

along with the dynamic Lagrangian sub-grid scale model. In the last section, an overview on the solver algorithm is reported.

Chapter 3 is dedicated to investigation of the natural convective flow in a cavity, with two isothermal walls differently heated and two conductive boundaries. First, an experimental case is reproduced without the conjugate heat transfer between solid boundaries and the fluid flow. The results satisfactorily reproduce the experimental and numerical data presented in literature. Then the fluid-solid heat transfer is simulated and the experimental thermal profile reproduced. Finally, the conjugate heat transfer is used to study the influence on different boundary materials to the overall fluid motion. It is pointed out that thermal conductors and insulators strongly influence the flows in different ways.

Chapter 4 reports the study of the evaporation and condensation on a plate located in a square enclosure. The plate is hot while the enclosure is cold, both are wet. A preliminary simulation without conjugate heat transfer and where the water is allowed to evaporate and condensate but the water film thickness does not change, is performed. The statistically steady state configuration is reached and analysed. Then, this configuration is used to initialise other realistic simulations, where the heat transfer and the water film evolution is made active. Three simulations are carried out changing the materials of the plate. The different thermal-physical properties of the materials influence the plate cooling process and the evolution of the fluid flow. The results are analysed and commented.

Chapter 5 presents a review of the physical properties of thermal radiation and the derivation of the complete radiative heat transfer equation. The first section reports the principle of radiation and the radiative behaviour of different materials. The radiative parameters, variables and quantities are described. In the second section, radiation from an ideal blackbody is presented. In the final section, the governing equation for radiative heat transfer in participating media are stated.

Chapter 6 describes the P_1 -approximation. An overview of the main approaches for the resolution of the radiative equation is reported, followed by the description of the mathematical background of the general spherical harmonic approximation method. Then, the P_1 -model is presented, along with the radiative surface heat transfer equation. In the last part, a modified method (that tries to overcome the drawbacks of the P_1) is sketched.

Chapter 7 shows the numerical implementation and the validation of the radiative model aforementioned. First, the set of governing equations are summarised. Then, the radiative model implementation is described: parts of the code are explicitly reported and commented. Finally, the new solver is validated against several benchmark cases, the interaction of radiation with convection and conduction is carefully analysed, the effects of surface radiative heat transfer are studied for a test case. The simulation results are compared with several numerical data presented in literature, and the

prediction capability of the P_1 -model is discussed.

Chapter 2

Simulation methodology

Contents

2.1	Governing equations	8
2.1.1	Evaporation and condensation of thin water film	9
2.1.2	Solid-fluid thermal coupling	11
2.2	Review of simulation approaches	12
2.2.1	Direct Numerical Simulation	14
2.2.2	Reynolds-Average Simulation	14
2.2.3	Large-Eddy Simulation	15
2.2.4	Hybrid approaches	16
2.3	LES turbulent model	16
2.3.1	Smagorinsky model	17
2.3.2	Dynamic Lagrangian turbulent model	18
2.3.3	Extension of dynamic Lagrangian model to active scalars	20
2.3.4	LES governing equations	21
2.4	Numerical implementation	21

An overview of the mathematical model behind the numerical solver `coupledHeatVapourFoam`, build up within the Doctoral School *Environmental and Industrial Fluid Mechanics* of the University of Trieste, is given in this chapter. The solver has been developed, in the framework of OpenFOAM toolbox, by Dr Andrea Petronio [54] first, and Dr Paweł Sosnowsky [68] later.

A comprehensive description of the original solver is not the aim of this thesis. Therefore, just the main characteristics are here pointed out. Further details can be found in the Ph.D. theses [54, 68].

In the beginning, the governing equations are presented, along with the evaporation/condensation model and the conjugate heat transfer model. Then, a general summary of the principal numerical approaches to fluid dynamics problems is reported, followed by a focus on the large-eddy simulation approach and the dynamic Lagrangian turbulence model adopted. At the end, the numerical implementation is shortly outlined.

In the following, the subscripts are used to specify the particular use of a general quantity. If ϕ is a generic variable, then: ϕ_f is the fluid related variable; ϕ_s is the solid related variable; ϕ_w is related to vapour concentration; ϕ_w is the variable evaluated on the wall; ϕ_0 is the variable reference value; ϕ_{SGS} is the sub-grid scale quantity. The International System of Units is used to express the value of all quantities.

2.1 Governing equations

The `coupledHeatVapourFoam` is a multi-region solver. This means that it can deal with multiple computational domains (in our studies, solids and fluids) that interact one another. Different physical phenomena are simulated:

- ▶ the fluid dynamics is solved using the Large-Eddy Simulation (LES) method. The flow is considered incompressible, the Boussinesq approximation is adopted for buoyancy force, and dynamic Lagrangian turbulence model is used (cf. following section 2.3);
- ▶ temperature diffusion is ruled by convection and conduction in fluid domains, just conduction in solid domains. The boundary heat exchange between solid and fluid media is computed by the Conjugate Heat Transfer (CHT) technique (cf. following section 2.1.2);
- ▶ the presence of a mixture in fluid medium can be simulated. A general mixture model is applied to the case of water vapour in air. The vapour evaporates and condensates on a thin water film above solid boundaries, diffuses in the fluid domain, contributes to the boundary heat flux and buoyancy force (cf. following section 2.1.1).

All the three phenomena are strictly related and strongly interact among them. The reciprocal influences are maximum onto the solid-fluid boundaries. Here the conjugate heat transfer between media takes place, along with the release or absorption of latent heat by water condensation or evaporation, and the mass transfer between the liquid and vapour phase. Furthermore, in natural convection problems, buoyancy force peaks and triggers turbulent fluctuations near the solid boundaries.

The governing equations for the fluid domain are: the continuity equation, the momentum equation, the buoyancy force equation. They read, respectively:

$$\frac{\partial u_i}{\partial x_i} = 0, \quad (2.1)$$

$$\frac{\partial u_i}{\partial t} + \frac{\partial u_i u_j}{\partial x_j} = -\frac{1}{\rho_0} \frac{\partial p}{\partial x_i} + \nu \frac{\partial^2 u_i}{\partial x_j \partial x_j} - \frac{\rho}{\rho_0} g \delta_{i2}, \quad (2.2)$$

$$\frac{\rho}{\rho_0} = 1 - \beta_T (T - T_0) - \beta_\omega (\omega - \omega_0), \quad (2.3)$$

where u is the fluid velocity, p is the pressure, T is the temperature, ρ is the space-time variable fluid density, ω is the solute concentration. Moreover, ν is the molecular kinematic viscosity, g is the gravity acceleration and $\beta_{T/\omega}$ is the thermal/solute expansion coefficient. The vapour concentration is defined as

$$\omega = \frac{m_v}{m_a + m_v}, \quad (2.4)$$

in which m_v and m_a are the mass of vapour and air, respectively.

Temperature and vapour concentration in fluid medium are both modelled as active scalars. They are diffused and transported within the fluid according to:

$$\frac{\partial T_f}{\partial t} + u_j \frac{\partial T_f}{\partial x_j} = \alpha_f \frac{\partial^2 T_f}{\partial x_j \partial x_j} + S_f, \quad (2.5)$$

$$\frac{\partial \omega}{\partial t} + u_j \frac{\partial \omega}{\partial x_j} = \alpha_\omega \frac{\partial^2 \omega}{\partial x_j \partial x_j}, \quad (2.6)$$

where $\alpha_{f/\omega}$ is the thermal/vapour diffusion coefficient, and S_a represents the heat source due to vapour condensation.

Temperature diffusion in solid media is ruled by the classical equation of diffusion:

$$\frac{\partial T_s}{\partial t} = \alpha_s \frac{\partial^2 T_s}{\partial x_j \partial x_j} + S_s, \quad (2.7)$$

where α_s is the solid thermal diffusivity and S_s is the sink term due to evaporation process.

In the next section 2.1.1 a model for the source/sink term is proposed. Equation (2.14) provides an explicit expression of this term.

2.1.1 Evaporation and condensation of thin water film

The wetting layer is not solved directly, rather it is modelled under the thin film assumption: the scalar H represents the film thickness at the boundary and its evolution equation is derived from the mass balance:

$$\frac{\partial H}{\partial t} = \frac{\rho_a}{\rho_w} U_\omega, \quad (2.8)$$

where ρ_a is the air density, ρ_w is the water density and U_ω is the magnitude of evaporation/condensation velocity. After the investigation of Petronio [54], the value $\rho_a/\rho_w = 0.001$ is adopted in our numerical simulations.

If the gas is made of a binary mixture, in which the two species are not soluble (like air and vapour), such velocity can be estimated by:

$$\mathbf{U}_\omega = -\frac{\alpha_\omega}{1 - \omega_\Gamma} \left(\frac{d\omega}{dn} \Big|_\Gamma \right) \mathbf{n}, \quad (2.9)$$

where the subscript Γ indicates that the quantities are evaluated at the solid-fluid interface, \mathbf{n} is the versor normal to the wall, oriented toward the fluid phase. In literature, such estimation is sometimes named as the *semi-impermeable* model (cf. Petronio [54] and Welty *et al.* [82]).

The water film is considered in thermal equilibrium with air and solid media. In fact, adopting the thin film assumption, the water onto the wetted surface has a very short diffusion time with respect to other system components.

In order to solve equation (2.9), the value of vapour concentration at the interface Γ is required. It can be computed by:

$$\omega_\Gamma = \frac{M_v}{M_a} \frac{p_{sat}(T_\Gamma) \phi_\Gamma}{p_{atm} - \left(1 - \frac{M_v}{M_a}\right) p_{sat}(T_\Gamma) \phi_\Gamma}, \quad (2.10)$$

where $M_a = 28.97, g/mol$ and $M_v = 18.02 g/mol$ are the values of molar mass of air and water vapour respectively; p_{atm} and p_{sat} are the vapour atmospheric pressure at actual and at saturation condition, respectively; ϕ_Γ is the relative humidity evaluated at the interface by:

$$\phi_\Gamma = \frac{P}{p_{sat}(T_\Gamma)}, \quad (2.11)$$

with P is the equilibrium vapour pressure. If the wall is wet, the relative humidity is assumed to be $\phi_\Gamma = 1$, while if it is dry $\phi_\Gamma = 0$. The Buck's equation provides an evaluation formula for saturation pressure:

$$p_{sat}(T) = 611.85 \exp \left[\frac{17.502 (T - 273.15)}{240.9 + (T + 273.15)} \right], \quad (2.12)$$

under the hypothesis of the atmospheric pressure value equal to $p_{atm} = 101325 Pa$. Note that this expression is strictly valid at water-air interface.

The last term that has to be specified, is the heat source or sink $S_{f/s}$ due to the water change of phase: evaporation subtracts energy, whereas condensation releases it. The energy exchanges occur onto the fluid/solid interface, and can be expressed as a boundary heat flux vector:

$$\mathbf{q}_{ev/con} = \rho^* L_h \mathbf{U}_\omega, \quad (2.13)$$

where $\rho^* = \rho_v + \rho_a$ and ρ_v is the vapour density, $L_h = 2.26 \times 10^6$ is the latent heat of vaporisation (also called *enthalpy of vaporisation*). The value of vapour density is set to $\rho^* = 1$, as proposed by Petronio [54], and L_h is considered constant throughout the process.

The heat flux (2.13) is not directly employed in the balance of boundary heat exchanges. It is rather used to derive the temperature source/sink term, that is added to the first cell next to the boundary. The latter approach is adopted because it has been empirically found to be more numerically stable with respect to the former. If condensation occurs air is heated, thus the source term S_f in equation (2.5) has a positive value and $S_s = 0$ in equation (2.7). Conversely, if evaporation occurs the solid is cooled, hence $S_f = 0$ and S_s assume negative values. The source/sink term is non-zero only on one side of the interface (air or solid).

The source/sink term represents the energy stored in the cell, therefore it is the divergence of the heat flux:

$$S_{f/s} = -\frac{\rho^* L_h}{(\rho C_p)_{f/s}} \nabla \cdot \mathbf{U}_\omega, \quad (2.14)$$

and it has to be divided by the heat capacity at constant pressure of the medium on which is applied, in order to be inserted in temperature equation.

It can be noticed that equation (2.14) is not mathematically well defined, since \mathbf{U}_ω is defined by (2.9) just to solid-fluid interface. With an abuse of notation, the symbol \mathbf{U}_ω represents here the zero-extension of the evaporation/condensation velocity field to fluid domain: \mathbf{U}_ω is computed by (2.9) on the solid-fluid interface, while it is set to be the zero-vector elsewhere.

The vapour transport equation (2.6) is provided with the Dirichlet condition (2.10) if boundaries are wetted, and switches to the Neumann condition

$$\left. \frac{d\omega}{dn} \right|_\Gamma = 0, \quad (2.15)$$

if the water film completely evaporates. The boundary condition (2.15) does not allow diffusive flux at the dry surfaces. The surfaces are considered dry when H decreases under a certain value. In that case, the U_ω is forced to be zero and re-condensation is not anymore allowed.

More details on the evaporation/condensation vapour model herein described, can be found in Petronio [54].

2.1.2 Solid-fluid thermal coupling

The temperature equations (2.5) and (2.7) are provided with boundary conditions accounting for the solid/fluid heat transfer mechanism.

A thermal coupling boundary condition at the solid-fluid interface Γ is introduced, enforcing the continuity of temperature and the balance of the

heat fluxes:

$$T_s|_{\Gamma} = T_f|_{\Gamma} \quad (2.16)$$

$$k_s \left(\frac{\partial T_s}{\partial n} \right) = k_f \left(\frac{\partial T_f}{\partial n} \right) \quad (2.17)$$

where n denotes the normal to the surface and k is the thermal conductivity. Different techniques are available in literature to perform the coupling of the thermal field at the interface (see, among the others Quarteroni and Valli [57]). A Neumann-Neumann decomposition method is here applied, assuring the balance of both (2.16) and (2.17) below a prescribed tolerance. More details on the coupling methodology herein employed can be found in Sosnowski [68] and Sosnowski *et al.* [69].

2.2 Review of simulation approaches

The motion of a Newtonian fluid is ruled by the momentum equation together with the continuity equation. When a temperature gradient and/or a solute (in our investigations water vapour in air) is present, a buoyancy force arises and an additional term needs to be added to equations.

The complete set of equations has been displayed in section 2.1; here we focus our attention on the momentum equation. If the fluid is assumed to be incompressible and the buoyancy force is taken into account via the Boussinesq approximation, the momentum equation reads:

$$\frac{\partial u_i}{\partial t} + \frac{\partial u_i u_j}{\partial x_j} = -\frac{1}{\rho_0} \frac{\partial p}{\partial x_i} + \nu \frac{\partial^2 u_i}{\partial x_j \partial x_j} - \frac{\rho}{\rho_0} g \delta_{i2}, \quad (2.18)$$

with the notation already introduced.

Mathematically, once that temperature T and solute concentration ω are given, equations (2.1-2.3), provided with boundary conditions, completely describe a fluid-dynamic system. Numerically, the correct resolution of these equations requires a sufficiently fine computational grid. If the flow is in a turbulent regime, a high grid resolution is needed, eventually leading to a high time-consuming computation.

Turbulence can be described through its characteristics (cf. Lumelly [73]), but an exact and synthetic definition is missing. However, following Piomelli [55], we can say that “turbulence is an irregular, chaotic state of fluid motion that occurs when the instabilities present in the initial or boundary conditions are amplified, and a self-sustained cycle is established in which turbulent eddies (coherent region of vorticity) are generated and destroyed”. In Figure 2.1, the turbulent eddies in a water channel can be visualised.

The direct resolution of the governing equations is also known as a Direct Numerical Simulation (DNS). It is the more straightforward and natural



Figure 2.1: Water channel with turbulence structures. Digital modification of an original draw by Leonardo da Vinci (~ 1508).

approach. However, the numerical solution of turbulent flow systems can be also achieved using different approximation methods.

The chaotic nature of turbulence inspired the filtering approach: the velocity field is decomposed into two parts:

$$u_i = \underbrace{\langle u_i \rangle}_{\text{main}} + \underbrace{u'_i}_{\text{fluctuation}}, \quad (2.19)$$

where the angular brackets represent an averaging operation. When the equations of motion are averaged, one obtains the equations that describe the evolution of the mean quantities, and the fluctuations terms that include the effects of turbulence. In order to close the system, the fluctuations terms need to be modelled by a turbulence model.

If the average is performed in time, the operation takes the name of Reynolds average and leads to the Reynolds-Averaged Navier-Stokes Equations (RANSE). If it is performed in space, it is also called space filter and leads to the Large-Eddy Simulation methodology.

From a mathematical point of view, a time average and a space filter of a chaotic field u_i can be generally expressed by a convolution integral (cf. Germano [24]) that reads:

$$\langle u_i(\mathbf{x}, t) \rangle = \int u_i(\mathbf{x}', t') G_{\ell, \theta}(\mathbf{x} - \mathbf{x}', t - t') dt' d\mathbf{x}', \quad (2.20)$$

where ℓ and θ are the characteristics filter length and time, respectively, and $G_{\ell, \theta}$ is the convolution nucleus, such that

$$\int G_{\ell, \theta}(\mathbf{x} - \mathbf{x}', t - t') dt' d\mathbf{x}' = 1. \quad (2.21)$$

Formally, the class of filters (2.20) parametrised by ℓ and θ , constitutes a hierarchy of filters that includes the direct approach.

The three main simulation methodologies aforementioned are now briefly described.

2.2.1 Direct Numerical Simulation

The DNS is the more natural approach to the fluid dynamic problems. The unfiltered governing equations are discretised and numerically solved. No additional turbulence model needs to be adopted. Within the filter operation framework, the unfiltered equations can be recovered applying the trivial filter:

$$\langle u_i(\mathbf{x}, t) \rangle = u_i(\mathbf{x}, t), \quad (2.22)$$

obtained when $\ell = 0$ and $\theta = 0$, *i.e.* the characteristics length and time are zero.

Assuming that the computational grid is fine enough to capture also the smallest scales of motion, the DNS provides an accurate transitional (time-dependent) solution of the fluid dynamics systems. The only source of error is the numerical discretisation itself, since no approximation model is used.

Even if the DNS gives the most reliable results, it has an important drawback: in order to resolve all the scale of motion, a number of grid points proportional to

$$\text{grid points} \sim Re^{9/4} \quad (2.23)$$

is required, where Re is the Reynolds number, that is the ratio between the inertial forces and the viscous forces:

$$Re = \frac{UL}{\nu} \quad (2.24)$$

where U is the characteristic velocity and L is the characteristic length of the system. Turbulent flows are characterised by high values of Reynolds number and the computation cost scales like Re^3 (cf. Pope [56]). Thus, the DNS of a turbulent flow can lead to a tremendous computational effort. For this reason, approximation methods have been developed.

2.2.2 Reynolds-Average Simulation

In a Reynolds-Average Simulation (RAS), the governing equations are averaged in time using the filter:

$$\langle u_i(\mathbf{x}, t) \rangle = \frac{1}{\theta} \int_t^{t+\theta} u_i(\mathbf{x}, t') dt', \quad (2.25)$$

where θ is a time interval much longer than the characteristic time of turbulent scales. The fluctuation term that appears after averaging, is named Reynolds stress. A large number of turbulent models have been developed for the parametrisation of the Reynolds stress.

The RAS methodology is widely used in many engineering applications. The main advantage of such simulations is the ability to predict the fluid dynamics of fairly complex configurations with a relative low computational

cost. However, this approach has an important shortcoming: the RAS turbulence models have to represent a wide range of scales of motion, that can be strongly affected by the particular configuration (geometry, boundary conditions) of the case under consideration. It seems not possible to find a universal turbulence model, valid for different flow configurations. Moreover, only a statistical steady state configuration can be simulated (as a result of the long-time average operation) and the transitory fluid regime is not captured.

2.2.3 Large-Eddy Simulation

The LES is a method intermediate between DNS and RAS. In this case, the governing equations are filtered by a spatial filter:

$$\langle u_i(\mathbf{x}, t) \rangle = \bar{u}_i(\mathbf{x}, t) = \int u_i(\mathbf{x}', t) G_\ell(\mathbf{x} - \mathbf{x}') d\mathbf{x}', \quad (2.26)$$

where the overbar notation for the filtered quantities is usually preferred to the angular brackets notation. Different convolution nucleus can be used. When the governing equations are numerically solved, an implicit filter is defined by the computational grid (cf. Sagaut [64]):

$$G_{\bar{\Delta}}(\mathbf{x} - \mathbf{x}') = \begin{cases} \frac{1}{\bar{\Delta}} & \text{if } |\mathbf{x} - \mathbf{x}'| \leq \frac{\bar{\Delta}}{2} \\ 0 & \text{otherwise} \end{cases} \quad (2.27)$$

where the filter length is the local grid width, defined by

$$\ell = \bar{\Delta} = (\Delta_x \Delta_y \Delta_z)^{1/3}, \quad (2.28)$$

and $\Delta_{x/y/z}$ are the local cell dimensions in x, y, z directions, respectively.

LES exactly computes the large (compare to the grid size) structures of motion, while the small scales of motion (*i.e.* with a characteristic length smaller than the grid cells width) are modelled with a Sub-Grid Scale (SGS) turbulence model. The different scales of motion of a turbulent flow are sketched in Figure 2.2. The small scales tend to be more isotropic and less case-dependent than the large ones. Hence, it is expected that the LES turbulent models will be simpler and more universal than the RAS models:

The LES approach provides an unsteady and three-dimensional solution for turbulent fluid flow problems. Furthermore, it requires a coarser mesh compared to DNS, but still finer compared to RAS. For this reason, it is less computationally demanding than a DNS, but more than a RAS. Nonetheless, since the large scales unsteady motion are explicitly solved, LES is expected to be more accurate and reliable than RAS for flows in which the large scale unsteadiness is significant.

In the present work, the LES methodology is adopted together with the dynamic Lagrangian turbulent model, that is presented in the following section 2.2.4.

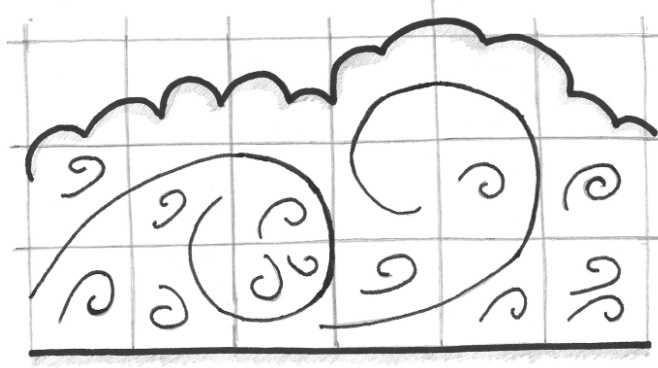


Figure 2.2: Sketch of the different scales of motion of a turbulent fluid flow, compared with the computational grid size.

2.2.4 Hybrid approaches

Other approaches have been developed starting from the three previously described. Just few of them are here mentioned.

The Unsteady-RANS (URANS) equations have been derived from the classical RAS approach. In URANS the time derivative term remains, leading to simulations that are able to capture unsteady features of the flow.

A large number of hybrid approaches, that mix the RAS with LES or DNS, have been recently developed. One of the most widespread of these methods is the Detached-Eddy Simulation (DES), first proposed by Spalart *et al.* [70]. Essentially, during a DES, the URANS simulation is performed near the boundaries, while the LES method is used elsewhere.

A similar technique is adopted for the Partial-Averaged Navier-Stokes (PANS) simulations (ref. Girimaji *et al.* [26]). In this case, the dissipation rate of the turbulent kinetic energy and the mesh size are used as criteria to switch from RAS to a DNS.

2.3 LES turbulent model

In this section, the filtered momentum equations are presented and the dynamic Lagrangian turbulent model is derived.

Applying the implicit grid filter (2.27) to the momentum equations (2.18), ones obtains:

$$\frac{\partial \bar{u}_i}{\partial t} + \frac{\partial \bar{u}_i \bar{u}_j}{\partial x_j} = -\frac{1}{\rho_0} \frac{\partial \bar{p}}{\partial x_i} + \nu \frac{\partial^2 \bar{u}_i}{\partial x_j \partial x_j} - \frac{\partial}{\partial x_j} \tau_{ij}^{RST} - g \frac{\rho}{\rho_0} \delta_{i2}, \quad (2.29)$$

where the fluctuations term, named also *residual stress tensor*, is defined by:

$$\tau_{ij}^{RST} = \overline{u_i u_j} - \bar{u}_i \bar{u}_j. \quad (2.30)$$

The residual tensor can be divided in the anisotropic and isotropic part:

$$\tau_{ij}^{RST} = \underbrace{\tau_{ij}}_{\text{anisotropic}} + \underbrace{\frac{1}{3}\tau_{kk}^{RST}\delta_{ij}}_{\text{isotropic}}. \quad (2.31)$$

If the residual kinetic energy is defined by

$$K_R = \frac{1}{2}\tau_{kk}^{RST}, \quad (2.32)$$

then the fluctuation contribution to the governing equations can be rewritten as:

$$\frac{\partial}{\partial x_j}\tau_{ij}^{RST} = \frac{\partial}{\partial x_j}\tau_{ij} + \frac{2}{3}K_R. \quad (2.33)$$

The isotropic part is included in the pressure term, that is redefined as

$$\bar{p} = \bar{p} + \frac{2}{3}K_R, \quad (2.34)$$

while the anisotropic part has to be modelled with a turbulent model.

2.3.1 Smagorinsky model

In the context of LES, the anisotropic residual stresses τ_{ij} is usually called *Sub-Grid Scale* (SGS) stress tensor. Indeed, this term can be interpreted as the contribution of the small scales of motion (*i.e.* smaller than the grid width) to the large scales.

In order to model τ_{ij} , some physical assumptions have to be adopted. First, it is assumed that the small scales contribution can be modelled by an increasing of fluid viscosity:

$$\tau_{ij} = -2\nu_{\text{SGS}}\overline{S_{ij}}, \quad (2.35)$$

where ν_{SGS} is the sub-grid scale viscosity and

$$\overline{S_{ij}} = \frac{1}{2} \left[\frac{\partial \bar{u}_i}{\partial x_j} + \frac{\partial \bar{u}_j}{\partial x_i} \right] \quad (2.36)$$

is the strain rate tensor. This model is also known as *eddy-viscosity model*.

Second, the SGS viscosity has to be derived. Smagorinsky [67] proposed the following relation to link the eddy viscosity to the strain rate tensor:

$$\nu_{\text{SGS}} = c_s^2 \Delta^2 |\overline{S_{ij}}|, \quad (2.37)$$

where c_s^2 is the Smagorinsky constant for SGS momentum fluxes. Note that the constant c_s^2 is always positive, thus the energy transfer is everywhere from the large scales to the small scales and energy backscattering is not allowed.

The Smagorinsky constant can be evaluated from analytical considerations, experiments or DNS. The main drawback of setting c_s^2 to constant value, relies in the assumption of flow homogeneity. Close to solid boundaries, where the turbulent length-scales decrease, the Van Driest damping function is usually applied to overcome such limitation.

2.3.2 Dynamic Lagrangian turbulent model

In a non-homogeneous flow, the best suited approach is to determine c_s^2 dynamically (see Germano *et al.* [25] and Lilly [42]). Among the possible choices of dynamic models, the use of the Lagrangian dynamic SGS model of Meneveau *et al.* [45] allows to tackle problems without any homogeneity directions. In dynamic models, the sub-grid scale quantities are estimated from the resolved scales using an additional test filter, denoted by an angle bracket over-bar, of width $\widehat{\Delta} = 2\overline{\Delta}$.

The theoretical background of this procedure is the Germano identity, that links the sub-grid scale tensors computed using the two different filters:

$$L_{ij} = \mathcal{T}_{ij} - \widehat{\tau}_{ij} = \widehat{\overline{u_i u_j}} - \widehat{\overline{u_i} \widehat{u_j}}, \quad (2.38)$$

then, the stress tensors of the large and small scales can be modelled by the Smagorinsky eddy-viscosity model, leading to:

$$\widehat{\tau}_{ij} = \widehat{\overline{u_i u_j}} - \widehat{\overline{u_i} \widehat{u_j}} \cong -2c_s^2 \overline{\Delta}^2 |\widehat{S}| \widehat{S}_{ij},$$

and

$$\mathcal{T}_{ij} = \widehat{\overline{u_i u_j}} - \widehat{\overline{u_i} \widehat{u_j}} \cong -2c_s^2 (2\overline{\Delta})^2 |\widehat{S}| \widehat{S}_{ij}.$$

Inserting the latter in (2.38), we obtain an over-determined system of equations for the unknown c_s^2 . In order to solve the system we should minimize the error associated to the use of Smagorinsky approximation, defined as:

$$e_{ij} = L_{ij} - 2\overline{\Delta}^2 \left[c_s^2 |\widehat{S}| \widehat{S}_{ij} - 4c_s^2 |\widehat{S}| \widehat{S}_{ij} \right] \quad (2.39)$$

$$= L_{ij} - c_s^2 M_{ij}, \quad (2.40)$$

where the tensor M_{ij} is defined in equation (2.39).

The Lagrangian model is obtained by minimizing this error (in a least-square sense) under the assumption that c_s does not vary along the fluid-particle Lagrangian trajectories, and the coefficient is determined as:

$$c_s^2 = \frac{\mathcal{I}_{LM}(\mathbf{x}, t)}{\mathcal{I}_{MM}(\mathbf{x}, t)} \quad (2.41)$$

where the numerator and denominator can be expressed by integrals arising from the minimization procedure, that are solutions of the following

equations:

$$\frac{\partial \mathcal{I}_{LM}}{\partial t} + \bar{u}_k \frac{\partial \mathcal{I}_{LM}}{\partial x_k} = \frac{1}{T} (L_{ij} M_{ij} - \mathcal{I}_{LM}), \quad (2.42)$$

$$\frac{\partial \mathcal{I}_{MM}}{\partial t} + \bar{u}_k \frac{\partial \mathcal{I}_{MM}}{\partial x_k} = \frac{1}{T} (M_{ij} M_{ij} - \mathcal{I}_{MM}). \quad (2.43)$$

The relaxation time-scale is assumed to be:

$$T = \theta \bar{\Delta} (\mathcal{I}_{LM} \mathcal{I}_{MM})^{-1/8}, \quad \theta = 1.5, \quad (2.44)$$

after the analysis of Meneveau *et al.* [45].

Theoretically, the Smagorinsky constant (2.41) cannot assume negative values. The squaring underlines this hypothesis. In order to enforce the condition $c_s^2 \geq 0$, a numerical *clipping* is performed on factors \mathcal{I}_{LM} and \mathcal{I}_{MM} : after the resolution of the partial differential equations (2.42,2.43), if \mathcal{I}_{LM} assumes negative values in some points, in that points it is set to zero; if \mathcal{I}_{MM} assumes negative values in some points, in that points it is set to very small positive value (since it is used as denominator, it cannot be set to zero).

Observation. *The turbulent model used in this work, is the dynamic Lagrangian model above described.*

For the sake of completeness, it can be pointed out that the numerical solutions of the partial differential equations (2.42,2.43) are not strictly necessary. An approximate solution is given by a sequence specified by recursion:

$$\begin{cases} \mathcal{I}_{LM}^{n+1}(\mathbf{x}) = \epsilon [L_{ij} M_{ij}]^{n+1}(\mathbf{x}) + (1 - \epsilon) \cdot \mathcal{I}_{LM}^n(\mathbf{x} - \bar{\mathbf{u}}^n \Delta t) \\ \mathcal{I}_{LM}^0(\mathbf{x}) = c_{s,0} [M_{ij} M_{ij}]^0(\mathbf{x}) \end{cases} \quad (2.45)$$

where $c_{s,0} = 0.0256$ is a classical value for the Smagorinsky constant, and

$$\begin{cases} \mathcal{I}_{MM}^{n+1}(\mathbf{x}) = \epsilon [M_{ij} M_{ij}]^{n+1}(\mathbf{x}) + (1 - \epsilon) \cdot \mathcal{I}_{MM}^n(\mathbf{x} - \bar{\mathbf{u}}^n \Delta t) \\ \mathcal{I}_{MM}^0(\mathbf{x}) = [M_{ij} M_{ij}]^0(\mathbf{x}) \end{cases} \quad (2.46)$$

with

$$\epsilon = \frac{\Delta t^n}{1 + \Delta t/T^n}, \quad T^n = \theta \bar{\Delta} (\mathcal{I}_{LM}^n \mathcal{I}_{MM}^n)^{-1/8}.$$

We refer to Meneveau *et al.* [45] for a derivation and a physical interpretation of these alternative equations.

2.3.3 Extension of dynamic Lagrangian model to active scalars

Similarly to what have been done in section 2.3.2 with momentum equations, the implicit grid filter can be applied also to the temperature (2.5) and vapour concentration equations (2.6). The filtered equations read, respectively:

$$\frac{\partial \overline{T_f}}{\partial t} + \frac{\partial \overline{u_j T_f}}{\partial x_j} = \alpha_f \frac{\partial^2 \overline{T_f}}{\partial x_j \partial x_j} - \frac{\partial}{\partial x_j} h_i + \overline{S_f}, \quad (2.47)$$

$$\frac{\partial \overline{\omega}}{\partial t} + \frac{\partial \overline{u_j \omega}}{\partial x_j} = \alpha_\omega \frac{\partial^2 \overline{\omega}}{\partial x_j \partial x_j} - \frac{\partial}{\partial x_j} \lambda_i. \quad (2.48)$$

The application of the filter gives rise to SGS heat flux and SGS vapour flux. Assuming the gradient diffusivity hypothesis (cf. Pope [56]), they can be expressed by:

$$h_i = \overline{T_f u_i} - \overline{T_f} \overline{u_i} = -\alpha_{f,\text{SGS}} \frac{\partial \overline{T_f}}{\partial x_i} \quad (2.49)$$

and

$$\lambda_i = \overline{\omega u_i} - \overline{\omega} \overline{u_i} = -\alpha_{\omega,\text{SGS}} \frac{\partial \overline{\omega}}{\partial x_i} \quad (2.50)$$

where $\alpha_{f,\text{SGS}}$ and $\alpha_{\omega,\text{SGS}}$ are the sub-grid scale thermal and vapour diffusivity.

In analogy with Smagorinsky model for SGS stress tensor (cf. section 2.3.1), the SGS diffusivity can be expressed by:

$$\alpha_{f,\text{SGS}} = c_t^2 \overline{\Delta}^2 |\overline{S}_{ij}| \quad \text{and} \quad \alpha_{\omega,\text{SGS}} = c_\omega^2 \overline{\Delta}^2 |\overline{S}_{ij}|, \quad (2.51)$$

where c_t^2 and c_ω^2 are, respectively, the Smagorinsky constant related to the SGS thermal fluxes and the SGS vapour concentration.

Armenio and Sarkar [7] showed that the constants c_t^2 can be computed in analogous way as c_s^2 : the tensors L_{ij} and M_{ij} are replaced by similar expressions for heat flux, respectively:

$$E_j = \widehat{\overline{u_j T}} - \widehat{\overline{u_j}} \widehat{\overline{T}} \quad (2.52)$$

and

$$Q_j = 2 \overline{\Delta}^2 \left(\widehat{\overline{|\overline{S}| \frac{\partial \overline{T}}{\partial x_j}}} - 4 \widehat{\overline{|\overline{S}|}} \widehat{\overline{\frac{\partial \overline{T}}{\partial x_j}}} \right). \quad (2.53)$$

Then, the factors \mathcal{J}_{EQ} , \mathcal{J}_{QQ} are computed through equations analogous to (2.42) and (2.43), namely:

$$\frac{\partial \mathcal{J}_{EQ}}{\partial t} + \overline{u_k} \frac{\partial \mathcal{J}_{EQ}}{\partial x_k} = \frac{1}{\text{T}} (E_j Q_j - \mathcal{J}_{EQ}), \quad (2.54)$$

$$\frac{\partial \mathcal{J}_{QQ}}{\partial t} + \overline{u_k} \frac{\partial \mathcal{J}_{QQ}}{\partial x_k} = \frac{1}{\text{T}} (Q_j Q_j - \mathcal{J}_{QQ}), \quad (2.55)$$

using the formula (2.44) for relaxation time. Finally, the Smagorinsky constant for thermal fluxes is computed as:

$$c_t^2 = 2 \frac{\mathcal{J}_{EQ}(\mathbf{x}, t)}{\mathcal{J}_{QQ}(\mathbf{x}, t)}. \quad (2.56)$$

The numerical clipping, described in section 2.3.2 for Smagorinsky constant, is also applied to \mathcal{J}_{EQ} and \mathcal{J}_{QQ} .

The derivation of c_ω^2 is carried out with the same procedure already described for c_t^2 . Once the vapour concentration ω has been substituted to the temperature T , exactly the same formulae have to be used. Hence, we avoid to explicitly report the mathematical formulation of the dynamic Lagrangian SGS model for the SGS vapour flux.

2.3.4 LES governing equations

Substituting the SGS stress tensor (2.35), SGS heat flux (2.49) and SGS vapour flux (2.50) in the filtered equations for momentum (2.29), temperature (2.47) and vapour concentration (2.48); we obtain the governing equations for LES. Rearranging the right hand side of the equations, they read:

$$\frac{\partial \bar{u}_i}{\partial x_i} = 0, \quad (2.57)$$

$$\frac{\partial \bar{u}_i}{\partial t} + \bar{u}_j \frac{\partial \bar{u}_j}{\partial x_j} = -\frac{1}{\rho_0} \frac{\partial \bar{p}}{\partial x_i} + (\nu + \nu_{\text{SGS}}) \frac{\partial^2 \bar{u}_i}{\partial x_j \partial x_j} - \frac{\rho}{\rho_0} g \delta_{i2}, \quad (2.58)$$

$$\frac{\rho}{\rho_0} = 1 - \beta_T (\bar{T}_f - T_0) - \beta_\omega (\bar{\omega} - \omega_0), \quad (2.59)$$

$$\frac{\partial \bar{T}_f}{\partial t} + \bar{u}_j \frac{\partial \bar{T}_f}{\partial x_j} = (\alpha_f + \alpha_{f,\text{SGS}}) \frac{\partial^2 \bar{T}_f}{\partial x_j \partial x_j} + S_f, \quad (2.60)$$

$$\frac{\partial \bar{\omega}}{\partial t} + \bar{u}_j \frac{\partial \bar{\omega}}{\partial x_j} = (\alpha_\omega + \alpha_{\omega,\text{SGS}}) \frac{\partial^2 \bar{\omega}}{\partial x_j \partial x_j}, \quad (2.61)$$

where the SGS quantities are computed with the dynamic Lagrangian model already described.

2.4 Numerical implementation

The numerical implementation is carried out taking advantage of OpenFOAM version 2.1.0, a open source C++ library and toolbox.

The code works with unstructured meshes using a finite volume method. The solution of equations is performed using the Pressure-Implicit with Splitting of Operators (PISO), as formulated in most OpenFOAM solvers, based on Issa [34] and Issa *et al.* [35], and later improved by Oliveira and Issa [50]. As discussed, a SGS Lagrangian dynamic model, both for momentum and scalar transport, is implemented for the present investigations while

the thermal coupling procedure at the interface is that one of Sosnowski *et al.* [69].

The overall resolution algorithm is now briefly illustrated:

- ▶ **first**, the temperature equation is solved for all the domains (fluids and solids);
- ▶ **second**, the vapour concentration equation is solved in the fluid domain, followed by the Navier-Stokes equations;
- ▶ **third**, temperature sub-loop starts and performs the thermal coupling between solid-fluid domain taking in account the thermal contribution of evaporation and condensation;
- ▶ **fourth**, the vapour equation is solved again and the water film thickness is updated.

In order to ensure a better numerical stability during the thermal coupling computation (third step), the heat flux due to evaporation and condensation (2.13) is not directly imposed as boundary condition. Instead, the already explained strategy (adding the temperature source/sink term (2.14) on the first cell next to the boundary) is adopted.

More details on the numerical implementation for thermal coupling and evaporation-condensation models can be found in Sosnowsky [68] and Petronio [54], respectively.

Chapter 3

Turbulent buoyant flow in a confined cavity with conjugate heat transfer

The results present in this chapter have been published in the journal paper: C. Cintolesi, A. Petronio, V. Armenio, *Large eddy simulation of turbulent buoyant flow in a confined cavity with conjugate heat transfer*, Physics of fluids, 27 (2015).

Contents

3.1	Introduction	24
3.2	Simulation methodology	28
3.2.1	Mathematical model	28
3.2.2	Numerical methods	28
3.2.3	Algorithm and implementation	29
3.3	Non-dimensional parameters	29
3.4	Problem description and settings	30
3.4.1	Case geometry	31
3.4.2	Computational domain	32
3.4.3	Characteristic parameters and physical coefficients	32
3.4.4	Validation: initial and boundary conditions	33
3.5	The flow field without CHT	34
3.5.1	The mean field	34
3.5.2	Second order statistics	38
3.6	Simulation with conjugate heat transfer	38
3.6.1	Temperature profile within mild steel walls	41
3.7	Analysis of thermo-fluid dynamics interaction using different materials	44

3.7.1	Simulations settings and procedure	45
3.7.2	First order flow statistics	47
3.7.3	Fluid flow turbulent statistics	54
3.7.4	Temperature distribution within the solid media	57
3.8	Conclusions	62
3.9	Appendix: additional validation analysis	64

Turbulent natural convection in enclosure is a paradigmatic case for wide class of processes of great interest for industrial and environmental problems. The solid-fluid thermal interaction, the anisotropy of the turbulence intensity in the flow field along with the transient nature of heat transfer processes, pose challenges regarding the numerical modelling. The case of a square cavity with differently heated vertical walls and two horizontal conductive plates is studied at $Ra = 1.58 \times 10^9$. The study is carried out numerically, using large-eddy simulation together with a dynamic Lagrangian turbulence model and a conjugate heat transfer method to take into account heat transfer at the solid surfaces. First, validation is carried out against literature experimental and numerical data. The results of validation tests evidence the limitations of using the adiabatic conditions as a model for reproducing an insulator. In fact, the adiabatic condition represents the asymptotic behaviour which is often difficult to reach in real conditions. Successively, the model is used to investigate the effect on the flow field of different materials composing the horizontal walls. Initial conditions representative of physical experiment are used. In order to reduce the CPU-time required for a simulation with insulating materials at the walls, a four-step temperature advancement strategy is proposed, based on the artificial reduction-first and recover-later of the specific heat coefficient C_p of the materials at different stages of the simulation. The conductivity of the solid media is found to influence the flow configuration since heat transfer at the solid walls substantially modifies the turbulent field and makes the flow field less homogeneous along the horizontal direction.

3.1 Introduction

Turbulent natural convection in closed volumes is one of the most important subjects in applied physics both from a theoretical perspective and for implications in engineering systems.

In these systems, a temperature gradient, for example originated by differently heated walls, gives rise to buoyancy forces driving the fluid and triggering turbulence.

The correct modelling and reproduction of such flows is of great interest both in environmental flows, like convective boundary layer or the convective motion ruled by heating of vertical walls of skyscrapers at neighbour scale, as in industrial applications. In the latter cases, among the others, natural convection rules (with increasing Rayleigh and Reynolds numbers) the process of cooling of electrical equipments or collectors of solar energy, the efficiency in building ventilation and the energy efficiency in home appliances.

Neglecting the solid-fluid thermal coupling in the above mentioned applications may result in an oversimplification of the system itself, eventually leading to incorrect results. Moreover the transient nature of the heat transfer process along with the complexity of the geometry and the anisotropy of turbulent fluctuations poses challenges regarding mathematical modelling. Specifically, coupling between thermal conductive solid walls and convective motion, may play a crucial role in the development of the fluid dynamics and the overall process of heat transfer.

The present study aims at assessing the influence of the conductive boundary on the buoyancy-driven flow, with a specific focus onto heat coupling mechanism between fluid and solid media.

We consider the differentially heated square cavity (DHSC). It is one of the most investigated, both numerically and experimentally, benchmark cases for the understanding of natural convection. In this system the flow is, essentially, two-dimensional; it is driven by buoyancy arising from fluid heated by a hot vertical wall and cooled by the opposite one. The vertical walls are considered at constant temperature whereas the horizontal plates are usually assumed adiabatic. Despite the simplicity of geometry and boundary conditions, the system displays all the main features of natural convection in a confined environment and it thus appears an appropriate test case for the investigation of the solid-fluid media thermal interaction. The high sensitivity of the flow to the boundary conditions requires accurate experimental studies on one side, and accurate mathematical modelling and numerical methods on the other.

Mergui and Penot [46] analysed experimentally the DHSC, providing reference data useful to calibrate and validate numerical models. Salat *et al.* [65] questioned about the achievement of adiabatic conditions in experiments reported in [46]. They highlighted the strong influence of temperature boundary conditions imposed in numerical models, especially near the horizontal boundaries and in the corner region. In order to match the experimental data of [46], it was necessary to switch from adiabatic to Dirichlet boundary condition, imposing the temperature experimental profile along the horizontal walls.

Further experiments on the same configuration cavity were carried out by Tian and Karayiannis [75, 76] and Ampofo and Karayiannis [5], taking into consideration the conductivity of the horizontal walls. Detailed data

about mean quantity profiles and turbulent statistics were provided and are here considered as reference data for the present study.

From a mathematical point of view, the three main mathematical frameworks to study DHSC are, respectively, the Reynolds-Averaged Navier-Stokes Equations (RANSE), Direct Numerical Simulation (DNS) and Large-Eddy Simulation (LES). RANSE has been usually applied considering two-dimensional motion, which is a reasonable assumption when the horizontal aspect-ratio of the cavity is larger than unity. Salat *et al.* [65] compared the results of the first two approaches and observed that two-dimensional RANSE simulations are less accurate in reproducing the corner flow and the core stratification, while they give a good description of the general flow field at a relative low computational cost. Other authors indicate additional elements that could be crucial for an accurate simulation: Omri *et al.* [51] performed RANSE simulations with the shear-stress-transitional $k - \omega$ turbulence model, underlining the importance of using a realistic temperature distribution on the boundary walls; Hsieh and Lien [29] used an unsteady RANSE approach in conjunction with the $k - \epsilon$ model at low- Re number, emphasising the computational difficulties of reproducing convective flow with low turbulence intensity and underlining the need of a reliable turbulence model; Ibrahim *et al.* [31] recently studied the effect of thermal radiation using a two-dimensional LES (which has to be considered as an unsteady RANSE), and suggested that this phenomenon is responsible for the increased temperature in the core region of the cavity observed in the experimental studies.

Among the more recent numerical studies we refer to the work of Peng and Davidson [53] who performed LES with dynamic Sub-Grid Scale (SGS) turbulence model, imposing the experimental temperature profile as boundary condition at horizontal walls. The results were in good agreement with the experimental data although the root-mean square statistics were in general overestimated. Bosshard *et al.* [10] employed a dynamic model in a LES, carried out by means of a spectral numerical method, together with adiabatic conditions on horizontal boundaries; Zimmermann and Grol [83] imposed a linear distribution of temperature and considered a compressible approach instead of using the Boussinesq approximation.

In many situations, the exchange of thermal energy between the fluid and the solid media occurs even if strong insulating materials are considered. Hence, the adiabatic condition has to be considered as an idealized condition. To the knowledge of the authors, the thermal coupling between the two media has never been considered to assess the impact of the solid thermal properties on the flow developing within the DHSC. From a modeling point of view, this implies the coupled solution of the flow field and the thermal field within the solid, with appropriate conditions at the fluid-solid interface. This problem is referred in literature as Conjugate Heat Transfer (CHT).

A review of the techniques to treat this subject is in Dorfman and Renner

[19], while Duchaine *et al.* [20, 21] describe in details some coupling strategies and analyse their stability properties and efficiency. The CHT was also studied by Tiselj *et al.* [77] who carried out a DNS for two-dimensional turbulent channel flow and studied the propagation of the temperature fluctuations inside the wall when different oscillatory boundary conditions are imposed. Garai *et al.* [23] extended this latter work, analysing the convective instability on heat transport in channel flow and the variation into the solid-fluid interface when the physical properties of the solid boundary change.

Although DHSC is a geometrically simple and idealised configuration, it poses some challenging issues:

- ▶ the influence of the conductive solid boundaries on the fluid domain cannot be neglected;
- ▶ the characteristic diffusion time of temperature within the solid matter can be of some orders of magnitude higher than that in the fluid, meaning that long simulation time is required to reach a statistical steady state;
- ▶ accurate turbulence modelling techniques should be used, able to reproduce localised and anisotropic turbulent flow.

Previous researches focused only on one of the above mentioned issues. In the present work we try considering all issues, applying a reliable and accurate turbulence model together with a thermal coupling technique, allowing for a more realistic study of the flow field as well as the thermal state of the solid conductive boundaries.

The development of the numerical model is carried out within the OpenFOAM framework, taking advantage of its flexibility and capability to treat complex cases. The large-eddy simulation methodology, together with a Lagrangian dynamic model for sub-grid scale momentum and temperature fluxes, leads to the possibility to investigate accurately the complex inhomogeneous turbulent field developing within the DHSC. The CHT technique allows to represent realistically the fluid-solid coupling across the interface, taking into account for the thermal properties of the solid medium.

The chapter is organized as follows: section 3.2 presents the mathematical model and the numerical implementation used for simulations; section 3.3 describes some non-dimensional parameters suitable for studying this physical problem; section 3.4 describes the DHSC and supplies details on the simulation settings; in section 3.5 the numerical solver for fluid flow is validated against experimental and numerical literature results; in section 3.6 the temperature advancement strategy is discussed and the implementation of CHT is validated against experimental data; section 3.7 is focused on the analysis of the fluid-thermal field obtained using different conductive materials; in section 3.8 concluding remarks are given.

3.2 Simulation methodology

The notation used is the same than in chapter 2, and also here the International System of Units is used to express the value of all quantities.

3.2.1 Mathematical model

The study of thermal interaction between solid and fluid media involves three main actors: the fluid with its inner dynamics, the diffusion of heat in the solid medium, the heat transfer at the interface. All these phenomena have to be modelled through a set of appropriate equations.

The governing equations have been describe in section 2.1, but, for the sake of clarity, they are here reported without the vapour concentration contribution. The fluid flow in the cavity is ruled by:

$$\frac{\partial u_i}{\partial x_i} = 0, \quad (3.1)$$

$$\frac{\partial u_i}{\partial t} + u_j \frac{\partial u_i}{\partial x_j} = -\frac{1}{\rho_0} \frac{\partial p}{\partial x_i} + \nu \frac{\partial^2 u_i}{\partial x_j \partial x_j} - \frac{\rho}{\rho_0} g \delta_{i2}, \quad (3.2)$$

$$\frac{\rho}{\rho_0} = 1 - \beta_T (T - T_0), \quad (3.3)$$

where: u is the fluid velocity; p is the pressure; T is temperature and T_0 is the reference one; ρ is the space-time variable density in the fluid flow while ρ_0 is the reference density; ν the molecular kinematic viscosity; g the gravity acceleration; β_T is the thermal expansion coefficient.

The temperature equation for fluid domain reads as:

$$\frac{\partial T_f}{\partial t} + u_j \frac{\partial T_f}{\partial x_j} = \alpha_f \frac{\partial^2 T_f}{\partial x_j \partial x_j}. \quad (3.4)$$

where we denote with α_f the molecular thermal diffusivity.

In the solid medium the space-time temperature evolution has to be modelled. The governing equation is the classical law of diffusion

$$\frac{\partial T_s}{\partial t} = \alpha_s \frac{\partial^2 T_s}{\partial x_j \partial x_j}. \quad (3.5)$$

A thermal coupling boundary condition depicted in section 2.1.2, acts onto the solid-fluid interface.

3.2.2 Numerical methods

The LES approach is used in the fluid flow simulations. The SGS viscosity and thermal diffusivity are computed using the dynamic Lagrangian model reported in section 2.3.

The standard Smagorinsky model is employed for comparison purposes, with the settings reported by Peng and Davidson [53], namely $c_s^2 = 0.044$. In this case, the Reynolds analogy for the SGS eddy diffusivity of temperature $\alpha_{\text{SGS}} = \nu_{\text{SGS}}/Pr_t$, with a turbulent Prandtl number equal to $Pr_t = 0.4$. The Van Driest damping function is used to reduce the turbulent length-scales near the walls.

3.2.3 Algorithm and implementation

The solver `coupledHeatVapourFoam` is used for the simulations. The algorithm structures is sketched in section 2.4.

The governing equations are discretised in space using a second-order central difference scheme; time integration is performed using an implicit backward differencing scheme which uses the variables at the previous two time-steps, resulting in second order accuracy in time (more details are in the OpenFOAM official Programmer's Guide [2]). Overall, the algorithm is second-order accurate both in time and in space.

3.3 Non-dimensional parameters

Parameters characterising the physics of natural convection are: Prandtl number, the ratio between momentum diffusivity and thermal diffusivity

$$Pr = \frac{\nu}{\alpha}; \quad (3.6)$$

Rayleigh number, ratio between buoyancy and viscous forces

$$Ra = \frac{g\beta_T\Delta TL^3 Pr}{\nu^2}, \quad (3.7)$$

where L is the system characteristic length.

For transient phase problems, the characteristic diffusion time τ of the solid materials is defined. It is a measure of the time required to reach thermal equilibrium:

$$\tau = \frac{L^2}{\alpha} = \frac{\rho C_p L^2}{k}. \quad (3.8)$$

where $\alpha = k/(\rho C_p)$ and k is the heat conductivity coefficient, C_p is the specific heat coefficient at constant pressure.

Moreover, Garai *et al.* [23] use the thermal activity ratio (TAR), a parameter which quantifies heat transfer effects through the interface:

$$TAR = \sqrt{\frac{(k\rho C_p)_{fluid}}{(k\rho C_p)_{solid}}}. \quad (3.9)$$

This is the ratio between the thermal effusivity of the fluid and of the solid medium, respectively. The effusivity of a material determines the behaviour

of the interface in presence of transient heat sources (see Marín [44]). From a theoretical point of view, this quantity can be found in the analytical solution of the *infinitely fast flame* problem, reported also by Duchaine *et al.* [21].

The equation of heat flux q_{iff} at the interface between a semi-infinite solid (at temperature T_1) and a semi-infinite gas (at temperature T_2), reads as:

$$q_{iff}(t) = \frac{T_2 - T_1}{1 + TAR} \sqrt{\frac{(k\rho C_p)_{gas}}{\pi t}}; \quad (3.10)$$

that is a rearrangement of equation (4), page 553 of [21]. From equation (3.10), it appears that large values of TAR correspond to weaker heat flux across the interface. Conversely smaller values of TAR imply a larger heat flux and hence a stronger interaction between solid and fluid.

To better understand the meaning of thermal effusivity and diffusion time, we can consider the solution of the heat equation for a semi-finite homogeneous solid, *i.e.* a solid bounded by the plane $x = 0$ and extending to infinity along the positive x direction. In such a way the problem is reduced to one dimension, and it is an interesting idealised case of the heat diffusion on the solid boundaries of our cavity. If the initial temperature of the solid is T_2 and we apply a constant temperature T_1 over its surface, the analytical solution¹ for the heat flux q is:

$$q(x, t) = \frac{1}{\sqrt{k\rho C_p}} \frac{(T_2 + T_1)}{\sqrt{\pi t}} e^{-\frac{x^2}{2\alpha t}}. \quad (3.11)$$

Equation (3.11) shows that the heat flux at the surface is inversely proportional to the thermal effusivity of the solid. Moreover the thermal energy is diffused according to a Gaussian law, both in time and space. The quantity $\ell = 2\sqrt{\alpha t}$ is the diffusion length-scale of the solid: if $\ell \gg L$ the temperature distribution at a distance L from the surface is almost time-independent. Hence to reach the thermal equilibrium a time

$$t \gg \frac{L^2}{4\alpha} = \frac{\tau}{4}$$

is required.

3.4 Problem description and settings

The general problem of natural convection is studied for the case of square cavity. Specifically, we reproduce the experiment of Tian and Karayianis [75, 76] and we refer to the simulations of Peng and Davidson [53] for validation of numerical solver for fluid phase.

¹Among the others we can refer to Marín [44] for a brief derivation of this formula.

3.4.1 Case geometry

The experimental cavity considered in [75, 76] has dimension of $0.75\text{ m} \times 0.75\text{ m} \times 1.5\text{ m}$. The fluid motion is, on average, two dimensional and develops in the x, y -plane, while the spanwise z -direction is of homogeneity for the turbulent flow. The cavity is surrounded by four narrow sheets of conductive boundaries made of mild steel, and two guard cavities on the faces normal to the z -direction. The left and right vertical walls have a thickness of 0.006 m and are maintained at a constant temperature of $T_h = 323.15\text{ K}$ (50°C) and $T_c = 283.15\text{ K}$ (10°C), respectively. The two horizontal walls, with a thickness $H = 0.0015\text{ m}$, are free to conduct heat and are surrounded by a thick insulator. This consist of a polystyrene block of thickness 0.1 m that is covered with an additional wood plate. Room temperature is maintained at $T = 303.15\text{ K}$ (30°C), chosen to be equal to the enclosure average temperature. The controlled ambient temperature and the guard cavities are designed to maintain the minimum mass and heat transfer across the cavity. More details in experiment settings can be found in [75].

Peng and Davidson [53] reproduced this experiment numerically, but the heat-transfer process between solids and fluid was not considered. Therefore, the simulations performed by the authors took into account the fluid domain in the cavity only, replacing the solid envelop with suitable boundary conditions. In the spanwise direction a periodic condition is used. The computational domain was reduced to form a cubic domain of edge $L = 0.75\text{ m}$, after proving that correlation among quantities decay to negligible values after just half domain size in the homogeneous direction.

The computational domain is sketched in Figure 3.1. In a preliminary simulation all the solid elements were taken into account, except for the external wood plates for which details were not provided in the reference article. Then, the two vertical sheets of mild steel were not considered and, thus, replaced by suitable boundaries conditions for the fluid domain. In fact, it turned out that the interposition of the solid bodies between the isothermal source of temperature and the fluid, did not produce any observable effects either on the flow field or within the solid medium. This is due to the fact that the solid boundaries are made of a very narrow slice of high conducting material and the temperature difference from the isotherm boundary and the interior of the cavity is large. For this reason, we choose to avoid the thermal-coupling between the fluid and the vertical sheets, replacing it with a constant temperature condition on the boundaries of the fluid domain.

In order to perform faster simulations, and following [53], the domain size in the spanwise direction was $L_z = 0.75\text{ m}$, thus reduced by a factor 2 with respect to the reference experiment. This was estimated to be long enough to capture the flow features using periodic boundary conditions along the homogeneous direction.

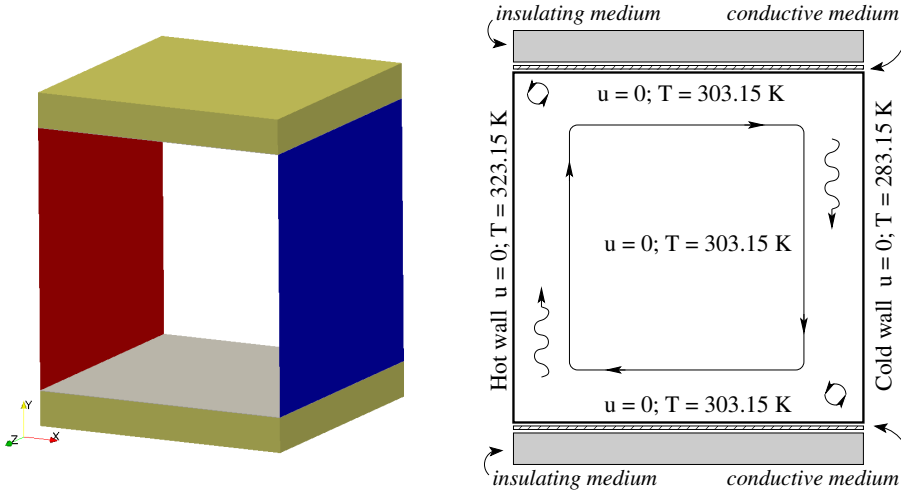


Figure 3.1: Problem sketch.

The origin of axes is located in the bottom left corner of the square and x , y are the horizontal and vertical direction, respectively.

3.4.2 Computational domain

The mesh of the fluid domain is generated as in Peng and Davidson [53]. The internal part of the cavity is discretised using $96 \times 96 \times 64$ grid cells, regular along the spanwise direction and stretched near the walls in the x, y -plane. A double-side stretching function, based on hyperbolic tangent, is used:

$$r(\xi) = \frac{1}{2} \left(1 + \frac{\tanh(\delta(\xi - 1/2))}{\tanh(\delta/2)} \right), \quad (3.12)$$

with a stretching factor $\delta = 6.5$ in such way to have 12 computational nodes within $r^+ < 10$, where r is the wall-normal coordinate.

The two horizontal conductive bodies are considered and discretised with a grid of $96 \times 5 \times 64$ cells. The grids are stretched along the vertical direction using equation (3.12). Stretching is performed in such a way that the adjacent cells of the interface on the solid and fluid parts have the same size.

The insulator blocks are discretised by $96 \times 30 \times 64$ grid cells. As for the conductors, the mesh is stretched in order to match the cells on the interfaces between two different domains. The mesh dependency is discussed in Appendix 3.9.

3.4.3 Characteristic parameters and physical coefficients

The fluid considered is air at 303.15 K (30°C); Table 3.1 lists the physical parameters used. The Rayleigh number is $Ra = 1.58 \times 10^9$, while the param-

ν	m^2/s	1.575×10^{-5}
α	m^2/s	2.219×10^{-5}
ρ	kg/m^3	1.165
C_p	$J/(kg \cdot K)$	1.005×10^3
k	$W/(m \cdot K)$	0.026
β_T	$1/K$	3.33×10^{-3}
Pr_t	–	0.71

Table 3.1: Physical parameters of air at 303.15 K (30 °C).

eters for the conductive solid medium are those of the mild steel reported in Table 3.2 in section 3.6.1.

The coordinates are made non dimensional with the characteristic length $L = 0.75m$. Other characteristic scales of the problem are: the buoyant velocity $U_0 = \sqrt{g\beta_T\Delta TL} \cong 1m/s$, the characteristic time $t_0 = L/\sqrt{g\beta_T\Delta TL} \cong 0.75s$, the difference of temperature between the two vertical isothermal walls $\Delta T = (T_h - T_c) = 40K$.

The statistics presented are performed both in space (along the homogeneous direction) and time, when not otherwise specified. Given a generic variable ϕ , the notation $\langle\phi\rangle$ always represents the average along the homogeneous z -direction and in time. This latter, for a time interval equal to about three turnover times of the main vortex in the cavity, roughly estimated as $t_{ave} \cong 60t_0$. To calculate the root-mean square resolved quantities, the resolved fluctuations are computed $\phi' = \phi - \langle\phi\rangle$, then the root-mean square is $[\phi]_{rms} = \sqrt{\langle\phi'^2\rangle}$.

3.4.4 Validation: initial and boundary conditions

The validation of the numerical model is carried out against the simulation data of Peng and Davidson [53] as well as the experimental data of Ampofo and Karayiannis [5] and of Tian and Karayiannis [75].

Two classes of simulations are performed: first, the fluid flow solver is validated in absence of conjugate heat transfer at the interfaces; then, thermal coupling is considered and the temperature distribution on solid media is compared with experimental data.

For the validation of fluid solver, a non-slip condition is prescribed at the four walls, while the initial internal flow starts from rest. Solid media are replaced by suitable boundary conditions: constant temperatures T_h and T_c are set respectively for the left and right vertical boundaries of the cavity. On the horizontal boundaries, the temperature distribution provided by the experiment is enforced (see [75], Figure 3, page 852). The internal initial

temperature is set to be $T_i = (T_h + T_c)/2 = 303.15 \text{ K}$ (30°C), the average between hot and cold walls temperature.

The validation of the thermal coupling mechanism involves the two horizontal conductive sheets and the insulator blocks. The initial and boundary conditions are illustrated in Figure 3.1. Again, fluid starts from rest, a non-slip condition is applied at the fluid boundaries and the initial temperature of the fluid is T_i . Solid media are also set at the initial temperature T_i , that is the room temperature specified in [75].

As regards boundary conditions for the temperature field, at the interfaces between fluid-conductors and conductors-insulators the conjugate heat transfer mechanism is activated. On the left and right sides of the horizontal conducting sheets and insulating blocks we set a constant temperature, equal to that of the adjacent isothermal wall. This latter choice is justified by the experimental apparatus scheme reported on [75] (see Figure 2 on page 851), where it appears that the horizontal solid blocks are in contact with the isothermal vertical walls. The external faces of insulating blocks are maintained at room temperature T_i .

For both simulations, periodic conditions are set along the spanwise direction for all variables. The spanwise extension of the domain is long enough to allow development of fully developed turbulence. Specifically, the analysis of correlation functions of velocity and temperature along the spanwise direction (not reported) has shown a complete decay in less than half domain size (see Moin and Mahesh [49] for a discussion).

Additional analysis (for the case without the CHT) on the mesh and time-step dependency, and on the quantification of the unresolved turbulent scales parametrised by the SGS model, is in Appendix 3.9.

3.5 The flow field without CHT

Here we show results of simulations for the fluid domain. After a statistical steady state has been reached, the averaging time to obtain the first and second order statistics corresponds roughly to three turnover times of the main cavity vortex.

3.5.1 The mean field

Figure 3.2 shows the non-dimensional mean vertical velocity and temperature over lines, close to the hot wall, at three significant heights: $y/L = 0.2, 0.5, 0.8$.

Vertical velocity profiles, in Figure 3.2a, are in a general good agreement with reference experimental and numerical results, except for the standard Smagorinsky model. Our dynamic Lagrangian model reproduces the decrease of the vertical velocity far from the wall better than the other models. On the other hand, the quality of the results obtained with the standard

Smagorinsky model, is definitively not good. This has to be attributed to the model itself which is not able to adapt to the local features of the flow field.

Temperature profiles, shown in Figure 3.2b, are quite well reproduced by all models at the intermediate height where comparison with experimental data is possible; some small discrepancies are present in the outer region where radiation effects, not modelled by all numerical simulations, may be present (for a discussion see [31]). At the other locations, all models give results very close to each other.

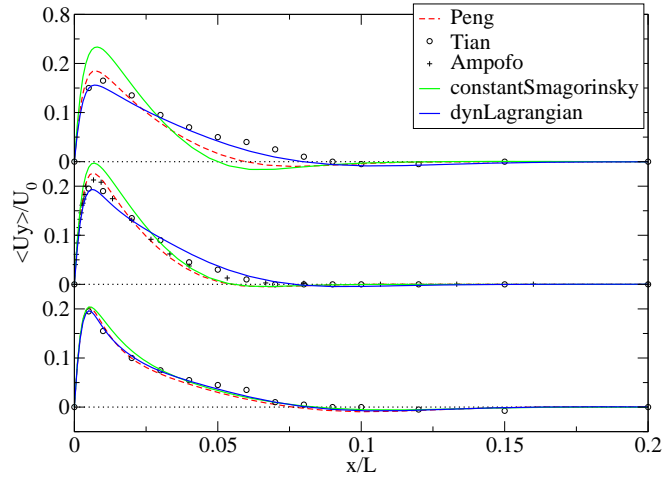
Figure 3.3a shows the distribution of mean non-dimensional horizontal velocity component along a vertical centreline ($x/L = 0.5$). Experimental data are not available for this quantity. The three numerical results share the qualitatively behaviour. Our simulation gives results very similar to those of Peng and Davidson [53], who performed LES with a dynamic Lagrangian SGS model. On the contrary, the standard Smagorinsky model strongly over-predicts the peak velocity in the boundary layer close to the wall.

Comparison among temperature vertical profiles are depicted in Figure 3.3b. All numerical results practically collapse over the experimental data. The peak of temperature in the thermal boundary layer is just slightly over-predicted by the LES of [53].

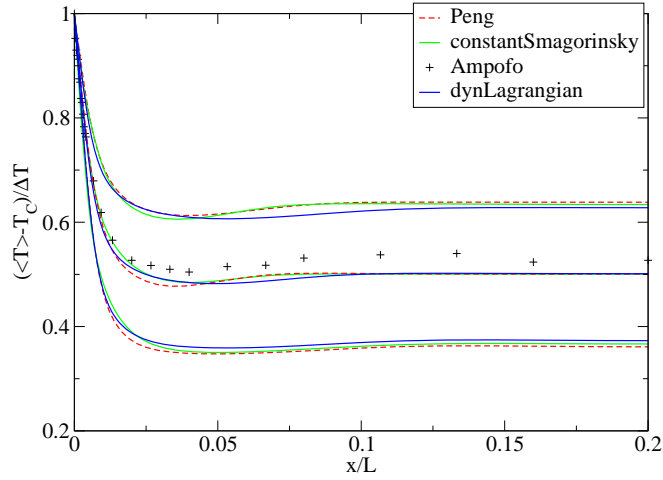
Figure 3.4a shows the streamlines of the mean velocity field. They are in a good qualitative agreement with those depicted in [53] (see their Figure 4a at page 327). The motion mainly develops close to the walls through the generation of a main circulation and, hence, of four boundary layers. They are narrow close to the two vertical walls, whereas they are thicker at the two horizontal walls. This is expected because the motion is ruled by buoyancy effects arising mainly close to the vertical walls. Low-speed recirculation regions, elongated in the horizontal direction, develop within the core region.

Isothermals are shown in Figure 3.4b. Anti-symmetry with respect to the diagonals of the cubic cavity is evident; for the sake of simplicity the discussion is focused just on the upper part of the cavity. Hot air is confined in the upper left corner, as a result of temperature transport by the velocity field along the vertical direction. There, the fluid is cooled and spread over an horizontal region of thickness $r/L \cong 0.1$ near the top wall. The core region, approximately a square delimited by $0.15 < x/L < 0.85$ and $0.15 < y/L < 0.85$, is characterised by very small velocities and a stable stratification of the flow.

The mean flow exhibits the presence of small vortexes at the top-left/bottom-right corners (Figure 3.5). At these corners the fluid vertical velocity is high because of the buoyancy effects generated by the lateral hot/cold walls, thus generating recirculations and high-speed boundary layers at the horizontal top/bottom walls. These boundary layers, while developing toward the right/left direction loose momentum and the velocity decreases before deviating downward/upward due to buoyancy generated by the cold/hot lat-

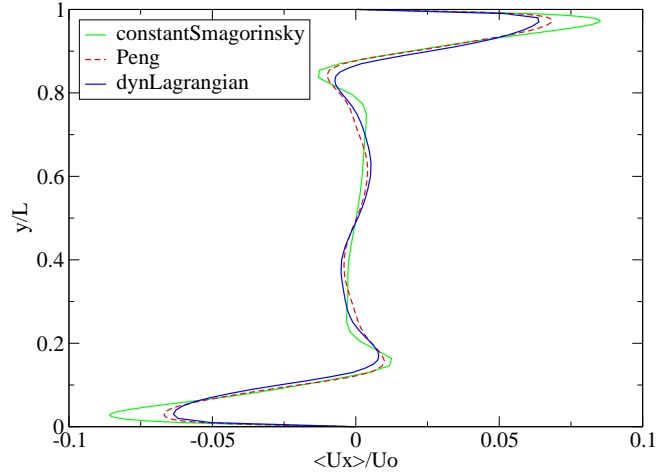


(a) Non-dimensional vertical velocity.

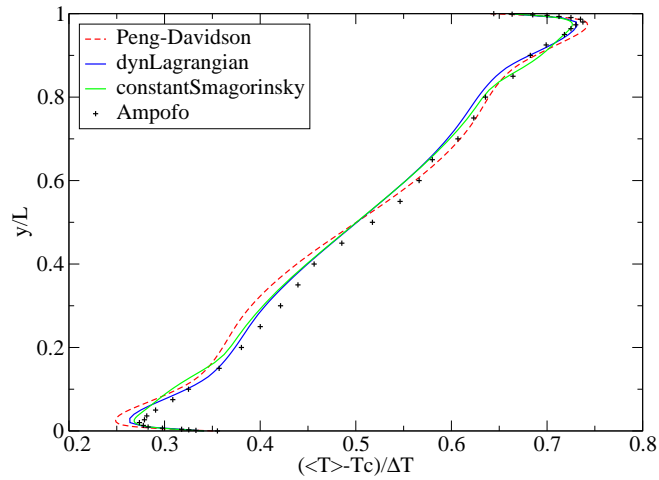


(b) Non-dimensional temperature.

Figure 3.2: Comparison of mean quantities at three different heights along the cavity: $y/L = 0.2, 0.5, 0.8$. Dash line, LES by [53]; circles, experiment by [75]; crosses, experiments by [5]; solid light green line, simulation with standard Smagorinsky model; solid dark blue line, simulation with dynamic Lagrangian model.



(a) Non-dimensional horizontal velocity.



(b) Non-dimensional temperature.

Figure 3.3: Comparison of mean quantities at the vertical centreline $x = 0.5L$. Dash line, LES by [53]; crosses, experiments by [5]; solid light green line, simulation with standard Smagorinsky model; solid dark blue line, simulation with dynamic Lagrangian model.

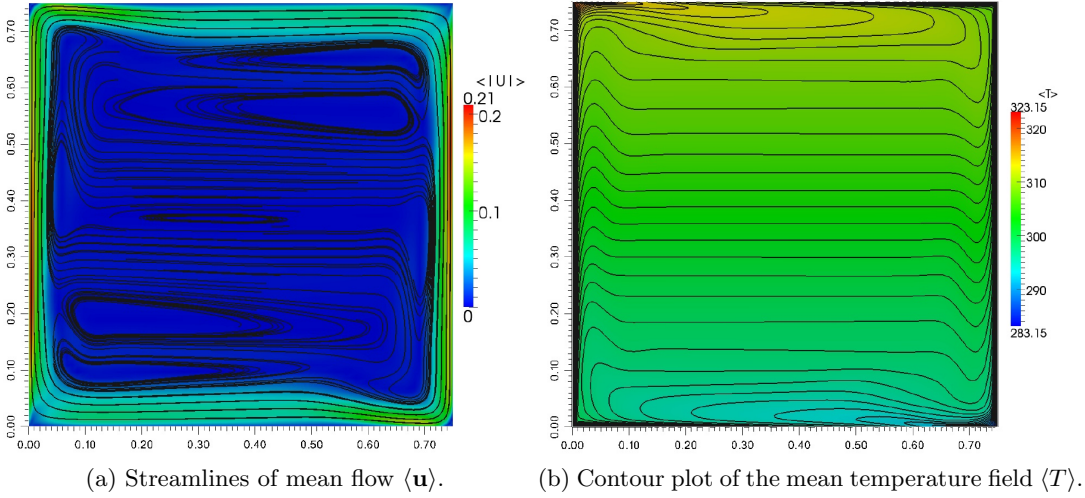


Figure 3.4: Mean flow and thermal field.

eral wall. At the two horizontal walls typical horizontal convection occurs. This drives the flow from the cold toward the hot region at the bottom wall, and from the hot toward the cold region at the top wall.

The corner vortex dimension is in good agreement with that reported in [53]: the separation point is located at $x_1/L = 0.9832 \pm 0.0003$ on the top horizontal boundary. A second, smaller and weaker vortex appears very close to the corner; its separation point is located at $x_2/L = 0.9967 \pm 0.0003$ and this structure is mostly driven by the main vortex surrounding it.

3.5.2 Second order statistics

The second order statistics are now discussed. Figure 3.6 presents the root-mean square (RMS) of quantities at the same three vertical levels as in Figure 3.3.

Overall, the agreement with experimental data is satisfactory. Our results with dynamic Lagrangian model are similar to those of [53] in which a dynamic SGS model was adopted. The profiles of temperature root-mean square do not improve with respect to previous simulations. However the discrepancies, wherever present, do not affect the general feature of the flow and thermal fields.

3.6 Simulation with conjugate heat transfer

The validation of the heat transfer model is performed looking at the temperature profile development.

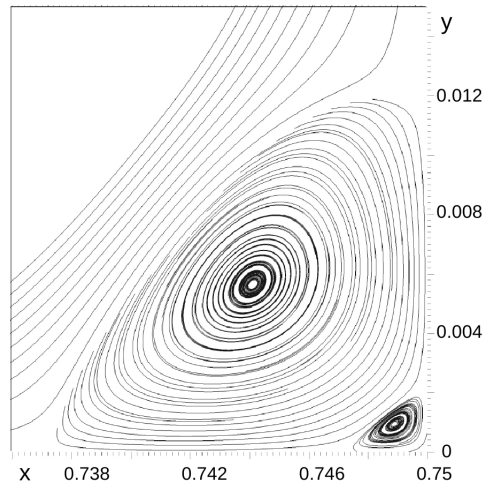


Figure 3.5: Mean flow, streamlines at the right-bottom corner neighbouring the cold wall.

The main concern in the analysis of fully developed temperature distribution in a solid body regards the diffusion time-scale related to geometric features and boundary conditions, that can largely exceed the adjustment time of the flow.

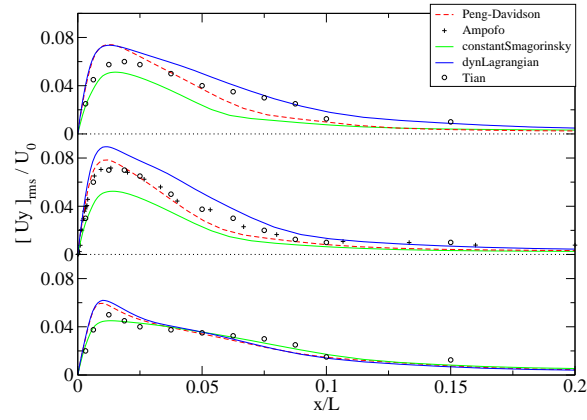
Moreover, the implementation of thermal coupling by itself, increases the computational cost and may require a small computational time-step, depending on the physical characteristics of the solid material. Preliminary simulations have shown that an insulator-type material needs smaller time-steps than a conductor-type one, thus increasing the CPU time required to reach a statistical steady state. Under this conditions the simulation may become extremely expensive even for a simple configuration.

In this context, a *shortcut* is introduced to obtain the steady state temperature profile of solid boundaries. As discussed in section 3.3, the time required to completely diffuse temperature within the horizontal solid medium can be estimated as:

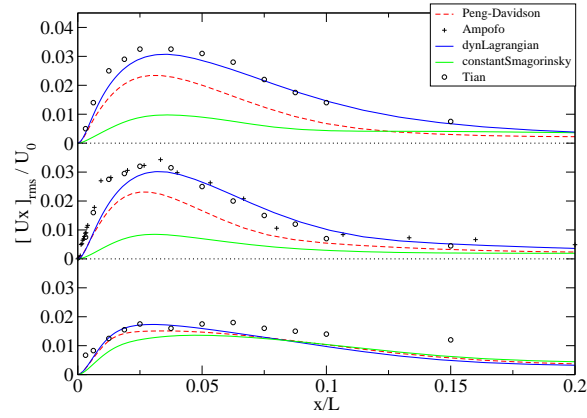
$$t \sim \frac{\rho C_p L^2}{k}, \quad (3.13)$$

where L is the characteristic length of the solid body. If we artificially decrease the specific heat capacity C_p we will decrease also the time required to reach the stable temperature profile. From a physical point of view this means that the material is able to conduct temperature faster. From a mathematical side, this choice does not influence the heat transfer mechanism, because equations (2.16) and (2.17) do not involve the C_p , and allows reaching the correct stationary profile. Indeed equation (3.5) for steady state reduces to the Laplace equation

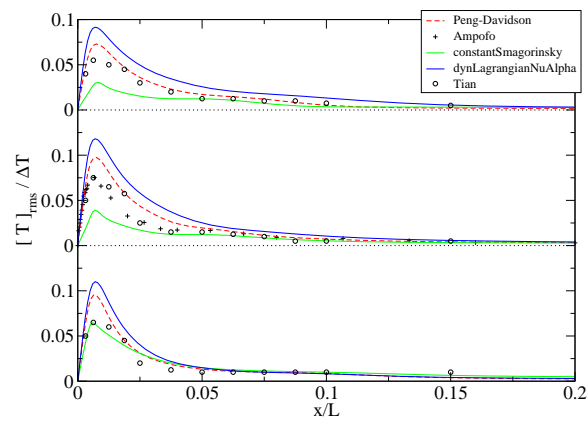
$$\nabla^2 T = 0, \quad (3.14)$$



(a) Non-dimensional vertical velocity RMS.



(b) Non-dimensional horizontal velocity RMS.



(c) Non-dimensional temperature RMS.

Figure 3.6: Root-mean square of flow quantities near the hot wall, at three levels $y/L = 0.2, 0.5, 0.8$ from bottom to the top. Dash line, LES by [53]; circles, experiment by [75]; crosses, experiments by [5]; solid light green line, simulation with standard Smagorinsky model; solid dark blue line, simulation with dynamic Lagrangian model.

that is independent from specific heat capacity. Thus the solution is determined only by boundaries conditions.

Therefore, in our simulation we use the following temperature advancement strategy:

1. **First approximation** (APP) - simulation with real-medium parameters is run till the fluid part is fully developed. The system is not at a steady state because temperature profile on solid conductive boundaries has not converged to a statistical steady state.
2. **Drugging period** (DRG) - in order to reach thermal equilibrium, the C_p of the solid material is decreased by few orders of magnitude and the simulation run again for a period comparable with the reduced characteristic diffusion time. Temperature diffusion process is now much faster and the temperature profile reaches steady state rapidly.
3. **Homogenisation** (HOM) - temperature distribution in the solid medium is averaged in space in presence of homogeneous directions, or for few time-steps. This is done in order to eliminate the non-physical thermal fluctuations arising with the decreased specific heat coefficient.
4. **Final adjustment** (ADJ) - the actual value of C_p is restored and simulation restarts. After an initial adjustment transient the system can be considered to be in a steady state.

With this procedure, the stationary (in a statistical sense) distribution of temperature in the solid body is reached in a reasonable time, virtually accelerating the temperature diffusion process along the direction over which the body is elongated. This strategy may be generalised for cases involving more solid domains interacting among them.

Another approach for the (DRG)-step is to solve the Laplace equation (3.14) instead of the diffusion one (3.5). From a physical point of view, this corresponds to the limit case of $C_p \rightarrow 0$; thus temperature diffuses instantaneously over the solid domain. The steady profile depends only on the instantaneous interfacial heat flux, and is established automatically at each computational time-step. This alternative method has been found to lead to numerical instabilities, caused probably by the sharp difference of temperature at the interface. More tests are required to address this problem.

3.6.1 Temperature profile within mild steel walls

The validation of thermal coupling mechanism is here discussed. We refer to section 3.4.4 for the description of general settings used.

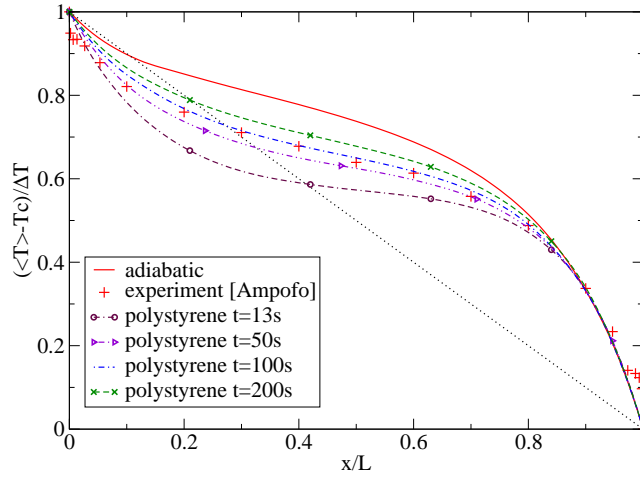


Figure 3.7: Temperature distribution over centreline of the top steel sheet. Comparison between experiment data (labelled *experiment*), simulation with the polystyrene insulator at different times (labelled *polystyrene*), and a perfect insulator at steady state (labelled *adiabatic*).

A first CHT simulation is run to analyse the interaction between the physical elements present in the experiment by Tian and Karayiannis [75]: fluid is in contact with the horizontal mild steel sheets that, in turn, are in contact with polystyrene elements as shown in Figure 3.1.

The characteristic diffusion time for the mild steel sheets is $\tau = 4.8 \times 10^4 s$ (corresponding to 13 hours), obtained using the parameters reported in Table 3.2 and considering the sheet length $L = 0.75m$. When the advancement strategy is applied, the specific heat capacity is decreased by three orders of magnitude while keeping unchanged C_p of insulating bricks of polystyrene. Thus the diffusion time is reduced to about $\tau \sim 50s$.

A second simulation is then performed: since the presence of the insulator is negligible when the stable temperature profile is reached, polystyrene is replaced by adiabatic condition on the external faces of the horizontal mild steel sheets. This condition mimics the presence of a perfect insulator.

Figure 3.7 shows the non-dimensional temperature distribution over an horizontal line at the mid-height of the top sheet, for the two cases. Note that the two horizontal plates (top and bottom) behaves in the same way. In our analysis we focus on the top one.

If the CHT is replaced by an idealised adiabatic condition, the temperature on the sheet is determined by the left/right isothermal temperatures, resulting into a linear distribution along the horizontal direction, *i.e.* x -axis. When the CHT is active, the temperature within the solid medium is still

dominated by the constant temperature at the tips of the sheet, but its longitudinal distribution is ruled by the fluid-solid and solid-solid interactions.

Temperature at different time, when polystyrene is present, are reported: after a time $t = 100s$ of simulation (corresponding to $\Delta t = 10^5s$, or 27 hours of physical time), the temperature profile reaches a quasi-steady configuration qualitatively similar to the experimental profile. Afterwards, the process slows down because temperature starts to diffuse into the insulator. This process is faster at the beginning when the temperature gradient is larger, and it slows down after that the temperature starts to diffuse in the region near the solid-solid interface and the temperature gradient becomes smaller and smaller.

The simulation is interrupted before reaching the asymptotic regime, because on one side it takes a huge amount of time (even if the C_p -decreased strategy is applied) and, on the other side, the steady distribution on the polystyrene depends on the boundaries conditions on its external part only, that are not specified in the description of the experiment. Therefore the exact experiment configuration cannot be reproduce.

Nevertheless, the simulation exhibits a transitional behaviour, that, at a certain time fits the experimental profile. This may suggest that the experimental profile is still in a transitional phase, and a much longer time would have been requested to obtain the asymptotic profile. In fact, the characteristic diffusion time for the polystyrene is $\tau = 3.6 \times 10^5s$, when the characteristic length is $L = 0.75m$, the time required to reach the asymptotic temperature profile in the insulator is of the order of days. The reference paper [75] does not provide information about the time elapsed from the start of the experiment. However, the authors reported that an incense smoke was used as seeding, and that this smoke lasted in the air cavity for more that 24 hours. Thus, assuming an experimental elapsed time of the order of one day, we may argue that it was substantially less than the polystyrene diffusion time, which is of the order of 4 days.

On the contrary, the case with ideal insulator (adiabatic condition) reaches a steady configuration which appears quantitative different from the experimental profile. This is expected since polystyrene is not a perfect insulator.

To summarise, the analysis carried out in this section shows that the implementation of CHT is able to reproduce realistically way the time evolution of a physical process where heat transfer between solid and fluid media is involved. Also, the four-step procedure herein developed allows to obtain the realistic behaviour with an acceptable computational cost. Third, a simplified adiabatic condition might be not able to reproduce correctly experimental data, since sometimes the asymptotic condition is hardly reachable in physical experiments.

MATERIAL	C_p	ρ	k	$\rho C_p \times 10^{-3}$
Units	$J/(kg \cdot K)$	kg/m^3	$W/(m \cdot K)$	$J/(m^3 \cdot K)$
Polystyrene	1300	15	0.03	19.5
Glass wool	675	52	0.04	35
Charcoal	840	240	0.05	202
PVC*	900	1300	0.19	1170
Gypsum	1080	1200	0.43	1296
Concrete stone	653	2300	0.93	1502
Sandstone*	920	2300	1.70	2116
Lead	1296	11300	35.80	14644
Steel (mild)	500	7830	45.30	3915
Graphite	670	1870	130.00	1253
Magnesium	1000	1730	160.00	1730
Copper	390	8910	393.00	3475
Neosyle	—	—	100	100

Table 3.2: Thermal physical properties of some materials expressed in the International System of Units. Data from [1], except for those labelled with * that are taken from [69].

3.7 Analysis of thermo-fluid dynamics interaction using different materials

In this section we study the influence of conductive walls on the fluid flow. The temperature profile on the horizontal solid sheets is greatly affected by the thermal characteristics of the medium, which, in turn, influences the buoyancy-driven flow.

Once we assign the physical properties of the fluid and the geometry of the case, the behaviour of solid boundaries depends on few main parameters:

- ▶ the volumetric heat capacity ρC_p , that represents the thermal inertia of the solid, namely the tendency to maintain its own temperature profile against the temperature fluctuations of the fluid. Hence, it is more related to the temperature distribution within the solid media;
- ▶ the thermal conductivity k , that is links to the heat transfer at the interface, so also to the capability of the materials to modify the fluid temperature. It qualitatively determines the general fluid motion and it rules the interfacial heat flux.

These two quantities are not completely independent on each other in a real medium: usually a thermal insulator has a low conductivity and low heat capacity, while a conductor has high conductivity and capacity (*i.e.* the case of metals). Table 3.2 reports the thermal properties of some common

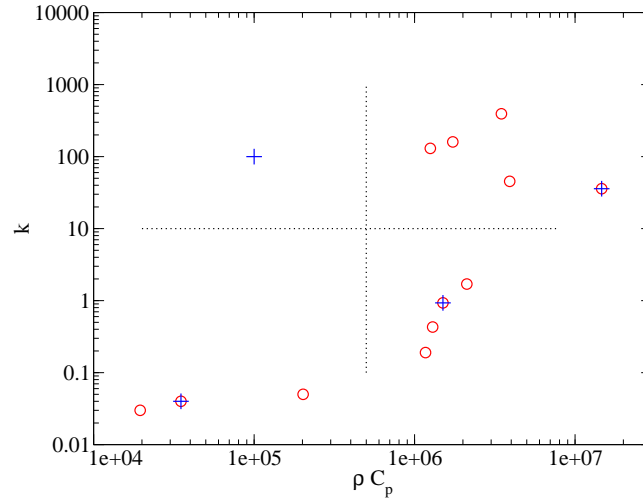


Figure 3.8: Relation between thermal conductivity and the specific heat: the circles represent materials of Table 3.2; the pluses represent materials used in simulations.

materials, while Figure 3.8 shows the distribution of these materials with respect to their own properties. Materials with high conductivity and low capacity are difficult to find in nature. However the rapid development of material science might lead to the production of materials with these characteristics; for this reason we also consider a *virtual* material belonging to this group, called Neosyle².

The following simulations investigate the effect of different materials composing the horizontal walls on the development of the thermo-fluid dynamic field. Five simulations are performed: one with a perfect insulator, the others reproducing the cases shown in Table 3.3, representing the four possible combinations of high/low conductivity and high/low thermal inertia. As already mentioned, Neosyle does not exist in nature, but it is taken as representative of the category with relatively high thermal conductivity and relatively small specific heat, arbitrary chosen as $k = 10^2 \text{kg}/\text{m}^3$ and $\rho C_p = 10^5 \text{J}/(\text{kg} \cdot \text{K})$ respectively.

3.7.1 Simulations settings and procedure

First, we run the case with perfect insulator boundaries, where the coupling condition at the solid-fluid interface is replaced by the adiabatic condition.

In order to reduce the computational time, the simulation is initialised using the fluid flow final configuration obtained by the validation case of

²Fancy name compound of ancient Greek words $\nu\acute{\epsilon}\omicron\varsigma$ (*neos*) “new”, and $\acute{\upsilon}\lambda\eta$ (*yle*) “material, substance”.

	$\rho C_p < 10^6$	$\rho C_p > 10^6$
$k > 10$	Neosyle: $\tau = 5.6 \times 10^2,$ $\alpha = 1.0 \times 10^{-3},$ $TAR \cong 1.75 \times 10^{-3}$	Lead: $\tau = 2.3 \times 10^5,$ $\alpha = 2.45 \times 10^{-6},$ $TAR \cong 2.4 \times 10^{-4}$
$k < 10$	Glass wool: $\tau = 3.65 \times 10^5,$ $\alpha = 1.54 \times 10^{-6},$ $TAR \cong 2.3 \times 10^{-1}$	Concrete: $\tau = 0.9 \times 10^6,$ $\alpha = 0.62 \times 10^{-6},$ $TAR \cong 0.5 \times 10^{-2}$

Table 3.3: Solid boundaries characteristics. Neosyle is a material with $k = 10^2 \text{kg/m}^3$ and $\rho C_p = 10^5 \text{J/(kg} \cdot \text{K)}$ that does not exist in nature.

thermal-coupling, reported in section 3.6.1. The simulation is run until reaching a statistically steady state.

For cases with real horizontal solid sheets, the external insulator blocks present in the experimental apparatus are replaced by an adiabatic condition at the external boundaries of the horizontal sheets; fixed temperature is set at the tips (coherent with the contiguous vertical isotherm boundaries of the fluid domain); CHT is considered during the evolution time of the process at the horizontal solid-fluid interface.

The initial temperature for solid media is set to be the room temperature $T_i = 303.15 \text{K}$, in analogy of validation settings in section 3.4.4. In order to reduce the transient phase, a linear temperature distribution may be imposed along the x -direction. This is the asymptotic distribution in case of absence of solid-fluid interaction. Here we have chosen to set an uniform temperature distribution along the solid sheet because it is closer to an initial experimental situation.

Simulations with CHT are carried out following the temperature advancement strategy described in section 3.6. For the (APP)-step, the final configuration obtained from the perfect insulator is used as a initial field. In the (DRG)-step, C_p is decreased by three orders of magnitude, and simulations are run for $\Delta t_1 = 50 \text{s} \cong 67 t_0$ for Neosyle, lead and concrete. For the glass wool case, the drugging period is reduced to $\Delta t_1 = 20 \text{s} \cong 27 t_0$ since the thermal coupling for strong insulator dramatically increases the computational time.

In the (HOM)-step, temperature is averaged on the homogeneous z -direction. In the (ADJ)-step, the correct heat capacity is restored and simulations are run again for $\Delta t_2 = 10 \text{s} \cong 13 t_0$, a period long enough to bring to steady state condition the fluid/solid interaction. Afterwards, data are collected for successive $\Delta t_3 = 60 \text{s} \cong 80 t_0$ for the statistical analysis. In this

time interval the systems are considered in a quasi-steady state, *i.e.* the evolution of temperature within solid media is negligible during Δt_3 .

The time simulated in the (DRG)-step is equivalent to a physical time $\Delta t_{phy} \sim 13 \text{ hours}$ for all materials except for glass wool, for which it corresponds to $\Delta t_{phy} \sim 5 \text{ hours}$. The estimation of the physical time can be obtained from the non-dimensional time parameter:

$$\Pi_t = \frac{\Delta t_1}{\tau_{red}} = \frac{\Delta t_{phy}}{\tau_{phy}}; \quad (3.15)$$

where τ_{red} is the characteristic time computed with the reduced C_p , and τ_{phy} is the characteristic time of the actual materials. This non-dimensional time must be the same for the systems with actual and reduced specific heat. Notice that Π_t gives also an estimation of the degree of thermal development of solid media: $\Pi_t > 1$, temperature has reached a steady profile; $\Pi_t < 1$, temperature is still evolving. Table 3.4 reports the non-dimensional time for our cases.

The interval Δt_1 was observed to be sufficient to reach a stationary distribution of temperature within the solid just for the Neosyle case; it was not long enough for the other materials having larger characteristic diffusion times.

Even if the statistical steadiness for the systems is not reached, the transitional configurations obtained can be representative of applications and experimental apparatus. For this reason we retained all cases, limiting our attention just to the differences arising in transitional configurations, sharing the same physical time.

However, Neosyle and the perfect insulator deserve particular attention: they represent fully developed systems for the categories of conductors and insulators, respectively.

3.7.2 First order flow statistics

In the following, we classify under the general definition of insulators the materials with low k (glass wool and concrete) and conductors those with large k (Neosyle and lead).

Figure 3.10 shows the streamlines of the mean velocity field for the five cases. The most interesting features are the recirculation regions at the horizontal walls, near the top-left and bottom-right corners, which are absent in our case with perfect insulator. To the knowledge of the authors, previous works [53, 75, 76] studying the effects of conductive boundaries in a cavity, did not report about this flow feature, which, in fact, is a direct consequence of temperature distribution at the boundaries arising after the solid-fluid thermal interaction.

The system is antisymmetric respect to the two diagonals of the domain. For this reason we focus the following analysis only in the top-left region.

As a general feature, hot air blows up from the vertical left wall and impacts the cavity ceiling, then it bounces off and the original upward vertical motion deviates along two directions: a prevalent horizontal one and a weaker, downstream, vertical one. The deflection of the main stream creates two low-speed regions highlighted in Figure 3.10: one is on the left side of the impact region where the corner vortex appears; the other is on its right side close to the horizontal wall.

In the case of the perfect insulator, the velocity is not large enough to generate flow separation; in the other cases, the wall conducts heat and tends to warm up the fluid near the left wall and to cool it near the right wall. Therefore a thin layer of colder fluid travels towards the right wall after being deflected, giving rise to a vertical buoyancy force that pushes the flow closer to the horizontal plate. This causes an increase of horizontal velocity, thanks to the reduction of the flow section. The increased velocity produces flow separation and generates a recirculation bubble of warm fluid. This bubble is found to be larger for conductors since they better cool down the fluid, while it disappears with the perfect insulator.

Figure 3.9, clearly shows the role of the CHT on the temperature distribution close to the horizontal top wall. The perfect insulator (*i.e.* adiabatic conditions) produces an homogeneous distribution of temperature along the horizontal direction. This feature is shared by the other insulators (glass wool and concrete). Moving toward conductors, and in particular for Neosyle the flow temperature decreases from left to right. This happens because the conductor supplies and drains heat respectively by the left and right side of upper portion of the cavity. In all cases the core region exhibits a stable thermal stratification: as shown in the following section 3.7.3 the turbulent fluctuations are almost absent far from the walls.

Figure 3.10 depicts the streamlines of the mean flow. The cases other than perfect insulator and Neosyle may suffer from lacking of steadiness. Most of the fluid motion takes place near the boundaries, within a layer $r/L < 0.1$, in form of a clockwise circulation driven by the convective processes at the two vertical walls. Successive analysis (see Figure 3.12a and 3.13a) will show that outside of this region the magnitude of the velocity drops by more than one order of magnitude. The remaining flow field is characterised by stable stratification and horizontally elongated low-speed vortexes in the upper region of the cavity, below the top boundary layer. The perfect insulator case produces a more uniform distribution of the temperature along the horizontal wall and this reflects onto a more streamlined velocity field. The conductor cases, and specifically the Neosyle, where a statistically steady case has been reached, exhibits two triangularly shaped horizontal vortex structures, that are the result of the horizontal temperature gradients already discussed.

In Figure 3.11 the presence of the typical corner vortex is shown together with the recirculation bubble. Table 3.4 reports the location of separation

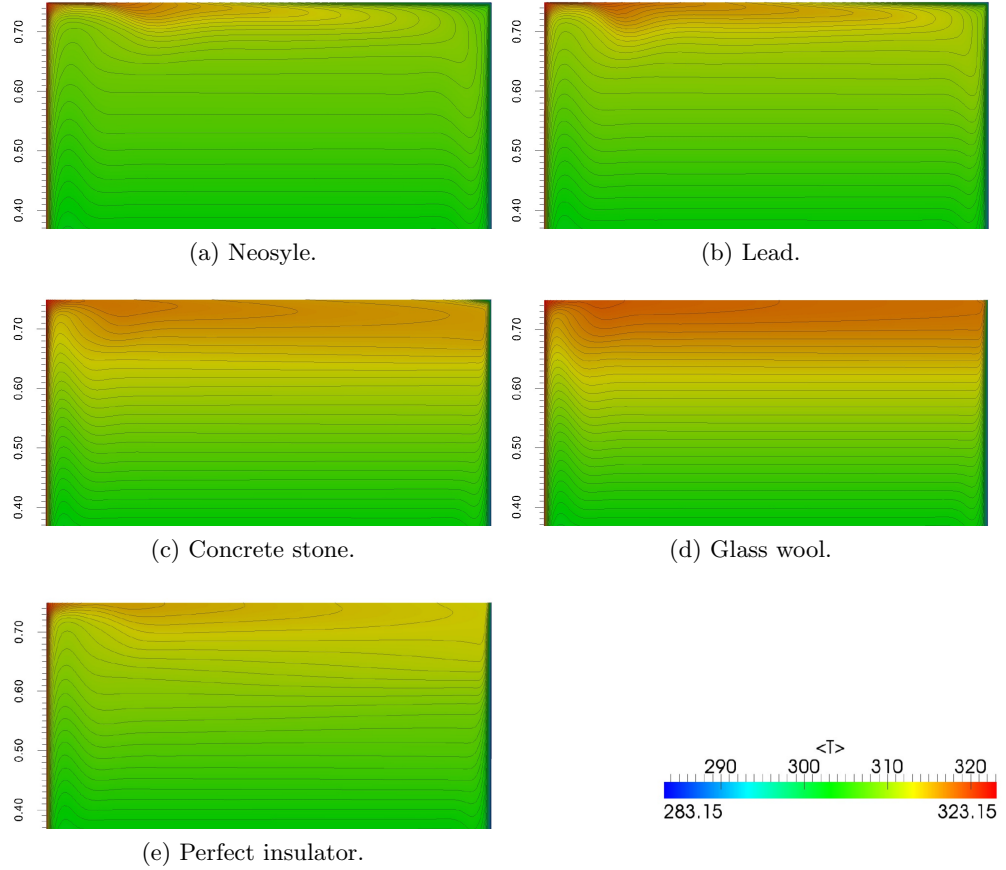


Figure 3.9: Temperature contour plot of the upper half-part of the cavity.

and reattachment points and the height of the bubbles, together with the index Π_t of thermal development of the plates.

Again, we focus on the two cases where statistical steadiness has been reached. The main difference stands in the absence, in the insulator case, of the small horizontal vortex placed at the top wall. This structure is persistent, displaying low-intensity turbulence fluctuations. It is generated from the heat transfer mechanism at the fluid/solid interface, which enhances the vertical velocity of the flow approaching the top horizontal wall. In case of Neosyle, the bubble is at steady condition while, for other materials, is present but still slowly evolving in time.

Other minor difference between Neosyle and perfect insulator is that the stable vertically-elongated vortex, localised in the centre of figure, appears a bit different in shape. For the other cases, this feature is not present on the average, but the instantaneous fields show the occurrence of some unstable vortexes in the same region. At this simulation stage, the turbulence fluctuations rapidly destroy the structure.

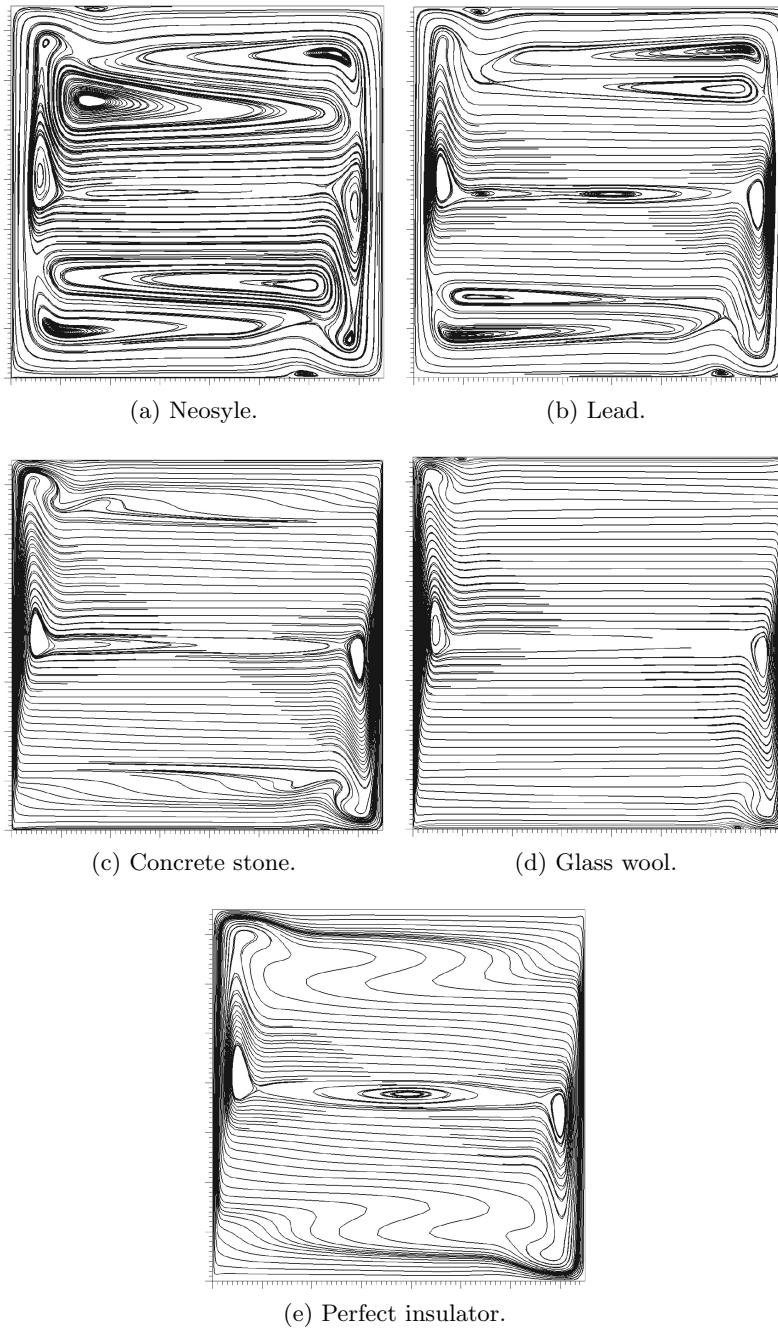


Figure 3.10: Streamlines of $\langle U \rangle / U_0$.

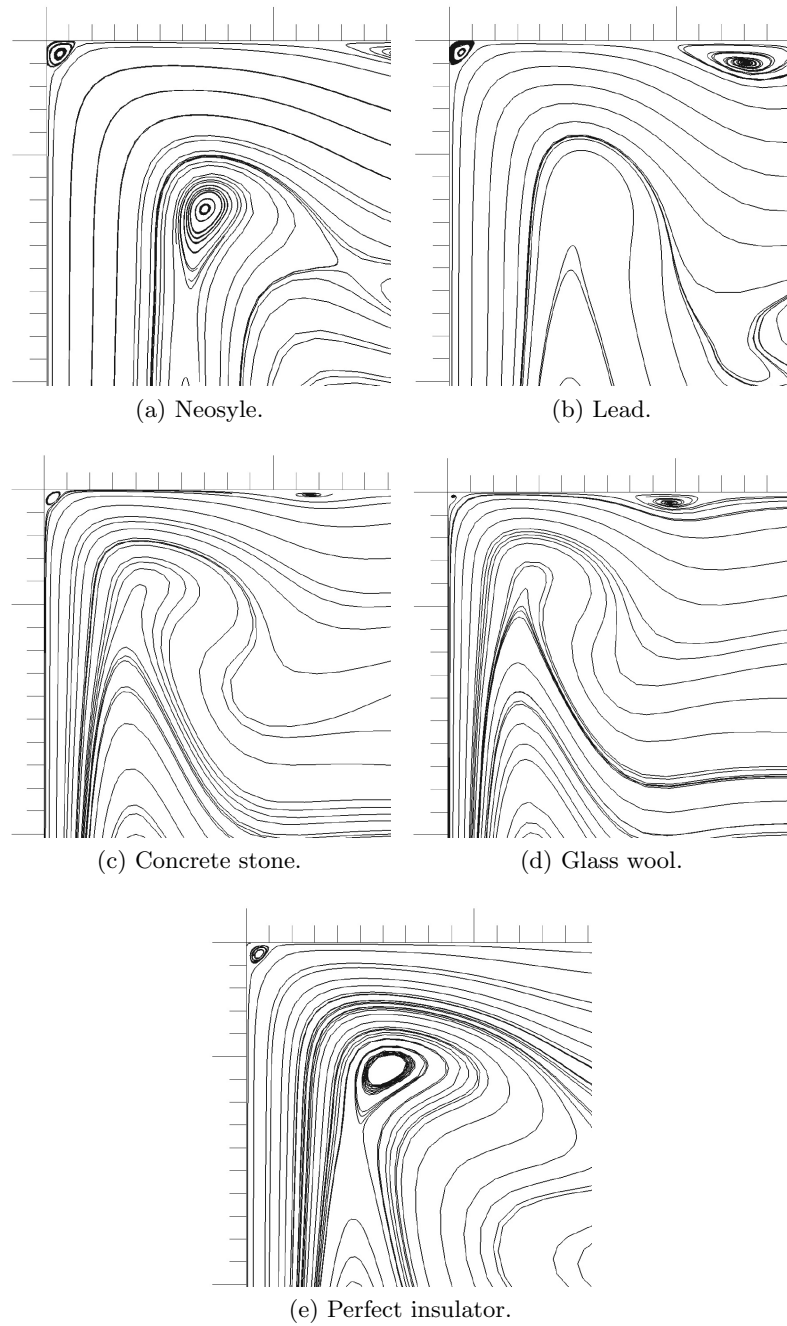


Figure 3.11: Focus on the corner streamlines. The square has an edge of $0.2L$.

	Separation point [x/L]	Reattach. point [x/L]	Height [h/L]	Π_t [-]
Neosyle	0.167	0.267	0.0267	90
Lead	0.120	0.207	0.0267	0.22
Concrete	0.127	0.173	0.0067	0.05
Glass wool	0.087	0.153	0.0067	0.05
Perfect Insulator	-	-	-	-

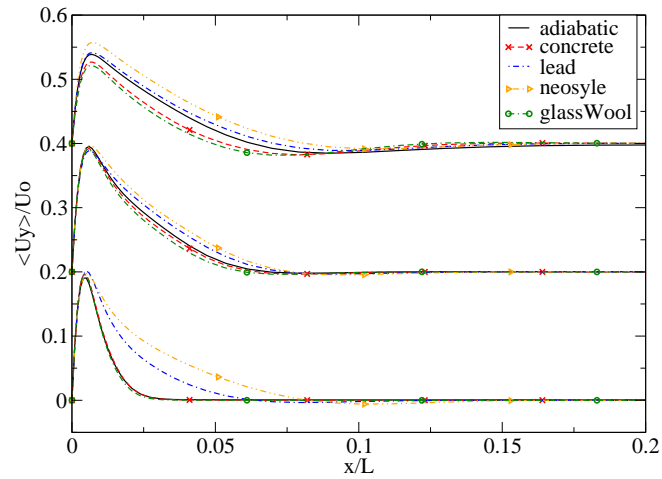
Table 3.4: Geometrical characteristics of the recirculation bubbles on the top horizontal plate, and non-dimensional time parameter. Columns: first, location of separation point; second, location of reattachment point; third, maximum distance from the plate (h) of the bubble; fourth, non-dimensional time $\Pi_t = \Delta t_1 / \tau_{red}$, where Δt_1 is the time simulated in (DRG)-step and τ_{red} is the characteristic time computed with the reduced C_p coefficient. Geometrical estimation from the stream line plots; absolute error $e_{abs} = \pm 0.003$.

Figure 3.12 reports the profiles of non dimensional temperature and vertical velocity at the three heights as in Figure 3.2.

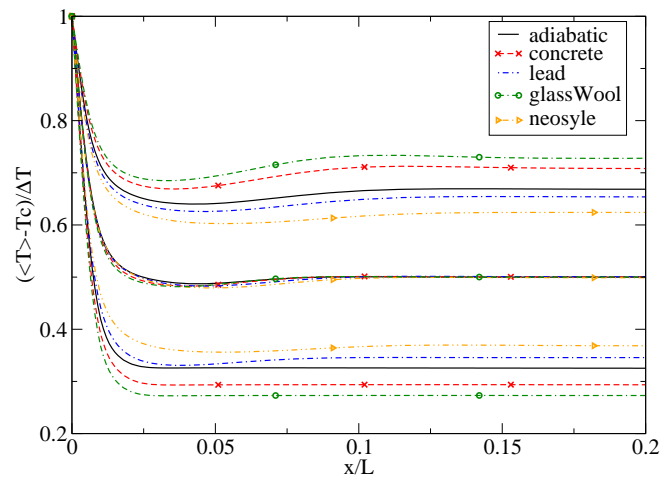
The vertical velocity near the hot wall (Figure 3.12a) does not exhibit significant differences from case to case at heights $y/L = 0.5$, whereas at $y/L = 0.8$ vertical velocity is higher for the Neosyle than for the perfect insulator. This difference is even more evident at level $y/L = 0.2$. In fact, here air is warmed up not only by the isothermal vertical wall, but also by the adjacent conducting floor of the cavity which, in turn, produces a wide region of convective flow.

The temperature profiles in Figure 3.12b do not differ among them in the near wall region. However, the temperature in the region farther from the wall is larger in case of conductors rather than for insulators close to the bottom surface ($y/L = 0.2$), whereas the opposite is true at $y/L = 0.8$. This follows from the accumulation of high/low temperature occurring close to the top/bottom boundaries in case of insulator media, phenomenon not present when the horizontal plates are made of conducting materials.

Figure 3.13 shows non-dimensional mean horizontal velocity and temperature on vertical lines near the top walls, at three significant distances from the hot wall: $x/L = 0.2, 0.5, 0.8$. In case of Neosyle, a more energetic horizontal velocity is observed close to the cavity ceiling. In case of perfect insulator the velocity decreases more rapidly along the horizontal and this may be related to the horizontal homogenisation of the thermal field in the



(a) Non-dimensional vertical velocity.



(b) Non-dimensional temperature.

Figure 3.12: Non-dimensional mean vertical velocity and temperature profile close to the hot wall, taken along the three horizontal lines as in Figure 3.2.

near wall region. The other insulator cases suffer for a transient behaviour, the flow field is not completely developed and it is characterised by smaller velocities. Along the line $x/L = 0.2$ the velocity peaks at different vertical locations in cases of perfect insulator and Neosyle, correspondingly to the location of the recirculation bubble (see Figure 3.11 and Table 3.4).

The vertical distribution of temperature (Figure 3.13b) indicates that, in case of Neosyle, the thermal field varies substantially along the horizontal direction close to the top wall, whereas this does not happen for the perfect insulator. This scenario is explained by the fact that conductors supply/drain temperature to/from the fluid region in a not homogeneous way moving downstream along the horizontal wall.

3.7.3 Fluid flow turbulent statistics

Turbulent statistics near the top and left walls are presented in the following. The core region is characterised by a weak laminar flow: at a distance of $0.2L$ from the walls $T_{rms} \sim 0$ and $\mathbf{u}_{rms} \sim 0$. For this reason, we focus our attention in the near-walls region.

Figure 3.14, 3.15 show the vertical and horizontal turbulent temperature fluxes. The results can be interpreted via the gradient-diffusion hypothesis (cf. Pope [56]): turbulent transport of temperature can be represented as a down-gradient mechanism, that can be modelled by

$$\langle T'_f u'_i \rangle = -\alpha_{eff} \frac{\partial T_f}{\partial x_i}, \quad (3.16)$$

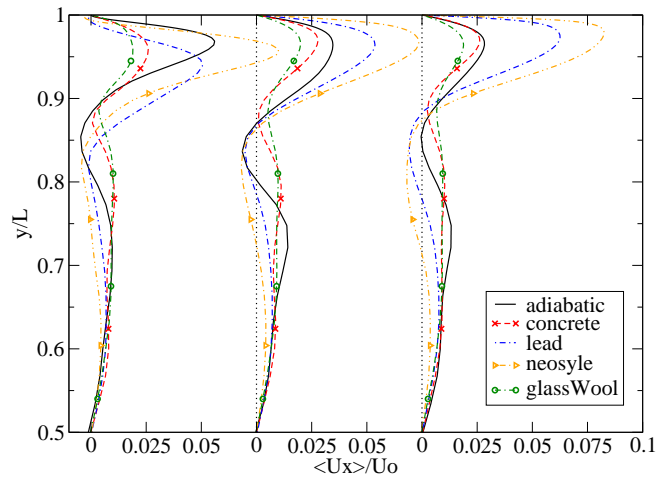
where $\alpha_{eff} > 0$ is the effective diffusivity. Hence, the temperature gradient has opposite sign with respect to the turbulent fluxes.

Although for the sake of completeness we show results for all cases, here we discuss the difference between Neosyle and the perfect insulator.

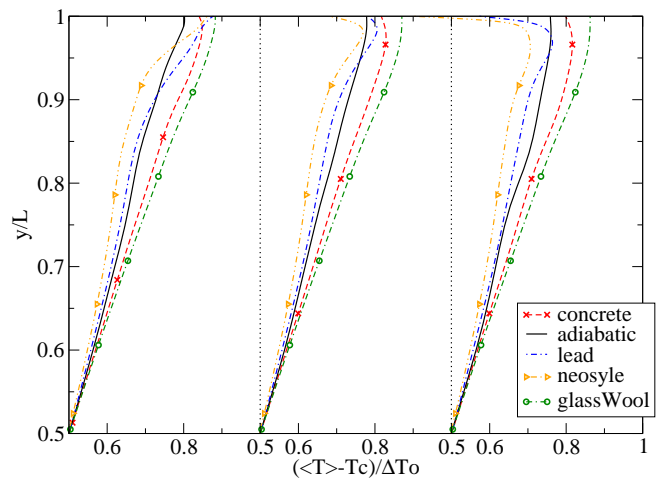
Figure 3.14 shows the average horizontal turbulent temperature flux in a region $1 \times 0.2L$ close to the top wall. Also, streamlines are reported for the sake of clarity. A feature common to all cases is the negative spot near the left corner: this corresponds to a positive horizontal turbulent heat flux, that increases the overall horizontal heat convection from the hot wall. The perfect insulator case has a larger negative plume thanks to the lack of the recirculation bubble, while Neosyle presents a positive spot near the right corner.

In this thin region, close to the horizontal wall, turbulence drives heat from the right to the left lowering the air temperature. This effect is evident in Figure 3.13b on line $x/L = 0.8$, where the fluid temperature of Neosyle case decreases rapidly while approaching the top boundary.

Figure 3.15 shows the average vertical turbulent temperature flux on a strip $0.2 \times 1L$ near the vertical hot wall. In all cases a zone of negative



(a) Non-dimensional horizontal velocity.



(b) Non-dimensional temperature

Figure 3.13: Non-dimensional mean horizontal velocity and temperature profile close to the top wall, along three significant vertical lines: $x/L = 0.2, 0.5, 0.8$.

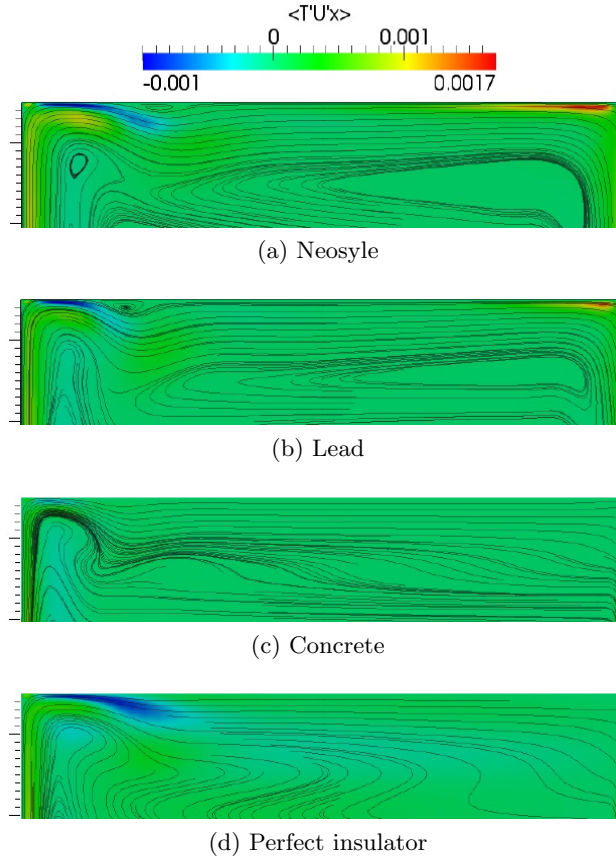


Figure 3.14: Temperature fluxes $\langle u'_x T' \rangle / U_0 \Delta T$ near the top horizontal wall. Strips height $0.2L$, width $1L$. Streamlines as in Figure 3.10 are also reported. There are no significant differences between concrete and glass wool, so the latter is not reported.

flux near the top corner is present, more intense for conductors than for insulators. In this region the vertical heat flux is positive.

In the Neosyle case the cold air layer in the left-bottom corner region triggers a local convection region, which is identified by positive vertical thermal fluxes. The perfect insulator case does not exhibit such a behaviour, as expected. The effects of this mechanism reflect also in the less localised vertical velocity profile of the Neosyle case, as shown in Figure 3.12a, at line $y/L = 0.2$.

Figure 3.16 reports the averaged RMS of temperature, vertical and horizontal velocity near the horizontal top wall.

In conjunction with the previous plots of heat fluxes, Figure 3.16a exhibits a significant increase of turbulence for Neosyle, near the right wall. On the other hand, the perfect insulator is characterised by low fluctuations

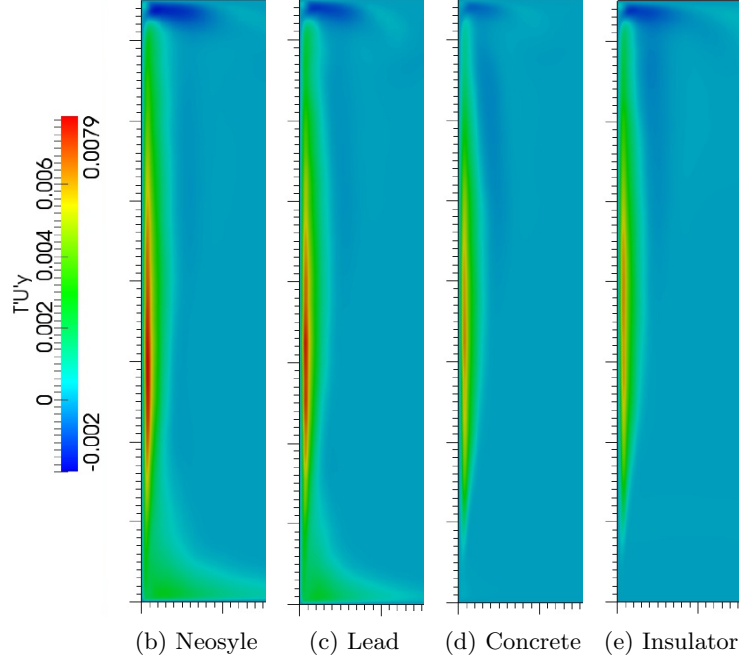


Figure 3.15: Temperature fluxes $\langle u'_y T' \rangle / U_0 \Delta T$ near the left vertical wall. Strips height $0.1 L$, width $0.2 L$. There are no significant differences between concrete and glass wool, so the latter is not reported.

on lines $x/L = 0.5, 0.8$. Over the same lines, Figure 3.16b points out that horizontal fluctuations for conductors are localised near the horizontal wall, where unstable stratification triggers turbulence.

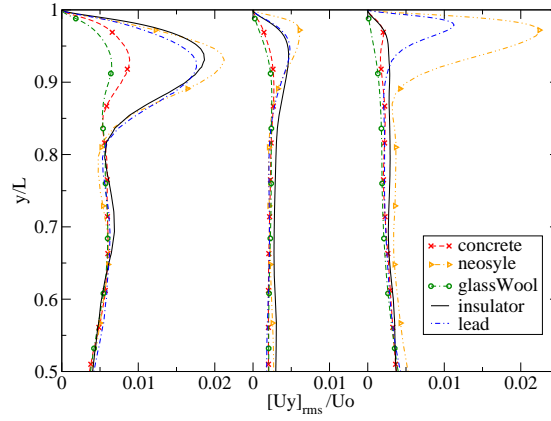
In Figure 3.16c the temperature RMS highlights the main difference between perfect insulator and the real materials. The adiabatic condition allows for higher temperature fluctuation on the wall, that damp thermal gradient and homogenise temperature near the horizontal wall. This eventually inhibits the formation of some flow structures, as the recirculation bubble. For the real materials, fluctuations peak near the horizontal plates while, for the ideal insulator they are scattered on the centre region.

3.7.4 Temperature distribution within the solid media

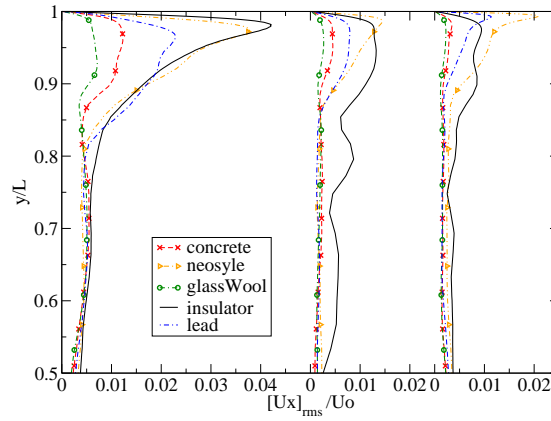
In presence of fluid-solid coupling the interfacial heat transfer modifies the temperature distribution in the solid media.

Temperature diffuses in plates along vertical and horizontal direction of propagation, that have two different characteristic time:

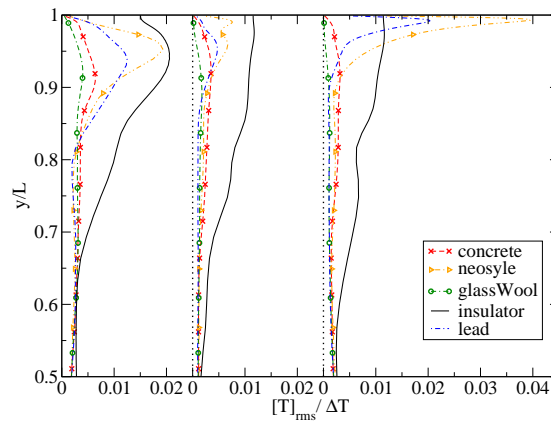
$$\tau_{hor} = \frac{L^2}{\alpha_s} \quad \text{and} \quad \tau_{ver} = \frac{H^2}{\alpha_s}, \quad (3.17)$$



(a) Vertical velocity RMS.



(b) Horizontal velocity RMS.



(c) Temperature RMS.

Figure 3.16: Velocity and temperature root-mean square near the top horizontal wall. Plots over vertical lines at the three significant heights as in Figure 3.2.

where $L = 0.75m$ and $H = 0.0015m$ are the height and the width of the plates, respectively. Therefore, horizontal diffusion is extremely slower with respect to vertical diffusion, since $\tau_{ver} = 4 \times 10^{-6} \tau_{hor}$. Due to the high value of the geometrical aspect ratio (thus, independent from the substance properties), the time required to balance the effects of the isothermal edges of the plate and the solid-fluid heat exchange may be huge.

The horizontal characteristic diffusion time of the materials used in the present investigation, reported in Table 3.3, results to be far larger than the flow setting time.

Figure 3.17a shows the temperature profile along a centreline within the solid plate for different materials. The simulations are carried out up to different development stages as it is shown by the non-dimensional time in Table 3.4. The transitory profiles suggest that, at the early stages, heat transfer from the fluid to the solid medium rapidly increases the internal temperature. This occurs uniformly along the horizontal x -direction, and is a very fast process since vertical diffusion is very fast. After that, the tip effects become increasingly important and the isothermal walls modify the longitudinal temperature distribution: the hot vertical wall warms the horizontal solid medium on the left side, whereas the opposite occurs at the right edge due to the presence of the cold isothermal wall.

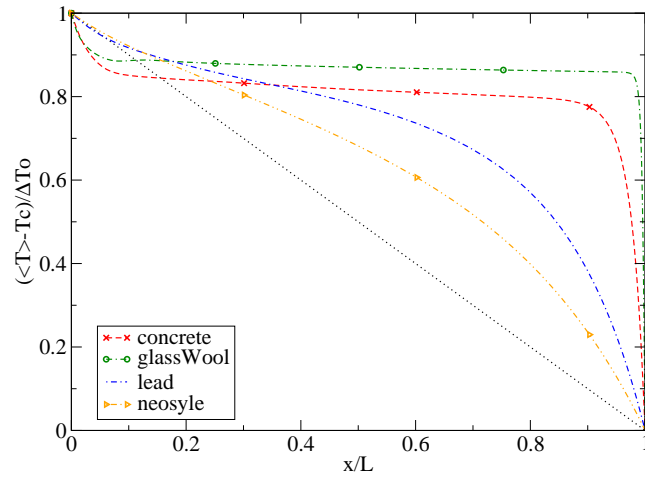
The statistical steady temperature profiles within the solid are given by Laplace equation (3.14), that does not depend on any physical parameter of materials. They are determined only by the heat flux across the solid-fluid interface, that is ruled by equation (2.17). Indeed, it is expected that materials with similar thermal conductivity, tend to develop a similar temperature distribution.

Conductors exhibit an internal temperature profile, on average, higher than the linear profile, reflecting the inhomogeneity in the vertical heat flux along horizontal direction. For insulators the steady state profiles are predicted to have a distribution closer to a linear one, with a lower average temperature with respect to conductors, but this behaviour is still not appreciable in our transitory/transitional results.

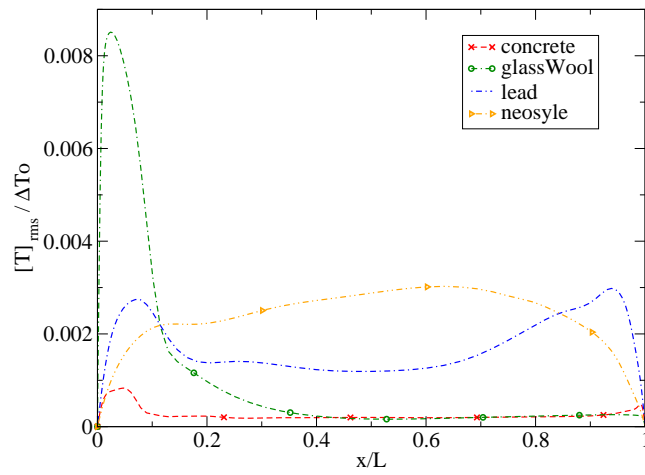
Figure 3.17b shows the temperature root-mean square profiles along the horizontal centerline within the top solid medium. The temperature RMS within the solid is nearly constant along the vertical direction, as reported in Figure 3.18. This is an effect of the small value of characteristic time for vertical diffusion: the horizontal sheets are thin enough to be strongly influenced by the interfacial fluxes.

Looking at Figure 3.17b, we can identify three thermal areas in the top solid medium. Note that the description for the upper part of the cavity repeats in an anti-symmetric way for the lower part:

The impact zone ($0 \lesssim x/L \lesssim 0.2$): the hot fluid plume hits against the cavity ceiling. Heat transfer is dominated by the hot incoming flow.



(a) Non-dimensional temperature distribution.



(b) Non-dimensional temperature RMS.

Figure 3.17: Profile along the horizontal center-line of top solid wall.

Thermal perturbations in the case of concrete are less-intense and more localised, while, in case of glass wool, they are more intense and distributed. This occurs because glass wool has a smaller ρC_p that allows for a better thermal fluctuation. Also, lead case presents a maximum of temperature fluctuations in this region. On the contrary Neosyle exhibits a smoother and qualitatively different profile. In fact the recirculation bubble appears farther from the vertical wall, and the hot plume can exchange heat with the solid medium over a wider interfacial region, before fluid separation.

The parallel flow region ($0.2 \lesssim x/L \lesssim 0.8$): here fluid motion is parallel to the horizontal wall. Conductor materials exhibit larger levels of fluctuations, while insulators have almost no fluctuations. Heat transfer is less influenced by convective motion. Indeed this is a region of lower turbulence level (see Figure 3.16) and the thermal fluxes are almost absent (see Figure 3.14 and 3.15) with respect to other regions.

The fall-down region ($0.8 \lesssim x/L \lesssim 1$): here the flow deviates downward and internal solid temperature decreases. In cases of insulators, see Figure 3.17a, a rapid diminution of internal temperature occurs: in case of glass wool it decays very close to the right wall and temperature fluctuations are practically absent ($T_{rms} \sim 0$); in case of concrete, a small level of temperature fluctuations is present; lead is colder in this region and the interfacial interaction generates more fluctuations; Neosyle presents the smoother behaviour.

Finally, the thermal fluctuations at the solid-fluid interface are analysed. TAR is the key parameter for studying the perturbations at the boundaries, and it relates the degree of interaction between the two phases, as discussed in section 3.3. For the four materials herein considered, TAR differs by orders of magnitude, as reported in Table 3.3.

Figure 3.18 shows temperature instantaneous fluctuations at the top solid surface. As the TAR decreases, the interface exhibits a larger level of fluctuations, except for the glass wool case. In materials characterised by smaller TAR, the fluctuations are more spread around the plate, whereas for large values of TAR, fluctuations remain localised in a region close to hot wall where the vertical flow impact the top solid surface.

However, it has to be pointed out that a direct comparison between the materials cannot be performed. In fact, equation (3.11) suggests that the solid-fluid heat flux is inversely proportional to the effusivity, and directly proportional to the temperature difference. Since the solid media are all at different thermal evolution stages, the internal temperatures of the materials are quite different from case to case, as already shown in Figure 3.17b. Thus the effects of different effusivities are overcome by the different temperature gradients.

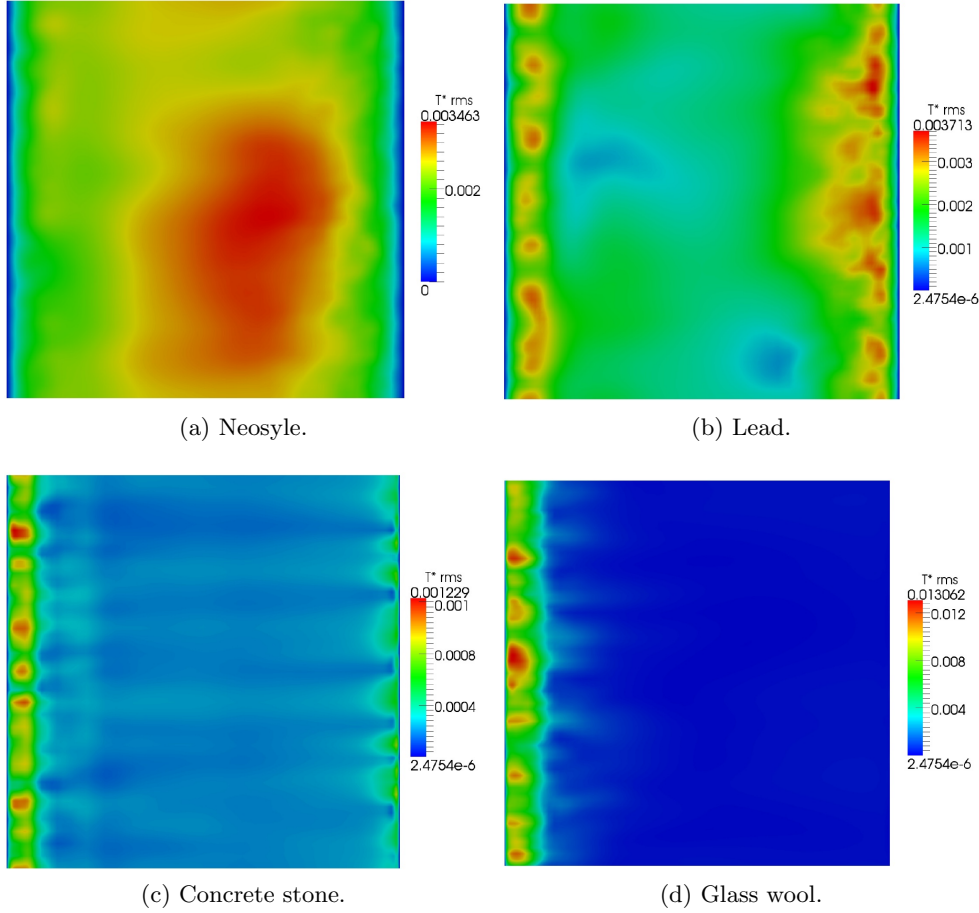


Figure 3.18: Temperature instantaneous fluctuations on the interface between fluid and top wall, $T^* = T'/\Delta T$.

3.8 Conclusions

Turbulent natural convection in a enclosure is studied numerically, via large-eddy simulations. A Lagrangian dynamic sub-grid scale model is adopted to determine the turbulent sub-grid scale viscosity and temperature diffusivity, while the conjugate heat transfer between solid media and fluid flow is taken into account by the method developed by Sosnowski *et al.* [69]. The implementation of the numerical model is carried out within the OpenFOAM framework.

A paradigmatic case is analysed: a square cavity, filled with air, having two different heated vertical walls and two conductive horizontal boundaries, separated from the outside by insulator blocks. The Rayleigh number is chosen to be $Ra = 1.58 \times 10^9$ as in previous literature studies.

First, the code is validated against experimental and numerical data

given in [75, 76, 5] and [53], respectively. Flow statistics are in good agreement with those reported in literature. Specific attention is paid to thermal coupling validation. In our numerical experiment, the conductive sheets and the insulator blocks as in the benchmark experiment are taken into account. The temperature distribution is correctly reproduced. However the numerical results and a theoretical analysis of temperature diffusion time, shows that in the experiment diffusion process is still in an evolution stage which can elapse over few days. This highlights the fact that sometimes, the adiabatic condition commonly used in numerical simulations, and intended to mimic a perfect insulator, may be representative of an asymptotic behaviour difficult to reach in real cases.

The model is successively applied to study, in the same flow configuration as in the literature experiments, the impact of different solid media on the flow features and temperature distribution. Specifically conjugate heat transfer is considered at the top/bottom horizontal plates, usually modelled as perfect insulators. Four materials are considered: two conductors and two insulators. An additional simulation is carried out considering perfect insulating walls, reproduced by applying the adiabatic condition.

The problem of the characteristic time of temperature diffusion in solid media is addressed. The geometrical dimensions of the horizontal plates lead to two different diffusion times for horizontal and vertical direction, respectively. The asymptotic steady-state thermal configuration is reached after a time comparable with the horizontal characteristic time, that could be huge for materials with low thermal diffusivity. In order to perform numerical simulations representative of physical experiments, the initial conditions for the temperature field in the solid and fluid media have been set close to those of typical experiments.

To study the system, in order to circumvent the problem associated with low diffusivity of some materials, leading to an excessive developing time non affordable in numerical simulations, a four-step procedure is developed. It consists in the use of a temperature advancement strategy based on the artificial reduction of the C_p of the solid medium during the early stage of development of the flow field, and to recover its actual value for obtaining the final flow configuration. The same physical time is reproduced in all cases and different degrees of thermal development were thus reached, depending on the characteristics of the solid media; for the high conductor case (Neosyle) and the perfect insulator case only, the system reached the steady state.

The two cases are, hence, considered as representative of the two categories of conductors and insulators. All cases are characterised by anti-symmetry with respect to the diagonals of the cavity and, hence the discussion has been developed for a portion of the domain, invoking anti-symmetry for the remaining part.

Except for perfect insulator, a recirculation bubble close to horizontal

walls, near the top-left and bottom-right corners is observed.

Further, the presence of conductors produces stronger turbulence on the top-right corner that increases the buoyancy force in that regions and results in high fluid velocity near the horizontal walls.

The core region is always characterised by weak stable stratification and, for conductors, nearly laminar flow developing along horizontally shaped low-speed recirculating flow. Temperature inside horizontal plates presents profile higher than linear distribution for conductors, while for real insulator cases, it is still evolving. Fluctuations at the solid-fluid interface are less intense than in the insulator cases and diffused over the horizontal sheets.

Perfect insulator can be considered as the asymptotic limit for insulating media, when $k \rightarrow 0$. However, the analysis clearly shows that the flow features may be different from real insulating materials when the asymptotic regime has not been reached.

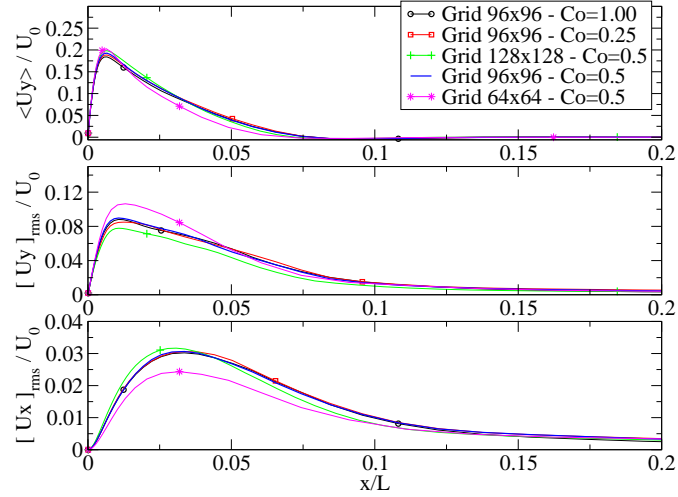
Finally, in the present investigation, it has been mentioned that disagreements in the temperature profile in the core region within the cavity may be due to the effects of thermal radiation here not considered. Radiation models are currently under analysis, and will be implemented in the near future in our model.

3.9 Appendix: additional validation analysis

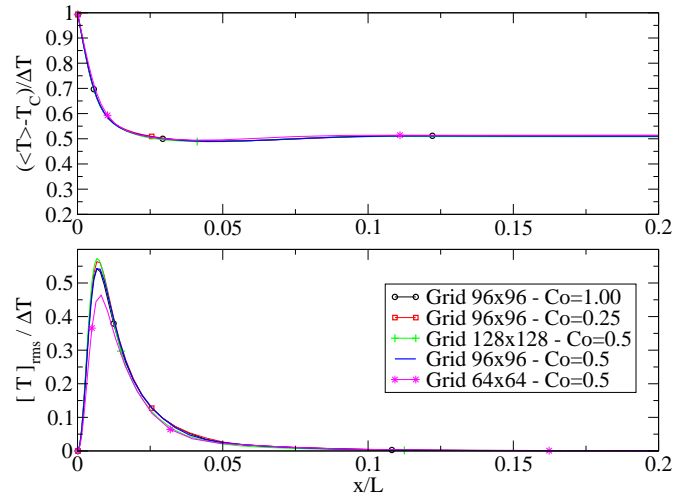
In section 3.5, the validation of the numerical model is carried against literature numerical and experimental data. In order to corroborate the simulation methodology adopted, additional analysis is reported in this appendix: first mesh and time-step dependency are investigated; then we estimate the mesh size and time-step employed with respect to the Kolmogorov length and time-scale to detect the range of sub-grid scale parametrised during the simulation.

Mesh and time-step dependency: the reference case in absence of CHT, described in section 3.4.4, is reproduced again with four different settings:

1. the mesh resolution is held to $96 \times 96 \times 64$ cells but the Courant number of the simulation is increased to $Co = 1$;
2. the mesh is held as in the previous case but the Courant number of the simulation is decreased to $Co = 0.25$;
3. the time-step is held at $Co = 0.5$, but a finer mesh is used, with a resolution of $128 \times 128 \times 64$ points;
4. the time-step is held at $Co = 0.5$, but a coarser mesh is used, with a resolution of $64 \times 64 \times 64$ points.



(a) Fluid flow quantities: (top) vertical velocity profile; (center) vertical RMS; (bottom) horizontal RMS.



(b) Temperature profile and root-mean square: (top) temperature profile; (bottom) temperature root-mean square.

Figure 3.19: Comparison of non-dimensional quantities for different mesh resolutions and time-steps. Quantities are plotted along an horizontal line at height $y/L = 0.5$, near the hot wall.

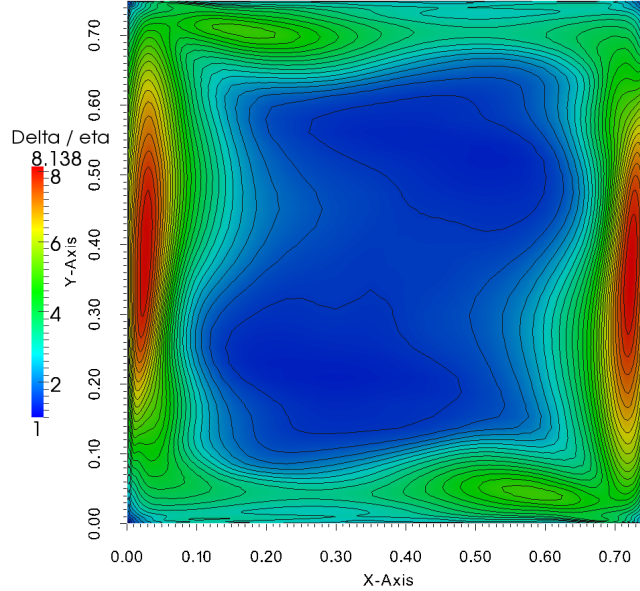


Figure 3.20: Contour plot of the ratio $\bar{\Delta}/\eta$ between the local cell width and the Kolmogorov length scale.

The Courant number is defined, cell by cell, as $Co = \Delta t |\bar{u}| / \delta x$, where Δt is the time step, $|\bar{u}|$ is the velocity magnitude through the cell and δx is the cell size in the direction of the velocity.

An analysis of grid dependency in the spanwise direction was done by Peng and Davidson [53] for the same case, hence it is not repeated here. We use the same number of grid points as in [53] along the spanwise direction in all cases. The results are compared with those of the reference simulation reported in section 3.5, which has a grid resolution of $96 \times 96 \times 64$ points and $Co = 0.5$.

The simulations with finer and coarser meshes are stretched in such way that the first cell near the wall has the same width as in the reference simulation. After a statistical steady state is reached, the statistics are computed during a period of time roughly corresponding to one turnover time of the main cavity vortex, for all simulations.

Figure 3.19a shows the non-dimensional first and second order statistics for the velocity field. The quantities are plotted near the hot wall, along the horizontal centreline ($y/L = 0.5$) within the cavity. The results obtained with different time-steps practically collapse over the same curves, thus the results are substantially time-step independent for a wide range of values of the Courant number.

As regards space resolution, simulation with finer mesh slightly differs from the reference case: a slightly higher peak of the vertical velocity is

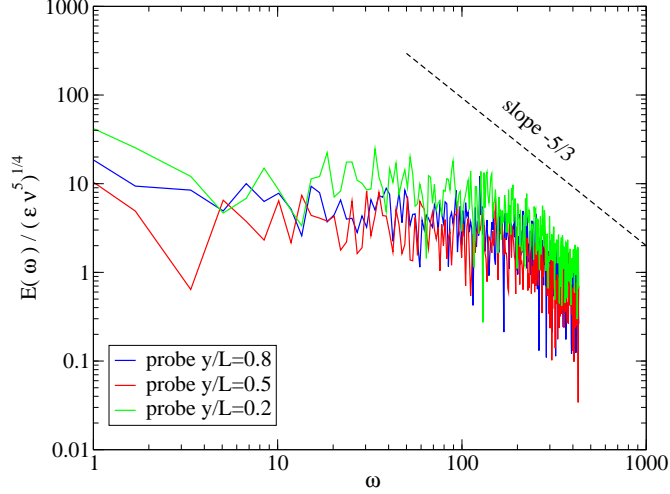


Figure 3.21: Normalized time power spectra of the resolved turbulent kinetic energy $\kappa = \langle u'_i u'_i \rangle / 2$. The data used are recorded at three probes located near the hot vertical wall ($x/L = 0.007$), in the mid-plane ($z/L = 0.5$), at three characteristic heights ($y/L = 0.2, 0.5, 0.8$).

observed together with second-order statistics closer to the experimental data. On the contrary, the simulation with the coarser mesh exhibits less accurate results. The vertical velocity profile has slightly higher peak and lower values farther from the wall. The RMS of the vertical velocity is overestimated while that of the horizontal one is underestimated.

Figure 3.19b reports the mean and RMS temperature profile along the same horizontal centreline as in Figure 3.19a. The temperature profiles do not vary from case to case, while the second order statistics of temperature obtained with the coarse mesh case are lower than in the other cases.

Overall, the grid size used in our study, which is the same as that used in [53], is able to reproduce the first and second-order statistics of the flow accurately. The choice of the time-step within a wide range of values of Courant numbers does not affect the quality of the results.

Turbulent length scales: to get information on the range of spatial scales not resolved in the simulation, the Kolmogorov turbulent length-scale $\eta = (\nu^3 / \langle \epsilon \rangle)^{1/4}$, where ϵ is the turbulent dissipation rate, is computed for the reference simulation. The dissipation rate ϵ was calculated considering the sum of resolved and SGS contributions.

Figure 3.20 shows a contour plot of the ratio $\bar{\Delta} / \eta$ between the local cell width and the turbulent length scale η . The figure clearly shows that turbulence is present near the walls. The values of $\bar{\Delta} / \eta \sim 1$ in the core region of the cavity must be intended as representative of low-level turbulence,

nearly laminar, region. The local cell width is one order of magnitude larger than η in the boundary layers developing near the vertical walls, whereas the ratio decreases close to the horizontal walls, where the boundary layer is less energetic.

Figure 3.21 reports the time power spectra of the resolved turbulent kinetic energy, computed by using the Fourier transform of data recorded at three probes located near the vertical hot wall at $x/L = 0.007$ (approximately where the vertical velocity has a peak), at $z/L = 0.5$ and at three different heights $y/L = 0.2, 0.5, 0.8$. A well-defined inertial sub-range $E(\omega) \sim \omega^{-5/3}$ cannot be detected, indicating that this is a low Reynolds number turbulent flow where the production range of scales is not completely separated from the dissipation one. This is typical of wall-resolving LES where the near wall thin boundary layer has to be appropriately resolved.

The ratio between the simulation time-step Δt and the Kolmogorov turbulent time-scale $\tau_k = \sqrt{\nu/\epsilon}$ at the three locations is $\Delta t/\tau_k < 1$, indicating that the whole turbulent spectrum is resolved in time. This is typical of LES of low Reynolds number flows run with values of Courant number smaller than unity.

To summarise, the analysis suggests that most turbulent scales are directly resolved in the simulation, which can be classified as *quasi-DNS* according to the definition given in Spalart *et al.* [70].

Chapter 4

Thin film evaporation and condensation from a hot plate in enclosure

The results present in this chapter have been submitted for publication as journal paper: C. Cintolesi, A. Petronio, V. Armenio, *Large-eddy simulation of thin film evaporation and condensation from a hot plate in enclosure: first order statistics*, International Journal of Heat and Mass Transfer.

Contents

4.1	Introduction	70
4.2	Problem description	74
4.3	Mathematical and numerical approach	75
4.4	Simulation settings	75
4.4.1	Computational grid	75
4.4.2	Boundary and initial conditions	76
4.4.3	Non-dimensional parameters	78
4.5	Results and discussion	79
4.5.1	Preliminary simulation	79
4.5.2	Drying-process simulations	82
4.6	Conclusions	95
4.7	Appendix: turbulence analysis	97

Numerical investigation of water evaporation and condensation in buoyancy driven flow, along with the thermal coupling between fluid and surrounding solids, is interesting for many industrial applications. The physical complexity of the evaporation and condensation processes, the mutual

thermal influence of water change of phase and solid-fluid heat transfer, the anisotropy of turbulence quantities are challenging problems from numerical and theoretical side. The archetypal case of a vertical hot plate inside a cold square enclosure, filled with humid air, is studied. The solid surfaces are wetted by a thin water film. The plate cooling process due to film evaporation is analysed. Numerical simulation adopts the large-eddy methodology along with the dynamic Lagrangian sub-grid scale model. The conjugate heat transfer technique accounts for the solid-fluid thermal coupling, while the water phase is modelled under the thin film assumption. First, a preliminary case with isothermal solid boundaries and fixed film thickness is reproduced at $Ra = 5 \times 10^8$. The absence of surface heat transfer leads to analogous distribution of temperature and humidity. The cavity is characterised by strong stratification that confines the motion in the upper part. Successively, conjugate heat transfer and water film model are activated, and three cases are performed changing the plate material. The specific heat ρC_p of materials is the parameter controlling the plate cooling process, that is mainly due to evaporation. An analysis of the dew-point temperature suggests that recondensation onto the plate surface cannot occur, even for materials that are rapidly cooled.

4.1 Introduction

Natural convection in presence of water evaporation and condensation plays a crucial role in a number of natural and industrial processes. A realistic and accurate numerical reproduction of such phenomena is a challenging problem from both numerical and theoretical viewpoints.

Several physical effects can influence the natural convective systems: thermal radiation from solid bodies as well as from fluid medium; thermal-fluid interaction between solid and fluid media; Dufour and Soret effects; the fog formation in case of high humidity. From a numerical point of view, in most applications, flows cannot be considered laminar and an accurate reproduction of turbulence is required. Moreover, the Boussinesq approximation for incompressible flow, cannot be applied in systems with high temperature and humidity differences.

A detailed description of evaporation and condensation on wetted surfaces, can be found in de Gennes [18] and Oron *et al.* [52]. Thiele [74] gave also an overview on the complex physical processes involved. Heat transfer mechanisms occurring in such flows are addressed in Incropera *et al.* [32], Welty *et al.* [82], and Lienhard [41].

In many works oriented toward practical applications, the complex interaction between liquid phase and solid surfaces is modelled through the thin film assumption: water is considered distributed over the solid surface as a continuous thin film, even if it can spread like liquid patches or sessile

droplets.

Russo *et al.* [63] used Direct Numerical Simulations (DNS) to simulate a low Reynolds number turbulent channel flow. A Lagrangian model was used to simulate the water droplet distribution in air. The effects of heat and mass transfer by evaporation/condensation on the wall-normal distribution of the temperature statistics of the droplets were investigated.

The same approach was used by Bukhvostova *et al.* [12], where compressible and incompressible solvers were tested and compared. The same turbulent droplets-laden channel flow as in [63] was studied. The compressible and incompressible approaches showed similar results for fluid dynamics quantities, but relevant discrepancies for thermal quantities were evidenced. The authors concluded that, overall, the compressible solver is more accurate.

Many other works investigated the effects of evaporation and condensation in closed systems, in the laminar-flow regime.

The paper of Sun *et al.* [71] reports an accurate study of laminar natural convection in different geometries, using a compressible low-Mach number model. The case of a two-dimensional square cavity was mostly analysed. A thin film of liquid water wets the walls and the domain is filled with humid air. Condensation and evaporation phenomena occur when the temperature of external walls is increased or decreased in time. The general features of the fluid motion were discussed, together with the time evolution of the averaged temperature and density, and the spatial distribution of the liquid film. The presence of circular motion near the vertical walls and Rayleigh-Bénard cells near the horizontal ones, strongly influence the distribution of water film. On the contrary, the film thickness was shown to be nearly independent on variations of the wall temperature.

Laaroussi and Lauriat [36] studied a two-dimensional square cavity. The compressible low-Mach approach was adopted, and the thermal coupling between fluid and the solid boundaries of finite thickness was simulated. The cavity has two differentially heated vertical walls, one with constant temperature and the other cooled by means of the heat exchange with the surrounding environment. Different initial configurations were taken into account. It turned out that the solid boundaries interact with fluid mixture leading to non negligible effects: in transient regime the thickness of the bounding walls influence the condensation rate, while the solid temperature distribution changes with respect to the relative humidity of the fluid. From a numerical point of view, it was pointed out that low-Mach number solution depends on the initial conditions. A comparison between compressible low-Mach and incompressible Boussinesq approach was also performed. The two methods gave similar results when the initial temperature was uniform and equal to the average of the wall temperatures.

Similar investigation was carried out by Costa [14]: first the case of Sun *et al.* [71] was replicated, then the case of two-dimensional duct of circular

cross section was analysed. Although, overall, the thermo-fluid dynamic field was similar to that of the square cavity case, some features were different, (for example the Rayleigh-Bérnard cells were not detected).

The forced channel flow is also a widely studied case, both numerically and experimentally. The work of Huang *et al.* [30] focused on the heat and mass transfer in a rectangular duct, with water film evaporation and condensation over the horizontal walls and an uniform inflow of moist air. Simulations were carried out for three-dimensional, steady-state flow in laminar regime. The Boussinesq approximation was adopted. A wide range of simulations were performed, changing the temperature of wetted walls, the relative humidity, the Reynolds number of the inlet flow and also the aspect ratio of the duct. Talukdar *et al.* [72] investigated the vapour mass flux released from a horizontal water pool. Simulations of a three-dimensional rectangular duct, were validated in a laminar regime.

Experiments on the same case were performed by Iskra and Simonson [33], both for laminar and turbulent regimes. The effects of forced convection on evaporation were investigated by varying the velocity of the air passing through the duct.

Raimundo *et al.* [58] proposed an analysis of the phenomena of evaporation and condensation at heated water free surface. Both simulations and experiments were carried out. The numerical solver used the Reynolds-Averaged Navier-Stokes (RANS) approach, with a two-layers $k-\epsilon$ turbulence model. The flow was assumed incompressible and a local computation of thermal-physical parameters was employed instead of the usual Boussinesq approximation. The experimental facilities consisted of a test chamber in wind tunnel. The dependence of the evaporation/condensation rate on air-water temperature difference, relative humidity and airflow velocity were analysed. It turned out that the airflow is the most influencing factor.

The natural convection in cavity filled with one or several obstacles is also of great importance in many real applications. Laguerre *et al.* [38] performed an interesting analysis of the domestic refrigerators. Numerical studies of natural convection with heat and moisture transfer in a rectangular cavity containing a homogeneous distribution of sphere [37] and cylinders [39] were also performed. Simulations were carried out in a two dimensional domain, under the hypothesis of laminar flow, and taking into account the thermal radiation by the solids boundaries (but not the participating fluid medium). An experiment, reproducing a rectangular cavity containing a regular distribution of cylindrical obstacles, was used to validate the numerical solver for humidified and non-humidified air. The general features of flow were well predicted, while the model used was not able to correctly reproduce the local features of the flow, temperature and humidity. Das and Reddy [17] focused on the analysis of heat and airflow in a two-dimensional cavity with two differentially heated walls, two insulating walls and a central square solid body. Conduction and convection phenomena were investigated

changing the conductivity of substances, the Rayleigh numbers, and the inclination of the cavity.

Water change of phase also influences the system thermodynamics. Evaporation/condensation on solid surfaces absorbs/releases heat; in a wide range of applications these effects strongly alter the temperature at the solid boundaries. To obtain reliable results, the thermal interaction between the two media has to be simulated. This problem is referred in literature as conjugate heat transfer. Dorfman and Renner [19] presented a review of the approaches employed to face this problem. A detailed description of the main coupling strategies can be found in the work of Duchaine *et al.* [20],[21], who also analyzed the numerical stability and efficiency of the coupling algorithms. Sosnowski *et al.* [69] proposed a Neumann-Neumann thermal coupling technique, that was used in Cintolesi *et al.* [13] for studying the turbulent natural convection in a square cavity with conductive boundaries.

As already highlighted, systems with natural convection, evaporation and condensation are characterised by high degree of complexity. Many physical phenomena can interact among them and drastically influence the flow field. However, the factors that mainly affect these systems in practical applications are: (i) turbulence; (ii) heat exchange between solid/fluid media; (iii) thermal radiation with participating fluid. The latter becoming more important as the humidity content increases.

In the present work we study evaporation and condensation processes from a solid body in a enclosure, at an applicative scale, representative, for example, of home appliances. Among the others, a dishwasher during the drying phase, evaporation from food in a oven, condensation in a fridge. The numerical model retrieves all the relevant physical features of such processes: turbulence is treated by means of a dynamic Lagrangian Large-Eddy Simulation (LES) methodology [45], which is suitable to deal with the complex geometry of a real device; buoyancy force, triggered by temperature and humidity differences, is considered by means of the Boussinesq approximation; evaporation and condensation processes are modelled through a specific boundary conditions, allowing for a simplified treatment of the water film, for the temperature and humidity equations; the heat can be transferred from solid to fluid domains (or *vice versa*) taking into account the latent heat due to evaporation (condensation). The inclusion in the model of the radiative thermal effects is in progress and will be included in a successive study.

The paper is organised as follows: section 4.2 describes the enclosure and supplies details on the case geometry; section 4.4 describes the computational mesh and the simulation settings; in section 4.5 the results are reported and discussed; in section 4.6 we give concluding remarks; in appendix 4.7 second order statistics and surface temperature fluctuations are reported.

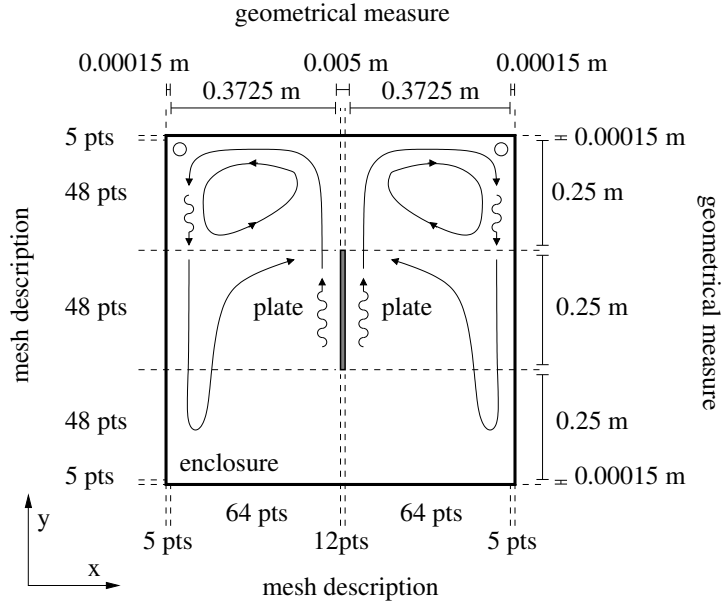


Figure 4.1: Schematic of the case investigated: the square cavity is filled with a mixture of air and vapour, it contains a hot internal plate and is surrounded by an external cold enclosure. In the cavity interior, the main initial fluid flow is sketched; geometrical information are on the top and left side; mesh grid information are on the bottom and left side.

4.2 Problem description

The case geometry, reported in Figures 4.1 and 4.2, is composed of a cubic domain of edge 0.75 m surrounded by a narrow metallic coat (the enclosure) and containing a rectangular plate (the plate). Among the possible industrial devices, it may be representative of a simplified dishwasher. The fluid motion is two-dimensional, on average, and develops on the x, y -plane. The spanwise z -direction is of homogeneity for the turbulent flow. The enclosure is composed of mild steel sheets of thickness $H_e = 0.00015\text{ m}$. The plate is a solid rectangle with a vertical section of $H_p \times L_p = 0.005\text{ m} \times 0.25\text{ m}$, located at the middle of the cavity.

The scenario investigated is the following: the external enclosure is colder than the internal plate; both are wet by a thin water film. The humid air is driven by thermal and vapour gradients. As time goes on, water evaporates from the plate, cooling it down. In the meantime, air becomes more humid and the vapour condensates over the enclosure.

The evaporation and condensation processes are investigated for different materials of the internal plate. A detailed description of the simulation setting is given in section 4.4.2, while the mathematical and numerical models adopted are described in the following section.

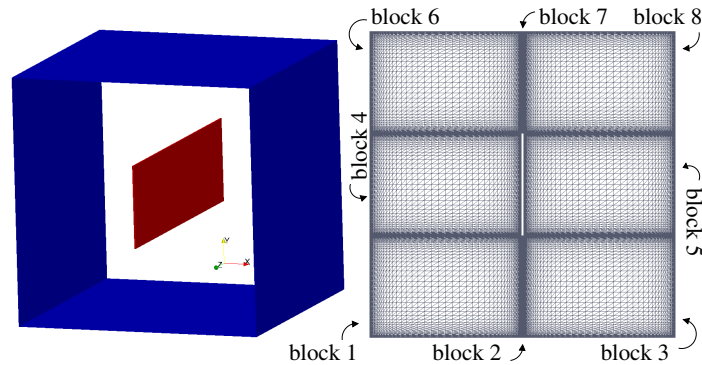


Figure 4.2: Sketch of the cavity-plate case: left, a three dimensional overview of the cavity; right, z -normal section of the mesh for fluid domain.

4.3 Mathematical and numerical approach

Different physical phenomena have to be modelled by a suitable set of mathematical equations: the mixing convection for the fluid flow, the boundaries heat exchange between solid and fluid media, the vapour diffusion and evaporation/condensation on a thin water film above solid boundaries.

The complete mathematical model has been described in chapter 2, and is not here reported. The governing equations are solved using the LES methodology, along with the dynamic Lagrangian SGS model for turbulent viscosity, thermal diffusivity and vapour diffusion.

Simulations are carried out using the `coupledHeatVapourFoam` solver, already described in chapter 2. Equations are discretised with a second-order central difference scheme in space, and a backward difference scheme in time. Thus ensuring a global accuracy of the second order.

More details on the numerical implementation for thermal coupling and evaporation-condensation models can be found in Sosnowsky [68] and Petronio [54], respectively.

4.4 Simulation settings

The settings and the physical assumptions adopted for the problem described in section 4.2, are illustrated hereafter.

4.4.1 Computational grid

The three elements composing the case (fluid, external enclosure, internal plate) are discretised with different meshes.

The fluid domain is discretised with a multi-block grid. The block dimensions are reported in Figure 4.1 and the mesh structure is sketched in

Figure 4.2. The eight blocks composing the mesh are stretched near the walls with a double-side stretching function, based on hyperbolic tangent:

$$r(\xi) = \frac{1}{2} \left(1 + \frac{\tanh(\delta(\xi - 1/2))}{\tanh(\delta/2)} \right). \quad (4.1)$$

where ξ are the coordinates of equispaced partition. Different stretching factor δ are used for vertical (δ_y) and horizontal (δ_x) directions. The grid is stretched in such a way that the cells at the interface between two blocks have the same dimensions. The narrow blocks (number 2 and 7 in Figure 4.2) are discretised using $12 \times 48 \times 64$ points, with stretching factors $\delta_x = 6$ and $\delta_y = 5$. The other blocks are discretised with $48 \times 48 \times 64$ points and a stretching factors of $\delta_x = \delta_y = 5$. The mesh stretching ensures at least 8–10 computational nodes within $y^+ \leq 10$ near the vertical and horizontal walls (for the preliminary simulation that is presented in Section 4.4.2).

The enclosure mesh is built in a similar manner, in a way to ensure the same cell dimensions at the fluid-enclosure interface. Along the interface, the mesh follows the structures of the fluid domain blocks; at the interface normal direction, the steel sheets are discretised with 5 points.

The plate mesh is the same of the fluid narrow blocks, in order to ensure the same cell dimensions on fluid interface. Thus the grid is composed of $12 \times 48 \times 64$ points with stretching factors $\delta_x = 6$ and $\delta_y = 5$.

4.4.2 Boundary and initial conditions

First, a simplified preliminary case is run, in order to provide an univocal initial configuration for the drying-process cases described in Section 4.2.

In the preliminary case, the enclosure and the plate have an uniform internal temperature of $T_e = 283.15 \text{ K}$ and $T_p = 333.15 \text{ K}$, respectively. The CHT is switched-off and replaced by a constant temperature condition on the solid faces. Therefore, the temperature of the solid media is not allowed to change. The fluid starts from rest and the no-slip condition is set on the solid boundaries. A water film of thickness $H_i = 0.0001 \text{ m}$ wets the faces of the plate and of the enclosure. The film thickness is held constant, even if the water is allowed to evaporate and condensate. The physical parameters used for air and vapour are listed in Table 4.1. Along the spanwise direction, periodic conditions are set for all variables. The simulation time-step dt is computed at each iteration to guarantee that the maximum Courant number is $Co = dt|\bar{\mathbf{u}}|/\delta x \leq 0.5$; where $|\bar{\mathbf{u}}|$ is the velocity magnitude through the cell and δx is the cell size in the direction of the velocity.

The absence of thermal coupling and the presence of an inextinguishable water film, allows to reach a statistical steady state configuration. In such configuration, the rate of evaporation from the plate is balanced by the rate of condensation on the enclosure, and the fluid domain results saturated of vapour.

Air		
ν	$[m^2/s]$	1.568×10^{-5}
α_a	$[m^2/s]$	2.220×10^{-5}
$(C_p)_a$	$[J/(kg \cdot K)]$	1.005×10^3
ρ_a	$[kg/m^3]$	1.165
k_a	$[W/(m \cdot K)]$	0.026
β_T	$[1/K]$	3.300×10^{-3}
Vapour		
α_ω	$[m^2/s]$	3.29×10^{-5}
ρ^*	$[kg/m^3]$	1
β_ω	–	0.63
L_h	$[J/kg]$	2.26×10^6
ρ_w	$[kg/m^3]$	1×10^3

Table 4.1: Physical parameters used in this study of air and vapour at 303.15 K (30 °C), atmospheric pressure.

The preliminary simulation is run for a time interval sufficient to fully develop the fluid motion. The simulation is considered at steady state when the volume-average value of vapour concentration within the fluid domain remains constant in time. Starting from a dry air condition ($\omega = 0$), vapour concentration reaches the asymptotic average value $\omega_{asy} = 0.025$ after roughly $\Delta t = 360t_0$ (more than two minutes of physical time).

The boundary conditions for drying-process simulations are the same as those of the preliminary one, but the CHT is switched on over the solid faces in contact with air. Also, the water film is now allowed to change its thickness according to equation (2.8). Three drying-process simulations are performed changing the material of the internal plate, while the external enclosure is always made of mild steel. The materials used are listed in Table 4.2, together with their thermal properties.

The materials are chosen to be representative of three main classes, respectively that of good thermal insulator (PVC), intermediate thermal insulator (porcelain), and good thermal conductor (mild steel). Such materials are samples of three categories of high/low conductivity k and high/low heat capacity ρC_p . In principle, a fourth category exists having high k and low ρC_p , but ordinary materials do not have these characteristics, thus it is not considered in this study. A detailed discussion on these thermal categories can be found in Cintolesi *et al.* [13].

MATERIAL		PVC	Porcelain	Steel
C_p	$[J/(kg \cdot K)]$	900	750	500
ρ	$[kg/m^3]$	1300	260	7830
k	$[W/(m \cdot K)]$	0.19	2.20	45.30
$\rho C_p \times 10^{-3}$	$[J/(m^3 \cdot K)]$	1170	195	3915
$\alpha_s \times 10^5$	$[m^2/s]$	0.016	1.130	1.160
$\tau_{ver} \times 10^{-3}$	$[s]$	390.62	5.53	5.38
τ_{hor}	$[s]$	156.25	2.20	2.20

Table 4.2: Thermal physical properties of materials used for drying-process simulation. Data taken from [1], except for data of *Poly Vinyl Chloride* (PVC) taken from [69].

4.4.3 Non-dimensional parameters

The parameters related to the thermal-solute convection are: the total Rayleigh number, that characterises the buoyancy-driven flows

$$Ra = \frac{g\beta_T}{\nu\alpha_a} \Delta T L^3 + \frac{g\beta_\omega}{\nu\alpha_\omega} \Delta \omega L^2, \quad (4.2)$$

composed by the sum of thermal and solute contributions. It can be interpreted as the ratio between the destabilising effect of buoyancy forces and the stabilising effect of momentum and thermal diffusion.

The total Grashof number, that also includes a thermal and a solute contribution

$$Gr = \frac{gL^3}{\nu^2} (\beta_T \Delta T + \beta_\omega \Delta \omega), \quad (4.3)$$

is the ratio between the buoyancy and viscous forces.

The characteristic temperature diffusion time in a solid medium

$$\tau = \frac{\ell^2}{\alpha_s}, \quad (4.4)$$

which gives the time-scale needed by the solid to conduct temperature along a distance ℓ .

The characteristic velocity for bounded flows dominated by buoyancy force, defined as

$$U_0 = \sqrt{(\beta_T \Delta T + \beta_\omega \Delta \omega) g L}, \quad (4.5)$$

where L is the length scale of the system. The time scale is computed as $t_0 = L/U_0$.

For the problem under consideration we set: $\Delta T = (T_p - T_e) = 50 K$ the initial difference of temperature between the plate and the enclosure; $\Delta \omega = \omega_\Gamma(T_p) - \omega_\Gamma(T_e) = 0.1255$ the initial difference of vapour concentration

at plate and enclosure surface; $L = 0.375$ the characteristic length (half of the cavity edge).

With these choices, the preliminary simulation is characterised by a global Rayleigh number of $Ra = Ra_T + Ra_\omega \simeq 5 \times 10^8$, a Grashof number of $Gr \simeq 5 \times 10^8$ and a characteristic velocity of $U_0 = 0.95 \text{ m/s} \simeq 1 \text{ m/s}$.

The variables are made non-dimensional as: length $x/2L$; time t/t_0 ; temperature $(T - T_e)/\Delta T$; velocity u_i/U_0 ; vapour concentration ω/ω_{asy} ; water film thickness H/H_i .

4.5 Results and discussion

To the knowledge of the authors, no experimental or numerical results are available for a validation of the present (or similar) case.

The numerical solver was previously tested in all its parts: the evaporation and condensation process was successfully validated against different benchmark cases by Petronio [54]; the thermal coupling implementation was tested in the work of Sosnowski *et al.* [69]; the accuracy of the flow solver and of the turbulent model were verified in the case of turbulent natural convection in square cavity with conjugate heat transfer, [13].

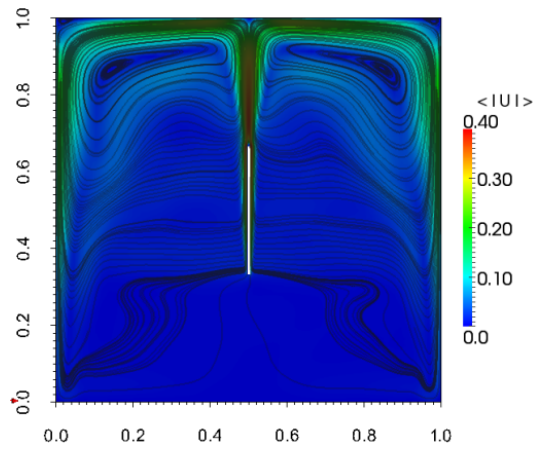
The computational domain in the homogeneous direction is chosen large enough to ensure the development of the largest turbulent scales. The autocorrelation functions are checked for the final configuration of the preliminary simulation. It is found that autocorrelations decay to small values. This suggests that the domain z -direction is large enough to allow the use of periodic condition. The grid stretching near the solid walls ensures a direct computation of the flow boundary layer. However, the high stretching herein employed does not affect the dynamical computation of turbulent SGS stresses, as discussed in [13].

4.5.1 Preliminary simulation

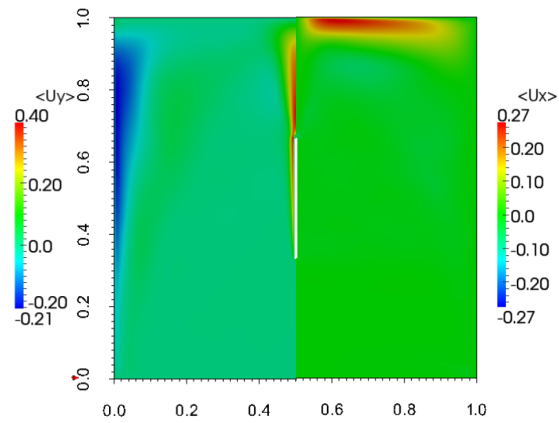
The results of the preliminary simulation are now discussed. In this section the angular brackets indicate the average in time and in the spanwise direction. The time average is computed over a period of $13 t_0$ (corresponding to 5s of physical time), after that the statistical steady state has been reached.

Figure 4.3 displays the spatial distribution of mean quantities. For all flow variables, the system is symmetric with respect to the vertical centreline; thus, hereafter the right side of the cavity is discussed.

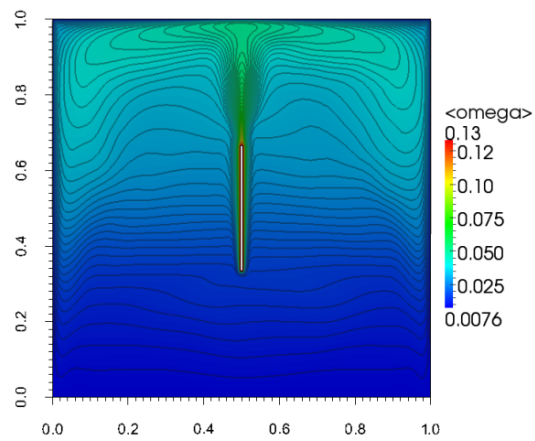
In Figure 4.3a the velocity magnitude contour plot is shown along with the flow streamlines, while Figure 4.3b depicts the distribution of the velocity components in the cavity. The flow is driven by the buoyancy force arising in correspondence of the hot plate and the vertical cold enclosure walls. It is qualitatively sketched in Figure 4.1. The main stream is localised near



(a) Streamlines of the average velocity $\langle |\mathbf{u}| \rangle$.



(b) Distribution of velocity components over the fluid domain: left, the vertical component $\langle u_y \rangle$; right, the horizontal component $\langle u_x \rangle$.



(c) Contour plot of average vapour concentration $\langle \omega \rangle$.

Figure 4.3: Mean flow, thermal field and vapour concentration for the preliminary simulation.

the boundaries and three zones of high speed motion can be identified in Figure 4.3b, namely:

Ascending region: is a thin vertical plume with width as large as that of the plate, extending approximately in the range $0.65 \lesssim y/2L \lesssim 0.95$. It is generated by the air blowing up from the hot vertical plate. The vertical velocity here is at its climax, that is estimated to be $|U|_{max} \simeq 0.4 \text{ m/s}$.

Horizontal-flow region: is located along the ceiling (the enclosure horizontal top wall), between $0.55 \lesssim x/2L \lesssim 0.90$ and $0.95 \lesssim y/2L \lesssim 1$. In this zone, the main stream loses velocity and air flows towards the vertical cold wall of enclosure. The contact with ceiling decreases the air temperature and allows corner-flow separation and a recirculation vortex is generated in the top corner;

Descending region: is a triangular-shaped zone, with the two sides extending in the ranges $0.25 \lesssim y/2L \lesssim 0.95$ and $0.90 \lesssim x/2L \lesssim 1$ respectively. Hot air reaches the cold vertical wall, and the buoyancy force is triggered by the high temperature difference pushing air downward.

Outside these regions, the fluid motion is less intense. The upper-half cavity ($0.5 \gtrsim y/2L$) is characterised by a diagonal-flow that drives air from the descending to the ascending region. This flow is sensibly weaker than the others previously described. Between the diagonal-flow and the horizontal-flow region, a stable recirculation vortex is generated. It is elongated along the horizontal direction and the centre is located approximately on the square off-diagonal at $c = (0.85, 0.85)$ in non-dimensional units. In the bottom-half cavity ($0.5 \lesssim y/2L$), far from the vertical walls, air is almost at rest. Figure 4.3c displays the contour plot of vapour concentration. The contour plot of temperature is similar, thus it is not reported. This is expected: in absence of CHT, the source term in equations (2.5) and (2.6) disappears. Hence, T and ω are ruled by similar equations, both provided with Dirichlet boundary conditions, and with similar diffusion coefficients (cf. Table 4.1). We limited our attention to ω ; analogous considerations can be done for temperature.

Fluid domain is strongly stratified: the larger amount of vapour is localised in the upper-half of the cavity, while the bottom-part is characterised by a homogeneous low concentration of vapour.

The horizontal centreline ($y/2L = 0.5$) sharply separates the two regions. Vapour reaches the maximum in the proximity of the hot plate (as a result of the strong evaporation process) and in the ascending region. Humidity is transported by the flow, therefore high value of ω can be found in the horizontal-flow region and in the descending region.

The top corner region is characterised by a lower vapour concentration due to the fact that this region is separated by the main flow, since the corner vortex creates a sort of relative dry air bubble. Condensation occurs when the ascending flow impinges the ceiling, and when air approaches the enclosure walls. A rapid reduction of vapour close to the cold boundaries is detected. The bottom-half of cavity is characterised by a homogeneous vapour distribution.

The asymptotic volume-average values $\omega_{asy} = 0.025$ is useful to check when the simulation arrived at steady state, but it cannot give any information about the local vapour concentration. Indeed, ω is strongly non-homogeneously distributed.

Velocity, temperature and vapour concentration profiles over a number of selected lines are presented in the following sections, where they are compared with those of the drying process simulations.

4.5.2 Drying-process simulations

The drying-process simulations are now discussed. In order to reach the final configuration (fluid at rest; constant vapour concentration; thermal equilibrium among enclosure, plate and air), a long physical time is required, eventually leading to huge simulation efforts.

All cases are run for about $\Delta t = 160t_0$, corresponding to 60s of physical time. At this time, the systems are still in a transitory phase. However, this period is meaningful to analyse the influence of the different plate materials on the overall thermal-solute dynamics.

Time evolution of global quantities

Figure 4.4 reports the main quantities involved in the evaporation/condensation process, averaged over suitable portions of domain. The average quantities could not be significant from a local point of view, because of the strong non-homogeneous distribution of the variables. However, they are useful to analyse the time evolution of the different simulations.

Figure 4.4a shows the time evolution of the non-dimensional temperature, averaged over the vertical surface of the plate. When CHT is active, evaporation subtracts heat from the plate. The process is ruled by equation (2.7) that, at the first cell near the solid surface, reads as:

$$\frac{\partial T_s}{\partial t} = \frac{k_s}{(\rho C_p)_s} \frac{\partial^2 T_s}{\partial x_j \partial x_j} - \frac{\rho^* L_h}{\rho C_p} U \omega. \quad (4.6)$$

The sink term due to evaporation is balanced by the conduction term, that transports heat from the interior onto the surface of the plate. The heat transfer between solid and fluid introduces an additional sink of heat.

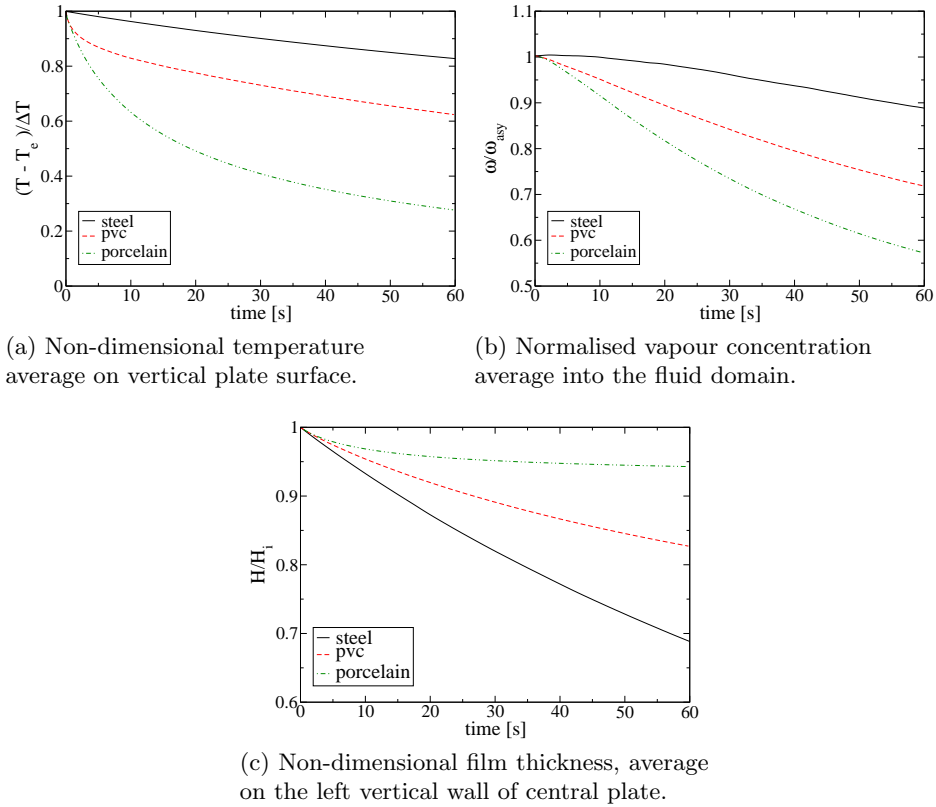


Figure 4.4: Global quantities for the dying-process simulations.

Overall, the heat transfer process is dominated by the evaporation sink term, because of the high value of the latent heat coefficient L_h . Steel plate experiences the lowest decrease of temperature: its high specific heat capacity ρC_p allows for smaller heat subtraction by evaporation. In this case temperature decreases almost linearly in time. PVC has an intermediate heat capacity. Initially it exhibits a high decrease of temperature, followed by an almost linear decrease. Porcelain has the lowest value of ρC_p , thus temperature has a strong non linear decay.

The floor (bottom horizontal enclosure wall) exhibits an almost negligible increase of temperature. The vertical walls and ceiling behave in an opposite way with respect to the plate (not shown): the mean surface temperature increases due to vapour condensation.

Figure 4.4b depicts the time variation of average vapour concentration in air, which is strictly related to the evolution of enclosure and plate temperatures. When CHT is switched on, the plate starts cooling down and evaporation is inhibited. In the meantime the enclosure is warmed up, leading to a reduction of condensation rate. The balance between the reduction

of evaporation and condensation, determines the increase or decrease of mean vapour concentration.

In general, this rate is influenced by the thermal proprieties of the solid materials and by the enclosure. In our cases, it is crucial that the surfaces over which condensation occurs, are much more extended than the evaporating surfaces. Therefore, the quantity of water evaporated decreases (on average) much more than the water condensed and all cases exhibit a reduction of ω .

The differences among materials are related to their thermal inertia, since materials that maintain the plate hotter release more vapour in air: steel has a high level of vapour thanks to the higher plate temperature; PVC shows an almost linear reduction of ω ; porcelain has the faster decreasing due to the fast plate cooling and, hence, the higher reduction of water evaporation.

Figure 4.4c reports the average thickness of water film onto the vertical plate surface. The complete film consumption process takes long time. This is due to the high level of vapour concentration in air that limits the evaporation rate. Up to the available simulation time, steel and PVC continue to reduce the film thickness, while porcelain basically reaches a steady condition and (on average) cannot allow for more evaporation than 5% of the water onto the plate.

Dew-point temperature estimation

In the previous Section, it was pointed out that porcelain is subject to a rapid cooling process. In order to understand if the phenomenon of vapour recondensation on the plate surface can occur, the dew-point temperature is here estimated.

The dew-point temperature is defined as the temperature at which humid air has to be cooled down to reach vapour saturation (at constant pressure and water content). A simple and well-known analytical form for the dew-point temperature T_{dp} is

$$T_{dp} = \frac{c \ln(P/a)}{b - \ln(P/a)}, \quad (4.7)$$

where P is the actual water vapour pressure that can be computed by equation (2.11), while a, b, c are empirical constants. Barenbrug [8] evaluates such constants as $a = 6.105$, $b = 17.27$, $c = 237.7$, if the air temperature is in the range $0^\circ C < T < 60^\circ C$. We refer to Lawrence [40] for a description and a derivation of equation (4.7).

Usually, an explicit expression of T_{dp} depending on temperature and relative humidity is derived, using the so called (*Magnus formula*) to evaluate the saturation pressure as a function of temperature. However, we are interested to a relation that involves surface vapour concentration ω_Γ instead of relative humidity.

Inverting equation (2.10) for the variable $P = p_{sat}(T_\Gamma) \phi_\Gamma$, we obtain:

$$P = \frac{\omega p_{atm}}{\frac{M_v}{M_a} + \omega \left(1 - \frac{M_v}{M_a}\right)}. \quad (4.8)$$

Substituting (4.8) in equation (4.7), we obtain an expression to estimate the surface dew-point temperature.

The average vapour concentration value, shown in Figure 4.4b, is used to compute T_{dp} in our drying-process cases. The dew-point temperature assumes low values ($T_{dp} < 287K$) during the entire time interval simulated. It goes under the minimum values T_e after about 30s for porcelain case. The other materials maintain (on average) higher plate temperature than the dew-point one during the simulations. Thus, vapour recondensation on the plate surface cannot take place.

General motion

Data analysis is carried out on the initial configuration $t = 0$ and on three intermediate configurations at times $t = 15, 30, 60 s$, corresponding to 25%, 50%, 100% of the total simulated interval, respectively. For each material, the intermediate configurations exhibit small changes among them, thus only the last is discussed.

The velocity streamlines and the T, ω contour plots for the final time $t = 160t_0$, are here discussed. The quantities are averaged in spanwise direction and in time, over an interval $\Delta t = 1s \simeq 2.5t_0$. The fluid flow is assumed to be homogeneous also in time during this short interval.

In Figure 4.5 the velocity streamlines are reported, together with the contour plots of velocity magnitude. The main flow exhibits a good symmetry with respect to the vertical centreline, except for the bottom part. In this region the flow is almost absent since the fluid is strongly stratified. Hence, the streamlines in the bottom-half cavity are not significant.

All cases maintain the main flow structures described in section 4.5.1; in particular the corner vortices and the recirculation vortices can be clearly seen. However, a general decrease of velocity magnitude can be observed.

In steel case, the velocity is higher than in the PVC one. Both cases show a flow field similar to that of the preliminary simulation: the recirculation vortices in the upper-half of the cavity are horizontally elongated, and the diagonal-flow maintains the curve trajectory (almost vertical near the vertical walls, deflecting on horizontal direction when approaching the ascending region). Porcelain case experiences the stronger velocity decay in the ascending region. Velocity field becomes comparable (in magnitude) among the three zones of motion beforehand described. The diagonal-flow does not show the vertical-horizontal behaviour described for steel and PVC, but has a straighter trajectory. The recirculation vortices are less horizontally elongated and follows the corner shape.

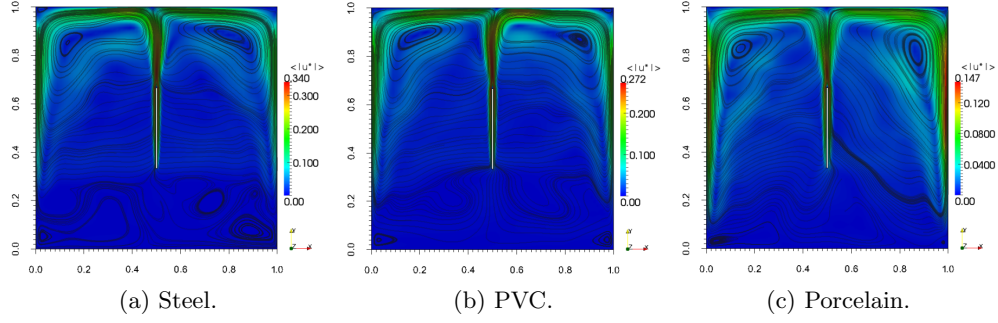


Figure 4.5: Velocity $\langle |\mathbf{u}^*| \rangle = \langle |\mathbf{u}/U_0| \rangle$ streamlines and magnitude for the final time configuration.

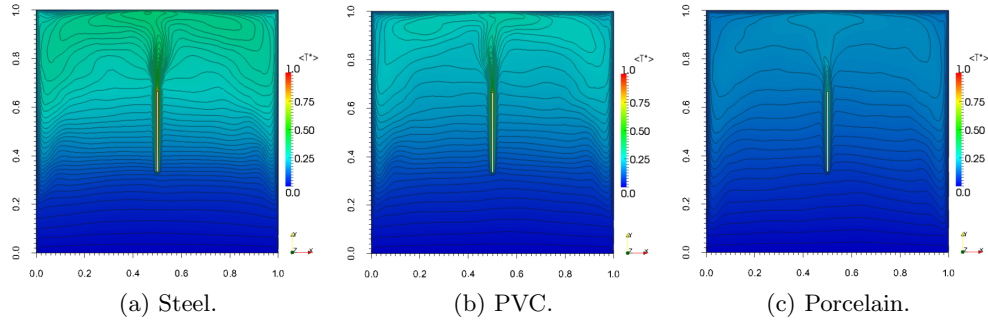


Figure 4.6: Non-dimensional temperature $\langle T^* \rangle = (\langle T \rangle - T_e)/\Delta T$ contour plot for the final time configuration.

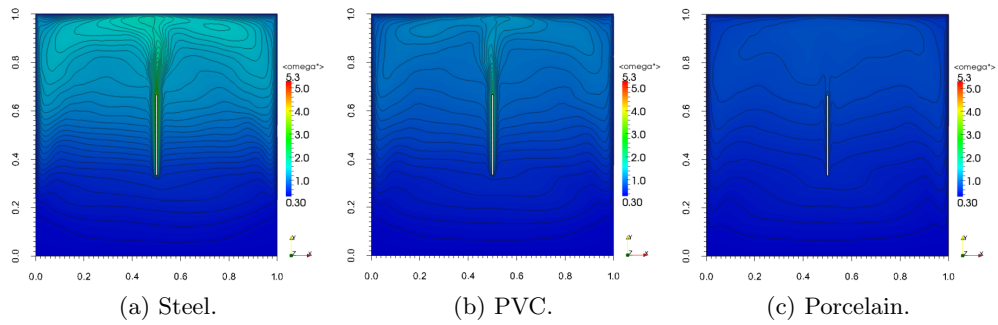


Figure 4.7: Non-dimensional vapour concentration $\langle \omega^* \rangle = \langle \omega \rangle / \omega_{asy}$ contour plot for the final time configuration.

The velocity reduction is found to be proportional to the temperature drop. The velocity peak values at the end of simulations are reduced by: 85% for steel, 68% for PVC, 36% for porcelain with respect to the initial values. These values are, in general, well correlated with the drop of average temperature on the plate surface (reported in Figure 4.4a).

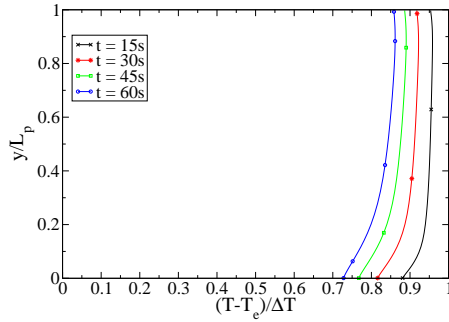
Figure 4.6 depicts the temperature contour plots. As expected, the behaviour of fluid temperature follows the variation of plate surface temperature. The steel case maintains a configuration similar to the initial one (not reported, ref. to Figure 4.3c): air is hot in the ascending and horizontal-flow regions, while it is cooled down near the vertical walls. The cavity is strongly non homogeneous and it is clearly divided into two parts: the upper-half has higher temperature, especially in the main flow regions; the bottom-half has a lower and more uniform temperature distribution. In the PVC case, the upper-half of the cavity is more homogeneous with respect to the steel case. A plume of hot air is only detected in the ascending region. A strong thermal stratification between the upper- and bottom-half cavity is still visible. On the contrary, the porcelain case is affected by a strong cooling process. The fluid domain is characterised by a weak thermal stratification, with a low vertical temperature gradient.

Figure 4.7 reports the distribution of the non-dimensional vapour concentration. The general behaviour resembles that one of temperature. However, for all materials, ω decreases more rapidly than temperature. Comparing, for example, Figure 4.7c with 4.6c, it can be seen that the vapour concentration is almost uniform in vertical direction, while temperature exhibits a positive vertical gradient. When CHT is considered, the contour lines of vapour concentration and temperature are not anymore similar to each other, as it happens for the preliminary case. This is due to the different boundary conditions imposed: temperature undergoes CHT boundary conditions (2.16), (2.17) and is affected by the heat source/sink term (2.14); whereas ω is computed at the interface by (2.10). This latter is a monotone function that decreases rapidly with temperature. When the surface loses heat, the boundary conditions reduce more the vapour concentration than the temperature. From a physical point of view, when plate temperature decreases, both evaporation and heat transfer are reduced in the fluid. Evaporation decreases more rapidly than the thermal heat transfer, leading to a different ω distribution with respect to T .

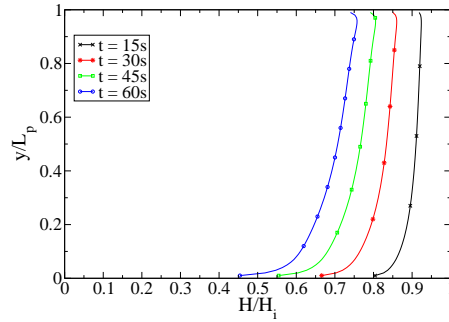
Surface quantities

The distribution of temperature and water film over the solid body surfaces, is now discussed. For the three drying-process simulations, the scalars are sampled at different transitory stages; namely at time $t = 15, 30, 45, 60$ s corresponding to 25%, 50%, 75%, 100% of the simulated period, respectively.

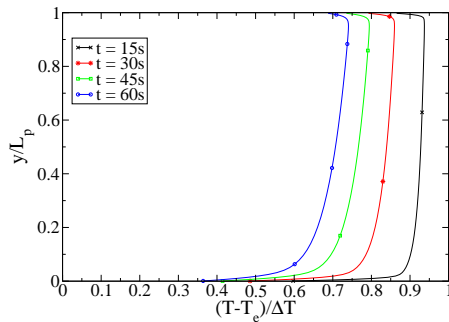
Figure 4.8 reports the non-dimensional temperature over the plate ver-



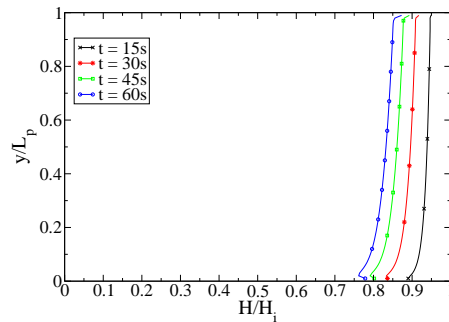
(a) Temperature on steel plate centreline.



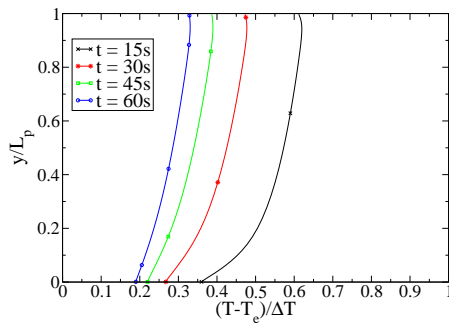
(b) Water film height over the steel plate.



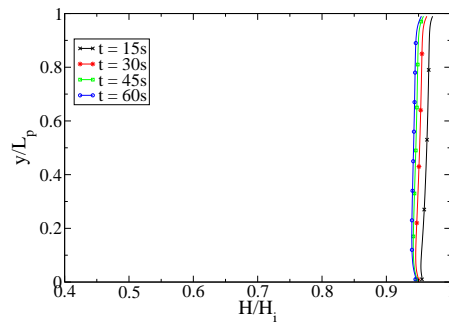
(c) Temperature on PVC plate centreline.



(d) Water film height over the PVC plate.



(e) Temperature on porcelain plate centreline.



(f) Water film height over the porcelain plate.

Figure 4.8: Plate scalar distribution for drying-process simulations, average in spanwise direction. First row: non-dimensional temperature profile on the plate vertical centreline; second row: non-dimensional water film height onto the plate vertical wall.

tical centreline (upper panel), and the non-dimensional film thickness on the vertical plate surface (lower panel). In both cases the quantities are averaged along spanwise direction. The H profile on the plate left surface coincides with that one on the right surface, by virtue of system symmetry. Temperature is plotted over the plate centreline. Thermal conductors (steel and porcelain) show a negligible temperature variation between the surface and the centreline; except at the very beginning, when evaporation starts. The insulator (PVC) has a small temperature variation (3% maximum). Anyway, this effect is negligible; thus, the temperature over the centreline and on the plate surface are essentially the same.

Figures 4.8a,b,c show that the temperature decrement is ruled by the material heat capacity: the lower ρCp is, the higher the plate cooling is. Table 4.2 summarises the thermal coefficients and parameters of the three materials under consideration. For all cases, the plate bottom region, $y/L_p \lesssim 0.1$, experiences the higher cooling. This is due to the contact with drier air from the bottom-half cavity, that supports evaporation. In the upper zone, $0.1 \lesssim y/L_p$, temperature distribution is more homogeneous, and the decrease time-rate is in agreement with Figure 4.4a.

When the plate is made of steel, a smooth thermal transition from the bottom to the upper zone occurs. Indeed, the high conductivity α_s allows for a fast temperature diffusion in vertical direction (cf. the vertical characteristic diffusion times τ_{ver}). In the upper zone, the vertical T gradient is negligible. The PVC plate exhibits a sharp drop of temperature at bottom edge. Since PVC is a strong thermal insulator, the plate internal conduction is not as fast as in steel to supply heat on the bottom zone; indeed, it has a quite high τ_{ver} . The porcelain plate has similar conduction coefficient as steel, then it has a smooth final thermal profile. However, the strong initial cooling process causes a large drop of temperature in the bottom zone, that can be just partially recovered by internal conduction, eventually leading to a vertical temperature gradient in the first profile, at $t = 15s$.

Figures 4.8b,e,f show that the evaporation process is directly influenced by temperature. Again, the reduction rate is in agreement with the time evolution of the averaged film thickness, reported in Figure 4.4c. Steel case has a downward reduction of water film, stronger in the bottom zone. This is due to the intense evaporation supported by the impact of dry air coming from the bottom-half cavity region, as above mentioned. PVC case displays an almost homogeneous H reduction, but there is a minimum peak in the bottom end point. It is generated by the strong temperature drop already discussed. Porcelain case exhibits a negligible decrease of water film. Evaporation occurs mainly during the first seconds, and it is almost homogeneous along the plate surface.

Figure 4.9 reports the non-dimensional temperature and film thickness distributions on the cavity ceiling, for the final time $t = 160t_0$. The scalars are averaged in spanwise direction. The transitory configurations are not

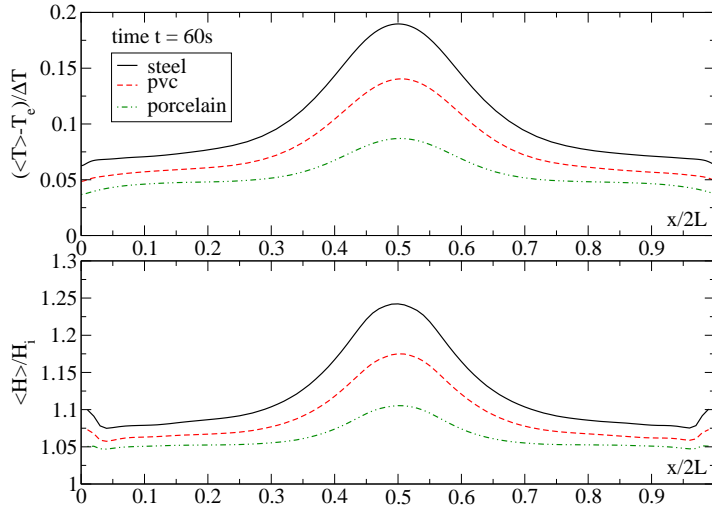


Figure 4.9: Scalar distribution on enclosure ceiling for drying-process simulations. Top figure, non-dimensional temperature over the ceiling centreline; bottom figure, non-dimensional water film thickness over the ceiling.

reported, since they show a simple linear increase of all quantities. Temperature profile over the ceiling centreline is the same as at the interface, because of the high characteristic conduction time of steel.

By virtue of symmetry, we focus our attention in the left ceiling side, $y/2L < 0.5$. Three different regions can be identified:

- ▶ impinging area $0.5 \geq y/2L \gtrsim 0.3$. The ascending plume of hot and humid air impinges the ceiling in this area. At the point $y/2L = 0.5$, film thickness and temperature peak; then T is partially diffused by steel conduction, while H is not subject to this phenomenon (for this reason film thickness decreases more rapidly than temperature when $y/2L \rightarrow 0.3$);
- ▶ intermediate area $0.3 \gtrsim y/2L \gtrsim 0.05$. The underlying flow is almost horizontal and both temperature and film thickness experience a moderate decrease;
- ▶ corner area $0.05 \gtrsim y/2L \geq 0$. Roughly, it corresponds to the flow corner vortex zone. Temperature slightly decreases, due to diffusion effects. On the other hand, the film thickness sharply increases due to local lower temperature.

The behaviour of the ceiling is qualitatively unaltered when the plate material is varied. As expected, the values of the scalars are higher for materials that maintain hotter and more humid air.

The distributions on the enclosure vertical wall and floor, are briefly discussed here on. The left and right vertical walls display a linear distribution of both T and H . Temperature is maximum at the top and decreases linearly going downward. Vertical walls are warmer for steel case than for porcelain one (as for the ceiling), while PVC case shows an intermediate behaviour. The same holds for film thickness.

The floor maintains essentially unaltered the initial temperature. An almost negligible temperature increase is detected near the corner, as an effects of thermal conduction from the vertical walls.

Local profiles

The general flow features are now investigated on suitable locations. The preliminary and drying-process simulations are reported for the final time $t = 160t_0$, and the quantities are averaged both in spanwise direction and for a short time interval, as in section 4.5.2.

Figure 4.10a depicts the non-dimensional temperature, vertical velocity and vapour concentration over a horizontal line at level $y/2L = 0.5$, near the plate surface. Other levels are not reported since they do not show significant differences.

In all cases, the air dynamics is confined in a tiny boundary layer. This is not affected by the main fluid motion, because the diagonal-flow and the above ascending region directly merge together, without involving the near-plate flow. Conversely, the boundary layer is controlled by the plate temperature. All quantities are in accordance with the plate temperature evolution. It is interesting that the vapour concentration, unlike temperature and velocity, decreases uniformly for the different materials. This effect can be explained considering the boundary condition (2.10) for ω : the function $\omega_T(T)$ is not linear with temperature, but it decreases more for higher temperatures than for lower ones. Thus, the preliminary case and steel case exhibit approximately the same drop of vapour concentration that the PVC and porcelain cases; even if the difference of temperature between the former is smaller than between the latter.

Figure 4.10b reports the non-dimensional temperature, horizontal velocity and vapour concentration over a vertical line at the mid distance from the plate and the left vertical wall ($x/2L = 0.25$). Temperature and vapour concentration are highly correlated.

In cavity bottom zone ($y/2L \lesssim 0.3$) all the profiles are practically unaffected by variation of the plate material. This is the region where fluid is not influenced by the upper region, thank to the thermal-vapour stratification, and it is almost at rest. In central zone ($0.3 \lesssim y/2L \lesssim 0.7$) conduction is the main heat transfer mode, since the horizontal and vertical (not reported) velocity components are almost zero. In upper zone ($0.7 \lesssim y/2L$) convection dominates and profiles exhibit different behaviour, depending on the plate

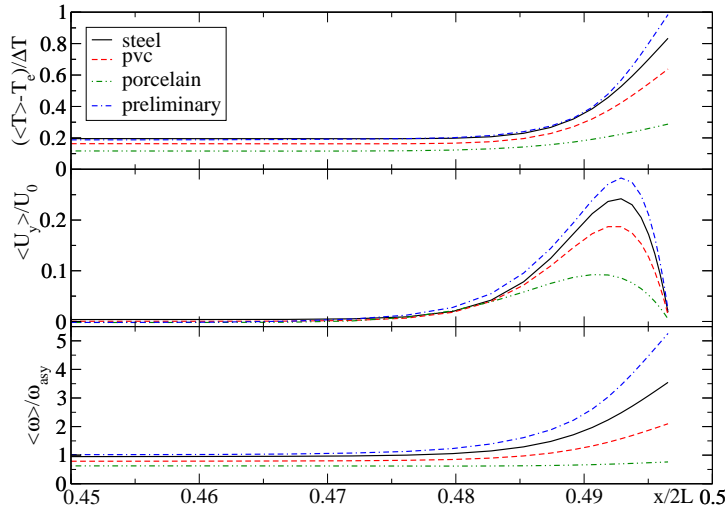
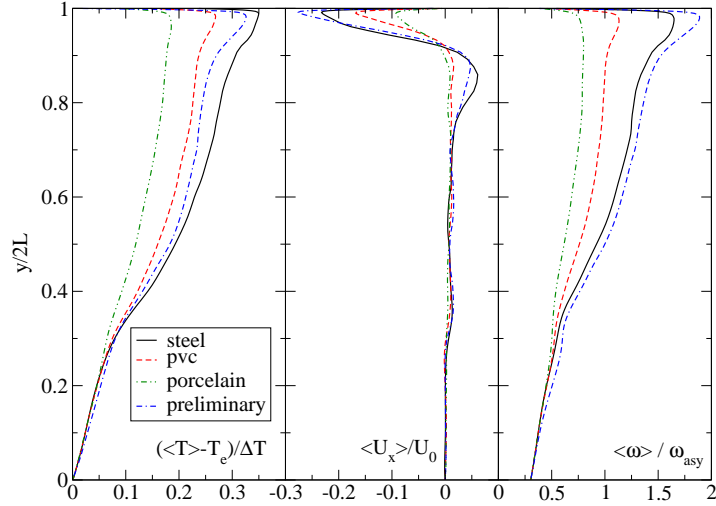
(a) Plots over a line $y/2L = 0.5$.(b) Plots over a line $x/2L = 0.25$.

Figure 4.10: Averaged of non-dimensional temperature, velocity components, vapour concentration for final time configuration.

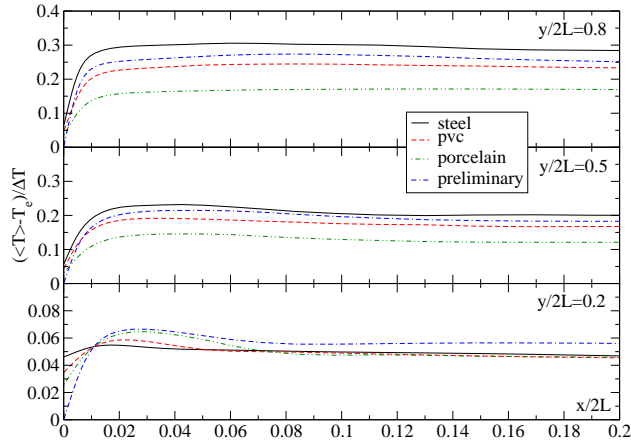
material.

Steel case and the preliminary one are particularly interesting. Figure 4.10b shows that the horizontal velocities are similar in the two cases: near the ceiling, in correspondence of the horizontal-flow ($y/2L \gtrsim 0.9$), air flows towards the enclosure vertical wall; just above, in correspondence of the diagonal-flow ($0.8 \lesssim y/2L \lesssim 0.9$) it flows in the opposite direction. These two flows affect the vapour profile: the former transports humid air from the plate, leading to a slight increase of vapour concentration; the latter transports dryer air from the enclosure and decreases ω . The vapour concentration in the horizontal flow region is higher for preliminary case, because isothermal plate maintains higher level of evaporation. Temperature has an opposite behaviour. The preliminary simulation is affected by the stronger cooling effect of the enclosure walls. As a result, the temperature near the ceiling is lower than in the steel case. Also the diagonal-flow (that comes from the vertical wall) decreases air temperature. In the steel case the enclosure is warmed up by the CHT. Thus, air is maintained warmer near the ceiling and in the diagonal-flow region.

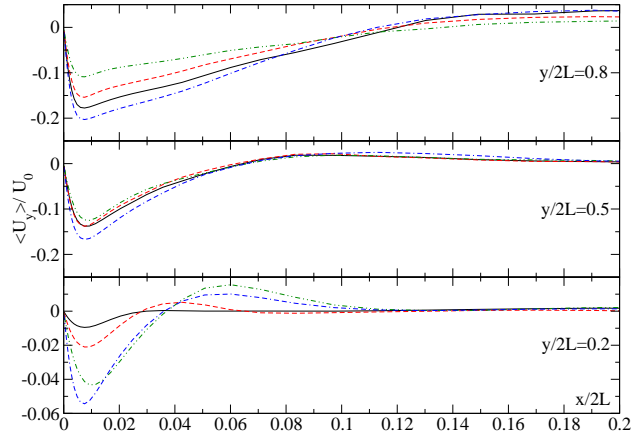
Figure 4.11 displays the non-dimensional temperature, vertical velocity and vapour concentration over three horizontal lines at levels $y/2L = 0.8, 0.5, 0.2$, near the vertical wall enclosure.

Figure 4.11a shows temperature profiles. At the top ($y/2L = 0.8$) and mid ($y/2L = 0.5$) levels, the distributions are in agreement with Figure 4.10b: for steel case, temperature is maintained higher than in preliminary case, due to the higher temperature of the enclosure walls. The behaviour at the bottom ($y/2L = 0.2$) level is somehow interesting. Non-dimensional temperature values are one order of magnitude lower than in the other plots. Close to the wall, the profiles are affected by the enclosure temperature: steel maintains higher values since it is able to warm up the wall, while in the preliminary case temperature decreases to the value of the isothermal cold wall. Farther from the wall influence, about $x/2L \gtrsim 0.01$, the order is reversed: in porcelain and preliminary simulations, temperature slightly increases with respect to steel and PVC cases. This effects can be explained taking into account the velocity profiles in Figure 4.11b: since the hot air coming from the upper-half on the cavity is diffused by convection, the higher vertical velocity of porcelain and preliminary cases allow for a higher temperature.

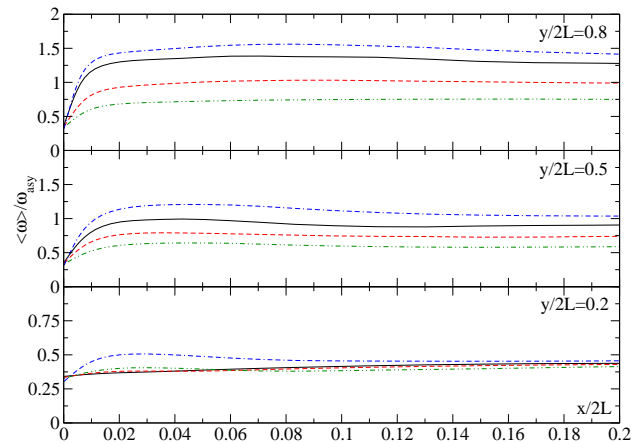
Figure 4.11b reports the vertical velocity component. At the top level, the flow is governed by the buoyancy force generated by the thermal gradient between enclosure and fluid: cases with lower wall temperature exhibit higher velocity. At the mid level, the differences among drying-process simulations disappear. Indeed, in the bottom-half of the cavity the strong thermo-solutal stratification takes place: the buoyancy force generated by the wall is balanced by the opposite buoyancy force due to the underlying cold and dry air. In the bottom level the balance between these two forces



(a) Averaged of non-dimensional temperature.



(b) Averaged of non-dimensional vertical velocity.



(c) Averaged of non-dimensional vapour concentration.

Figure 4.11: Spanwise and partial time average of non-dimensional temperature, vertical velocity, vapour concentration for final time configuration. Plots over lines near the vertical enclosure wall, at three height $y/2L = 0.8, 0.5, 0.2$, respectively from the top to the bottom in each figure.

breaks. Steel and PVC cases, that have stronger stratification (cf. Figures 4.6, 4.7), experience a velocity decrease; while porcelain case, that is not stratified, maintains higher velocity. The preliminary case is an exception, as it is highly stratified but has the highest velocity. This is due to the larger buoyancy force generated by the thermal and humidity gradient at the vertical wall, that overcomes the stratification counter force. Farther from the wall ($0.04 \lesssim y/2L$) porcelain and preliminary cases have positive velocity values. This is the area where the diagonal-flow starts. PVC case has lower values. Steel case does not show any positive velocity, meaning that the diagonal-flow starts from higher level.

Figure 4.11c depicts the vapour concentration distribution. At the top and mid levels, condensation decreases ω near the wall. Further from the wall, the profiles are coherent with temperature: when air is more warm, it is also more humid. At the bottom level, there are no differences among the cases. Vapour does not condense, thus there is no near wall decrease. In Figure 4.11a we have notice that porcelain and preliminary cases have high temperature profile at bottom level (with respect to steel and PVC cases); hence also a higher vapour value is expected. Preliminary simulation exhibits higher ω , but porcelain case doesn't. The reason is that, in porcelain case, evaporation stops and the humidity in the cavity is low. Hence, convection cannot bring significant amount of vapour towards the bottom region.

4.6 Conclusions

Evaporation and condensation in a turbulent buoyancy driven flow are studied *via* large-eddy simulations. The dynamic Lagrangian sub-grid scales model is chosen to compute the SGS viscosity, along with the SGS thermal and vapour diffusivity. The presence of water phase is modelled by a thin water film. The solid-fluid thermal coupling is taken into account through the conjugate heat transfer procedure described in Sosnowski [69] (conduction), and by the evaporation source/condensation sink boundary term described in Petronio [54] (water change of phase). The numerical solver is developed within the OpenFOAM[®] software framework.

The case of a vertical hot plate inside a cold enclosure, filled with humid air, is studied. Both the plate and the enclosure are initially wet by a thin water film, and the enclosure is thermally isolated from outside. Evaporation from the plate and the subsequent cooling process is investigated. The numerical solver has been validated in Cintolesi *et al.* [13] for what concern the fluid dynamics and the CHT procedure; and in Petronio [54] for evaporation/condensation model.

First, a preliminary case is simulated: the water film thickness is not allowed to change and the CHT is not considered. Anyway, water can evap-

orate and condensate. The result is a statistical steady state configuration, where the buoyancy flow is generated near the plate and the top vertical enclosure walls. This preliminary configuration is characterised by a Rayleigh number of $Ra = 5 \times 10^8$.

The absence of surface thermal interaction leads to an analogous distribution of temperature and vapour, as expected after an analysis of the mathematical model. A realistic reproduction of thermal and humidity distribution cannot be achieved neglecting the solid-fluid surface heat transfer. A strong thermal and humid stratification arises: the cavity is sharply divided into a warm and humid top region, and a relative cold and dry bottom part. The general flow is described and three main regions of motion are identified. The stable stratification inhibits the formation of recirculation regions developing along the entire cavity height. Instead, smaller recirculation vortexes appear in the top half-cavity.

Successively, the CHT and water film model are switched on and three simulations are performed, changing the plate material, in order to study the different evolution of the system. The materials are chosen to have different thermal properties. The complete evaporation of water film can require a long physical time, thus it is not entirely simulated. We reproduce the first 60s of the physical time, when the systems are still in transitory phase. This period is crucial to investigate the influence of different plate materials on the overall fluid dynamics. Heat transfer by evaporation and condensation is found to overcome the other heat transfer modes during the cooling of the plate. The material thermal inertia ρC_p is the parameter that controls the cooling process: high values of thermal inertia cause a slight decrease of temperature, whereas low values lead to fast cooling. As soon as the plate loses heat, the overall flow velocity is reduced and the thermal and vapour stratification become weaker.

The average plate temperature evolution in time is reported: high- ρC_p materials show a linear temperature reduction, while low- ρC_p materials display an initial sharp and a subsequently moderate heat loss. The plate film thickness and air vapour concentration evolve according to temperature behaviour. The water film exhibits a negligible reduction for low- ρC_p , whereas the reduction is between 20 – 30% for high- ρC_p . At the enclosure surfaces, the condensation takes place mainly onto the ceiling, in a narrow region just above the plate, where the hot and humid air impinges the wall.

An analysis of the dew-point temperature suggests that, for the cases herein examined, even for materials that are rapidly cooled down, the vapour recondensation onto the plate surface cannot occur.

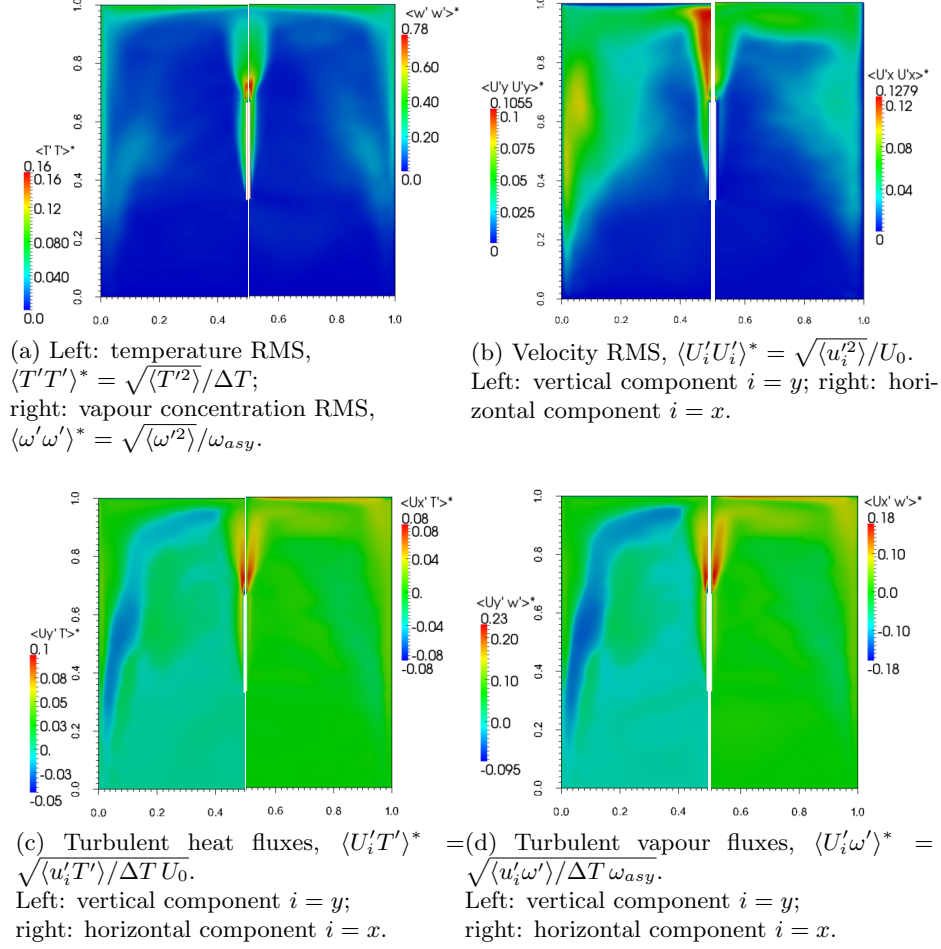


Figure 4.12: Temperature, vapour and velocity root-mean square (RMS), together with the turbulent heat fluxes and vapour fluxes.

4.7 Appendix: turbulence analysis

The second order statistics are now discussed. We focus our attention on the preliminary simulation, since it is a statistical stationary case. Also, the temperature fluctuations on the plate vertical wall and enclosure ceiling are reported for the final configuration of the drying process simulations.

Preliminary case turbulence

The second order statistics of the preliminary case are computed over the time range reported in section 4.5.1. If ϕ is a generic variable and the angular brackets indicate the average in time and in the spanwise direction, then the resolved fluctuations are computed as $\phi' = \phi - \langle \phi \rangle$ and the resolved

root-mean square (RMS) is computed as $[\phi]_{rms} = \sqrt{\langle \phi' \phi' \rangle}$ and normalised by suitable constants.

An overview of turbulence statistics is given in Figure 4.12, where the RMS values and turbulent fluxes into the cavity domain are depicted.

Figure 4.12a shows the temperature and vapour concentration RMS. The fluctuations of ω are sensibly higher than the temperature fluctuations, essentially because of the high level of evaporation and condensation. The spatial distributions are similar for both quantities: fluctuations are confined near the walls and peak in the ascending region (near the plate). Specifically, they are localised: very close to the plate vertical faces; near the ceiling and the top corners; in the upper part of the enclosure, near the vertical walls. A weak positive spot is localised at the beginning of the diagonal-flow. In this zone the hot and humid air, flowing down from the upper-half cavity, impinges the cold and dry air of the bottom-half cavity and starts to rise up again.

Figure 4.12b reports the vertical and horizontal velocity RMS. The vertical RMS are localised in the high-speed motion zones already described in section 4.5. The higher values are located in the ascending and in the descending regions, where the downward buoyancy force is triggered. The diagonal flow is almost laminar when it merges with the ascending region. The horizontal RMS reach the maximum just above the palate, and they are non-zero in the upper-half cavity, specifically in the horizontal flow region.

Figures 4.12c,d display the turbulent heat and vapour fluxes. As expected, the vapour fluxes are stronger than thermal fluxes. However, the spatial distributions are similar, thus we discuss just the thermal fluxes, taking advantage of the gradient-diffusion hypothesis (cf. Pope [56]). Apart from the peaks in the ascending region, it is interesting to notice the presence of negative vertical fluxes in the diagonal flow zone, and positive horizontal fluxes close to the ceiling. The former indicates that turbulence transports cold and dry air from the cavity bottom-half to the upper-half, against the stable thermal-vapour stratification; the latter transports cold and dry air in opposite direction with respect to the horizontal flow.

The quantities RMS over a number of significant lines are reported in Figure 4.13. Also in this case, temperature and vapour concentration exhibit an extremely similar behaviour; even if the fluctuations of ω assume higher values than the thermal ones. Again, we discuss only the temperature RMS profiles.

Figure 4.13a shows the statistics over a horizontal line $y/2L = 0.5$ near the plate; it can be analysed in conjunction with Figure 4.10a. As expected, temperature RMS are localised near the plate and vanish on the plate surface (since the thermal-coupling is not activated). When the solid surface is approached, the horizontal velocity RMS have lower values and decay faster than the vertical ones. The vertical buoyancy force arises and governs the fluid motion near the plate. The vertical velocity RMS maintain not small

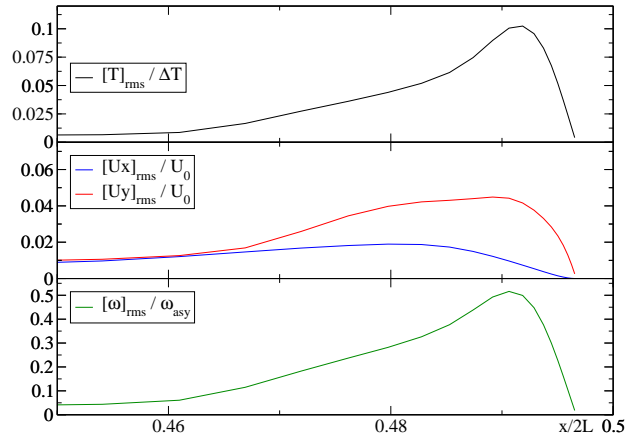
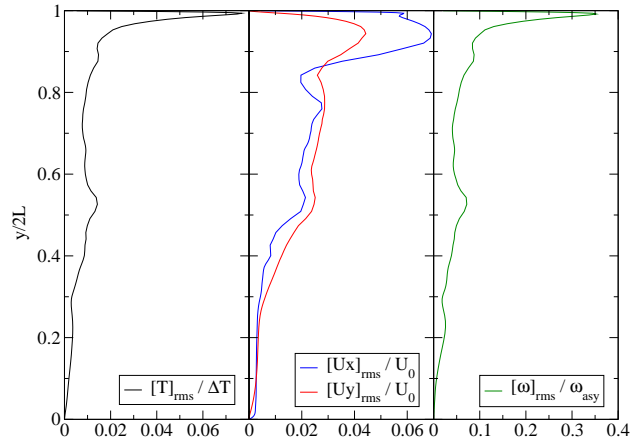
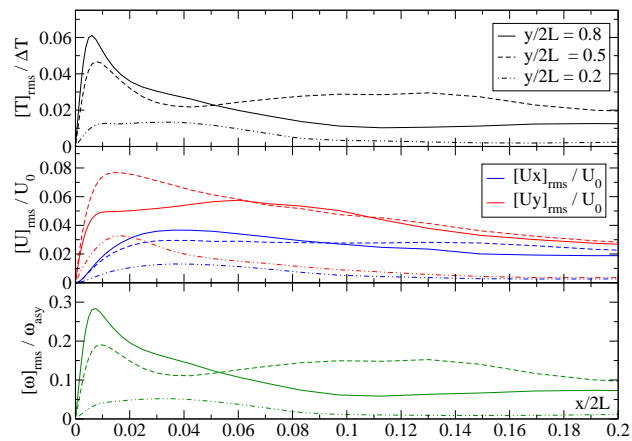
(a) Plots over the line $y/2L = 0.5$, near the plate.(b) Plots over the line $x/2L = 0.25$ (c) Plots over the lines $y/2L = 0.2, 0.5, 0.8$, near the vertical enclosure wall.

Figure 4.13: Normalised root-mean square of temperature, vertical and horizontal velocity, vapour concentration.

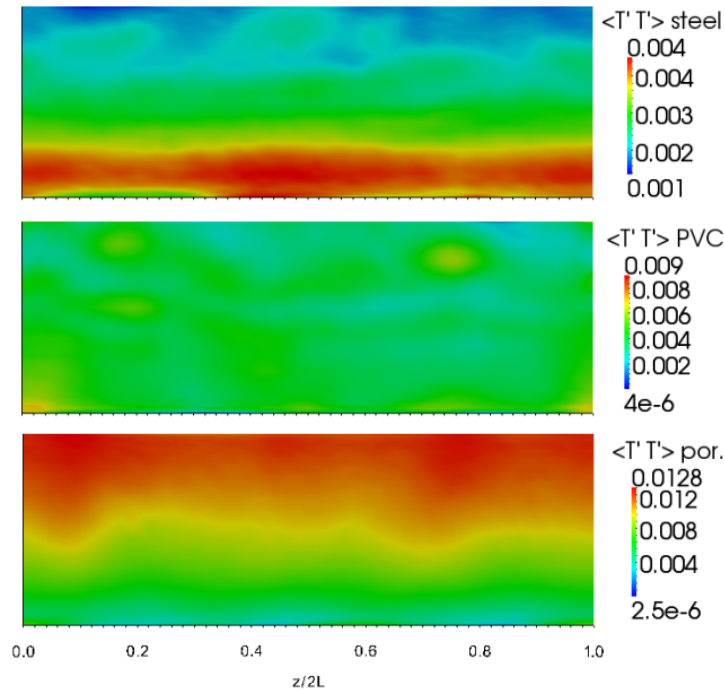


Figure 4.14: Temperature fluctuations onto the vertical fluid-plate interface, for the drying-process simulations.

values also for $x/2L < 0.48$, where vertical velocity is (on average) zero. This suggests the presence of a non-stable velocity field in the proximity of the plate surface.

Figure 4.13b reports the quantities over a vertical line $x/2L = 0.25$ near the ceiling. The three zone of motion identified in Figure 4.10b can be used to analyse this plot: the bottom and central zones are almost laminar, while the turbulences are higher in the upper zone. Temperature (and vapour) RMS peak very close to the ceiling, where the cooling effect (condensation effect) of the ceiling is higher. The velocity RMS reach the maximum in the horizontal flow region; the horizontal velocity RMS have a small, localised, decrease in correspondence of the diagonal flow (that is almost laminar). It is interesting to notice that, approximately at the mid-high $y/2L = 0.5$, all the RMS show a small increase. Probably, it is due to the strong temperature-vapour stratification that sharply divides the cavity upper-half and bottom-half at this height (cf. Figure 4.3): the perturbation of the stratification interface generates extra fluctuations.

Figure 4.13c displays the turbulent quantities for the same horizontal lines as in Figure 4.11. Temperature RMS are lower than in the mid-line close to the plate, and almost disappear in the bottom level. The cavity stratification generates high fluctuations over the line $y/2L = 0.5$. Velocity

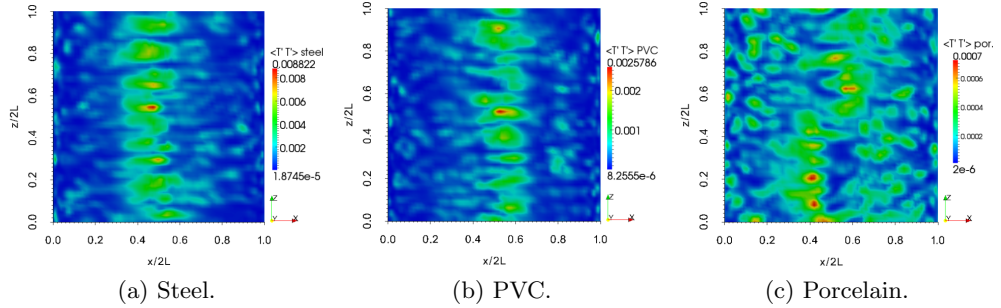


Figure 4.15: Temperature fluctuations onto the fluid-ceiling interface, for the drying-process simulations.

RMS are, on the contrary, higher than in near plate zone. In accordance with Figure 4.12b, the vertical velocity fluctuations peak in the mid-line. The horizontal velocity RMS are more homogeneous and smoothly decrease to zero near the wall.

Dry-process surfaces temperature fluctuations

The temperature fluctuations on plate and ceiling, for the drying-process simulations at time $t_0 = 60s$, are now briefly discussed. From here on, the angular brackets $\langle \phi \rangle$ indicate the average in spanwise direction and time, over the same interval reported in section 4.5.2.

Figure 4.14 shows the fluctuations of T on the vertical plate surface. The three materials exhibit a different behaviour, that is mainly determined by the thermal inertia ρC_p value and the internal temperature distribution. The plots can be read in conjunction with Figure 4.8. Steel case maintains a higher internal temperature, thus thermal fluctuations are localised in the plate bottom part, where the cold and dry air from the bottom-half cavity impinges the plate. Among the materials studied, steel has the highest ρC_p , hence it presents the lower thermal fluctuations. PVC case displays a homogeneous distribution, according to the internal temperature distribution. The fluctuation peaks are localised in the very bottom corner of the plate. Porcelain case presents an opposite behaviour with respect to steel: the plate is cold in the lower part, and the low specific heat capacity allows for high thermal fluctuations in the upper part.

Finally, the thermal fluctuations on the ceiling-fluid interface are reported in Figure 4.15. The different behaviour of materials is due to the temperature of the hot plume that rises from the plate.

Steel case produces the higher fluctuations, as a result of the high temperature of the air plume. Figure 4.15a shows a distribution of isolated spots, that are concentrated in the impinging area. PVC case generates an analogous configuration, while porcelain case gives rise to a more homoge-

neous distribution: a number of small, low intensity, thermal fluctuations are presented all-over the ceiling. This can be caused by the low temperature of air, that does not generate a central zone of high fluctuations. Moreover, when the horizontal flow is less strong, air can have a higher thermal interaction with the ceiling.

Chapter 5

Radiative Heat Transfer

Contents

5.1 Principles of thermal radiation	104
5.1.1 Definition and generation mechanisms	104
5.1.2 Qualitative aspects	106
5.1.3 Surface interactions with radiation	109
5.1.4 Spectral and directional dependency	111
5.1.5 Radiative quantities	111
5.1.6 Radiative behaviour of materials	114
5.2 Blackbody thermal radiation	118
5.3 RHT for participating media	121
5.3.1 Enclosure framework	122
5.3.2 Radiative transfer equation	122
5.3.3 Radiation scaling parameters	126
5.3.4 Energy and heat flux	127
5.3.5 Contribution to temperature equation	128
5.3.6 Radiative heat transfer on solid boundary	129

The general theory of thermal radiation has been extensively studied since the second half of the latest century. In this chapter the theoretical background of thermal radiation is reviewed. A short literature bibliography on this subject follows.

The textbook of Siegel and Howell [66] was one of the first attempt to organise and unify the knowledge in this field. The result is a detailed and rigorous book, where first, a comprehensive description of physical principles is presented, underlining all the limits of the theory and the complexity inherent in the practical quantification of the quantities involved. Then, a

large number of particular cases are studied under different simplification hypotheses, and some general engineering tools are presented.

The book of Modest [48] is another milestone in the field. The approach to the theory is clearly exposed and the notation is straightforward, even if sometimes the simplicity is to the detriment of completeness. The structure is similar to that of the previous book. More space is given to the engineering treatment of thermal radiation, with a description on a number of approximation methods that are generally used. This is one of the main reference for the present work.

The textbook of Viskanta [79] is focused on radiation in combustion systems. In the first part, the physics of radiation is introduced and the radiative transfer equation derived. Later, some interesting chapters are dedicated to study gases and particles interaction with radiation. In the conclusive part, the author focuses his attention to the specific cases of flames and combustion chambers.

Moreover, the work of Hottel and Sarofim [27], albeit quite outdated, needs to be mentioned. It collects a large number of details about the physical measurement of radiative quantities and particular approximation models for non-ideal cases.

5.1 Principles of thermal radiation

All materials continuously emit and absorb energy by radiation. The strength of radiative energy emitted depends on the internal energy of the emitting body, which, in the equilibrium state, is strictly related to the internal temperature. The emission does not need any medium to take place, it propagates at the speed of light, and cannot be interrupted. For these reasons, thermal radiation is a global and perpetual phenomenon able to affect all the elements of a system, almost instantaneously and uninterruptedly.

Physical systems including elements with high temperatures are strongly perturbed by radiation. Even in environmental applications, characterised by large space scale, radiative heat transfer is faster and more effective than convection and conduction heat transfer. In industrial applications, involving relative low temperatures (for example the common electric oven), thermal radiation can give rise to significant effects in the long term.

In this section, a short introduction to the physics behind thermal radiation is given.

5.1.1 Definition and generation mechanisms

During the 19th and 20th centuries, a number of independent experiments investigated the nature of light radiation, establishing its dual nature of electromagnetic wave and photons flux. This characteristic is often known

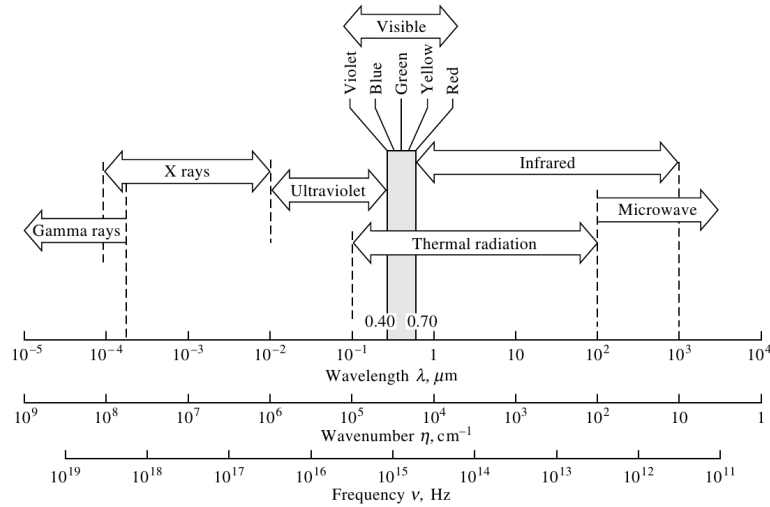


Figure 5.1: Electromagnetic wave spectrum for radiation travelling through vacuum, from Modest [48].

as wave-particle duality. It is a counter-intuitive concept. In this connection, Einstein and Infeld [22] wrote:

“But what is light really? Is it a wave or a shower of photons? [...] There seems no likelihood of forming a consistent description of the phenomena of light by a choice of only one of the two possible languages. It seems as though we must use sometimes the one theory and sometimes the other, while at times we may use either.”

The wave theory, based on the Maxwell equations, is used when the wave-nature of light is adopted; whereas the quantum theory is required when the effects due to the particle-nature become evident. Hereafter, we refer to radiation, as wave and as flux of photons, where the two definitions are considered interchangeable.

Thermal radiation is defined taking advantage of the wave approach. Depending on their behaviour, electromagnetic waves have been usually classified by rapport on the wavelengths.

Substances can radiate energy over the entire electromagnetic wave spectrum, but not all radiations are thermally relevant. The *thermal radiation* can be qualitatively defined as the electromagnetic waves emitted by a medium solely due to its temperature. Following Modest [48], such radiation occupies an intermediate wavelength range of the spectrum: from $0.1\mu\text{m}$ to $100\mu\text{m}$, namely from the ultraviolet to the mid-infrared including the visible light, as Figure 5.1 shows. Instead, Siegel and Howell [66] define the thermal radiation in a larger range, from $0.5\mu\text{m}$ to $1000\mu\text{m}$, including the

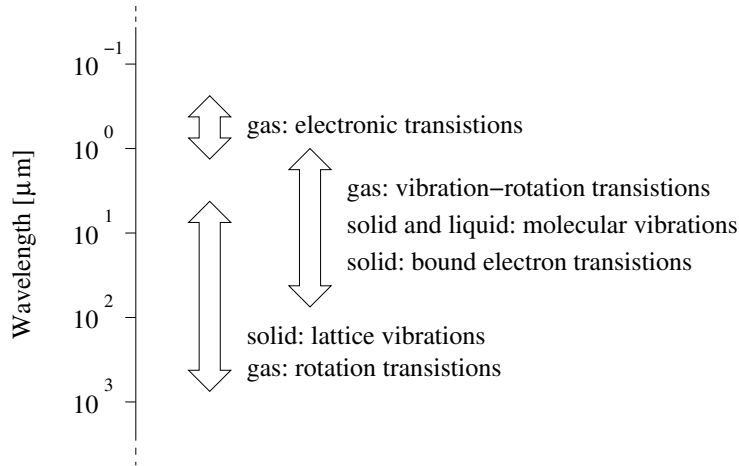


Figure 5.2: Production mechanism of thermal radiation, from Siegel and Howell [66].

microwaves. In view of the present work, where low-temperature systems are studied, the second definition is adopted. Thus, the low-energy emission are also taken into account.

Definition 1 (Thermal radiation). *The radiation characterised by a wavelength between $\lambda_{min} = 0.5\mu m$ and $\lambda_{max} = 1000\mu m$ is called thermal radiation.*

The mechanisms that generate thermal radiation are various. The energy emission in the thermal wavelength range depends on the molecular structure and, moreover, to the physical state of the irradiating matter.

Three mechanisms are mainly responsible for radiation emission-absorption phenomena, involving different amounts of energy: (i) a relative high level of energy is required to emit the ultraviolet radiations, generated by electrons after an orbital-jump; (ii) an intermediate amount of energy is necessary to spread the near-infrared waves, caused by the changing of molecular vibration; (iii) a smaller energy is required to change gases molecular rotation or the lattice vibration in solids, and these generate far-infrared radiation.

Figure 5.2 schematically shows the production mechanisms of thermal radiation for gas, solid and liquid substances.

5.1.2 Qualitative aspects

The complexity of the radiation heat exchange arises from the basic nature of radiation, that is completely different from conduction and convection. Before starting a mathematical analysis, few qualitative considerations can indicate the critical aspects of this subject. The essential peculiarities of radiation transfer are compared with the other two heat transfer mechanisms:

long-range phenomenon - radiation does not require any medium to transmit energy, it can be spread also in vacuum. On the contrary, conduction and convection can take place only inside the matter: conduction starts when energy is exchanged through the molecular lattice; convection occurs when energy is transferred by the collisions between molecules. Moreover, radiation transports energy at the speed of light (in vacuum), while the diffusion velocity for conduction and convection is much smaller.

Thus, radiative heat exchange has a long-range effect and it cannot be studied locally. Rather, all the system domain has to be taken into account. This affects, for example, the application of energy conservation principle. In the case of conduction and convection, an energy balance can be imposed on each infinitesimal volume, very large with respect to the material molecules, but small in comparison with the overall dimensions. Therefore, this principle can be expressed by a partial differential equation. In case of radiation, the energy balance has to be applied over the entire volume under consideration, leading to a much more complex integral equation.

temperature dependency - the heat flux¹ caused by conduction is described by the following diffusion equation

$$q = -\alpha \frac{\partial T}{\partial s},$$

where q is the heat flux, α the thermal conductivity, T is the temperature and s is taken as the direction of diffusion. The convective heat flux has a general form of the type

$$q = h\Delta T,$$

where h is the convective heat transfer coefficient. The coefficients α and h can be temperature dependent. Anyway, they can be kept constant in a wide range of applications, thus convective/conductive heat transfer are almost linearly proportional to temperature.

On the contrary, radiative heat flux does not have a general formula that can be shown, but it is in general proportional to the fourth power of temperature. In vacuum, for example, the maximum energy that can be radiated is

$$q = \sigma\Delta T^4,$$

where σ is the Stefan-Boltzmann constant. Consequently, thermal radiation becomes important with the rising of temperature, and prevails over the other heat transfer mechanisms at high temperature.

¹Here *heat flux* is the rate of energy transfer through a unit of area per unit of time, expressed by a scalar.

erratic behaviour of radiative parameter - the relevant properties of materials for conduction and convection are quite easy to determine and generally have a regular dependency on temperature. Thermal conductivity, kinematic viscosity, density, heat capacity, etc. of a wide range of substances are well known for different temperatures. Radiative parameters are quite difficult to measure and can show an erratic behaviour. They can strongly depend on different factors, such as the body material and the body manufacturing (*i.e.* the surface roughness can have a deep impact on the absorb radiation).

In order to numerically simulate the effects of thermal radiation, an accurate mathematical model and numerical solver is necessary, as well as a careful measurement of the physical parameters relative to the particular system considered.

quantum effects - quantum effects have to be taken into account also for convection and conduction, when the physical dimension of the studied body becomes comparable to their molecular structure. However, for a wide range of applications the classic physics laws are accurate enough. This is not true for thermal radiation, where quantum arguments must be invoked also in the study of some common radiative effects, such as the spectral distribution of energy emitted from a body and the radiative properties of gases.

Despite the complexity, the radiative heat exchange is of great interest for a wide range of engineering applications and its modellization is a very challenging problem from a theoretical point of view.

The first studies on this subject were finalised to the construction of space devices: they are subjects to a strong solar radiation that can considerably increase the internal temperature, since is difficult to spread it out in the vacuum. The same problem arises in relation to the dissipation of the heat produced inside the space vehicles as well as of the heat generated during the atmospheric re-entry.

Other applications can include: the investigation of combustion events (fires, furnaces, rocket nozzles, engines); nuclear reaction, inside the sun or for nuclear bomb and fusion reactor; sun emission, for the greenhouse effect and the development of solar energy collection.

Even at lower temperature, radiation can be interesting for industrial purposes. For example, it could happen that some water penetrates inside the car headlights. In that case, the heat spread by the light bulbs causes the water evaporation. The efficiency of the headlights can be decreased by vapour condensation onto the cold headlight surfaces (that ones in contact with the external environment).

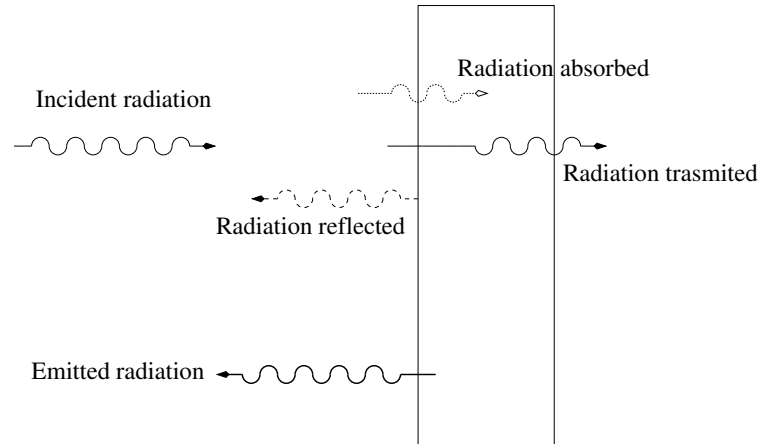


Figure 5.3: Interaction of incident radiation with a medium of finite thickness.

5.1.3 Surface interactions with radiation

All bodies both emit and receive thermal radiation from the surrounding environment. The interaction of incident radiant energy with the matter is sketched in Figure 5.3. When a ray impinges a homogeneous body, a first part of the radiation is reflected by the surface, a second part enters in the body and is completely absorbed, a third part travels through the medium and is transmitted farther. Thus, the effects of an incident radiation are not only related to the surface properties, but also to the underlying material. Base on these observations, three fundamentals radiative non-dimensional properties can be defined:

$$\text{Absorptivity, } \alpha \stackrel{\text{def}}{=} \frac{\text{absorbed fraction of incoming radiation}}{\text{total incoming radiation}}, \quad (5.1)$$

$$\text{Transmissivity, } \tau \stackrel{\text{def}}{=} \frac{\text{transmitted fraction of incoming radiation}}{\text{total incoming radiation}}, \quad (5.2)$$

$$\text{Reflectivity, } \rho \stackrel{\text{def}}{=} \frac{\text{reflected fraction of incoming radiation}}{\text{total incoming radiation}}, \quad (5.3)$$

The absorptivity can be measured experimentally, even if it is often not straightforward because it can depend on the directional and spectral characteristics of incident radiation. Transmissivity and reflectivity are even more complicated to measure, as they also depend on the outgoing directions of the rays. Either way, all the incoming radiations must be either reflected or absorbed or transmitted, therefore

$$\alpha + \tau + \rho = 1. \quad (5.4)$$

In general, these three phenomena have to be taken into account for an accurate investigation. However, some of these can be neglected in order to simplify the study of such complex subject. Particularly, it is common to define a body as:

- ▶ *Transparent* a substance that allows all the radiation entering in the body to be transmitted. In this case, no energy is absorbed, so $\alpha = 0$;
- ▶ *Opaque* a material that absorbs all the radiations that pass into the body. In this case no transmission can take place, so $\tau = 0$;
- ▶ *Black* an object in which all the rays can penetrate into the body and are internally absorbed. Thus, no reflection and transmission occurs, so $\rho = \tau = 0$.

A real body with one, or more than one, of these characteristics does not exist. However, a body can be considered transparent, opaque or black in order to facilitate the mathematical modelling of thermal radiation.

Apart from the interaction with external radiation, all bodies internally emit radiative energy. The fraction of this emission that escapes from the surface is defined as:

$$\text{Emissivity } \epsilon \stackrel{\text{def}}{=} \frac{\text{energy emitted from the surface}}{\text{maximum energy that can be emitted}}. \quad (5.5)$$

Emissivity is a non-dimensional parameter, usually measured in experiments in the normal surface direction. It can vary between $\epsilon \in [0, 1]$. A perfect emitter has $\epsilon = 1$ and is identified as a *blackbody*, (defined and analysed in section 5.2).

Observation. *For simplicity, we have not mentioned that the above defined quantities can depend on radiation wavelength, direction and surface temperature. In our investigation, we adopt the hypothesis of grey and diffuse radiation (cf. section 5.1.4), thus they can be considered constant.*

More details on the definition of radiative fundamental properties can be found, among the others, in M. Modest [48], chapter 3.

Using one of the Kirchhoff's laws for thermal radiation, a relation between the emissivity and absorptivity is derived.

Kirchhoff's law. *For a body of any arbitrary material, emitting and absorbing thermal electromagnetic radiation at every wavelength in thermodynamic equilibrium, the ratio of its emissive power to its dimensionless coefficient of absorption is equal to a universal function only of radiative wavelength and temperature. That universal function describes the perfect black-body emissive power*².

A corollary of this statement is the following: if the local thermodynamic equilibrium prevails, then the absorptivity and the emissivity are equal

$$\alpha = \epsilon \quad (5.6)$$

if thermal radiation is grey and diffuse (*i.e.* does not depend on wavelength and direction of propagation).

² Ref. to M. Planck. *The Theory of Heat Radiation*. Authorised translation by M. Masius. Ed. P. Blakiston's Son and Co. (1914). Page 35.

5.1.4 Spectral and directional dependency

As mentioned previously, an additional degree of complexity for the thermal radiation is that all quantities involved are dependent of many variables. Generally speaking they depend on time and space, but also on the direction of propagation (directional dependency) and on the type of waves that compose radiation (spectral dependency).

Each wave can be identified by its wavelength λ [m^{-1}], or by its frequency ν [Hz], or by other equivalent variables like wavenumber and angular frequency. The frequency does not change when light penetrates from one medium to another, whereas wavelength depends on the refractive index of the two media. For this reason, frequency is often used when participating media³ are studied. Instead, the wavelength is preferred when the fundamental laws are stated, since it has a simpler physical interpretation. The two quantities are related through the formula:

$$\nu = \frac{c_0}{\lambda_0}, \quad (5.7)$$

where c_0 is the speed of light in vacuum. If an electromagnetic wave is travelling within a medium, its wavelength λ changes according to $\lambda_0 = n\lambda$, with n the refractive index of the medium and λ_0 the wavelength in the vacuum.

In many engineering applications we can neglect the spectral or directional dependency. Indeed, by definition:

- ▶ *Grey radiation*, is when the radiative quantities do not depend on the frequency;
- ▶ *Diffuse radiation*, is when the quantities do not depend on the direction of propagation.

These assumptions can considerably simplify the mathematics of the radiative model.

5.1.5 Radiative quantities

When problems involving thermal radiation are investigated, we usually want to determine the energy radiated by a body surface. This can be quantified into two slightly different ways.

Definition 2 (Emissive power). *The spectral emissive power is the energy emitted from an infinitesimal surface area dA , per unit of time, on a specific*

³Thermal radiation can propagate through medium. If the medium interacts with radiation (*e.g.* absorbs, emits or scatters radiation) it is called a participating medium. Air is a typical participating medium when it contains water vapours and/or carbon dioxide and/or particle from combustion events.

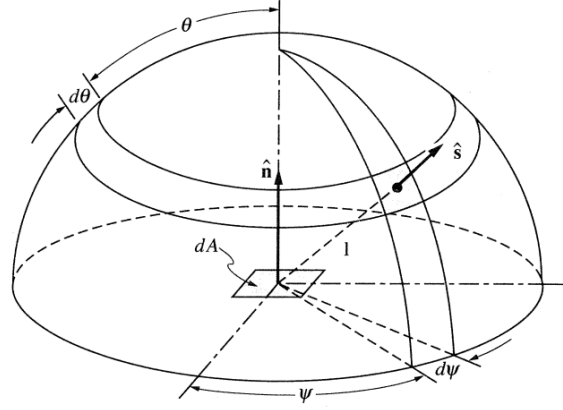


Figure 5.4: System of spherical coordinates, just the superior hemisphere is shown. The polar angle $0 \leq \theta \leq \pi$ is measured from the normal on the equatorial plane, the azimuthal angle $0 \leq \psi < 2\pi$ is measured from an arbitrary axis on the equatorial plane and the projection of the point on it. Versor \hat{s} indicates a point over the surface of unit radius sphere. We should note that with this choice of θ , the versor normal to equatorial plane \hat{n} cannot be expressed in this systems of coordinates.

wavelength λ . This is denoted by

$$e_{\lambda}(\mathbf{r}, \lambda), \quad (5.8)$$

where \mathbf{r} is the position vector of the radiant surface dA .

Integrating over the entire spectrum, we obtain the *total emissive power* of a surface:

$$e(\mathbf{r}) = \int_0^{\infty} e_{\lambda}(\mathbf{r}, \lambda) d\lambda. \quad (5.9)$$

This is the most natural way to define the radiative flux leaving a solid surface, but it is not suitable for participating media. Another quantity is defined in a slightly different way. Let us consider the infinitesimal surface dA that is radiating energy to surface dB , as in Figure 5.5, then:

Definition 3 (Radiative intensity). *The radiative spectral intensity is defined as the energy emitted per unit of time (on a specific wavelength λ and direction \hat{s}), from an infinitesimal surface area dA projected on direction \hat{s} , into an infinitesimal solid angle centred around the direction \hat{s} . This is denoted by*

$$I_{\lambda}(\mathbf{r}, \hat{s}, \lambda), \quad (5.10)$$

where \mathbf{r} is the position vector of the radiant surface dA .

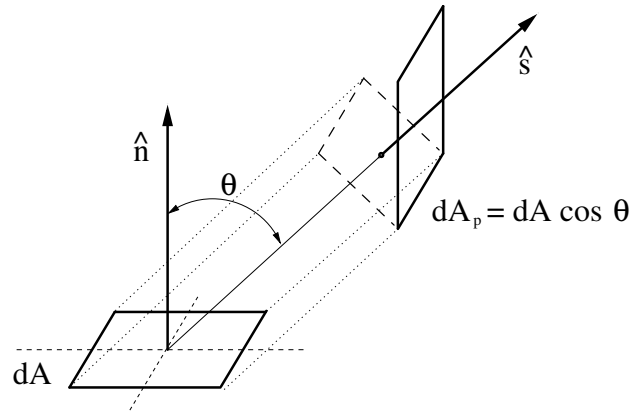


Figure 5.5: Infinitesimal radiative surface dA , and projected surface dA_p on direction $\hat{\mathbf{s}}$.

It is common to describe the direction of propagation of radiation in terms of spherical coordinates system. The coordinates system shown in Figure 5.4 is adopted, where the versor $\hat{\mathbf{s}}$ is used to indicate the direction instead of θ and ψ . This versor is related to the spherical coordinates *via* the relation:

$$\hat{\mathbf{s}} = (\sin \theta \cos \psi, \sin \theta \sin \psi, \cos \theta), \quad (5.11)$$

expressed in Cartesian coordinates.

Also in this case, the *total intensity* is obtained integrating over the wavelengths:

$$I(\mathbf{r}, \hat{\mathbf{s}}) = \int_0^{\infty} I_{\lambda}(\mathbf{r}, \hat{\mathbf{s}}, \lambda) d\lambda. \quad (5.12)$$

The two quantities above defined can be related one each other, integrating the intensity over all the possible directions of radiation, *i.e.* over a sphere surrounding the surface dA

$$e(\mathbf{r}) = \int_0^{2\pi} \int_0^{\pi/2} I(\mathbf{r}, \theta, \psi) \cos \theta \sin \theta d\theta d\psi. \quad (5.13)$$

Such relation relates the emissive power and the radiative intensity of an infinitesimal radiant surface. The above expression is also valid on the spectral basis.

Another quantity useful in radiative problems is the *radiative heat flux*, defined as:

$$\mathbf{q}_{\lambda} = \oint I_{\lambda}(\hat{\mathbf{s}}) \hat{\mathbf{s}} d\Omega. \quad (5.14)$$

where, with an abuse of notation, the circle on the integral means that the integration is done over all the possible solid angles.

The correspondent total quantity is again obtained integrating over the spectrum.

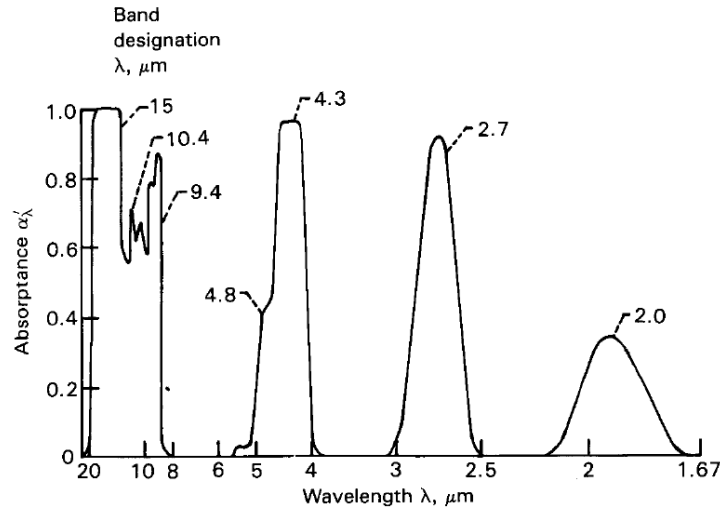


Figure 5.6: Spectrum of absorption bands for CO_2 gas at $T = 830\text{ K}$, from Siegel and Howell [66].

5.1.6 Radiative behaviour of materials

In the next sections, we review some radiative characteristics of different types of materials, trying to point out the physical processes that rule their radiative behaviour.

Solids and liquids

From a physical point of view absorption and emission of radiation is due to the interaction of the photons with the free electrons and the lattice structure. There are basic differences in radiative behaviour of electrical conductors and dielectrics. The link between electronic and radiative properties of materials are predicted by the classical electromagnetic theory (in the infrared range) and confirmed by the experiments.

In this section, the usual peculiarities of some substances are identified, without the claim to present the complete theory or to give absolute rules. There could be many exceptions to these general guidelines.

The manufacturing of the surface and the presence of chemical impurity, often play an important role in the radiative behaviour of an object. In order to point out the properties ascribe only to one material, we are going to consider smooth and pure body.

Metals: electrical conductors, in particularly metals, are often characterised by a high values of reflectively and low level of emissivity/absorptivity. Moreover, usually they have a low trasmissivity, so they can be considered opaque also if the body is relative thin.

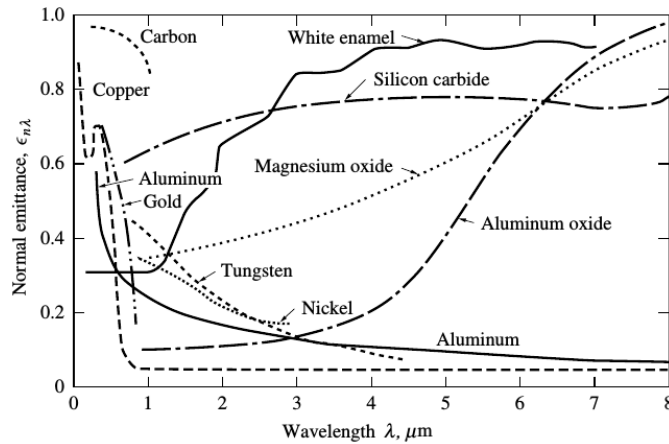


Figure 5.7: Spectral emissivity on the normal direction for selected materials, originally reported in F. M. White, *Heat Transfer*, Addison-Wesley (1984).

The emissivity is higher on the normal direction on the surface, but for a polished metal increases again when the direction of propagation approach the surface tangent.

Figure 5.7 shows the emissivity dependency of materials from the wavelength: in general the emissivity tends to increase with decreasing wavelength and reaches a maximum near the visible region, then it decreases rapidly with further decrease of wavelength.

With respect to the temperature, emissivity of pure metals increases with temperature in the infrared region: many metals show an emissivity proportional to the square root of absolute temperature for long wavelengths. However, for short wavelengths they show an opposite tendency and emissivity decrease as temperature is increased.

Non-metals: non-conductors have few free electrons and the radiative properties are dominated by the photons interaction with the crystal lattice. Thus, they are characterised by high values of emissivity/absorptivity, also for moderate temperatures, and small reflection.

The generalisation proposed for metals cannot be easily done for others materials. The reasons are the following: first, most non-metals are not polished enough to avoid the effects of a non-ideal surface, even if some exceptions exist, like glass and some plastics. Second, it is more common that non-metal body is not sufficient thick to be opaque. In this case the transmissivity effects should be taken into account, increasing the physical complexity. If we want to avoid the transmissivity effect in practical applications, the body can be made opaque by applying a coating of opaque material. Third, non-metals are often not pure as metals. They can have a

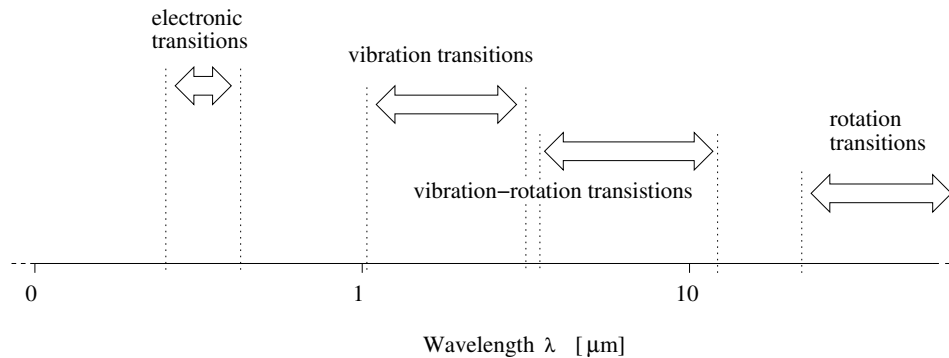


Figure 5.8: Sketch of gas spectral emissivity. The production mechanisms are due to electronic orbital transition, vibration and rotation energy changes in the molecules.

number of chemical impurities or particles (especially for liquids) that alter the response to radiation.

However, some general considerations can be done for an opaque non-metals emissivity: it is maximum on the surface normal direction; is almost constant for a wide range of wavelengths; it weakly depends temperature.

Gases

The radiation properties of gases exhibit a very irregular wavelength dependency, compared to the solids or liquids. As it is sketched in Figure 5.2, the thermal radiation is generated by different mechanisms of energy transitions that can occur within the substance. It turns out that the gas structure allows a significant emission and absorption only in certain wavelength ranges, especially for temperature $T < 10000 K$. Figure 5.6 shows an example of this phenomenon for the absorption of carbon dioxide; it is clearly visible that this gas absorbs radiation only in some specific bands of wavelengths.

To better understand this discontinuous behaviour, we must use the concept of discrete energy of quantum mechanics, and analyse the structures of gas particles. More details can be found in Siegel and Howell [66].

Particles

The electromagnetic waves propagation is qualitatively different in a non homogeneous medium, especially when small particles of impurities are present. The interaction with particles can change the direction of propagation of the waves, giving rise to the so-called *scattering* of thermal radiation. From the point of view of quantum mechanics, the scattering can be defined as an interaction between a photon and others particles, where the photon does not lose its entire energy (cf. Siegel and Howell [66], section 12-9). This

phenomenon is generated by three main mechanisms:

- (i) *diffraction*, when electromagnetic wave does not impact the particle but it is deviated;
- (ii) *reflection*, when electromagnetic wave collides with the particle and it is reflected by the surface;
- (iii) *refraction*, when electromagnetic wave changes its trajectory after being passed through the particle;

Figure 5.9 gives a schematic representation of these mechanisms. The key parameter, that determined the nature of the interaction, is the relative size of the particles with respect to the radiation wavelengths. This is called *size parameter* and it is expressed by the ratio:

$$\chi = \frac{2\pi a}{\lambda}, \quad (5.15)$$

where the particles are assumed of a spherical-type shape, and a is its effective radius. Three different scattering regimes can be determined by respect to the size parameter:

$\chi \ll 1$ - the interacting particles have very small size, and scattering is proportional to $1/\lambda^4$ (or in other words, to ν^4). This is called Rayleigh scattering and can be appreciated in the different colours of sky during the day. The inverse dependence on λ implies that the short waves (blue) are more scattered by atmospheric impurities than the long waves (red), thus our eyes perceive the sky as blue. Nevertheless, when the sun-light passes through a thick layer of air just red light remains, resulting in red sunset and sunrise.

$\chi \sim 1$ - this is called Mie scattering, and it is ruled by a complex interaction theory that has to take into account, among the other factors, the shape of particles and the polarisation effects.

$\chi \gg 1$ - the particles are bigger enough to be consider a small body. Interaction can be studied by geometric optics.

From an applicative point of view, the presence of scattering decreases the transmissivity of the medium, and can be quantified by the *scattering coefficient*:

$$\sigma_{s,\lambda}, \quad (5.16)$$

that can depend on the wavelength. This is defined as “the inverse of the main free path that a photon of wavelength λ will travel before undergoing scattering” (form Siegel and Howell [66]).

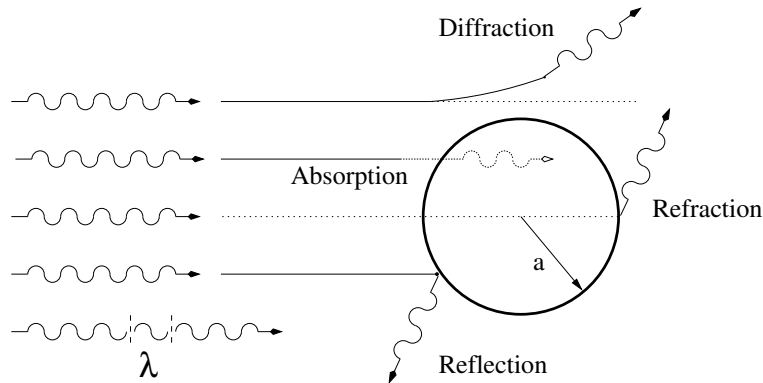


Figure 5.9: Interaction of electromagnetic radiation waves with a particle.

5.2 Blackbody thermal radiation

The first studies on radiation were devoted to understand the emission spectrum of the sun. These led to the fruitful concept of *blackbody* that, ultimately, represents an idealisation of the sun, from a radiative point of view. The following definition is taken from [66].

Definition 4. *A blackbody is a perfect absorber of incident radiation.*

In other words, a blackbody is an ideal body that allows all the incident radiations to pass into it and completely absorbs them internally, for radiation of all wavelengths and all angles of incidence. Hence, the blackbody does not allow any reflection and any transmission of energy.

All other properties of blackbody can be deduced by this definition. Particularly, it can be proved that:

- ▶ it is a perfect emitter in each direction and at every wavelength, therefore it must emit the maximum amount of energy in each direction and wavelength;
- ▶ the total energy emitted by radiation is a function only of the body temperature.

The energy radiated by a blackbody cannot be determined with the classical physics theory, but quantum arguments are needed. In 1896, Wilhelm Wien used experimental data and the thermodynamics theory to find the spectral distribution of a blackbody emissive power. The *Wien's law* is quite accurate for a large part of the spectrum, but fails in the small wavelengths range.

After few years, in 1901, Max Planck used quantum mechanics to derive a more general and accurate distribution, of which the Wien's law is an approximation. The *Planck's spectral distribution of emissive power* for a

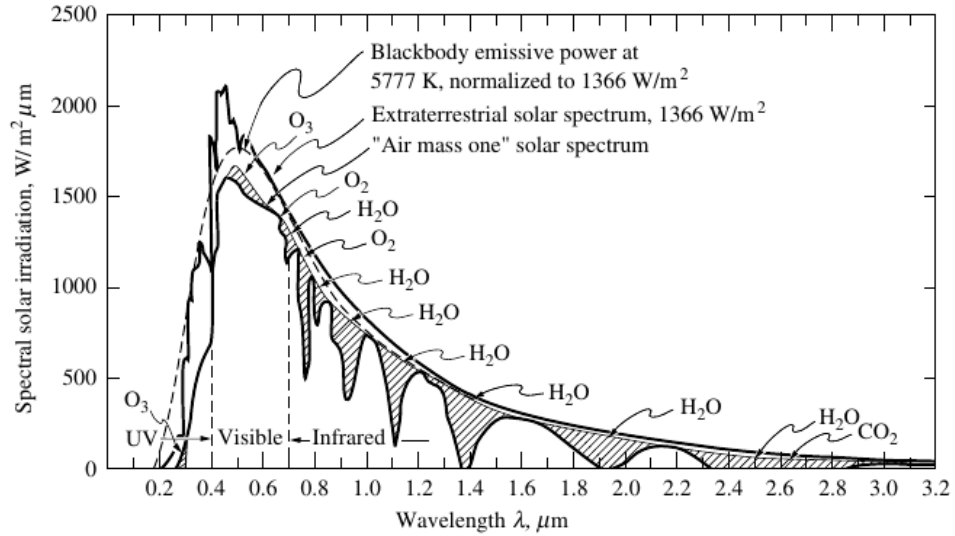


Figure 5.10: Sun spectrum onto Earth. From [48].

blackbody, bounded by transparent medium with constant refractive index n is:

$$e_{b,\lambda}(T, \lambda) = \frac{2\pi hc_0^2}{n^2 \lambda^5 [e^{hc_0/n\lambda kT} - 1]} \quad (5.17)$$

where k is the *Boltzmann's constant*, h is the so-called *Planck's constant*, and c_0 is the speed of light in vacuum, that have a typical values of:

$$\begin{aligned} k &= 1.3806 \times 10^{-23} \text{ J/K}, \\ h &= 6.626 \times 10^{-34} \text{ Js}, \\ c_0 &= 2.998 \times 10^8 \text{ m/s} \end{aligned}$$

A modern derivation of this result could be found on Brehm and Mullin [11].

The good agreement of this law with experimental data can be qualitatively appreciate in Figure 5.10, where the spectral emissivity of the sun onto the Earth is reported. The sun is assumed at an effective temperature of $5762K$. The influence of Earth atmosphere is limited to some specific wavelengths on which the air molecules are active, as discussed in section 5.1.6.

A plot of the emission power function $e_{b,\lambda}(T, \lambda)$ is shown in Figure 5.11. Some physical implications can be highlighted: energy emitted on all wavelengths increases when the body temperature increases, but it rises more rapidly for shorter wavelengths than for long wavelengths. The peak of radiate energy shifts toward the lower part of the spectrum, when temperature increases. For a body under $5000K$ only a small amount of energy would be in the visible part of the spectrum, and would not be sufficient to be detected by eyes.

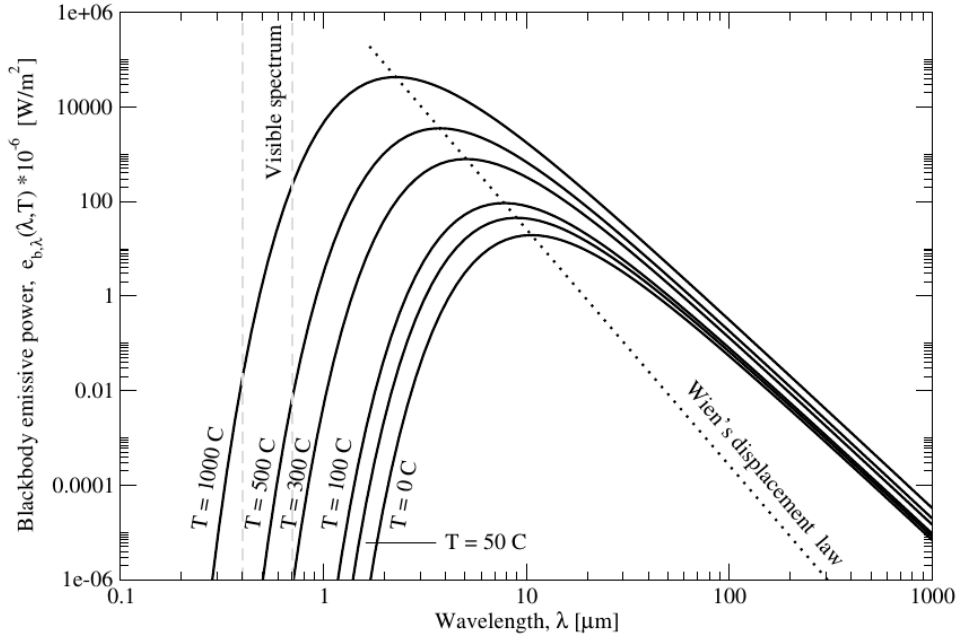


Figure 5.11: Spectral blackbody emissive power $e_{b,\lambda}(T, \lambda)$ for some low temperatures, and the Wien's displacement law (dash line).

The wavelengths at which the maximum energy is emitted, can be found by differentiating equation (5.17) and imposing the derivative to be zero. The equation obtained can be numerically solved, leading to the relation:

$$n\lambda_{max}T = constant = 2898\mu mK \quad (5.18)$$

that is one form of the *Wien's displacement law*.

A simple relation between spectral emissive power and the spectral intensity can be found. By virtue of the particular properties of blackbody, it can be proved that blackbody spectral intensity does not depend of the direction of propagation:

$$I_{b,\lambda}(\lambda) = I_{b,\lambda}(\hat{s}, \lambda), \quad (5.19)$$

that is, the blackbody radiation is diffuse. Then, the radiative heat flux emitted by a surface into a surrounding hemisphere is found computing the integral in equation (5.13):

$$e_{b,\lambda}(\lambda) = \pi I_{b,\lambda}(\lambda). \quad (5.20)$$

This relation is valid in general, for all bodies that emit diffuse radiation.

Observation. *The main disadvantage of expressing the emissive power as a function of λ , is that the light changes its wavelength when penetrates*

from a medium to another. In order to not take into account this additional phenomenon, the radiative quantities can be expressed in term of frequency ν .

In fact, the quantum mechanics state that a photon (or wave) has an associate energy of

$$E = h\nu; \quad (5.21)$$

since the energy must be conserved, the frequency of light does not depends on the medium in which it is travelling.

Using relation (5.7), the Planck's emissivity can be expressed with respect to frequency:

$$e_{b,\nu}(T, \nu) = \frac{2\pi h\nu^3 n^2}{c_0^2 [e^{h\nu/kT} - 1]}. \quad (5.22)$$

However, it is customary study this distribution using the λ -formulation because of its simpler physical interpretation.

The total emissive power of a balckbody can be determined by integrating equation (5.17) over the entire spectrum. The integral can be evaluated by complex integration, and can be expressed as

$$e_b(T) = n^2 \sigma T^4, \quad (5.23)$$

where σ is the *Stefan-Boltzmann constant*, theoretically evaluated

$$\sigma = 5.670 \times 10^{-8} \frac{W}{m^2 K^4}. \quad (5.24)$$

The experimental value of σ is slightly different from the theoretical one.

5.3 Radiative heat transfer for participating media

In the present section the mathematical model for thermal radiation exchange in presence of an absorbing, emitting and scattering medium is derived. The model obtained describes the radiative intensity field within an enclosures filled with a real interactive medium. It is used in many practical and engineering applications.

The derivation is carried out enforcing the radiative energy balance over the control volume in Figure 5.13, following Modest [48], chapter 8. First, the radiative intensity in vacuum is described, then all the other contributions due to the participating medium are added to the equation.

The mathematical details are omitted. The main results are reported, and it is underlined the physical meaning of the terms composing the final equation.

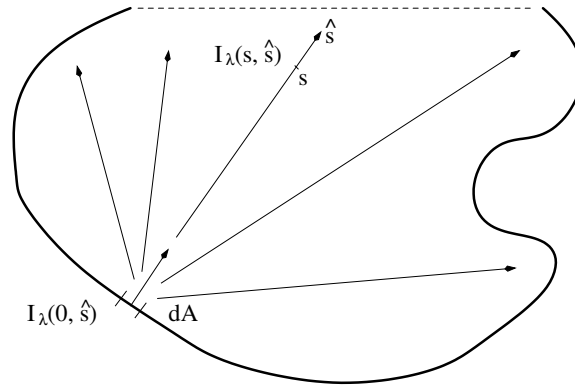


Figure 5.12: Sketch of enclosure, with solid surfaces (straight line) and an open surface (dash line). The surface dA radiate in all direction \hat{s} over the enclosure

5.3.1 Enclosure framework

The thermal radiation exchange is studied, performing an energy balance on a suitable virtual volume. The balance needs to be performed for all possible direction where radiation can propagate, thus it cannot be computed over an infinitesimal control volume, as for heat conduction and convection. A global balance have to be done. We define

Definition 5 (Enclosure). *Given a radiate infinitesimal surface dA , an enclosure for this surface is a close region surrounding dA .*

An enclosure for a system, is a virtual domain that is an enclosure for all the infinitesimal radiant surfaces that compose the system.

An example of enclosure is sketch in Figure 5.12. It has to be bounded, in order to account for all radiating directions, and it can be delimited by solid surfaces or open areas. In working problems, the enclosure is often determined by the geometry configuration.

The enclosure surfaces play an active role by the absorption, emission, reflection and transmission of radiation, as discussed in section 5.1.3. From mathematical point of view, the boundary conditions take into account this effects (cf. the following section 6.2.2).

5.3.2 Radiative transfer equation

The spectral radiative intensity (cf. definition 3) is here expressed as a function of \mathbf{r} the location vector, \hat{s} direction of propagation and ν the frequency, instead of the wavelength λ (to be conform with the majority of the literature). The evolution of intensity is derived along the direction \hat{s} and it is expressed as function of the line coordinate s .

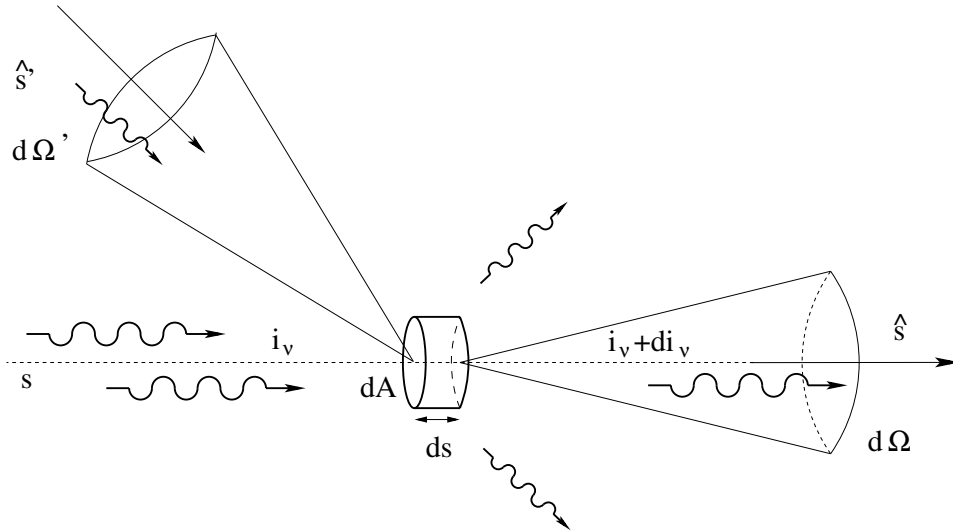


Figure 5.13: Control Volume for the derivation of radiation transfer equation, along a direction \hat{s} .

Nevertheless, in order to use a simpler notation, the dependency on the position \mathbf{r} will be not explicitly written.

Non-participating media

The radiative intensity in a non-participating media can be expressed in a very simple form, under the *instantaneous propagation hypothesis*: since the speed of light is very large with respect to any other time scale in applicative problems, it can be almost always assumed that radiation transport energy instantaneously everywhere in the medium.

Afterwards, considering just the balance of intensity passing from the two bases of the cylindrical control volume in Figure 5.13, we obtain that

$$I_\nu(s, \hat{s}) = \text{constant}. \quad (5.25)$$

This means that intensity is constant along a ray path, for any given direction. Note that this property come for the definition of intensity, and makes it particularly suitable for studying the participating media case. In fact, any variations of this quantity can be only due to absorption, emission or scattering by the medium. Instead, the emission power varies also with the direction of propagation.

Attenuation mechanisms

A radiation passing through a medium can be attenuated by absorption and scattering. In order to avoid the effects due to refraction, the refractive

index is considered constant, and the attenuation of thermal rays travelling in a straight direction is studied.

The intensity absorbed by the medium has been observed to be directly proportional to the intensity magnitude and the path length done through the medium:

$$dI_\nu|_{abs} = -\kappa_\nu I_\nu(s, \hat{\mathbf{s}})ds, \quad (5.26)$$

where the (positive) constant κ_ν is the *linear absorption coefficient*. It has the dimension of reciprocal length and it is inversely related to the mean free path of a photon into the medium before to be absorbed (cf. section 5.3.3).

The attenuation by scattering is known also as *out-scattering*, and it is due to the departs of a ray from its direction of propagation. It can be modelled in similar way as absorption:

$$dI_\nu|_{outSca} = \sigma_{s,\nu} I_\nu(s, \hat{\mathbf{s}})ds, \quad (5.27)$$

where $\sigma_{s,\nu}$ is known as *linear scattering coefficient*.

Note that, while absorption increases internal energy, the out-scattering just redistributes it on other directions.

The two coefficients already described, can be combined to determine the so-called *extinction coefficient* of a medium:

$$\beta_\nu = \kappa_\nu + \sigma_{s,\nu}. \quad (5.28)$$

Integrating over the geometrical paths $\hat{\mathbf{s}}$ of a ray, we obtain

$$\tau_\nu = \int_0^s (\kappa_\nu + \sigma_{s,\nu})ds', \quad (5.29)$$

also called *optical distance* based on the extinction coefficient, that is a measure of the ability to the medium of attenuate radiation of a specific frequency.

Augmentation mechanisms

Radiation can also be increased by the medium during its travel. The gain of energy can be caused by the emission of the medium itself, or by the *in-scattering*, *i.e.* the scatter of the rays from other directions to the direction of travel of the considered rays.

In analogous way as for absorption, also emission can be expressed as a linear function of the intensity and the path length travelled by the rays:

$$dI_\nu|_{emt} = \kappa_\nu I_{b,\nu}(s, \hat{\mathbf{s}})ds, \quad (5.30)$$

where the constant of proportionality is the same as for absorption. This is expected because, if the medium is in local thermodynamic equilibrium, the amount of absorbed energy has to be the same of the emitted energy.

The expression of the in-scattering term, needs particular attention and is the source of many difficulties in numerical discretisation. The contribution by all directions must be taken into account, therefore an integration over all solids angles is required. The balance of energy flux scattered from all incident directions \hat{s}' into direction \hat{s} , gives:

$$dI_\nu|_{inSca} = ds \frac{\sigma_{s,\nu}}{4\pi} \oint I_\nu(s, \hat{s}') \Phi_\nu(\hat{s}, \hat{s}') d\Omega', \quad (5.31)$$

where: $d\Omega'$ are the infinitesimal solid angles from which a radiation travelling in the direction \hat{s}' impinge dA ; and Φ_ν account for the the anisotropy of the scattering, and it is defined by:

Definition 6 (Scattering phase function). *The (normalised) scattering phase function*

$$\frac{1}{4\pi} \Phi_\nu(\hat{s}, \hat{s}'), \quad (5.32)$$

is the probability that a ray from one direction \hat{s}' , will be scattered into a certain other direction \hat{s} .

In other words, it can be seen as the intensity scattered in the direction \hat{s} divided by the intensity that would be scattered in \hat{s} if the scattering were isotropic, *i.e.* the same amount of energy would be scattered in all the directions. Indeed, if the scattering is isotropic, then

$$\frac{1}{4\pi} \oint \Phi_\nu(\hat{s}, \hat{s}') d\Omega' = 1 \quad \Rightarrow \quad \Phi_\nu \equiv 1. \quad (5.33)$$

This function could have a complicate formulation, depending on the process to be modelled. However, an usual estimation of non-isotropic scattering is the *linear-anisotropic scattering* model

$$\Phi(\hat{s}, \hat{s}') = 1 + A \hat{s} \cdot \hat{s}', \quad (5.34)$$

where the constant A is the anisotropic scattering factor. Other functions that can be used, are a simplified version of the *Henyeey–Greenstein phase function*; more details on this topic can be found in Modest [48], chapter 12.9 and following.

Radiative heat transfer equation

The final equation for radiative heat transfer (RHT) in participating media is obtained adding all the contributions above described, using the instantaneous propagation hypothesis and considering the process to be quasi-steady. It reads:

$$\frac{dI_\nu}{ds}(s, \hat{s}) = \kappa_\nu I_{b,\nu}(s, \hat{s}) - \beta_\nu I_\nu(s, \hat{s}) + \frac{\sigma_{s,\nu}}{4\pi} \oint I_\nu(s, \hat{s}') \Phi_\nu(\hat{s}, \hat{s}') d\Omega', \quad (5.35)$$

where s is the linear coordinate on the \hat{s} direction. This is an integral-differential equation and describes the thermal radiation in any arbitrary enclosure, for a fixed direction \hat{s} . The RHT equation can be solved providing suitable boundary conditions, that have to be modelled with respect to the enclosure surfaces radiative properties.

Observation. *The radiative transfer equation (5.35) is a quite complex. In order to solve radiative heat exchange problem, it has to be integrated over the entire spectrum and computed for all possible directions \hat{s} .*

The physical meaning of the equation terms are now briefly summarised:

- ▶ $\kappa_\nu I_{b,\nu}(s, \hat{s})$ - emission term: can be computed if the medium temperature field is known, thus it is accountable for the coupling with the other modes of heat transfer;
- ▶ $-\beta_\nu I_\nu(s, \hat{s})$ - extinction term: determines the reduction of intensity within the medium. Generally speaking, intensity has an exponential decay, depending on the optical thickness of the medium material (cf. following section 5.3.3);
- ▶ $\frac{\sigma_{s,\nu}}{4\pi} \oint I_\nu(s, \hat{s}) \Phi_\nu(\hat{s}, \hat{s}') d\Omega'$ - scatter term: increases the degree of complexity of the equation, due to its integral formulation. The most simple models are the isotropic scattering or linear-anisotropic scattering.

The RHT equation can be solved analytically just under simplification hypothesis and for very simple geometry. For all other cases, a numerical approach has to be used.

5.3.3 Radiation scaling parameters

There are two dimensionless parameters that arise naturally in the radiative heat transfer problems. In this section, they are defined as global parameters, neglecting the spectral dependency.

Definition 7 (Single scattering albedo). *The single scattering albedo ω is defined as*

$$\omega \stackrel{\text{def}}{=} \frac{\sigma_s}{\kappa + \sigma_s}, \quad (5.36)$$

the ratio of the spectral scattering coefficient to the extinction coefficient.

This intrinsic parameter characterises the relative importance of scattering with respect to absorption/emission. Two scattering regimes can be identified:

- ▶ *Low scattering, $\omega \sim 0$.* This represents both the case of high absorbing or emitting material $\sigma_s \ll \kappa$, or the case of no scattering medium $\sigma_s \sim 0$;

- ▶ *High scattering*, $\omega \sim 1$. This is the case in which $\sigma_s \gg \kappa$.

The second important parameter is the optical thickness, define in analogy with the optical distance (5.29), that governs the radiation field in a medium.

Definition 8 (Optical thickness). *The optical thickness, or opacity, is the measure of the ability of a medium to attenuate radiation. It is defined as*

$$\tau_L \stackrel{def}{=} (\kappa + \sigma_s)L, \quad (5.37)$$

where L is the characteristic length of the medium layer.

When κ does not vary along a path, the mean penetration distance of photon before absorption is the reciprocal of the spectral absorption coefficient, $\ell_p = 1/\kappa$. Then, the opacity is the ratio between the characteristic length of the system to the spectral photon free path:

$$\tau_L = L/\ell_p. \quad (5.38)$$

The *Knudsen number* is a similar non-dimensional number that arises in molecular transfer problem. Opacity is the reciprocal of Knudsen number for photons.

Three physical regimes interest can be identified:

- ▶ *Non participating media*, $\tau_L \sim 0$. Vanishing opacity denotes a non participating medium, in which radiation travels from boundary to boundary without any disturbance;
- ▶ *Optical thin medium*, $\tau_L \ll 1$. From a physical point of view, the medium emits and absorbs energy radiating from the boundaries, but it is not dense enough to receive any energy from the internal matter;
- ▶ *Self-absorbing medium*, $\tau_L \sim 1$. This is the most general case and the most complex from mathematical point of view;
- ▶ *Optical thick medium*, $\tau_L \gg 1$. In this case, if we consider a location far from the boundaries, the energy contributions must be local. Energy can come only from very close around it. Thus, the radiative transport behaves as diffusion process, like the molecular transport.

The optical thickness is one of the most important radiative parameter in problem involving participating medium.

5.3.4 Energy and heat flux

Radiative effects on temperature distribution, can be estimated using the spectral radiative intensity directly. However, the energy carried by thermal radiation can be expressed by the means of two more quantities: incident

radiation and radiative heat flux vector.

After definition 3, the *spectral radiant energy* stored in an infinitesimal volume dV , is computed as:

$$E_\nu = \frac{1}{c} \oint I_\nu(\hat{\mathbf{s}}) d\Omega = \frac{1}{c} G_\nu, \quad (5.39)$$

where c is the speed of light and the function

$$G_\nu = \oint I_\nu(\hat{\mathbf{s}}) d\Omega \quad (5.40)$$

takes the name of *incident radiation*. It is widely used in engineer applications.

The net heat flux onto a surface element is evaluated balancing the incoming and outgoing fluxes. Using definition (5.14), the *radiative heat flux vector* for participating media can be expressed as

$$\mathbf{q}_{rad} = \oint I_\nu(\hat{\mathbf{s}}) \hat{\mathbf{s}} d\Omega, \quad (5.41)$$

and it has to be integrated over the spectrum to obtain the relative total quantity.

When participating medium is considered, we are interested in the amount of net radiative energy that is deposited into a control volume. An energy balance analysis over a infinitesimal volume dV , shows that this deposited-energy can be expressed as

$$-\nabla \cdot \mathbf{q}_{rad} dV, \quad (5.42)$$

that is, the divergence of heat flux vector (cf. Modest [48], section 10.9). Using equation (5.41) and the radiative transfer equation (5.35), an explicit formula is derived

$$\nabla \cdot \mathbf{q}_{rad} = \kappa_\nu (4\pi I_{b,\nu} - G_\nu), \quad (5.43)$$

where G_ν is the incident radiation defined in formula (5.40).

5.3.5 Contribution to temperature equation

The temperature field, in a generic system, have to be determined taking into account all the three heat transfer mechanisms: convection, conduction and thermal radiation. The contributions of convection and conduction were widely studied, we can referred to Incropera *et al.* [32] for a discussion. We focus our attention on the effects of thermal radiation, that are:

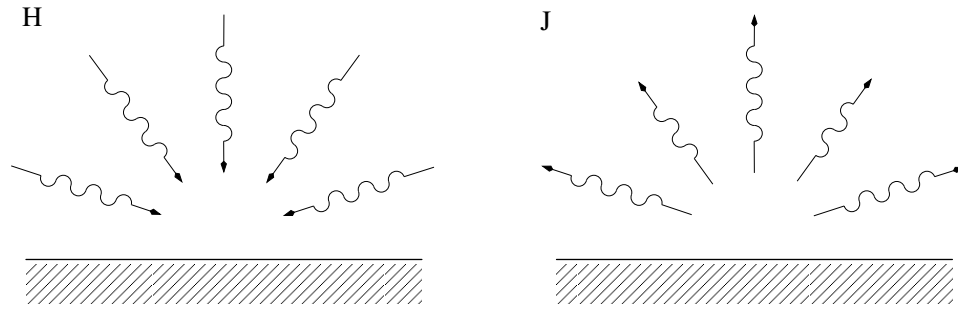


Figure 5.14: Thermal radiation balance onto a opaque surface. Left, incoming radiation; right, emitting radiation.

- ▶ the appearing of radiative heat flux on the enclosure boundaries;
- ▶ the alteration of internal temperature by means of radiation;
- ▶ the adding of radiation pressure tensor to the fluid dynamics pressure tensor.

While the first and the second contributions has an essential role, the third is negligible in most applications.

The conduction-convection-radiation temperature equation for incompressible fluid reads

$$\frac{\partial T}{\partial t} + \underbrace{\mathbf{u} \cdot \nabla T}_{\text{convection}} = \underbrace{\alpha \nabla^2 T}_{\text{conduction}} - \underbrace{\frac{1}{\rho C_p} \nabla \cdot \mathbf{q}_{rad}}_{\text{radiation}} + S, \quad (5.44)$$

where S is a source or sink of temperature within the medium, while \mathbf{u} is the velocity fluid field, α is the thermal diffusivity, ρ is the density and C_p is the heat capacity of medium.

5.3.6 Radiative heat transfer on solid boundary

The estimation of radiative contribution into the solid temperature equation is, in general, an extremely complex issue. All the effects of bodies interaction, describe in section 5.1.3, needs to be taken into account. However, a balance of heat losses and heat gains can be achieved under some restrictive, but realistic, hypotheses.

Consider a solid surface sketched in Figure 5.14. The net inward heat flux Q_w is given by the difference of total incoming radiation from the surrounding (the irradiation H) and the total heat flux leaving the surface (the radiosity J). Radiosity is the sum of reflected and emitted radiation. If the local thermal equilibrium is established and the solid surfaces are *opaque*,

radiative grey and *radiative diffuse*, then the energy balance gives:

$$Q_w = q_{out} - q_{in} \quad (5.45)$$

$$= (q_{emitted} - q_{reflected}) - q_{radiated} \quad (5.46)$$

$$= J_w - H_w, \quad (5.47)$$

after the previous definition of radiosity and irradiation. Moreover, we can simply express the total heat flux as the difference between emissive power and absorbed energy:

$$Q_w = \epsilon e_b - \alpha H_w. \quad (5.48)$$

In order to eliminate the irradiation, we can use both the previous expressions of Q_w and compute

$$Q_w - \alpha Q_w = (\epsilon e_b - \alpha H_w) - \alpha(J_w - H_w) \quad (5.49)$$

$$= \epsilon e_b - \alpha J_w. \quad (5.50)$$

Finally, since the surface is opaque and behaves as a grey body:

$$\epsilon = \alpha = 1 - \rho, \quad (5.51)$$

because transmissivity is null, and relation (5.6) holds. Thus,

$$Q_w = \frac{\epsilon}{1 - \epsilon} (e_b - J_w) \quad (5.52)$$

is the (scalar) radiative heat flux contribution onto the solid surface.

Radiosity is still an unknown of the equation. For a diffuse surface, it is simply proportional to the radiative intensity,

$$I(\mathbf{r}, \hat{\mathbf{s}}) = J(\mathbf{r})/\pi, \quad (5.53)$$

meaning that an observer is unable to distinguish emitted and reflected radiation on the basis of the directional behaviour. In general, it can be estimated in the framework of the thermal radiation model used; as it is shown in section 6.2.3 for the first order spherical approximation model.

The wall radiative flux is of particular importance where the conjugate heat transfer, between the fluid and the solid body, is taken into account. For a discussion on this topic, we refer to Howell *et al.* [28]; for the mathematical derivation of Q_w , we refer to Modest [48], chapters 4 and 5.

Chapter 6

Spherical harmonics approximation

Contents

6.1	Review of approximation methods	132
6.1.1	Discrete ordinates method	133
6.1.2	Spherical approximation method	134
6.1.3	Monte Carlo method	136
6.2	Spherical harmonics approximation	137
6.2.1	First order approximation: P_1 -model	140
6.2.2	Boundary conditions	142
6.2.3	Surface radiative heat flux	143
6.3	Modified differential approximation	144

This chapter is mainly devoted to outline the mathematical framework in which the P_1 -model is derived. The main reference is the textbook of Modest [48], where a detailed description of spherical harmonics approximation technique for radiative heat transfer problems is reported.

In the first part, a short overview on the most widely used approaches to the radiative problem is presented. The main idea behind the different methods is illustrated, along with a balance of the main advantages and disadvantages.

Later, the series expansion in terms of spherical harmonics function is described, and the fundamental steps to derive the P_1 -equation are traced. The approximated governing equation is then provided with suitable boundary condition (for opaque boundaries). An expression for the radiative boundary heat flux is also given.

In the end, an improvement of the P_1 -model is sketched.

6.1 Review of approximation methods

In spite of the mathematical complexity that is inherent in the radiative heat transfer equation, various radiative models have been developed in the last decades. The first attempts in this direction were done for neutron transport in astrophysics. Later, the pioneering studies on neutron have been adapted to radiation problem.

The main difficulties arising in the numerical solution of RHT equation are related to:

- ▶ *Geometry*: several models have been developed for one-dimensional or idealised cases, taking advantages of the simplification introduced by the elementary geometry. A realistic three-dimensional geometry requires general solution methods that cannot employ such simplifications;
- ▶ *Scattering*: a general mathematical model that accounts for anisotropic scattering can be extremely complex, while neglecting scattering leads to an oversimplification. A middle way is to adopt an isotropic (or linear anisotropic) scattering model;
- ▶ *Spectrum*: thermal radiation can exhibit strong non-grey effects. An accurate resolution has to deal with the spectral effects, however the majority of works adopts the grey hypothesis.

Nevertheless, we should take into account that the radiation properties (emissivity, emission coefficient, scattering coefficient, etc...) can depend on temperature and that, when radiation is combined with convection and/or conduction, a strong coupling arises between these heat transfer mechanisms.

A number of approximation methods, valid only under particular hypotheses, has been proposed and studied during the years: some of these are valid just in one or two dimensional cases and they cannot be easily generalised; the remaining ones been designed for specific geometry, like plane-parallel case; others else neglect the presence of participating gas medium and deal with the surfaces radiation only.

However, some approaches appear to be more general and adaptable to a wide range of applications. A complete review of such methods is beyond the scope of this thesis. We refer to Viskanta and Mengüç [81] and Viskanta [80] for a detailed overview. Additional information can be found in the textbooks of Viskanta [79], Modest [48], Siegel and Howell [66].

The most popular methods for numerical solution of radiative heat transfer today appear to be one, or a variation, of the following: view factor method, discrete ordinates method (DOM), spherical approximation (P_N) method, Monte Carlo method (MCM). The first just computes the radiation

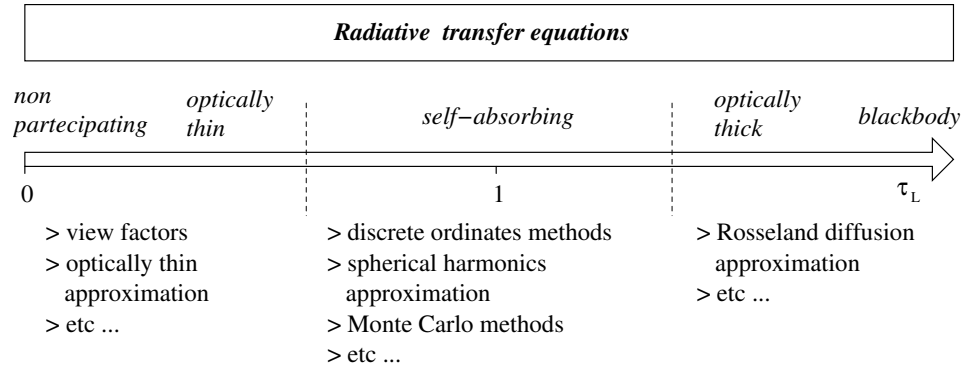


Figure 6.1: Overview of the main solution methods for radiative transfer equation.

exchange between surfaces and does not account for participating media. The second and the third are deterministic methods that transform the radiative integro-differential equation in a set of partial differential equations. The fourth uses a statistical approach and simulates a population of photons in order to predict the diffusion of radiation through the system.

The last three methods are briefly discussed in the following sections.

6.1.1 Discrete ordinates method

The general DOM approach is to discretise the directional intensity along a finite number of directions, and to approximate the integral term in radiative heat transfer equation by numerical quadrature.

Generally speaking, numerical quadrature transforms an integral into a finite sum of elements. If \hat{s}_i is a set of n discrete directions of propagation for radiation, then the integral (over all directions) of a generic quantity ϕ is approximated by

$$\oint \phi(\hat{s}) d\Omega = \sum_{i=0}^n w_i \phi(\hat{s}_i), \quad (6.1)$$

where w_i are weights associated to direction \hat{s}_i .

Applying the relation (6.1) to the integral term of governing equation (5.35), we obtain the following:

$$\frac{dI}{ds}(\hat{s}_i) = \kappa I_b(\hat{s}_i) - \beta I(\hat{s}_i) + \frac{\sigma_s}{4\pi} \sum_{j=0}^n w_j I(\hat{s}_j) \Phi(\hat{s}_j, \hat{s}_i). \quad (6.2)$$

This expression, provided with suitable boundary conditions, leads to a set of n coupled, linear, first-order partial differential equations in the unknown $I_i = I(\hat{s}_i)$.

Depending on the angular discretisation used, different models can be derived. The simplest and most accurate of such models is the so-called S_N

model, where the subscript N is related to the number of discrete directions used.

The DOM can be implemented for complex geometry and is able to simulate non-linear anisotropic scattering. It is widely used, since it can lead to accurate results.

However, the method cannot be easily extended on non-Cartesian mesh, its accuracy strongly depends on the quadrature scheme, a correct resolution requires a fine angular and spatial discretisation (thus, it is highly computational demanding). Indeed, this method is generally computationally expensive and it can considerably increase the overall computational effort for fine mesh simulations.

The main serious disadvantage is that the numerical quadrature does not ensure the conservation of radiant energy. Some other drawbacks of the method are the *false scattering* and the *ray effects*. The former is due to a coarse angular discretisation of the integral term and adulterates the radiative intensity distribution. The later is the result of directional discretisation error. For example, let us consider a single source radiating into the vacuum. If the directional discretisation is not fine enough, the numerical solution will not be a smooth radiative field outgoing from the source, but a set of rays emanating from the source. These rays can cause the *hot spots* (localised overestimation of heat transfer by radiation) that can wrongly influence the overall dynamics of simulation, especially if radiation is coupled with convection.

In order to overcome some of the limitations above-mentioned, the *finite volume methods* has been developed following the same philosophy. The spatial domain is decomposed in an unstructured mesh and the angular space at any location is discretised into non-overlapping control angles. It results in a better integration with the usual fluid solver and can be used in complex meshes. Moreover, the energy conservation over the discrete solid angles can be enforced.

6.1.2 Spherical approximation method

The idea behind the P_N method is to use the mathematical technique of series expansion, in terms of suitable functions, to deal with the radiation directional dependency and to simplify the integral terms in the governing equation. These suitable functions are the spherical harmonics $Y_\ell^m(\hat{\mathbf{s}})$, that will be described in section 6.2.

The general strategy is to expand the radiative intensity and the phase function in series of spherical harmonics, and to use their orthogonality properties over a sphere, to analytically solve the scattering integral term.

A short description of the procedure to derive the P_N -equation follows.

The expansion of radiation intensity reads

$$I(\hat{\mathbf{s}}) = \sum_{\ell=0}^{\infty} \sum_{m=-\ell}^{\ell} I_{\ell}^m Y_{\ell}^m(\hat{\mathbf{s}}), \quad (6.3)$$

where the coefficients I_{ℓ}^m are known. Expression (6.3) is substituted into the RHT equation, after also expanding the phase function in a similar way. The resulting equation can be multiplied by spherical harmonics, followed by integration over all directions. Exploiting the orthogonality properties of $Y_{\ell}^m(\hat{\mathbf{s}})$, the directional integrals are solved, and the radiation heat transfer equation (5.35) is transformed in a set of infinitely many coupled partial differential equations for the unknown I_{ℓ}^m .

Up to this point, no approximation has been done yet. The governing equation is just rewritten in a different form. In order to find a solution, the series is truncated until a finite order $\ell = N$. The final result is a set of $(1 + N)^2$ coupled partial differential equations. This method is called P_N -approximation because the spherical harmonics are defined from the Legendre polynomials that are notated as P_n . The subscript N indicates the order of series truncation.

The main advantage of spherical approximation method is to convert the directional radiative equation in relatively simple partial differential equation. The numerical implementation is not computationally expensive and, conversely to the DOM, the conservation of radiant energy is ensured.

Some drawbacks of the method are that it cannot deal with non-linear anisotropic scattering (because of the orthogonality of the spherical harmonics), and it is accurate for near-isotropic intensity distributions only. Moreover, as the discrete ordinates method suffers of a ray affects, the spherical approximation method can be affected by a *wave effects*. Some radiative waves can be negative, leading to an unphysical negative amount of energy in some points (see Modest [48], Figure 16-11 p. 532).

The low-order approximations could be inaccurate depending on the radiative characteristic of the medium (*e.g.* optical thickness). The accuracy increases slowly for higher order approximation while the mathematical complexity increases rapidly. It is known that the odd approximations are more accurate than the even. The most popular are the P_1 and the P_3 approximations. In our work we focus on the first-order approximation.

The mathematical description of the P_1 -model is discussed in following section 6.2, while its numerical implementation and validation are documented in chapter 7.

Regarding the P_1 -model, Modest [48] points out that it is suitable for simulate optical thin medium, but can fail in the limit of optical thick medium. In the last decades it was found that the method loses accuracy for optical thin case, but this is not the case in general issue: inaccurate

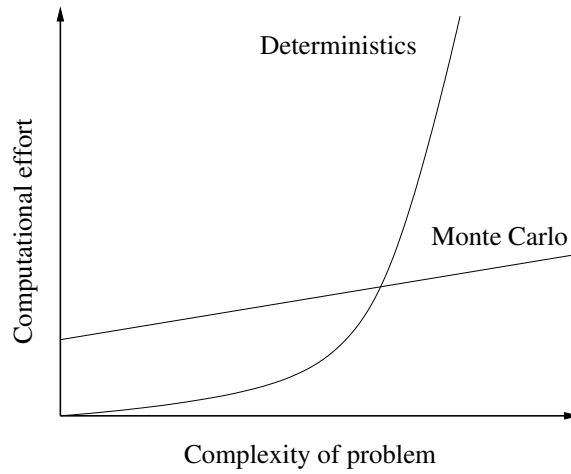


Figure 6.2: Sketch of the performance of Monte Carlo method (statistical) against conventional methods (deterministic).

results can be obtained when the optically thin medium acts as a radiation barrier between hot and cold surfaces, for example in cases of *collimated irradiation*¹.

A number of variations and improvements on the P_N methods has been proposed. Among the others, we turn our attention to the *modified differential approximation* model, that attempts to overcome the inaccuracy in strong anisotropic cases. A short overview of this model is given in section 6.3.

6.1.3 Monte Carlo method

Even if nowadays it is common to refer to the *Monte Carlo method*, this name is probably meaningless. Indeed, it does not represent a specific method, but a general approach that is based on statistical theory.

A general definition of the Monte Carlo approach is elusive, however Hermann Kahn² gives this description that includes the main ideas behind this technique:

The expected score of a player in any reasonable game of chance, however complicated, can in principle be estimated by averaging the results of a large number of plays of the game. Such estimation can be rendered more efficient by various devices which

¹ We have a collimated irradiation when the radiative “energy incident from a single distant source results in (near-) parallel rays from a unique direction \hat{s}_i , such as irradiation from the sun or from a laser” (Modest [48], p. 66).

²This citation is reported by Siegel and Howell [66] and it is contained in HERMANN KANN, *Applications of Monte Carlo*, Rep. No. RM-1237-AEC, Rand Corporation (1956).

replace the game with another known or have the same expected score. The new game may lead to a more efficient estimate by being less erratic, that is, having a score of lower variance, or by being cheaper to play with the equipment on hand. There are obviously many problems about probability that can be viewed as problems of calculating the expected score of a game. Still more, there are problems that do not concern probability but are none the less equivalent for some purpose to the calculation of an expected score. The Monte Carlo method refers simply to the exploitation of these remarks.

It is hard to give a simple and synthetic outline of the MCM for radiative heat transfer problem, as it is done for the deterministic methods (such as DOM and P_N -models). Generally speaking, the first step is to set up a suitable game (or model) that reproduces the behaviour of the radiative parameters and variables. At each time step the game is played many times and the results are collected. The thermal radiation variables are then determined averaging the samples obtained.

The main advantage of the Monte Carlo approach is that it is able to deal with very complex problems, requiring a relative low computational effort. Figure 6.2 qualitatively shows that for problems beyond a certain complexities the Monte Carlo approach is preferable to the classical deterministic methods.

The main disadvantages are that, since it is a stochastic method, it is affected by noise in the solution and it is not possible to ascribe a hundred percent confidence in the values obtained. When the radiation is coupled to other processes (such as convection and conduction), this noise can lead to instability issue. Moreover, the Monte Carlo methods can be difficult to integrate in the classical computational fluid dynamics solver, based on a deterministic approach.

Some attempts have been done to apply the statistical methods to thermal radiation. Among the others, a popular approach is the *ray-tracing* method. This method directly simulates the underlying physical processes (emission, absorption, scattering and reflection), from the emission to the absorption point of the ray. Unfortunately, it is known to be inefficient for optically thin medium and for reflective walls.

6.2 Spherical harmonics approximation

The technique of series expansion is a powerful tool that allows to solve complex problems with an arbitrary degree of accuracy. For example, the expansion in Fourier series is widely used in signal theory. It could be interpreted as the series expansion of a function, defined over a unitary

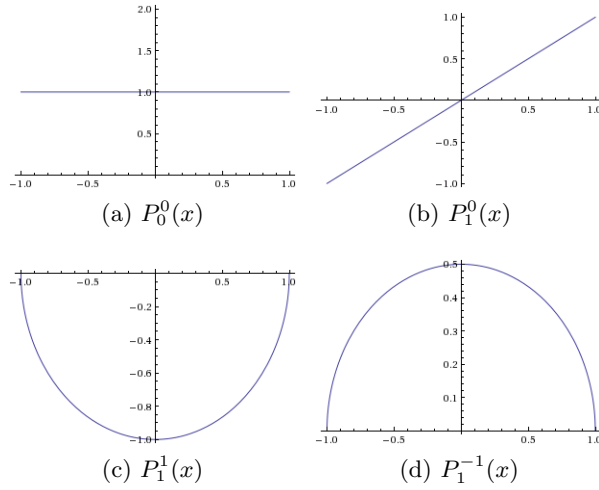


Figure 6.3: Some of the associated Legendre polynomials, used for the first order approximation.

circumference, on the eigenfunction of the second derivative operator on the circumference.

The radiative intensity $I(\mathbf{r}, \hat{\mathbf{s}})$ is essentially a scalar function on the surface of a unitary sphere surrounding the point \mathbf{r} . Thus, in analogy with the one-dimensional case, it can be expanded in series of eigenfunction of second derivative operator over the sphere Y_ℓ^m :

$$I(\mathbf{r}, \hat{\mathbf{s}}) = \sum_{\ell=0}^{\infty} \sum_{m=-\ell}^{\ell} I_\ell^m(\mathbf{r}) Y_\ell^m(\hat{\mathbf{s}}), \quad (6.4)$$

where $\hat{\mathbf{s}}$ is the versor of spherical coordinate systems, defined by equation (5.11), and the $Y_\ell^m(\hat{\mathbf{s}})$ are called the (non-normalised) *real spherical harmonics*. They can be defined in spherical coordinates by

$$Y_\ell^m(\theta, \psi) = \begin{cases} \cos(m\psi) P_\ell^m(\cos \theta) & m \geq 0, \\ \sin(|m|\psi) P_\ell^m(\cos \theta) & m < 0, \end{cases} \quad (6.5)$$

where the $P_\ell^m(x)$ are the so-called *associated Legendre polynomials* of order ℓ . A short presentation of associated Legendre polynomials and real spherical harmonics follows.

Associate Legendre polynomials

These functions are a generalisation of the *Legendre polynomials*, and constitute a complete orthonormal system for the power functions $1, x, x^2, \dots$ in the interval $x \in [-1, 1]$.

The associated Legendre polynomials, of order ℓ and degree m , are defined³ in the interval $x \in [-1, 1]$ by means of:

$$P_\ell^m(x) = (-1)^m \frac{(1-x^2)^{m/2}}{2^\ell \ell!} \frac{d^{m+\ell}}{dx^{m+\ell}} (x^2-1)^\ell \quad m = 0, \dots, \ell \quad (6.6)$$

while for negative values of the degree m , the following formula holds:

$$P_\ell^{-m}(x) = (-1)^m \frac{(\ell-m)!}{(\ell+m)!} P_\ell^m(x) \quad m = 0, \dots, \ell \quad (6.7)$$

after Arfken and Weber [6], formula (12.81.a). A graphical representation of some of these functions, used in the following to derive the approximated radiative transfer equation, is given in Figure 6.3.

This set of polynomials is orthogonal with respect to the order, in the sense that

$$\int_{-1}^1 P_\ell^m(x) P_{\ell'}^m(x) dx = \frac{2}{2\ell+1} \frac{(\ell+m)!}{(\ell-m)!} \delta_{\ell\ell'}, \quad (6.8)$$

where $\delta_{\ell\ell'}$ is the Kronecker symbol.

We point out that there is an incongruity between the above reported definition of P_ℓ^m and Modest [48] page 502, where it is reported: $P_1^1(\cos \theta) = P_1^{-1}(\cos \theta) = -\sin \theta$. According to equation 6.6 and the analogous equation (8.6.17) in Abramowitz and Stegun [4], the correct values have to be $P_1^1 = -\sin \theta$, and $P_1^{-1} = 1/2 \sin \theta$. Anyway, this discrepancy does not affect the derivation of P_1 -model by Modest [48], since the explicit values of associate Legendre polynomials are not directly used.

Spherical harmonics

The spherical harmonics are solutions of the Laplace equation in spherical coordinates. The non-normalised real expression of these functions is given by equation (6.5), and from the associated Legendre polynomials they inherit the orthogonality properties on the sphere surface:

$$\begin{aligned} \oint Y_\ell^m(\hat{\mathbf{s}}) Y_{\ell'}^{m'}(\hat{\mathbf{s}}) d\Omega &= \int_0^{2\pi} \int_0^\pi Y_\ell^m(\theta, \psi) Y_{\ell'}^{m'}(\theta, \psi) \sin \theta d\theta d\psi \quad (6.9) \\ &= \frac{4\pi}{2\ell+1} \frac{(\ell+m)!}{(\ell-m)!} \delta_{\ell\ell'} \delta_{mm'}. \quad (6.10) \end{aligned}$$

Notice that in mathematics, it is customary to normalise the harmonics functions in order to remove the constant in the right-hand side of equation (6.9).

³ They are uniquely defined to within a factor ± 1 , then there are two sign conventions for Legendre polynomials and also associated Legendre polynomials. We adopt the definition of Abramowitz and Stegun [4] and Courant and Hilbert [15], that included the alternating sign factor.

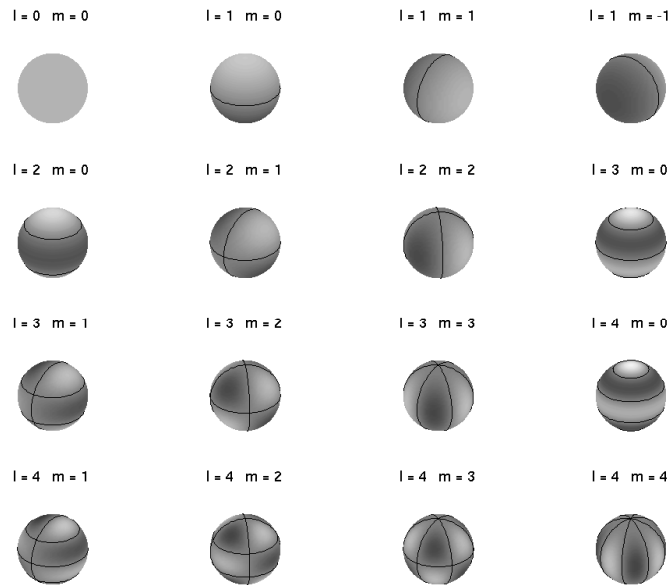


Figure 6.4: Representation of nodal meridian and parallel for the first spherical harmonics $Y_\ell^m(\theta, \psi)$, by courtesy of Dr. Luigi Barletti [9], lecture notes. Functions with negative m can be recovered from the corresponding ones with positive m , by rotation of an angle $\psi_m = \pi/2m$ around the polar axis.

Figure 6.4 shows a representation of the first spherical harmonics over the sphere surface. The black lines represent the nodal circles, *i.e.* the lines over which the functions are zero.

The mathematical analysis demonstrates that each Y_ℓ^m has $2m$ nodal meridians (derived from the zeros of $\cos(m\psi)$ and $\sin(|m|\psi)$) and $\ell - m$ nodal parallels (derived from the zeros of the associated Legendre functions). These nodal parallels and meridians divide the sphere surface in $(\max\{2m, 1\}) \times (\ell - m - 1)$ zones of alternated sign.

6.2.1 First order approximation: P_1 -model

In this section the equation of radiative heat transfer is approximated with a spherical harmonics expansion, truncated at the first order. This procedure is also known as P_1 -approximation.

For the sake of simplicity, we are going to assume the grey medium hypothesis (cf. section 5.3.2), implying that the radiative quantities are constant over the spectrum. Anyway, the procedure and the resulting equations are valid also for spectral variables.

Non-dimensional governing equation

The radiative heat transfer equation (5.35) is made non-dimensional in space by means of total optical distance τ , obtained from equation (5.29) by integration over the spectrum. Applying the relation:

$$d\tau = \beta ds \quad (6.11)$$

and using the total single scattering albedo coefficient ω , defined in equation (5.36), finally rearranging the terms, we obtain the non-dimensional radiative heat transfer equation for a grey medium:

$$\hat{\mathbf{s}} \cdot \nabla_{\tau} I + I = (1 - \omega) I_b + \frac{\omega}{4\pi} \oint I(\hat{\mathbf{s}}') \Phi(\hat{\mathbf{s}}, \hat{\mathbf{s}}') d\Omega', \quad (6.12)$$

where the subscript τ indicates that gradient is computed with the non-dimensional space variable.

This is an integral-differential equation in five independent variables: three space coordinates and two directional coordinates. The series expansion procedure transforms this equation into a set of partial differential equations, taking advantage of the orthonormal properties on the sphere of spherical harmonic functions.

The derivation procedure for the P_1 -model equations follows the one already discussed for a general P_N -model. However, for the sake of clarity, it is here sketched again: first the radiative intensity I is expanded in spherical harmonics, as in equation (6.4), together with the scattering phase function. Second, these series representations are substituted in radiative equation (6.12), that is subsequently multiplied by Y_{ℓ}^m . Third, the obtained equation is integrated over all directions.

Applying the orthogonality property (6.9), an infinite number of coupled partial differential equation for the unknown $I_{\ell}^m(\mathbf{r})$ are obtained. Any approximation is still done. In order to simplify the equations, in the next section the series expansion is truncated after a few terms.

Equation of P_1 -approximation

The first order approximation is obtained by truncation of series expansion beyond the order $\ell = 1$, that implies the following expression of the radiative intensity

$$I(\mathbf{r}, \hat{\mathbf{s}}) = I_0^0 Y_0^0 + I_1^{-1} Y_1^{-1} + I_1^1 Y_1^1 + I_1^0 Y_1^0, \quad (6.13)$$

where the $I_{\ell}^m(\mathbf{r})$ coefficients are depending on position and spherical harmonics depend only of direction $Y_{\ell}^m(\theta, \psi)$. The latter can be computed using the formulae (6.5), (6.6) and (6.7). The result follows:

$$I(\mathbf{r}, \hat{\mathbf{s}}) = I_0^0 + \frac{1}{2} I_1^{-1} \sin \theta \cos \psi - I_1^1 \sin \theta \sin \psi + I_1^0 \cos \theta \quad (6.14)$$

$$= a(\mathbf{r}) + \mathbf{b}(\mathbf{r}) \cdot \hat{\mathbf{s}} \quad (6.15)$$

where in the second line the representation of versor $\hat{\mathbf{s}}$ in spherical coordinates (5.11) is employed. The definitions of incident radiation function (5.40) and the hear flux (5.41) allow to rewrite the radiative intensity as:

$$I(\mathbf{r}, \hat{\mathbf{s}}) = \frac{1}{4\pi} [G(\mathbf{r}) + 3\mathbf{q}(\mathbf{r}) \cdot \hat{\mathbf{s}}]. \quad (6.16)$$

This result suggests that the zero-term of series expansion I_0^0 is proportional to the incident radiation, while the first order elements are related to the components of heat flux.

The last unknown to be specified is the scattering phase function. For the first order approximation, a linear anisotropic (or an isotropic) scattering is allowed only: even if a non-linear anisotropic function is used, the mathematical derivation leads in any case to the same final equation as for linear anisotropic case (cf. Modest [48], chapter 16.5). The linear anisotropic scattering phase function (5.34), given by

$$\Phi(\hat{\mathbf{s}}, \hat{\mathbf{s}}') = 1 + A\hat{\mathbf{s}} \cdot \hat{\mathbf{s}}', \quad (6.17)$$

is adopted.

Finally, substituting the approximated intensity (6.16) in the radiative transfer equation (6.12), we obtain:

$$\frac{1}{4\pi} \nabla_{\tau} \cdot [\hat{\mathbf{s}}(G + 3\mathbf{q} \cdot \hat{\mathbf{s}})] + \frac{1}{4\pi} (G + 3\mathbf{q} \cdot \hat{\mathbf{s}}) = (1 - \omega)I_b + \frac{\omega}{4\pi} (G + A\mathbf{q} \cdot \hat{\mathbf{s}}). \quad (6.18)$$

Multiplying by Y_{ℓ}^m as $\ell = 0, 1$ and integrating over a sphere, we can find the four equations constituting the P_1 -approximation of radiative heat transfer equation for radiative heat transfer in participating media.

These equations can be expressed as a set of first-order, coupled partial differential equations

$$\begin{cases} \nabla \cdot \mathbf{q} = \kappa(4\pi I_b - G), \\ \nabla G = -(3\kappa + 3\sigma_s - A\sigma_s)\mathbf{q}, \end{cases} \quad (6.19)$$

where the spatial variable is now dimensional. Note that the equations for isotropic scattering can be derived from the previous one, by imposing a zero anisotropic coefficient $A = 0$.

The system (6.19) can be solved for the incident radiation, leading to the following single elliptic second-order partial differential equation:

$$\nabla^2 G(\mathbf{r}) = \kappa(3\kappa + 3\sigma_s - \sigma_s A)(G(\mathbf{r}) - 4\pi I_b). \quad (6.20)$$

6.2.2 Boundary conditions

The determination of a suitable boundary condition for the spherical harmonics approximation is not a simple task. Usually, the solid boundaries are

assumed to be opaque body, *i.e.* all radiation that passes through the boundaries is internally absorbed (cf. section 5.1.3). In this case, the equation of radiative heat transfer (5.35) requires the normal boundaries intensity

$$I(\mathbf{r}_w, \hat{\mathbf{s}}) = I_w(\hat{\mathbf{s}}) \quad \text{for } \hat{\mathbf{n}} \cdot \hat{\mathbf{s}} > 0, \quad (6.21)$$

that is the intensity leaving the surface. The term I_w can be a very complex function depending on the radiative characteristics of the surface. Moreover, the boundary condition (6.21) must be translated into the formalism of spherical expansion.

In practical applications, three types of surfaces with different properties can be considered:

- ▶ surface diffusely emitting and reflecting: the exiting intensity is independent of direction;
- ▶ surface diffusely emitting and specular reflecting: the exiting intensity consists of diffuse emission and a fraction of diffuse reflection, plus a contribution due to specular reflection component;
- ▶ arbitrary properties: the emission is governed by directional emissivity and bidirectional reflection.

The simplest case of diffusely emitting and reflecting surface is here considered. For industrial applications at relative low temperatures (target of this work) this choice is justified. Indeed, such applications generally leads to study the radiation problem in close domain, where the spectral and directional dependence of variables are attenuated.

The P_1 -equation for incident radiation (6.20) can be provided by the so-called *Marshak's boundary condition*, derived from equation (6.21), that reads:

$$\hat{\mathbf{n}} \cdot \nabla G(\mathbf{r}_w) = \frac{\epsilon}{2 - \epsilon} \frac{3\kappa + 3\sigma_s - A\sigma_s}{2} (G(\mathbf{r}_w) - 4\pi I_b), \quad (6.22)$$

where ϵ is the surface emissivity (5.5). The derivation of this relation is omitted, for more details we refer to Modest [48].

6.2.3 Surface radiative heat flux

An expression of radiative heat flux onto the solid surfaces is now derived, according to the mathematical model of the P_1 -approximation.

The general expression of the surface radiative flux, presented in section 5.3.6, reads:

$$Q_w = \mathbf{q}_w \cdot \hat{\mathbf{n}} = \frac{\epsilon}{1 - \epsilon} (\pi I_b - J_w), \quad (6.23)$$

where the blackbody intensity $\pi I_b = e_b$ is given by (5.23), and the surface radiosity $J_w = J(\mathbf{r}_w)$ is the unknown to be determined. The spherical harmonics approximation is, unlike the other radiative model, a mathematical

approximation of the exact equations. Hence, in order to ensure the energy conservation, a suitable expression for the radiosity has to be derived using a series expansion in spherical harmonics. Following the derivation of the Marshak's boundary condition (cf. Modest [48] section 16.5), if the surface is opaque, radiative grey and diffuse, then the surface radiosity reads:

$$4J_w = G + 2Q_w. \quad (6.24)$$

Combining equation (6.23) and (6.24), the surface radiative flux for P_1 -approximation is found to be:

$$Q_w = -\frac{1}{2} \left(\frac{\epsilon}{2 - \epsilon} \right) [G - 4\pi I_b]. \quad (6.25)$$

Equation (6.25) presents some similarities with equation (6.22) for boundary condition.

6.3 Modified differential approximation

In chapter 7, the prediction capability of the model is investigated on some benchmark cases. Generally speaking, it is known that the P_1 -model may become inaccurate in cases where radiation displays a strong direction behaviour.

The radiative directional intensity $I(\hat{\mathbf{s}})$ inside a participating medium is due to two main sources: radiation originated within the medium (emitted or scattered), radiation originated from a surface (emitted or reflected). The former is usually varying smoothly with directions, since emission and scattering result in an isotropic radiative source. An exception is the case in which the medium is characterised by a high anisotropic scattering. The latter, instead, can display an irregular directional behaviour. In particular, for optical thin cases the medium is not able to homogenise radiation, leading to a rapid change of radiative intensity over the incoming directions. Indeed, the model can be very inaccurate for optically thin media.

Many efforts have been done to overcome this limit. Here the *modified differential approximation* is presented, as it has been formulated by Modest [48] for the P_1 -model. The main idea behind this modified method, is to compute separately the two aforementioned contributions on radiative intensity. The function $I(\mathbf{r}, \hat{\mathbf{s}})$ is formally divided in two parts:

$$I(\mathbf{r}, \hat{\mathbf{s}}) = I_w(\mathbf{r}, \hat{\mathbf{s}}) + I_m(\mathbf{r}, \hat{\mathbf{s}}), \quad (6.26)$$

where the term I_w represents the radiation originated by the enclosure surfaces, while I_m is the radiative source within the medium. The two terms are not completely independent: the surface radiation takes into account the

attenuation mechanisms due to absorption and scattering by the medium. This effect leads to the following formulation:

$$I_w(\mathbf{r}, \hat{\mathbf{s}}) = \frac{1}{\pi} J_w e^{-\tau_s}, \quad (6.27)$$

where τ_s is the optical thickness and J_w is the surface radiosity (the total outgoing radiation from surface).

Without going into the details, the surface radiosity can be predicted using a method for non-participating media, for example the view factor method. Instead, the contribution from within the media can be computed with the spherical approximation method, and using the Marshak's condition for cold surfaces (*i.e.* imposing $\epsilon = 0$). Finally, the two contributions can be added to obtain the total thermal radiation.

This method reduces to the view factors solution for optical thin limit (where the contribution from the medium vanishes), and to the unmodified spherical approximation solution for optical thick limit (where the surfaces contribution is overcome by the participating medium).

Chapter 7

Numerical implementation and validation

The study on thermal radiation and surface radiative heat transfer, presented in this chapter, will be extended and submitted in a journal for future publishing.

Contents

7.1	Radiative model summary	148
7.2	Implementation	153
7.2.1	Radiative heat transfer equations	153
7.2.2	Radiative heat source into the medium	154
7.2.3	Surface radiative heat transfer	158
7.3	Validation	160
7.3.1	Numerical model validation	162
7.3.2	Pure radiative heat transfer	164
7.3.3	Combined conduction and radiation	169
7.3.4	Combined conduction, convection and radiation	170
7.3.5	Surface radiative heat transfer	172
7.4	Conclusions	174
7.5	Appendix: Marshak's boundary condition	175

This chapter has been developed in a scientific cooperation with Professor Håkan Nilsson from Chalmers University of Technology (Gothenburg, Sweden), during a three-months period of research exchange.

The implementation of the radiative model for participating media and

boundary heat exchange is now reported, together with an accurate validation of the numerical code.

First, the P_1 -approximation for radiative heat transfer problems is summarised. For the sake of clarity, the complete set of governing equations for the fluid dynamics, temperature and radiation is also presented.

Subsequently, the numerical implementation of the mathematical model is documented. The implementation is done in the framework of OpenFOAM toolbox, which at the highest level mimics the mathematical syntax; thus the code results straightforward to read. Therefore parts of the code are directly reported and commented. Possible discrepancies between the theoretical formulae and the numerical equations are discussed.

Eventually the new developed solver is validated against several benchmark cases. Comparisons with the results of other radiative models permit an investigation on the limit and the prediction capability of P_1 -model adopted.

7.1 Radiative model summary

The P_1 -approximation for radiative heat transfer has already been described in chapter 6. Before presenting the numerical implementation of the mathematical model, the complete set of governing equations is here summarised.

In such equations, the unknown is the total incident radiation function (5.40), that reads:

$$G(\mathbf{r}) = \oint I(\mathbf{r}, \hat{\mathbf{s}}) d\Omega, \quad (7.1)$$

i.e. the integral over all directions of radiation, of total radiative intensity $I(\mathbf{r}, \hat{\mathbf{s}})$, defined by formula (5.12).

The radiative model has to consider several phenomena: interaction with participating medium, influence on the medium temperature distribution, thermal interaction with the solid boundaries.

The physical hypotheses behind the radiative model are here briefly reminded: the medium is considered grey (no wavelength dependency of the emission, absorption and scattering coefficients) and diffusive (the coefficients do not depend on the direction of propagation); while the enclosure surfaces are considered opaque (the rays, that penetrate into the body, are internally absorbed) and grey diffusive (surface reflection are not taken into account).

A description of the mathematical model for the three above-mentioned items follows.

Radiative heat transfer

The governing equations of P_1 -model for radiative heat transfer in participating media, read:

$$\begin{cases} \nabla^2 G(\mathbf{r}) &= \kappa(3\kappa + 3\sigma_s - \sigma_s A)[G(\mathbf{r}) - 4\sigma T^4(\mathbf{r})] \\ \hat{\mathbf{n}} \cdot \nabla G(\mathbf{r}_w) &= \frac{\epsilon}{2 - \epsilon} \frac{3\kappa + 3\sigma_s - \sigma_s A}{2} [G(\mathbf{r}_w) - 4\sigma T^4(\mathbf{r}_w)] \end{cases} \quad (7.2)$$

where T is the absolute temperature; \mathbf{r} and \mathbf{r}_w represent a point, respectively, in the enclosure interior and onto the enclosure boundaries; $\hat{\mathbf{n}}$ is the versor normal to the enclosure boundary surfaces. The second equation is also known as Marshak's boundary condition (6.22) for P_1 -approximation. The constant coefficients in (7.2) are:

κ - the total, linear absorption/emission coefficient, cf. (5.26);

σ_s - the total scattering coefficient, cf. (5.16);

A - the anisotropic scattering factor, cf. (5.34);

σ - the Stefan-Boltzmann constant, cf. (5.24);

ϵ - the solid surface emissivity, cf. (5.5);

and have been described in previous chapters 5 and 6.

For comparison purpose with literature results, the radiative heat flux (5.14) onto the enclosure surface is computed. In the framework of the P_1 -approximation, it reads:

$$Q_{rad} = \mathbf{q}_{rad} \cdot \hat{\mathbf{n}} \quad (7.3)$$

$$= -\frac{1}{3\kappa + 3\sigma_s - A\sigma_s} \nabla G \cdot \hat{\mathbf{n}} \quad (7.4)$$

$$= -\frac{1}{3\kappa + 3\sigma_s - A\sigma_s} \frac{\partial}{\partial \hat{\mathbf{n}}} G \quad (7.5)$$

where equation (6.19) for radiative heat flux vector is used.

Radiative heat source into the medium

The presence of thermal radiation introduces a heat source/sink inside the participating media. An explicit expression for radiative heat term is reported in sections 5.3.4, while the complete conduction-convection-radiation temperature equations is presented in section 5.3.5. Summarising, the temperature source/sink for grey radiation reads:

$$S_{rad}(\mathbf{r}) = -\frac{1}{\rho C_p} \nabla \cdot \mathbf{q}_{rad}(\mathbf{r}) = \frac{\kappa}{\rho C_p} [G(\mathbf{r}) - 4\sigma T^4(\mathbf{r})], \quad (7.6)$$

where ρ is the density of the medium, and C_p is the medium heat capacity at constant pressure.

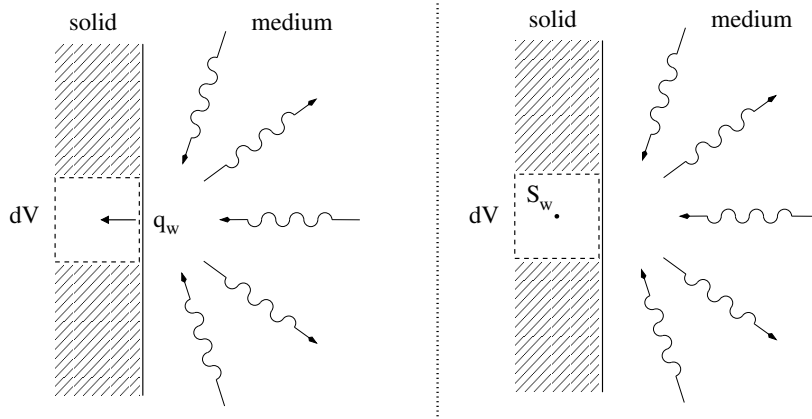


Figure 7.1: Radiation heat flux onto solid surface. Left, normal heat flux vector through the boundary (the vector was arbitrary chosen to point inside the control volume); right, heat source or sink term inside a boundary control volume.

Radiative heat flux onto enclosure surfaces

Thermal radiation leads also to an energy flux through the enclosure solid surfaces. The expression of the surface radiative heat flux for the P_1 -approximation, is derived in section 6.2.3. Heat flux (6.25) can be rewritten as a normal heat flux vector by:

$$\mathbf{q}_w(\mathbf{r}_w) = -\frac{1}{2} \left(\frac{\epsilon}{2 - \epsilon} \right) [G(\mathbf{r}_w) - 4\sigma T^4(\mathbf{r}_w)] \hat{\mathbf{n}}. \quad (7.7)$$

The radiative flux through the solid-medium interface can increase or decrease (depending on the balance between incident radiation and emitted energy) the solid body temperature.

From a numerical point of view, the heat transfer through the solid-medium interface can be computed in two ways: using the heat flux vector in a Neumann condition for temperature equation, or transforming the heat flux in an explicit source/sink term to be added in the temperature equation (in analogy to what has been done for the evaporation and condensation heat term; cf. section 2.1.1). The first approach is more natural and straightforward, while the second needs some explanation.

Let us define a *boundary control volume* as a control volume located inside the solid domain, that has at least one face belonging to the solid-medium interface. Let's consider now the infinitesimal boundary control volume dV depicted in Figure 7.1.

In order to determine the radiative energy that is deposited into (or withdrawn from) the volume, a radiative energy balance can be done on dV . Mathematically, the same problem was encountered in deriving expression

(5.43) for the radiation heat source into the medium (cf. Modest [48], section 10.9). If the heat flux vector is defined as zero on all the faces that are not part of the interface, then the energy stored in the boundary control volume is the divergence of the heat flux. Thus, the temperature source/sink term reads:

$$S_w = - \left[\frac{1}{\rho C_p} \right]_{solid} \nabla \cdot \mathbf{q}_w, \quad (7.8)$$

that is, the divergence divided by the thermal inertia of the solid material.

Governing equation summary

The complete equations used in the model are gathered in this paragraph. Boundary conditions are not reported, except for the Marshak's condition.

..... FLUID DOMAIN

- Fluid dynamics:

$$\frac{\partial u_i}{\partial x_i} = 0 \quad (7.9)$$

$$\frac{\partial u_i}{\partial t} + \frac{\partial u_i u_j}{\partial x_j} = -\frac{1}{\rho_0} \frac{\partial p}{\partial x_i} + \nu \frac{\partial^2 u_i}{\partial x_j \partial x_j} - \frac{\rho}{\rho_0} g \delta_{i2} \quad (7.10)$$

$$\frac{\rho}{\rho_0} = 1 - \beta_T (T - T_0) - \beta_\omega (\omega - \omega_0) \quad (7.11)$$

- Temperature transport¹:

$$\frac{\partial T_f}{\partial t} + u_j \frac{\partial T_f}{\partial x_j} = \alpha_f \frac{\partial^2 T_f}{\partial x_j \partial x_j} + \underbrace{\frac{\kappa}{\rho C_p} [G(\mathbf{r}) - 4\sigma T^4(\mathbf{r})]}_{S_{rad}} + S_f \quad (7.12)$$

- Vapour transport²:

$$\frac{\partial \omega}{\partial t} + u_j \frac{\partial \omega}{\partial x_j} = \alpha_\omega \frac{\partial^2 \omega}{\partial x_j \partial x_j} \quad (7.13)$$

- Incident radiation:

$$\nabla^2 G(\mathbf{r}) = \kappa(3\kappa + 3\sigma_s - \sigma_s A) [G(\mathbf{r}) - 4\sigma T^4(\mathbf{r})] \quad (7.14)$$

$$\hat{\mathbf{n}} \cdot \nabla G(\mathbf{r}_w) = \frac{\epsilon}{2 - \epsilon} \frac{3\kappa + 3\sigma_s - \sigma_s A}{2} [G(\mathbf{r}_w) - 4\sigma T^4(\mathbf{r}_w)] \quad (7.15)$$

..... SOLID DOMAIN

- Temperature diffusion¹:

$$\frac{\partial T_s}{\partial t} = \alpha_s \frac{\partial^2 T_s}{\partial x_j \partial x_j} - \underbrace{\frac{1}{\rho C_p} \nabla \cdot \mathbf{q}_w}_{S_w} + S_s \quad (7.16)$$

where

$$\mathbf{q}_w(\mathbf{r}_w) = -\frac{1}{2} \left(\frac{\epsilon}{2 - \epsilon} \right) [G(\mathbf{r}_w) - 4\sigma T^4(\mathbf{r}_w)] \hat{\mathbf{n}}. \quad (7.17)$$

¹Eventually provided with CHT b.c. - cf. section 2.1.2.

²Eventually provided with evaporation/condensation b.c. - cf. section 2.1.1.

7.2 Implementation

The details of the radiative model implementation, in the framework of OpenFOAM, are here reported.

The model is added to the solver `coupledHeatVapourFoam` developed by Andrea Petronio [54] and Paweł Sosnowsky [68], former students of Doctoral School *Environmental and Industrial and Fluid Mechanics* of the University of Trieste. The mathematical model and the main features of the solver has been described in chapter 2.

The author has extended the original solver. The above described radiative model has been included, in order to simulate the thermal radiation effects in a participating medium and onto solid boundaries. The new solver has been named `coupledHeatVapourRadiationFoam`.

From a numerical point of view, three main items have been added:

- (i) the equation for incident radiation G ;
- (ii) the radiative heat source S_{rad} in temperature equation of the medium;
- (iii) the surface radiative heat transfer (SRHT) onto the solid surfaces.

The numerical implementation of these three items is described in details in the following sections. Considering the complexity and the extension of the code, only the most significant features of the algorithm (and the relative code lines) are reported and commented. We refer to the OpenFOAM User Guide [3] and Programmer's Guide [2] for the code semantics.

The implementation of the P_1 -equations follows the structure of the P_1 radiative model proposed by OpenFOAM, version 2.1.0.

7.2.1 Radiative heat transfer equations

The incident radiation G is obtained solving the P_1 equation (7.2) in fluid domain. The code lines that solve the equation are contained in the `solveFluidRadiation.H` file:

```

1 // - Radiation model P1 - spherical approximation method.
2 // ref. Modest, "Radiative Heat Transfer", 2013
3
4 {
5     // stefan-boltzmann constant
6     dimensionedScalar sigmaSB
7     (
8         "sigmaSB",
9         dimensionSet(1, 0, -3, -4, 0, 0, 0),
10        5.670E-08
11    );
12
13    // Solve G transport equation

```

```

14     solve
15     (
16         fvm::laplacian(gammaf[i], Gf[i])
17         - fvm::Sp(kappaf[i], Gf[i])
18         ==
19         - 4.0*(kappaf[i]*sigmaSB*pow4(Tf[i]) + Ef[i])
20     );
21
22     // Calculate radiative heat flux on boundaries.
23     forAll(fluidRegions[i].boundaryMesh(), patchI)
24     {
25         Qrf[i].boundaryField()[patchI] =
26         -gammaf[i].boundaryField()[patchI]
27         *Gf[i].boundaryField()[patchI].snGrad();
28     }
29 }

```

Code 7.1: solveFluidRadiation.H

First, the variable `sigmaSB` is set as the Stefan-Boltzmann constant (5.24). Second, the governing equation for incident radiation (7.14) is rearranged as:

$$\nabla \cdot (\gamma \nabla G) - \kappa G = -4(\kappa \sigma T^4 + E), \quad (7.18)$$

and solved. Constant γ is defined in a part of the code here not reported, by

$$\gamma = \frac{1}{3\kappa + 3\sigma_s - \sigma_s A}, \quad (7.19)$$

while E is a (constant) external source of radiation. This last term is not included in the set of radiative heat transfer equations proposed in this thesis. However, it was present in the original OpenFOAM implementation of P_1 -model, and it is maintained in our code.

Equation (7.18) is equivalent to the first equation of system (7.2), except for the constant E , that is set to zero in all the simulations here presented.

In the last part, lines 24-28, the surface normal radiative heat flux (7.5) is also computed.

The Marshak's boundary condition (7.15) is specified in the boundary file `MarshakRadiation.C`. The implementation of the Marshak's condition proposed by OpenFOAM version 2.1.0, was completely checked and adopted in our code. For the sake of completeness, this implementation is analysed in appendix 7.5.

7.2.2 Radiative heat source into the medium

The radiative heat source/sink S_{rad} in medium (7.6) is added to the temperature equation for fluid domain, inside the file `solveFluidTEqn.H` here reported:

```

29 //- radiation contribution
30 dimensionedScalar sigmaSB
31 (
32     "sigmaSB",
33     dimensionSet(1, 0, -3, -4, 0, 0, 0),
34     5.670e-08
35 );
36
37 //- semi-implicit computation of radiation heat source
38 fvScalarMatrix Srad
39 (
40     (kappaf[i]*Gf[i] - 4.0*Ef[i])/rhoCpf[i]
41     - fvm::Sp(16.0*kappaf[i]*sigmaSB*pow3(Tf[i])/rhoCpf[i], Tf[i])
42     - (4.0*kappaf[i]*sigmaSB)*pow3(Tf[i])*(Tf[i] - 4.0*Tf[i])/rhoCpf[i]
43 );
44
45 //- save the old temperature field
46 volScalarField Told ( Tf[i] );
47
48 //- solve T equation
49 fvScalarMatrix TEqn
50 (
51     fvm::ddt(Tf[i])
52     + fvm::div(phiF[i], Tf[i])
53     ==
54     fvm::laplacian(alphaEff, Tf[i])
55     + fvc::div(EvCoSource)
56     + Srad
57 );
58
59 TEqn.relax();
60 TEqn.solve();
61
62 Tf[i].correctBoundaryConditions();
63
64 //- compute the variation between old and new T:
65 // this is used as a criteria to stop the G-T sub-loop in solveT.H
66 dimensionedScalar DELTA_T = max(mag(Tf[i]-Told));
67 VariationTf[i] = DELTA_T.value();

```

Code 7.2: solveFluidTEqn.H

The term S_{rad} is computed in lines 39-43. The computed formula reads:

$$S_{rad} = \frac{\kappa G - 4E}{\rho C_p} - S_p \left(\frac{16\kappa\sigma T^3}{\rho C_p}, T \right) - 4\kappa\sigma T^3 \frac{T - 4T}{\rho C_p}, \quad (7.20)$$

where function S_p discretises the arguments with an implicit schemes and multiply them (cf. Programmer's Guide [2]). This term is introduced to support the numerical convergence. Since the contribution of external source

$E = 0$, we obtain:

$$\begin{aligned} S_{rad} &= \frac{\kappa G}{\rho C_p} - Sp\left(\frac{16\kappa\sigma T^3}{\rho C_p}, T\right) - 4\kappa\sigma T^3 \frac{T - 4T}{\rho C_p} \\ &= \frac{\kappa G}{\rho C_p} - \frac{16\kappa\sigma T^4}{\rho C_p} - \frac{4\kappa\sigma T^4 - 16\kappa\sigma T^4}{\rho C_p} \\ &= \frac{\kappa}{\rho C_p} [G - 4\sigma T^4] \end{aligned}$$

that is the theoretical expression (7.6) for S_{rad} . Subsequently, the source term is added to the temperature equation in line 56.

The incident radiation G and the temperature T are now coupled variables, because they depend on each other. From a physical point of view, a local thermal equilibrium has to be established at each simulation time step.

Therefore, a radiation-temperature sub-loop is added: the equations for G and T (in fluid domain) are solved n times, till the maximum (among the cells) difference between temperature at step n and temperature at previous step $n - 1$ become lower than a fixed tolerance:

$$\text{VariationT} = \max_{cells} |T_n - T_{n-1}| < \text{maxRadErr}. \quad (7.21)$$

It is assumed that radiation and temperature are properly coupled, at a given time, if the coupling condition (7.21) is satisfied.

The radiation-temperature sub-loop is added in file `solveT.H`. Part of the file is displayed below:

```

58 // solving FLUID T
59 forAll(fluidRegions, i)
60 {
61     Info << "T for fluid region: " << fluidRegions[i].name() << endl;
62
63     #include "solveFluidRadiation.H"
64     #include "solveFluidTEqn.H"
65
66     //- coupling sub-loop between radiation and temperature
67     // (initialisation, VariationTf[i]=0)
68     while(VariationTf[i]>maxRadErr)
69     {
70         Info << "Radiation-Temperature loop: max_T_var "<< VariationTf[i]
71             << " NO MATCH: GvsT"<< endl;
72
73         #include "solveFluidRadiation.H"
74         #include "solveFluidTEqn.H"
75
76         radCorrCnt++;
77

```

```

78     // if we did too many iterations
79     if(radCorrCnt>maxRadIter)
80     {
81         Info << "*****" << endl;
82         Info << "* ERROR MAX Radiation ITERATIONS EXCEEDED *" << endl;
83         Info << "*****" << endl;
84         FatalErrorIn
85         (
86             "\nmain loop\n"
87             "radiation calculation\n"
88         )
89         <<"maximum number of radiation correction iterations "
90         <<"exceeded\n"
91         <<"no convergence of radiation heat source
92             and temperature distribution\n"
93         <<exit(FatalError);
94         return -1;
95     }
96
97 }
98 Info << "Radiation-Temperature loop: max_T_var "<< VariationTf[i]
99     << " MATCH: GvsT"<< endl;
100 }

```

Code 7.3: solveT.H

The temperature-radiation sub-loop is sketched in Figure 7.3b. Temperature and radiation equations are solved one time and then the coupling sub-loop starts. The coupling condition (7.21) is imposed at line 68. The variable `VariationT` is initialised as zero when simulation starts, then it is updated in file `solveFluidTEqn.H` (code 7.2, lines 66-67).

In order to avoid infinite sub-loop iterations, a limited number of cycles is allowed. The *if* statement at lines 79-95 checks if the maximum number of iterations `maxRadIter` is reached, and eventually stops the simulation.

The sub-loop returns the state of radiation-temperature coupling, that can be:

- ▶ Coupling achieved, the string “MATCH: GvsT” is returned: the coupling condition (7.21) is satisfied and the maximum number of iterations is not exceeded. The solver proceeds.
- ▶ Coupling not achieved, the string “NO MATCH: GvsT” is returned: the coupling condition is not satisfied, but the maximum number of iterations is not exceeded. Another iteration of the sub-loop is done.
- ▶ Failure, error message is returned: the coupling condition is not satisfied and the maximum number of iterations is exceeded. Simulation stops.

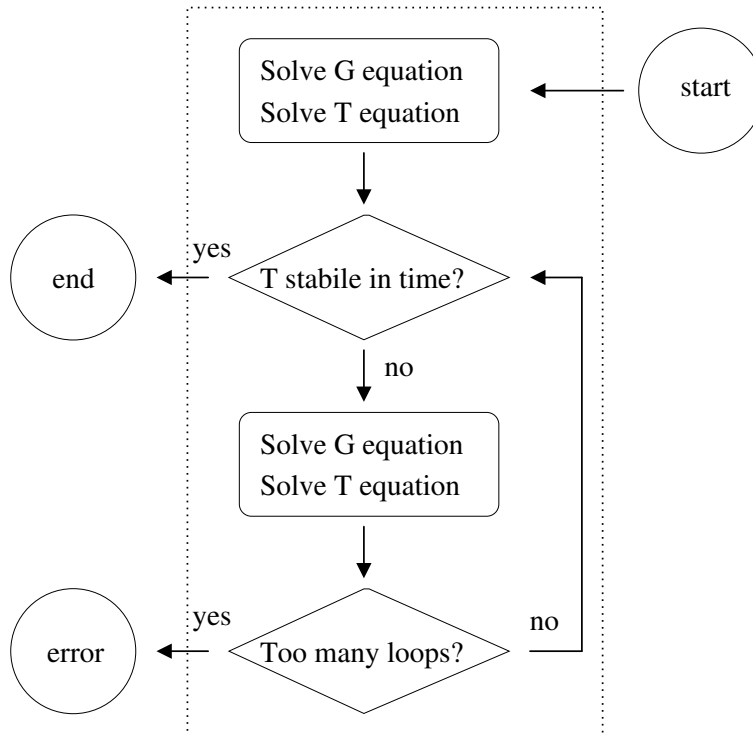


Figure 7.2: Scheme of temperature-radiation sub-loop.

The values of coupling tolerance `maxRadErr` and the maximum iterations `maxRadIter`, can be set by the user. Empirically, a tolerance of about `maxRadErr = 10-6` usually gives satisfactory results, while for most of the cases 2 – 5 sub-loop iterations are sufficient to achieve coupling. The value `maxRadIter = 10` is chosen as default settings.

7.2.3 Surface radiative heat transfer

The SRHT can be implemented, at least, in two ways: adding the radiative heat flux (7.7) in the conjugate heat transfer balance, cf. equations (2.16),(2.17); adding the radiative heat source (7.8) to the first solid cell near the interface as for the evaporation/condensation heat source, cf. equation (2.14).

It is found that the former approach can lead to numerical instability issues; hence, the latter is chosen: the modulus of boundary heat flux \mathbf{q}_w is computed, and the divergence term (7.8) is added to the solid temperature equation.

In order to compute the boundary heat flux \mathbf{q}_w , an auxiliary field `RadHF` is created. This field is everywhere set to zero, except for the solid-fluid

interface boundary values, where the radiative heat flux is stored. A suitable boundary condition `RadHFFvPatchScalarField` is created to compute q_w . Part of the code is showed below:

```

310 void RadHFFvPatchScalarField::updateCoeffs()
311 {
312     Info << "*** Updating RadHF for patch: " << patch().name()<<endl;
313
314     // Since we're inside initEvaluate/evaluate there might be
315     // processor comms underway. Change the tag we use.
316     int oldTag = UPstream::msgType();
317     UPstream::msgType() = oldTag+1;
318
319     // sigmaSB = Stefan-Boltzmann constant: default SI units: [W/m2*K4]
320     dimensionedScalar sigmaSB
321     (
322         "sigmaSB",
323         dimensionSet(1, 0, -3, -4, 0, 0, 0),
324         5.670E-08
325     );
326
327     // calculating new heat flux
328     scalarField radiationHeatFlux
329     (
330         0.5*(emissivity_/(2-emissivity_))
331         *
332         ( G() - 4*sigmaSB.value()*pow4(T()) )
333     );
334
335     if(isFluid())
336     {
337         forAll(radiationHeatFlux,fi)
338         {
339             // no heat flux into the fluid domain
340             radiationHeatFlux[fi] = 0;
341         }
342     }
343
344     // setting value and gradient
345     fvPatchScalarField::operator=(radiationHeatFlux);
346
347     fixedValueFvPatchScalarField::updateCoeffs();
348
349     // Restore tag
350     UPstream::msgType() = oldTag;
351 }

```

Code 7.4: `RadHFFvPatchScalarField.C`

First, the G and T boundary fields relative to fluid side are loaded (lines

not show). Then, in lines 328-333, the surface radiative heat flux

$$\text{radiationHeatFlux} = \frac{1}{2} \left(\frac{\epsilon}{2 - \epsilon} \right) [G(\mathbf{r}_w) - 4\sigma T^4(\mathbf{r}_w)], \quad (7.22)$$

is computed. Since the heat source has to be applied only to the solid side, the radiation heat flux is always set to be zero in the fluid domain (lines 335-342). At the end, the radiative heat flux values are stored in the `RadHF` boundary field (line 347).

The temperature source/sink term (7.8) is computed as the divergence of radiative heat flux, and added in temperature equation of the solid domain. Part of the code is displayed below:

```

21 // Thermal radiation source term
22 surfaceScalarField RadSource
23 (
24     fvc::interpolate(RadHFs[i]/(rhos[i]*Cps[i]))
25     * solidRegions[i].magSf()
26 );
27
28 // Temperature equation
29 solve
30 (
31     fvm::ddt(Ts[i])
32     ==
33     fvm::laplacian(k, Ts[i])
34     + fvc::div(EvCoSource)
35     + fvc::div(RadSource)
36 );
37
38 Ts[i].correctBoundaryConditions();

```

Code 7.5: `solveSolid.H`

The divergence is computed in two steps: first the heat flux is discretised with the Gauss theorem, then the function `div` is used. This is the usual discretisation procedure in OpenFOAM, for more details we refer to [2].

7.3 Validation

In this section, the validation of the numerical implementation is carried out, along with an investigation of the limits and the prediction capability of the P_1 -approximation.

Two geometries sketched in Figure 7.3 are studied: a grey medium (a) between two parallel infinitely long plates, and (b) within a square enclosure. These are, respectively, one-dimensional and two-dimensional cases extensively studied in literature. Several results, both analytical and numericals are available for comparison purpose.

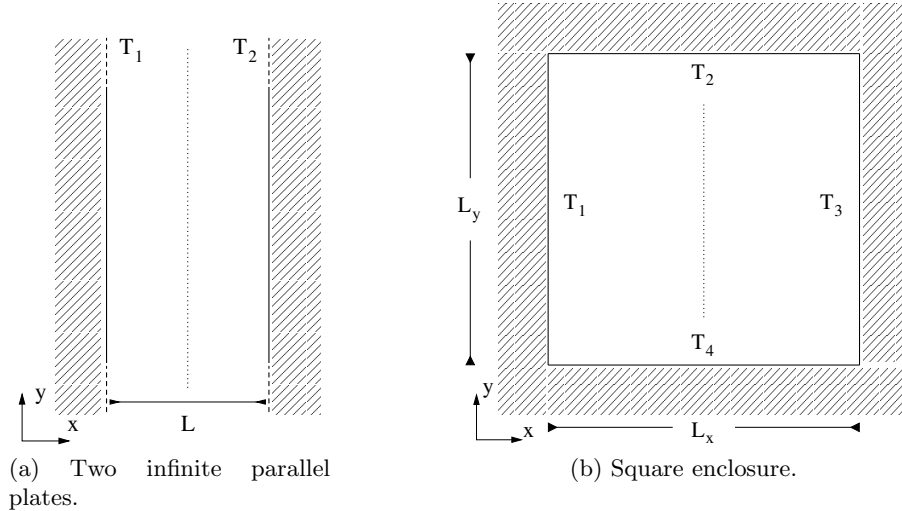


Figure 7.3: Geometry of the benchmark cases.

Different settings are used in order to widely test the prediction capabilities of the model. Particularly, the following points are investigated:

- ▶ Numerical implementation: the correctness of the implementation, within the OpenFOAM environment, is checked by comparing the numerical and the analytical solutions of the P_1 -model for case (a) - see section 7.3.1;
- ▶ Pure radiative heat transfer mechanism (*i.e.* in absence of conduction and convection) is investigated in both cases (a) and (b), for a wide number of combinations of radiative parameters - see section 7.3.2;
- ▶ Combined conduction and radiation heat transfer is analysed using case (b) - see section 7.3.3.
- ▶ Combined convection, conduction and radiation heat transfer is tested in case (a) - see section 7.3.4.

The attempt is to carefully validate the radiative model and, in the same time, to investigate the theoretical limits of the P_1 -model with respect to other models proposed in literature.

The surface radiative heat transfer is also tested in section 7.3.5. Conduction and radiation are simulated in a one-dimensional case, composed by a solid and a fluid medium. The heat transfer onto the fluid/solid surface is simulated and the resulting temperature distribution is commented.

7.3.1 Numerical model validation

The validation of numerical implementation is carried out on an isothermal and grey medium bounded by two isothermal black plates. The case geometry is sketched in Figure 7.3a. The medium temperature is T_m , while the two plates are both at temperature $T_1 = T_2 = T_w$. The plates are considered black (*i.e.* the emissivity is set to $\epsilon = 1$). The participating medium can absorb/emit and scatter radiation whether linearly or linear anisotropically.

This is a well studied case. The analytical solution of the P_1 -equations (7.2) is provided by M. Modest [48] (cf. chapter 16 - example 16.2) together with an exact solution of the complete RHT equations. The non-dimensional heat flux onto the plates is considered for comparison purpose:

$$\Psi = \frac{Q_{rad}}{\sigma(T_m^4 - T_w^4)}, \quad (7.23)$$

where Q_{rad} is the surface normal heat flux (7.5). For the sake of completeness, the analytical solution form [48] is also displayed:

$$\Psi_{ana} = \frac{2 \sinh \tilde{\gamma} \tau}{\sinh \frac{1}{2} \tilde{\gamma} \tau_L + \frac{1}{2} \sqrt{\frac{3-A\omega}{1-\omega}} \cosh \frac{1}{2} \tilde{\gamma} \tau_L}. \quad (7.24)$$

Equation (7.24) is made non-dimensional by means of the following parameters:

$$\tau = (\kappa + \sigma_s)x \quad (\text{optical distance}) \quad (7.25)$$

$$\omega = \frac{\sigma_s}{\kappa + \sigma_s} \quad (\text{linear scattering albedo}) \quad (7.26)$$

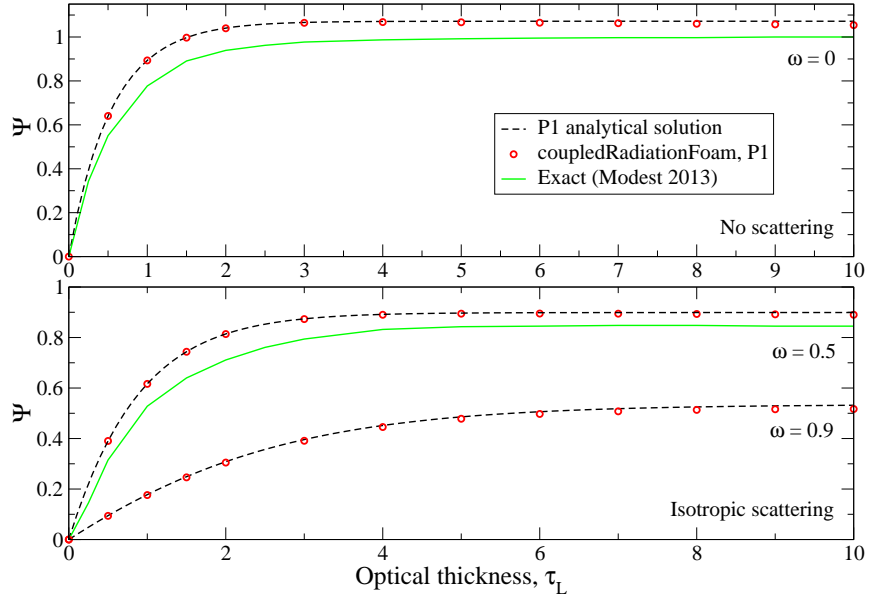
$$\tilde{\gamma} = \sqrt{(1-\omega)(3-A\omega)} \quad (\text{non-dim. diffusion coeff.}) \quad (7.27)$$

Because of the symmetry of the problem, the origin of the axis is placed in the mid-plane between the plates; thus the plates are located at $\tau = \pm\tau_L/2$.

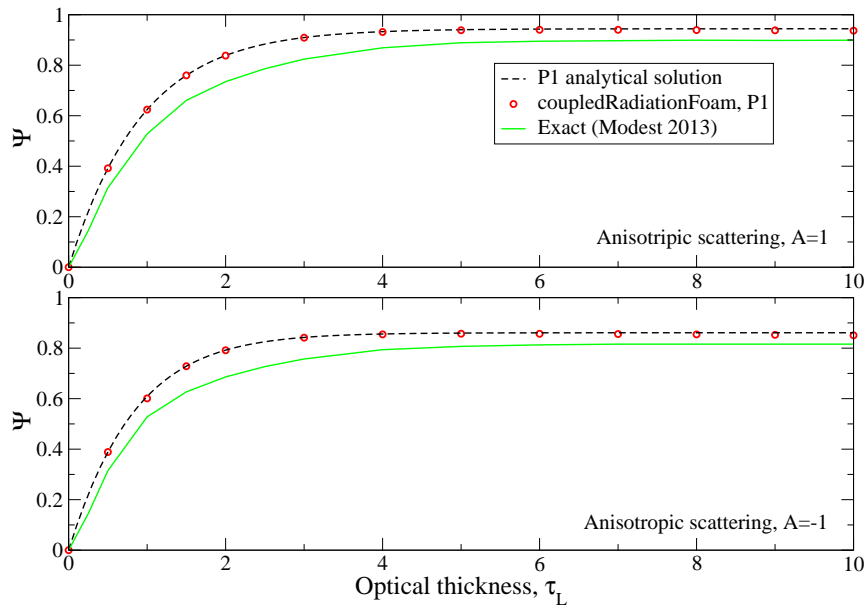
Figure 7.4a shows the heat flux both for non-scattering and linear scattering medium, while Figure 7.4b displays the case of an anisotropic scattering medium. In all the cases, the numerical solution fits the analytical one. Since these results are obtained using a large combination of the radiative parameters, we can conclude that the P_1 -equation is correctly implemented in the code.

The exact solution for this simple problem is also reported. A comparison with the P_1 solution highlights one of the major drawback of the spherical approximation method: the tendency to overestimate the thermal radiation flux. However, in this case the approximation is affected by a modest error.

Another consideration is related to the optical thickness. In the last decade, it was alleged that the P_1 -model is inaccurate in the optical thin



(a) Test without linear isotropic scattering, $A = 0$.



(b) Test with linear scattering $\omega = 0.5$ and two values of linear isotropic scattering A .

Figure 7.4: Isothermal grey solid medium between two parallel walls. Labels: dash line, analytical solution of P_1 -equation; red circle, numerical solution of P_1 -equation; green line, exact solution of the RHT equation by [48].

limit, *i.e.* $\tau \rightarrow 0$. Recent investigations show that this is not a general issue³. In the present case, we can notice that P_1 goes to the correct thin limit and loses more accuracy in the thick limit.

7.3.2 Pure radiative heat transfer

In this section the model is validated in cases where the temperature of the medium is just determined by thermal radiation, and convection and conduction are avoided.

Parallel plates

The parallel plates geometry is again used with other settings: the two plates are taken at different temperature $T_1 < T_2$, the scattering is avoided and the emissivity is fixed to $\epsilon = 1$. Comparisons are made with the analytical solution proposed by Howell, Siegel and Mengüç [28] for the non-dimensional surface heat flux (7.23) and the non-dimensional temperature:

$$\Phi = \frac{T^4 - T_2^4}{T_1^4 - T_2^4} \quad (7.28)$$

over an horizontal line $y = \text{const}$.

Figure 7.5a reports the non-dimensional temperature distribution for several values of optical thickness of the participating medium. The results are in good agreement with the reference solution, even if we can notice a slight deviation for low value of τ_L .

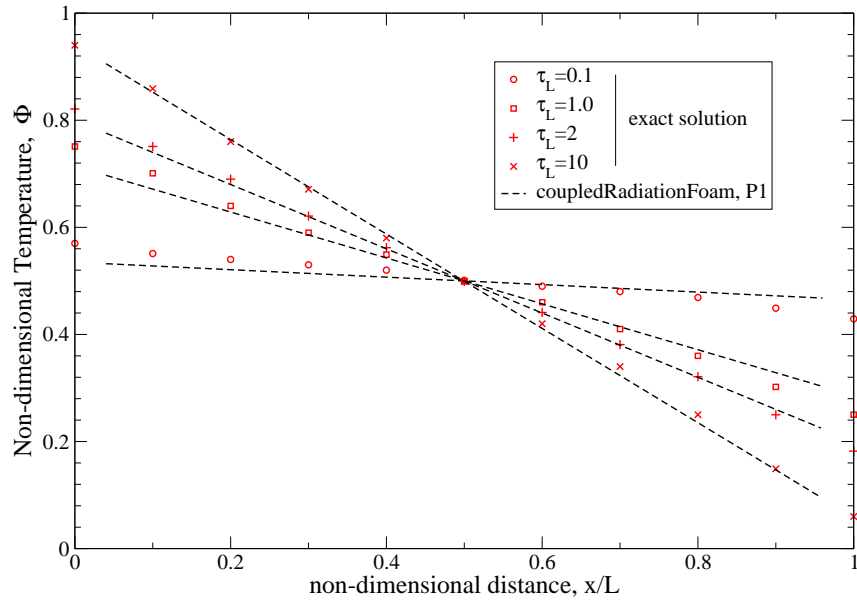
Figure 7.5b depicts the non-dimensional heat flux for a larger range of optical thickness values. The results fit the reference solutions fairly well.

The P_1 -model predictions are quite accurate. Particularly, the values of heat flux seems to be more accurate than in the previous section 7.3.1. The two cases are similar except for the presence, in the previous case, of a temperature step at the plate-medium interface. This unphysical discontinuity can affect the prediction of the model, and leads to less accurate results.

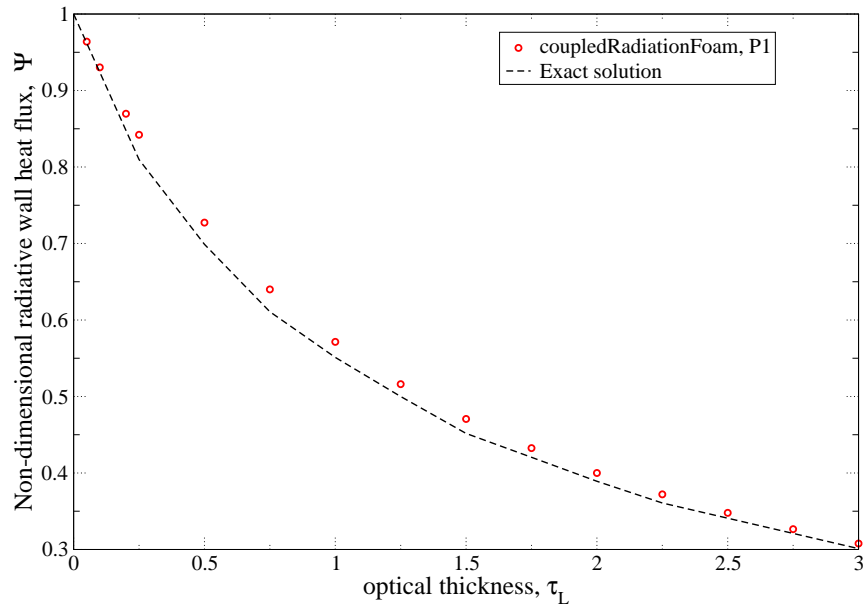
Grey medium in square enclosure

The geometry of a grey medium in a square enclosure is sketched in Figure 7.3b. Two cases are studied: (A) an absorbing/emitting but non-scattering medium and (B) a purely scattering medium. No analytical solution is available but different numerical studies for these cases can be found in literature.

³See the chapter dedicated to spherical approximation method in M. Modest [48] and compare with the second edition of the same textbook.



(a) Temperature distribution between the two plates for different optical thickness of the medium.



(b) Heat flux on the plates with respect to the optical thickness of the medium.

Figure 7.5: Isothermal grey solid medium between two parallel walls. Comparison between the P_1 -model and the exact solution given in [28].

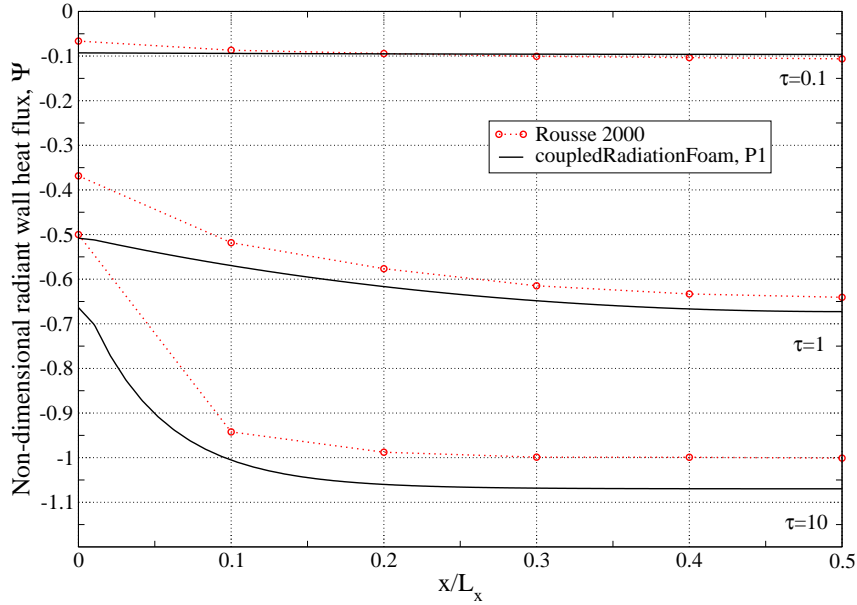


Figure 7.6: Non-dimensional heat flux on the bottom wall of the square enclosure. Labels: red circles, data from Rouse *et al.* [62]; black line, P_1 -model solution.

(A) *Absorbing/emitting but non-scattering medium*: the medium is at fix temperature $T_m > 0$, while the enclosure walls are cold $T_{1,2,3,4} = 0$. The walls have constant emissivity $\epsilon = 1$. Again the non-dimensional heat flux on the wall,

$$\Psi = \frac{Q_{rad}}{\sigma T_m^4}, \quad (7.29)$$

is plotted and compared with the numerical profile of Rouse *et al.* [61, 62]. They used a finite element method to solve the complete RHT equation. Also Crosbie and Schrenker [16] studied the same case, solving the same governing equation in a two-dimensional case. The latter is not reported here, since their data are in perfect agreement with the former one.

Figure 7.6 shows the heat flux on the bottom wall of the cavity, for three increasing values of optical thickness. The results become more and more inaccurate for optical thick medium. Particularly, the P_1 -model fails to reproduce the Ψ in the proximity of the vertical walls, where the increase of heat flux is underestimated.

The lack of accuracy for large value of τ_L is expected, since it is recognised that the P_1 -model is not suitable for optical thick media [48]. An explanation for the behaviour in the proximity of the vertical wall is proposed: the P_1 -equation provided with the Marshak's boundary condition, is not accurate when the walls emission strongly affects thermal radiation, *i.e.*

the effects of participating medium is limited. In the cavity corner region ($x/L_x < 0.1$) the radiative effects of the vertical and horizontal cold walls combine, leading to a decreasing of temperature and a less accurate prediction than in the central region ($0.1 < x/L_x < 0.9$).

(B) *Purely scattering medium*: the enclosure walls are all cold $T_{1,2,3} = 0$, except for the bottom wall that is hot $T_4 > 0$. Several cases have been simulated, changing the wall emissivity ϵ and the optical thickness τ_L . The non-dimensional surface heat flux

$$\Psi = \frac{Q_{rad}}{\sigma T_4^4}, \quad (7.30)$$

is compared with the result reported by Rouse *et al.* [62] and M. Modest [47], that uses a differential approximation to solve the radiative equation.

Figure 7.7a depicts the effects of the optical thickness on the heat flux, onto the bottom hot wall. Different simulations are performed fixing the emissivity to $\epsilon = 1$ (black surfaces) and increasing optical thickness τ_L . Surprisingly, the results become more accurate for optical thick media. Similar to previous simulation (A), the P_1 -model fails in the corner region. The heat flux is overestimated, probably due to the influence of the bottom hot wall.

In order to better understand the impact of the boundaries on the overall thermal radiation, the same cases are run with several decreasing values of the enclosure walls emissivity. Empirically, the value $\epsilon = 0.6$ allows a perfect reproduction for $\tau_L = 1$ and improves the prediction for the other cases. The profiles are reported with a dash blue line in Figure 7.7a.

This test can confirm the hypothesis that the Marshak's condition for P_1 -model does not reproduce correctly the walls radiation contribution: it tends to amplify the wall influence in the global radiation. Hence, this is the main source of error in those cases when wall radiation mainly rules the total radiation. In the last years, some efforts have been done to improve the P_1 -Marshak's condition⁴. Among the others, we refer to the work of Liu *et al.* [43] that introduced a corrective parameter in the Marshak's condition to obtain better predictions.

Figure 7.7b shows the effects of varying the walls emissivity, when the optical thickness is fixed $\tau_L = 1$. Overall, the results are largely overestimated. When the walls emissivity decreases, and the effects of the boundaries is less intense, the predictions are more accurate.

In conclusion, we can note that the case of pure scattering produces worst results than the case of pure absorbing/emitting medium. A priori, this is not expected because the contribution of the scattering on the governing

⁴The Marshak's condition is a general boundary condition for the P_N -model. The name P_1 -Marshak's indicates the particular formulation valid for the first order approximation

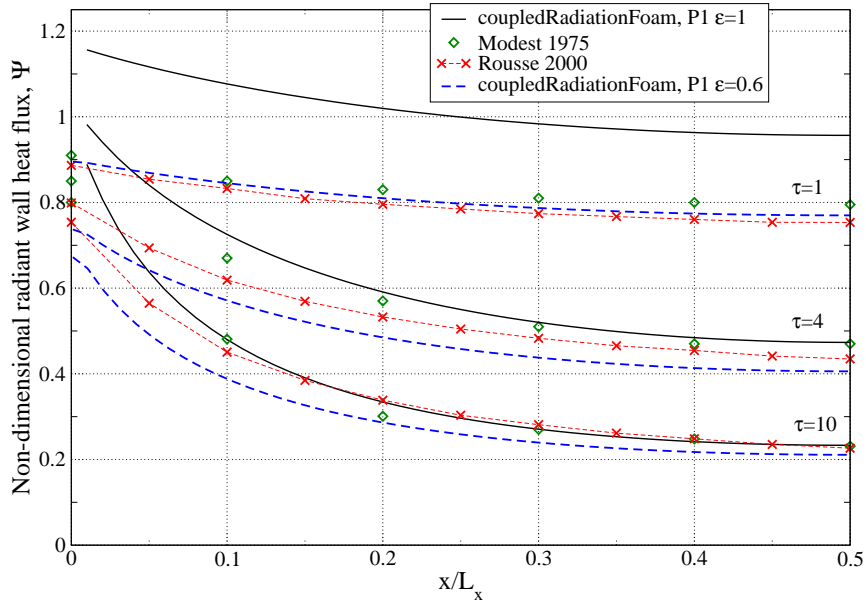
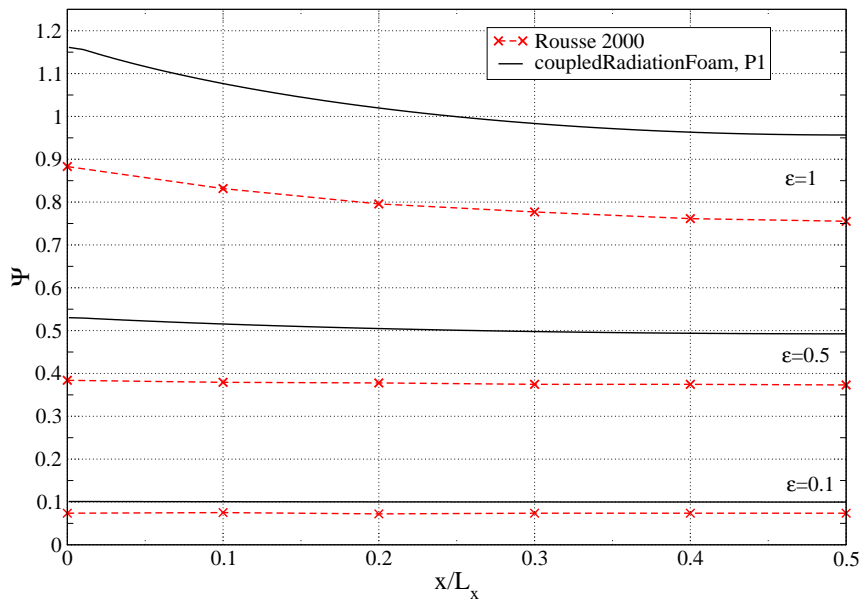
(a) Effects of the variation of wall emissivity ϵ .(b) Effects of the variation of optical thickness τ_L .

Figure 7.7: Non-dimensional heat flux on the bottom wall of the square enclosure. Labels: red cross, data from Rousse *et al.* [62]; green diamonds; data from Modest [47]; solid and dash line, P_1 -model solution.

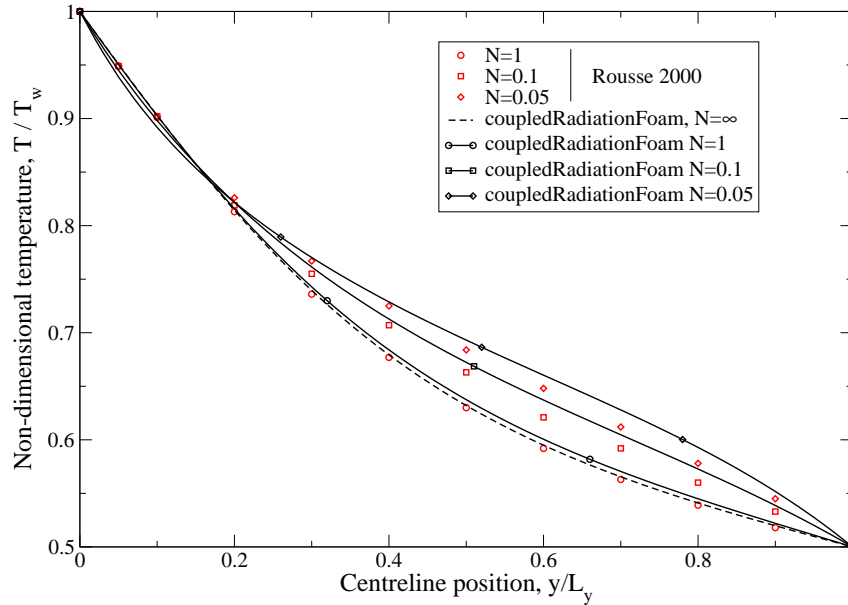


Figure 7.8: Non-dimensional temperature over a vertical centreline, for conduction and radiation in a square enclosure. Simulations for different Stark number N . Labels: red symbols, data from Rouse 2000 [62]; solid lines, P_1 -model; dash line, convection without radiation.

equations (7.2) is almost analogous to the absorbing/emitting contribution. The only difference in the use of the σ_s and κ is that the absorption coefficient multiplies the entire right hand side of the incident radiation equation. If $\kappa = 0$ the radiation equation would reduce to a Laplace equation, and G would be completely determined by boundary conditions. This is not happening if $\sigma_s = 0$. Therefore, it is not the presence of scattering that introduces an error, but the absence of the absorption/emission that gives more room to the boundaries influence.

7.3.3 Combined conduction and radiation

Radiation heat transfer is activated together with heat conduction. The case geometry is the square cavity depicted in Figure 7.3b. The bottom wall has a constant temperature $T_4 = T_w$ while the other walls have $T_{1,2,3} = T_w/2$. The medium is not scattering, the optical thickness is fixed at $\tau_L = 1$, and the walls are black $\epsilon = 1$.

The effects of conduction to radiation are ruled by the *Stark number* (also named *conduction-radiation parameter*) that reads:

$$N = \frac{(\kappa + \sigma_s)k}{4\sigma T_w^3} \quad (7.31)$$

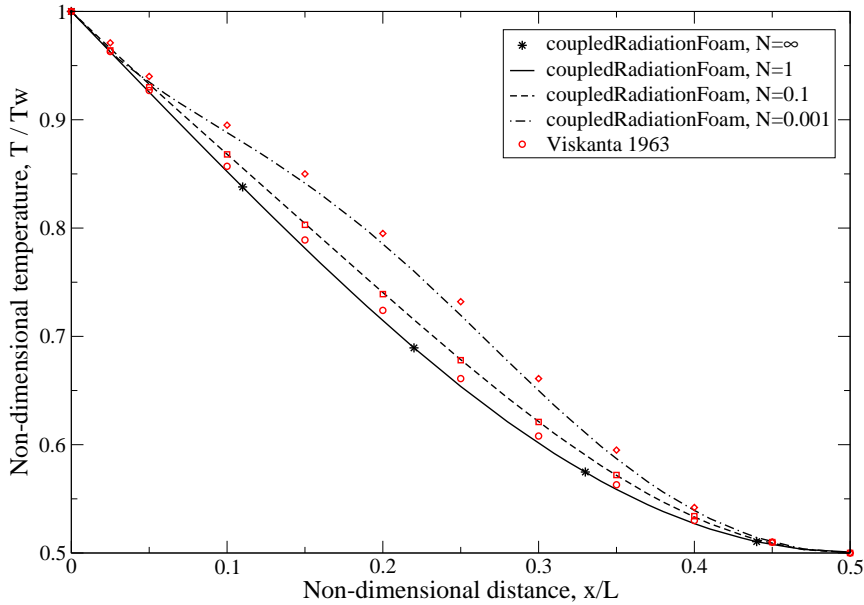


Figure 7.9: Non-dimensional temperature over the horizontal line $y = y_0$ where $T(y_0) = T_w/2$; in case of convection, conduction and radiation in plain channel. Simulations for different Stark number N . Labels: red symbols, data from Viskanta [78]; lines, coupledHeatVapourRadiationFoam, P_1 -model; black stars, coupledHeatVapourRadiationFoam without radiation.

where k is the medium thermal conduction coefficient. We refer to Viskanta [78] for a brief discussion on this non-dimensional number.

Figure 7.8 shows the non-dimensional temperature T/T_w for different values of the Stark number. The comparison is made with the numerical data of Rousse *et al.* [62] and Razzaque *et al.* [59, 60]. The two data set practically collapse one on the other, thus only the first is plotted. A simulation of conduction without radiation is also reported. In this case k is determined imposing $N = 1$ and switching off radiation. It is reported with the label $N = \infty$ with an abuse of notation.

There is a quite good agreement with the reference data. Although the temperature is slightly over-predicted in the proximity of the bottom wall.

7.3.4 Combined conduction, convection and radiation

The case studied by Viskanta [78] is here reproduced. Let's consider a fully-developed laminar flow within a plain channel in Figure 7.3a. The fluid between the plates is driven by a Poiseuille flow, that enters in the channel from the bottom and exits from the top. The velocity is given by

$$u_y(x) = 6\bar{u} \left[(x/L) - (x/L)^2 \right], \quad (7.32)$$

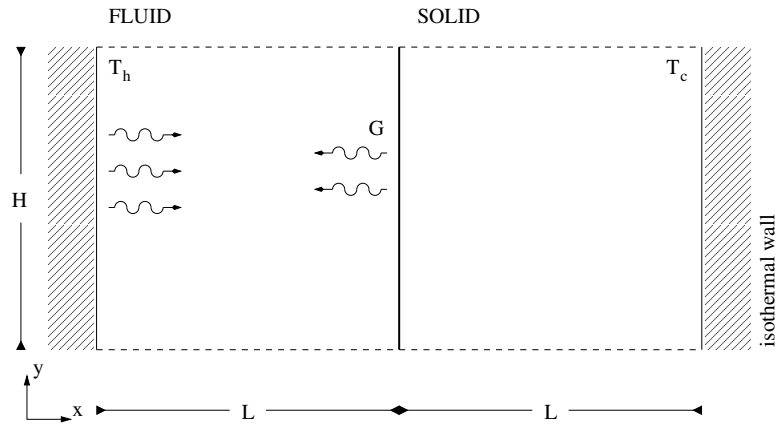


Figure 7.10: Geometry of the validation case for SRHT.

where the mean velocity is set $\bar{u} = 1$. Velocity variations on the other directions are neglected. The two vertical plates are isothermal with temperature $T_1 = T_2 = T_w$, the inlet boundary is at temperature $T_{in} = 0$, while the zero gradient condition is enforced in the outlet. The plates are black, thus $\epsilon = 1$, and the zero gradient condition is set for incident radiation G on the inlet and outlet. The participating medium is not scattering and the optical thickness is fixed to $\tau_L = 1$.

Three simulations are performed for three different values of Stark number. The non-dimensional temperature profile T/T_w is plotted for purpose of comparison with data of Viskanta [78] and Rousse *et al.* [62]. Anyway, since the results of the latter match very well with the data from the former, they are not reported. Viskanta [78] evaluate the integral-differential RHT equation with the Barbier's methods (three terms Taylor expansion).

Temperature is plotted over a horizontal line $y = y_0$ where $T(y_0) = T_w/2$. The location of y_0 changes for each simulation. Particularly, when N decreases and the effects of radiation overcome conduction, y_0 is located farther from the inlet. After preliminary tests, a channel long $y/L = 7$ is used for all the three cases.

Figure 7.9 reports the non-dimensional temperature profile at location y_0 . The results are in good accord with the reference values. When $N = 1$, radiation essentially does not affect the temperature profile. For lower values of Stark number, temperature is not altered in the proximity of the walls but it increases in the central region. Near the wall, temperature is still dominated by conduction because of the higher temperature gradient arising on the solid/fluid interface.

7.3.5 Surface radiative heat transfer

To the best of our knowledge, no benchmark cases for surface radiative heat transfer have been reported in literature.

The SRHT is here tested on a simple geometry: two infinite long rectangular domains, bounded by isothermal walls. Figure 7.10 sketches the aforementioned geometry. The left-side domain is filled with a fluid that is a radiative participating medium; the right-side domain is made of a solid, conductive and opaque material.

Thermal radiation propagates into the fluid domain and impinges the solid surface, where the SRHT takes place. The radiative heat, supplied to (or subtracted from) the solid surface, changes the temperature distribution within the solid domain. Simultaneously, in fluid domain, the radiation field is altered by the solid surface temperature, since the radiation emitted from the solid depends on temperature.

The characteristic width of the rectangular domains is $L = 1$. The left isothermal wall is at temperature T_h , higher than the right wall temperature T_c . The solid material is a good conductor, with an higher thermal conductivity with respect to fluid medium:

$$k_s = 4k_f, \quad (7.33)$$

where an obvious notation for the subscripts is used. The solid surfaces in contact with the fluid domain are black, therefore $\epsilon = 1$. The fluid is at rest, hence temperature is transported only by conduction and thermal radiation (no convection). The medium absorbs and emits but does not scatter radiation, and the radiative parameters are set as:

$$\tau_L = 1, \quad \omega = 0. \quad (7.34)$$

Different simulations are performed with increasing values of Stark number (7.31), namely:

$$N = \frac{(\kappa + \sigma_s)k}{4\sigma(T_h^3 - T_c^3)} = \begin{cases} 1 \\ 0.1 \\ 0.01 \end{cases} \quad (7.35)$$

obtained changing the isothermal walls temperatures. The case without thermal radiation is also simulated; it is notated $N = \infty$, with an abuse of notation. The non-dimensional temperature distribution

$$\Phi = \frac{T^4 - T_c^4}{T_h^4 - T_c^4} \quad (7.36)$$

is analysed.

Figure 7.11 shows Φ over an horizontal line through the fluid and solid domain. When radiation is neglected ($N = \infty$), conduction rules the system

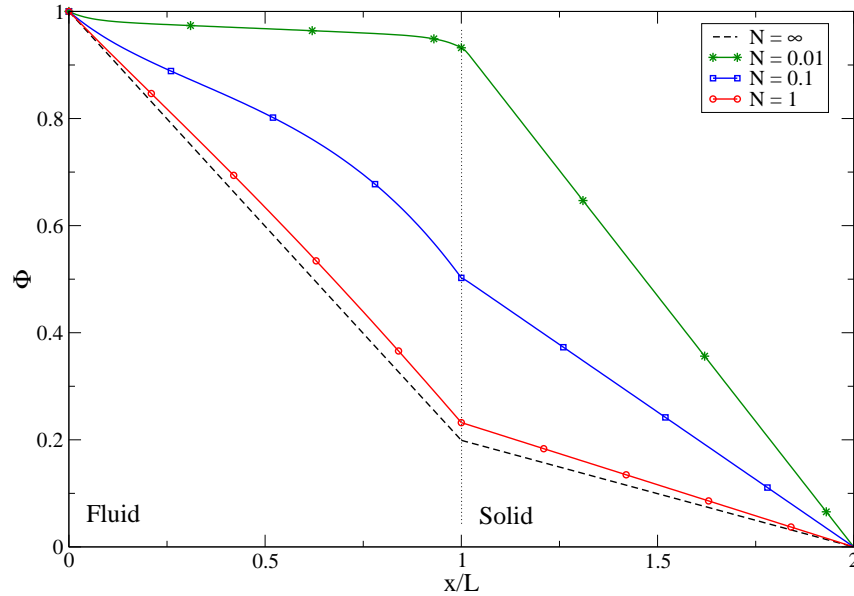


Figure 7.11: Surface radiative heat transfer in fluid and solid rectangular domains. When the Stark number N assumes lower values, thermal radiation become more effective with respect to conduction.

and the surface temperature is one fifth of the difference of temperature between isothermal walls. This is expected after the thermal conductivity (7.33) settings.

Thermal radiation increases the overall temperature of the system. With $N = 1$ the fluid and the solid surfaces are slightly heated up by the radiative effects, but the temperature distribution in the medium is still linear.

At $N = 0.1$ the radiation significantly heats up the solid surface and adulterates the medium temperature. Close the solid boundaries ($x/L \lesssim 0.1$ and $0.9 \lesssim x/L$), conduction still dominates and a quasi-linear thermal profile arises. In the fluid domain centre ($0.1 \lesssim x/L \lesssim 0.9$), radiation from the boundary and within the medium, overcome conduction and increases the temperature. Near the isothermal left wall, temperature shows a slighter decrease than near the right solid surface. This is expected, since thermal radiation is a phenomenon that goes like T^4 and, thus, it is much less effective near the cold boundary.

When radiation dominates ($N = 0.01$) the fluid domain is almost at the same temperature of the hot wall, and slightly decreases when the solid surface is approached.

More analysis, including convection, are requested to fully address the role of the different parameters of the system.

7.4 Conclusions

Validation of the radiative model summarised in section 7.1, is achieved. Several benchmark cases are reproduced and the results are compared with numerical data from different sources.

First, the numerical and analytical solutions of the P_1 -equation are compared in a simple case. Different settings for the radiative parameters are used. The numerical solutions always fits the analytical ones; hence, the implementation of the mathematical model is correctly carried out.

Second, the prediction capability of the P_1 -model is investigated with respect to other numerical models reported in literature. An excellent agreement with the reference solutions is achieved for the two parallel plates case. On the contrary, in square geometry cases the predictions are less accurate near the corners, where the solid boundaries generates a collimated irradiation, and for optical thick medium. These are two well known limits of the P_1 -model (cf. section 6.1.2 and [48]). Moreover, the model fails in reproducing a pure scattering medium. This is due to the fact that the governing equation (7.2) reduces to a Laplace equation when κ is set to zero. Thus, the incident radiation G is completely determined by the Marshak's boundary condition, that is recognised not to be accurate [43] and tends to overestimate the emitted radiation. Indeed, an artificial reduction of boundaries emissivity generates better predictions. When the participating medium is present, the effects of boundaries emission are reduced and, generally speaking, better results are achieved.

Subsequently, interaction of radiation with conduction and convection is studied. In both cases a good agreement with reference solutions is obtained.

Finally, the surface radiative heat transfer is tested in a simple case. Although the simulations performed cannot be compared with numerical or experimental data, the results are reasonable and in accordance with the physics of thermal radiation. Moreover, the solver appears to be numerically stable.

In summary, the P_1 -approximation model gives satisfactory prediction of thermal radiation effects, despite the simplicity of the mathematical model. In general, the model tends to slightly overestimate the RHT. Furthermore, it can lose accuracy in optical thick limit and when a collimate irradiation is generated from boundaries.

Although such limitations, the P_1 -approximation required a (extremely) lower computational cost if compared to more accurate methods, like DOM. This is essential in a non-steady simulation such LES, where a temperature-radiation coupling loop have to be performed in order to ensure the instantaneous thermal equilibrium.

7.5 Appendix: Marshak's boundary condition

In this appendix, the implementation of Marshak's boundary condition (7.15) used by `MarshakRadiation.C` is presented and described. Before to focus the attention on our particular case, the generic structure of the mixed boundary condition has to be explained.

The mixed boundary condition

The mixed condition is a combination of a fixed value (Dirichlet) and a fixed gradient (Neumann) boundary conditions, controlled by a weight variable. If ϕ is a generic variable and ϕ_p is its value on the boundary, the Dirichlet and Neumann boundary conditions read:

$$\phi_p = \phi_{ref} \quad (\text{Dirichlet}) \quad (7.37)$$

$$\phi_p = \phi_{int} + \Delta \frac{\partial \phi}{\partial \hat{n}} \quad (\text{Neumann}) \quad (7.38)$$

where ϕ_{ref} is the value at the boundary, fixed by Dirichlet condition; ϕ_{int} is the value at the centre of the boundary cell; $\partial \phi / \partial \hat{n}$ is the gradient normal to the boundary, fixed by Neumann condition; Δ is the distance between the face centre and internal cell centre. The *mixed* boundary condition is defined in OpenFOAM by the following equation:

$$\phi_p = w \phi_{ref} + (1 - w) \left(\phi_{int} + \frac{\partial \phi}{\partial \hat{n}} \Delta \right) \quad (7.39)$$

where w is a weight function.

The header file `mixedFvPatchField.H` includes a short description of mixed condition. In the `mixedFvPatchField.C` file is explicitly defined the `evaluate` function, that performs the computation:

```

160 template<class Type>
161 void mixedFvPatchField<Type>::evaluate(const Pstream::commsTypes)
162 {
163     if (!this->updated())
164     {
165         this->updateCoeffs();
166     }
167
168     Field<Type>::operator=
169     (
170         valueFraction_*refValue_
171     +
172     (1.0 - valueFraction_)*
173     (
174         this->patchInternalField()
175     + refGrad_/this->patch().deltaCoeffs()

```

```

176     )
177   );
178
179   fvPatchField<Type>::evaluate();
180 }

```

Code 7.6: mixedFvPatchField.C

Lines 168-177 report the implementation of equation (7.39), where the different terms correspond to:

$$\begin{aligned} \text{refValue}_ &= \phi_{ref} & \text{refGrad}_ &= \partial\phi/\partial\hat{n} \\ \text{this->patchInternalField}() &= \phi_{int} & \text{valueFraction}_ &= w \\ \text{this->patch}().\text{deltaCoeffs}() &= 1/\Delta \end{aligned}$$

This generic structures is adapted for computing different boundary conditions. In our particular case, this is used to reproduce the Marshak's boundary condition (7.2) in file MarshakRadiation.C.

Marshak's boundary condition implementation

Part of the code file MarshakRadiation.C is now reported and analysed.

```

155 void Foam::MarshakRadiationFvPatchScalarField::updateCoeffs()
156 {
157     if (this->updated())
158     {
159         return;
160     }
161
162     // Since we're inside initEvaluate/evaluate there might be processor
163     // comms underway. Change the tag we use.
164     int oldTag = UPstream::msgType();
165     UPstream::msgType() = oldTag+1;
166
167     // Temperature field
168     const scalarField& Tp =
169         patch().lookupPatchField<volScalarField, scalar>(TName_);
170
171     // Re-calc reference value
172     refValue() = 4.0*constant::physicoChemical::sigma.value()*pow4(Tp);
173
174     // Diffusion coefficient - created by radiation model
175     const scalarField& gamma =
176         patch().lookupPatchField<volScalarField, scalar>("gammaRad");
177
178     const scalarField temissivity = emissivity();
179
180     const scalarField Ep(temissivity/(2.0*(2.0 - temissivity)));

```

```

181
182 // Set value fraction
183 valueFraction() = 1.0/(1.0 + gamma*patch().deltaCoeffs()/Ep);
184
185 // Restore tag
186 UPstream::msgType() = oldTag;
187
188 mixedFvPatchScalarField::updateCoeffs();
189 }

```

Code 7.7: MarshakRadiation.C

First, some auxiliary variables are created:

$T_p = T(\mathbf{r}_w)$, the wall temperature (lines 168-169);

$\gamma = 1/(3\kappa + 3\sigma_s - \sigma_s A)$, taken from the radiation model (lines 175-176);

$E_p = \epsilon/2(2 + \epsilon)$, where ϵ is the solid body emissivity (lines 178-180);

and the following function values are set up:

$\text{refValue}() = 4\sigma T^4(\mathbf{r}_w)$ in line 172;

$\text{valueFraction}() = 1/[1 + \gamma/(\Delta E_p)]$ in line 183.

These last two are required by function `updateCoeffs()` at line 188, that returns the boundary values.

The explicit computation is not here specified, but it is inherited by the class `mixedFvPatchScalarField`. Tracking back to the code and following the class hierarchy in OpenFOAM source code, it turns out that the explicit computation is defined in the template class `mixedFvPatchField` that was presented in previous section.

The variables `valueFraction_` and `refValue_` are set in code 7.7, while `refGrad_ = 0` is set in a part of the same file not reported. Substituting this variables in equation (7.39), we obtain:

$$G(\mathbf{r}_w) = \frac{1}{1 + \frac{\gamma}{\Delta E_p}} 4\sigma T^4(\mathbf{r}_w) + \left[1 - \frac{1}{1 + \frac{\gamma}{\Delta E_p}} \right] G_{int}. \quad (7.40)$$

Rearranging this expression, we can verify that this is a numerical discretisation of Marshak's condition.

The equivalence of the two formulation can be mathematically checked in the simple case of an orthogonal and hexahedral mesh, for which the normal gradient of the equation (7.15) is discretised as

$$\frac{G_{int} - G(\mathbf{r}_w)}{\Delta} \cong \hat{\mathbf{n}} \cdot \nabla G(\mathbf{r}_w) = \frac{\epsilon}{2 - \epsilon} \frac{3\kappa + 3\sigma_s - \sigma_s A}{2} [G(\mathbf{r}_w) - 4\sigma T^4(\mathbf{r}_w)].$$

Formula (7.40) can be derived from the previous one, using the previous definition of the constants E_p and γ .

Bibliography

- [1] *ASHRAE Handbook Fundamentals - SI edition*, Ed. Ashrae, 2005.
- [2] AA. VV., *Programmer's Guide*, OpenFOAM Foundation, 15th December 2011.
- [3] AA. VV., *User Guide*, OpenFOAM Foundation, 15th December 2011.
- [4] M. ABRAMOWITZ AND I. A. STEGUN, *Handbook of Mathematical Functions*, Dover Publications, 1972.
- [5] F. AMPOFO AND T. KARAYIANNIS, *Experimental benchmark data for turbulent natural convection in air filled square cavity*, Int. J. Heat and Mass Transfer, 46 (2003), p. 3551.
- [6] G. B. ARFKEN AND H. J. WEBER, *Mathematical methods for physicists*, Academic press, 2001.
- [7] V. ARMENIO AND S. SARKAR, *An investigation of stably stratified turbulent channel flow using large-eddy simulation*, J. Fluid Mechanics, 459 (2002), p. 1.
- [8] A. W. T. BARENBRUG, *Psychrometry and Psychrometric Charts*, Cape and Transvaal Printers Ltd., 3rd ed., 1974.
- [9] L. BARLETTI, *Metodi matematici per le applicazioni*, lecture notes, Dipartimento di Matematica e Informatica "Ulisse Dini", Università di Firenze, 2013/2014.
- [10] C. BOSSHARD, A. DEHBI, M. DEVILLE, E. LERICHE, R. PURAGLIESI, AND A. SOLDATI, *Large eddy simulation of the differentially heated cubic cavity flow by the spectral element method*, Computers and Fluids, 86 (2013), p. 210.
- [11] J. J. BREHM AND W. J. MULLIN, *Introduction to the Structure of Matter*, John Wiley and Sons, 1989.

-
- [12] A. BUKHVOSTOVA, E. RUSSO, J. KUERTENA, AND B. GEURTS, *Comparison of dns of compressible and incompressible turbulent droplet-laden heated channel flow with phase transition*, Int. J. of Heat and Fluid Flow, 50 (2014), p. 445.
- [13] C. CINTOLESI, A. PETRONIO, AND V. ARMENIO, *Large eddy simulation of turbulent buoyant flow in a confined cavity with conjugate heat transfer*, Physics of fluids, 27 (2015). doi: 10.1063/1.4930815.
- [14] V. A. F. COSTA, *Transient natural convection in enclosures filled with humid air, including wall evaporation and condensation*, Int. J. Heat and Mass Transfer, 55 (2012), p. 5479.
- [15] R. COURANT AND D. HILBERT, *Methods of mathematical physics*, Interscience, 1953.
- [16] A. L. CROSBIE AND P. SCHRENKER, *Radiative transfer in a two-dimensional rectangular medium exposed to diffuse radiation*, Journal of quantitative spectroscopy and radiative transfer, 31 (1984), p. 339.
- [17] M. DAS AND K. REDDY, *Conjugate natural convection heat transfer in an inclined square cavity containing a conducting block*, Int. J. of Heat and Mass Transfer, 49 (2006), p. 4987.
- [18] P. G. DE GENNES, *Wetting: statics and dynamics*, Reviews of Modern Physics, 57 (1985), p. 827.
- [19] A. DORFMAN AND Z. RENNER, *Conjugate problems in convective heat transfer: Review*, Mathematical Problems in Engineering, 2009 (2009).
- [20] F. DUCHAINE, A. CORPRON, L. PONS, V. MOUREAU, F. NICOUD, AND T. POINSOT, *Development and assessment of a coupled strategy for conjugate heat transfer with large eddy simulation: application to a cooled turbine blade*, Int. J. Heat and Fluid Flow, 30 (2009), p. 1129.
- [21] F. DUCHAINE, S. MENDEZ, F. NICOUD, A. CORPRON, V. MOUREAU, AND T. POINSOT, *Conjugate heat transfer with large eddy simulation for gas turbine components*, Comptes Rendus Mecanique, 337 (2009), p. 550.
- [22] A. EINSTEIN AND L. INFELD, *Evolution of Physics*, Cambridge University Press, 1938.
- [23] A. GARAI, J. KLEISSL, AND S. SARKAR, *Flow and heat transfer in convectively unstable turbulent channel flow with solid-wall heat conduction*, J. Fluid Mech., 757 (2014), p. 57.
- [24] M. GERMANO, *Turbulence: the filtering approach*, J. Fluid Mechanics, 238 (1992), p. 325.

- [25] M. GERMANO, U. PIOMELLI, P. MOIN, AND W. CABOT, *A dynamic subgrid-scale eddy viscosity model*, Phys. Fluids, A3 (1991), p. 1760.
- [26] S. S. GIRIMAJI AND K. S. ABDOL-HAMID, *Partially-averaged navier stokes model for turbulence: Implementation and validation*, 43rd AIAA Aerospace Sciences Meeting and Exhibit, 2005-0502 (2005).
- [27] H. C. HOTTEL AND A. F. SAROFIM, *Radiative Transfer*, McGraw-Hill Book Company, first ed., 1967.
- [28] J. R. HOWELL, R. SIEGEL, AND M. P. MENGÜÇ, *Thermal Radiation Heat Transfer*, Taylor and Francis, fifth ed., 2011.
- [29] K. HSIEH AND F. LIEN, *Numerical modeling of buoyancy-driven turbulent flows in enclosures*, Int. J. Heat and Fluid Flow, 25 (2004), p. 659.
- [30] C. HUANG, W. YAN, AND J. JANG, *Laminar mixed convection heat and mass transfer in vertical rectangular ducts with film evaporation and condensation*, Int. J. of Heat and Mass Transfer, 48 (2005), p. 1772.
- [31] A. IBRAHIM, D. SAURY, AND D. LEMONNIER, *Coupling of turbulent natural convection with radiation in an air-filled differentially-heated cavity at $ra = 1.5 \times 10^9$* , Computers and Fluids, 88 (2013), p. 115.
- [32] F. INCROPERA, D. DEWITT, T. BERGMAN, AND A. LAVINE, *Fundamentals of heat and mass transfer*, John Wiley and Sons Inc., 6th ed., 2007.
- [33] C. ISKRA AND C. SIMONSON, *Convective mass transfer coefficient for a hydrodynamically developed airflow in a short rectangular duct*, Int. J. of Heat and Mass Transfer, 50 (2007), p. 2376.
- [34] R. I. ISSA, *Solution of the implicitly discretized fluid flow equations by operator-splitting*, J. Computational Physics, 62 (1985), p. 40.
- [35] R. I. ISSA, A. D. GOSMAN, AND A. P. WATKINS, *The computation of compressible and incompressible recirculating flows by a non-iterative implicit scheme*, J. Computational Physics, 62 (1986), p. 66.
- [36] N. LAAROSSI AND G. LAURIAT, *Conjugate thermosolutal convection an condensation of humid air in cavity*, Int. J. Thermal Sciences, 47 (2008), p. 1571.
- [37] O. LAGUERRE, S. BEN AMARA, G. ALVAREZ, AND D. FLICK, *Transient heat transfer by free convection in a packed bed of spheres: comparison between two modelling approaches and experimental results*, Appl. Therm. Eng., 28 (2008), p. 14.

-
- [38] O. LAGUERRE, S. BEN AMARA, AND D. FLICK, *Numerical simulation of simultaneous heat and moisture transfer in a domestic refrigerator*, Int. J. of Refrigeration, 33 (2010), p. 1425.
- [39] O. LAGUERRE, S. BEN AMARA, D. REMY, AND D. FLICK, *Experimental and numerical study of heat and moisture transfers by natural convection in a cavity filled with solid obstacles*, Int. J. of Heat and Mass Transfer, 52 (2009), p. 5691.
- [40] M. G. LAWRENCE, *The relationship between relative humidity and the dewpoint temperature in moist air: A simple conversion and applications*, Bulletin American Meteorological Society, 86 (2005), p. 225.
- [41] J. LIENHARD IV AND J. LIENHARD V, *A heat transfer textbook*, Phlogiston Press - Cambridge, 2.02 ed., 2012.
- [42] D. LILLY, *A proposed modification of germano subgrid-scale closure method*, Phys. Fluids, A4 (1992), p. 633.
- [43] F. LIU, J. SWITENBANK, AND E. S. GARBETT, *The boundary condition of the p_n -approximation used to solve the radiative transfer equation*, International Journal of Heat and Mass Transfer, 35 (1992), p. 2043.
- [44] E. MARÍN, *Characteristic dimension for heat transfer*, Lat. Am. J. Phys. Educ., 4 (2010), p. 56.
- [45] C. MENEVEAU, T. LUND, AND W. CABOT, *A lagrangian dynamic subgrid-scale model of turbulence*, J. Fluid Mechanics, 316 (1996), p. 353.
- [46] S. MERGUI AND F. PENOT, *Convection naturelle en cavité carrée différentiellement chauffée: investigation expérimentale à $ra = 1.69 \times 10^9$* , Int. J. Heat and Mass Transfer, 39 (1996), p. 563.
- [47] M. F. MODEST, *Radiative equilibrium in a rectangular enclosure bounded by gray walls*, Journal of quantitative spectroscopy and radiative transfer, 15 (1975), p. 339.
- [48] M. F. MODEST, *Radiative Heat Transfer*, Elsevier, third ed., 2013.
- [49] P. MOIN AND K. MAHESH, *Direct numerical simulation: a tool in turbulence research*, Annu. Rev. Fluid Mechanics, 30 (1998), p. 539.
- [50] P. J. OLIVEIRA AND P. I. ISSA, *An improved algorithm for the computation of buoyancy driven flows*, Numerical Heat Transfers, part B, 640 (2001), p. 473.

- [51] M. OMRI AND N. GALANIS, *Numerical analysis of turbulent buoyant flows in enclosures: influence of grid and boundary conditions*, Int. J. Thermal Sciences, 46 (2007), p. 727.
- [52] A. ORON, S. DAVIS, AND S. BANKOFF, *Long-scale evolution of thin liquid films*, Reviews of Modern Physics, 69 (1997), p. 931.
- [53] S. PENG AND L. DAVIDSON, *Large eddy simulation for turbulent buoyant flow in a confined cavity*, Int. J. Heat and Mass Transfer, 22 (2001), p. 323.
- [54] A. PETRONIO, *Numerical investigation of condensation and evaporation effects inside a tub*, Ph.D. thesis, School of Environmental and Industrial Fluid Mechanics, University of Trieste, 2010. NBN urn:nbn:it:units-9122.
- [55] U. PIOMELLI, *Large-eddy simulation of turbulent flows. Part 1: Introduction*, lecture notes, Department of Mechanical and Materials Engineering, Queen's University Kingston (Ontario) Canada, 2014.
- [56] S. POPE, *Turbulent Flows*, Cambridge University Press, 2000.
- [57] A. QUARTERONI AND A. VALLI, *Domain decomposition methods for partial differential equations*, Oxford University Press, 1999.
- [58] A. RAIMUNDO, A. GASPAR, A. VIRGÍLIO, M. OLIVEIRA, AND D. QUINTELA, *Wind tunnel measurements and numerical simulations of water evaporation in forced convection airflow*, Int. J. of Thermal Sciences, 86 (2014), p. 28.
- [59] M. M. RAZZAQUE, D. E. KLEIN, AND J. R. HOWELL, *Finite element solution of radiative heat transfer in a two-dimensional rectangular enclosure with gray participating media*, ASME Journal of Heat Transfer, 105 (1983), p. 933.
- [60] M. M. RAZZAQUE, D. E. KLEIN, AND J. R. HOWELL, *Coupled radiative and conductive heat transfer in a two-dimensional rectangular enclosure with gray participating media using finite elements*, ASME Journal of Heat Transfer, 106 (1984), p. 613.
- [61] D. R. ROUSSE, *Numerical predictions of two-dimensional conduction, convection, and radiation heat transfer. i. formulation*, International Journal Thermal Science, 315 (2000), p. 97.
- [62] D. R. ROUSSE, G. GAUTIER, AND J. F. SACADURA, *Numerical predictions of two-dimensional conduction, convection, and radiation heat transfer. ii. validation*, International Journal Thermal Science, 332 (2000), p. 97.

- [63] E. RUSSO, J. KUERTEN, C. VAN DER GELD, AND B. GEURTS, *Modeling water droplet condensation and evaporation in dns of turbulent channel flow*, J. of Physics Conference Series, 318 (2011).
- [64] P. SAGAUT, *Large eddy simulation for incompressible flows. An introduction*, Springer, 2000.
- [65] J. SALAT, S. XIN, P. JOUBERT, A. SERGENT, F. PENOT, AND P. LE QUÉRÉ, *Experimental and numerical investigation of turbulent natural convection in a large air-filled cavity*, Int. J. Heat and Fluid Flow, 25 (2004), p. 824.
- [66] R. SIEGEL AND J. R. HOWELL, *Thermal Radiation Heat Transfer*, Hemisphere Publishing Corporation, third ed., 1992.
- [67] J. SMAGORINSKY, *general circulation experiments with the primitive equations: I. the basic experiment*, Mon. Weather Rev., 91 (1963), p. 99.
- [68] P. SOSNOWSKI, *Numerical investigation of evaporation and condensation of thin films in conjugated heat transfer systems*, Ph.D. thesis, School of Environmental and Industrial Fluid Mechanics, University of Trieste, 2013. NBN urn:nbn:it:units-10080.
- [69] P. SOSNOWSKI, A. PETRONIO, AND V. ARMENIO, *Numerical model for thin liquid film with evaporation and condensation on solid surfaces in a systems with conjugated heat transfer*, Int. J. Heat and Mass Transfer, 66 (2013), p. 382.
- [70] P. SPALART, W.-H. JOU, M. STRELETS, AND S. ALLMARAS, *Comments on the feasibility of les for wings, and on a hybrid rans/les approach*, First AFOSR International Conference on DNS/LES - Ruston, Louisiana, (1997).
- [71] H. SUN, G. LAURIAT, AND X. NICOLAS, *Natural convection and wall condensation or evaporation in humid air-filled cavities subjected to wall temperature variations*, Int. J. Thermal Sciences, 50 (2011), p. 663.
- [72] P. TALUKDAR, C. ISKRA, AND C. SIMONSON, *Combined heat and mass transfer for laminar flow of moist air in a 3d rectangular duct: Cfd simulation and validation with experimental data*, Int. J. of Heat and Mass Transfer, 51 (2008), p. 3091.
- [73] H. TENNEKES AND J. LUMELEY, *A first course in turbulence*, MIT Press, 1999.
- [74] U. THIELE, *Structure formation in thin liquid films*, vol. 490, CISM International Centre for Mechanical Sciences, 2007. Chapter: Thin Films of Soft Matter.

-
- [75] Y. TIAN AND T. KARAYIANNIS, *Low turbulence natural convection in an air filled square cavity. Part I: the thermal and fluid flow fields*, Int. J. Heat and Mass Transfer, 43 (2000), p. 849.
- [76] Y. TIAN AND T. KARAYIANNIS, *Low turbulence natural convection in an air filled square cavity. Part II: the turbulence quantities*, Int. J. Heat and Mass Transfer, 43 (2000), p. 867.
- [77] I. TISELJ, R. BERGANT, B. MAVKO, I. BAJSIĆ, AND G. HETSRONI, *Dns of turbulent heat transfer in channel flow with heat conduction in the solid wall*, J. Heat Transfer, 123 (2001), p. 849.
- [78] R. VISKANTA, *Interaction of heat transfer by conduction, convection, and radiation in a radiating fluid*, ASME Journal, 85 (1963), p. 318.
- [79] R. VISKANTA, *Radiative transfer in combustion systems: fundamental and applications*, Begell House Publishers, 2005.
- [80] R. VISKANTA, *Computation of radiative transfer in combustion systems*, International Journal of Numerical Methods for Heat and Fluid Flow, 18 (2008), p. 415.
- [81] R. VISKANTA AND M. P. MENGÜÇ, *Radiation heat transfer in combustion systems*, Progress in Energy and Combustion Science, 13 (1987), p. 97.
- [82] J. WELTY, C. WICKS, R. WILSON, AND G. RORRER, *Fundamentals of momentum, heat, and mass transfer*, John Wiley and Sons Inc., 5th ed., 2008.
- [83] C. ZIMMERMANN AND R. GROLL, *Modelling turbulent heat transfer in a natural convection flow*, J. of Applied Mathematics and Physics, 2 (2014), p. 662.